AD-A283 854

JMENTATION PAGE

Form Approved
OMB No. 0704-0188

2. REPORT DATE	3. REPORT TYPE AND DATES COVERED
Aug 94	

4. TITLE AND SUBTITLE
Effects of Surface Roughness on Local Film Cooling Effectiveness and Heat Transfer Coefficients

5. FUNDING NUMBERS

6. AUTHOR(S)
Douglas Neal Barlow

7. PERFORMING ORGANIZATION NAME(S) AND ADDRESS(ES)
AFIT Students Attending:

Arizona State University

8. PERFORMING ORGANIZATION REPORT NUMBER
AFIT/CI/CIA

94-038D

9. SPONSORING/MONITORING AGENCY NAME(S) AND ADDRESS(ES)
DEPRTMENT OF THE AIR FORCE
AFIT/CI
2950 P STREET
WRIGHT-PATTERSON AFB OH 45433-7765

10. SPONSORING/MONITORING AGENCY REPORT NUMBER

11. SUPPLEMENTARY NOTES

12a. DISTRIBUTION/AVAILABILITY STATEMENT
Approved for Public Release IAW 190-1
Distribution Unlimited
MICHAEL M. BRICKER, SMSgt, USAF
Chief Administration

12b. DISTRIBUTION CODE

13. ABSTRACT *(Maximum 200 words)*

14. SUBJECT TERMS	15. NUMBER OF PAGES 295
	16. PRICE CODE

17. SECURITY CLASSIFICATION OF REPORT	18. SECURITY CLASSIFICATION OF THIS PAGE	19. SECURITY CLASSIFICATION OF ABSTRACT	20. LIMITATION OF ABSTRACT

EFFECT OF SURFACE ROUGHNESS ON LOCAL FILM COOLING EFFECTIVENESS AND HEAT TRANSFER COEFFICIENTS

by

Douglas Neal Barlow

A Dissertation Presented in Partial Fulfillment
of the Requirements for the Degree
Doctor of Philosophy

ARIZONA STATE UNIVERSITY

August 1994

EFFECT OF SURFACE ROUGHNESS
ON LOCAL FILM COOLING EFFECTIVENESS
AND HEAT TRANSFER COEFFICIENTS

by

Douglas Neal Barlow

has been approved

July 1994

APPROVED:

_____, Chairperson

_____

_____

_____

_____

Supervisory Committee

ACCEPTED:

_____
Department Chairperson

_____
Dean, Graduate College

ABSTRACT

In high temperature gas turbine engines, the life cycle of the hot section is extremely dependent on accurate design prediction of component temperature distribution. Particular attention must be paid to the film cooling performance of the first stage stator vanes where the highest heat loads are encountered. Recent investigations have determined during operation the smooth surface of high pressure turbine vanes become rough due to corrosion, oxidation and particulate impact. A transient experimental method has been developed to obtain both local heat transfer and cooling effectiveness information downstream of a row of film cooling holes on a rough flat plate. This investigation provides information on the effects of roughness on film cooling heat transfer for a Reynolds number and dimensionless boundary layer momentum thickness which match conditions applicable to the pressure side of the first stage turbine vane of the Pratt and Whitney F-100-PW229 engine. Data for film cooling on rough surfaces are extremely limited in the literature. However, comparison with the available data is made. The transient experimental procedure employed here uses encapsulated liquid crystal coatings and an automated computer vision data acquisition system to obtain detailed local data. In order to assess the method's success, detailed heat transfer data are also reported for smooth surface configurations. Comparison with available data shows good agreement indicating successful development of the technique. The test procedures and data acquisition methods are reported. Finite difference work is included to assess the rough surface model. 8.5% mainstream turbulence levels approach those found in actual first stage turbine stator vanes.

DEDICATION

I dedicate this dissertation to all of my family. Without their support and love I couldn't have been successful. Thank you Diana, Ben, Katie and Caralyn for enduring a seemingly endless life style change in order to make this possible.

ACKNOWLEDGEMENTS

Thank you Professor Leon Florschuetz for guidance during the last year of this work. Your supportive, trusting attitude has been a bright spot in this adventure.

When I picked a committee, I did so based not only on their scholarly knowledge, which is abundantly present, but more importantly based on their professional and social skills. With these skills, life is meaningful. Thank you Professor William Bickford, Professor Earl Logan and Professor Hans Mittelmann.

Dr. Yong Kim, I can't imagine success without your knowledgeable, questioning presence. Thanks for sharing your creative, can-do approach to engineering with me. God be with you.

Dr. Darryl Metzger brought me to Arizona State, believed in my abilities and pointed me in the right direction for this work. I wish he were here now. He loved his work in heat transfer and I hope he is happy with what I've done.

Thank you Col. Michael Smith, Col. Randy Stiles and Col. John Russell for supporting my studies officially and personally. In the future, I will endeavor to pay you and the Air Force back.

My friend Michael Schneider, Dr. Metzger once told me that a person only completely knows a few people during his life, but one of those is the person you survive your Ph.D. work with. Michael, together we've weathered the good and the bad and through it all we've always been there for the other guy. Freund für immer, foreign dude!

TABLE OF CONTENTS

LIST OF TABLES

LIST OF FIGURES

Figure Page

NOMENCLATURE

A	area
c_f	friction coefficient
c_p	specific heat of air
D	Film hole diameter
h	convective heat transfer coefficient where $q = h(T_r - T_w)$
$\bar{h}$	laterally averaged convective heat transfer coefficient
$\langle\bar{h}\rangle$	area averaged coefficient, obtained by streamwise averaging of $\bar{h}$
H	absolute local height of roughness elements
k	thermal conductivity
k_s	equivalent sand-grain roughness
M	blowing ratio, $\rho_f U_f / \rho_\infty U_\infty$
Nu_x	Nusselt number, hX/k
Pr	Prandtl number
Pr_t	turbulent Prandtl number
Ra	average surface roughness
Re_k	roughness Reynolds number, $u_\tau k_s / \nu$
Re_x	Reynolds number, $U_\infty X / \nu$
St	Stanton number, $h / \rho U_\infty c_p$
q	heat transfer rate per unit of area
T	temperature
t	time
U	velocity
u_τ	shear velocity
V	volume
X	distance downstream from trailing edge of film cooling hole
Y	distance perpendicular to convectively cooled surface
Z	distance laterally across surface measured from center of film hole
α	thermal diffusivity
ρ	density
η	film cooling effectiveness, $(T_r - T_\infty)/(T_f - T_\infty)$
η_{max}	maximum value of η at a given X
η_{min}	minimum value of η at a given X

$\bar{\eta}$ laterally averaged film cooling effectiveness at a given X

$\bar{\eta}_c$ film cooling effectiveness laterally averaged over $\pm\frac{1}{2}$ D of the film hole centerline

$<\bar{\eta}>$ area averaged effectiveness, obtained by stream wise averaging of $\bar{\eta}$

δ_1 displacement thickness of boundary layer

δ_2 momentum thickness of boundary layer

δ boundary layer thickness, $U=0.99U_\infty$

ζ lateral smoothness parameter, $\zeta = (\eta_{max} - \eta_{min}) / \bar{\eta}$ at a given X

τ time step

τ_o wall shear stress

ν kinematic viscosity

Subscripts

aw adiabatic wall

b blue

f film

g green

i initial

o no film flow

RS rough surface

r reference

r red

s smooth surface

w wall

∞ free-stream state

CHAPTER 1
INTRODUCTION

1.1 Background

The life cycle of the gas turbine hot section is extremely dependent on accurate design prediction of component temperature distribution. This distribution is necessary in establishing disk and turbine blade dimensions as well as turbine tip to shroud clearances. Prediction of the temperature distribution in the hot section requires extensive material property knowledge and accurate convective heat transfer information. The lack of reliable local heat transfer coefficients often leads the designer to be conservative using coolant flow in the disk and turbine cavities. As a result, an unnecessary penalty exists on the engine cycle causing higher specific fuel consumption and lower maximum thrust levels.

Engine manufacturers have recognized for over four decades that to increase overall engine efficiency, while maintaining high specific thrusts, the turbine inlet temperature must increase. Since 1950, the turbine inlet temperature has risen from the 1800°F area to well over 2800°F today. This rise in temperature has been made possible by the use of abundant turbine cooling and continuous improvements in high temperature materials. The need for turbine cooling was recognized almost from the inception of the first turbojet engine. Cooling studies were first performed in the 1940s and many investigations were carried out in the 1950s. Around 1960, turbine cooling was first used in a commercial aircraft engine (Oates, 1985). Tremendous improvements in blade materials, including single crystal alloys and directionally solidified eutectics, have permitted allowable metal temperatures

to increase from around 1600°F in 1960 to near 2100°F today. Unfortunately for engine performance, the temperature gap between turbine inlet temperature and allowable metal temperatures must be filled with turbine cooling. Exacerbating this difference is that hot spots entering the first stage turbine vane resulting from burner combustion patterns, often are 500°F above the average inlet temperature. To handle this temperature difference, convection, impingement, and film cooling are used by manufacturers.

The cooling flow required for modern aircraft engines is on the order of 20% of the compressor discharge flow. This large quantity of air reduces the advantages of high turbine inlet temperatures in two ways. First, the capability of the turbine to power the compressor is reduced because of lower temperatures. Secondly, the cooling air mixes with the mainstream flow, causing aerodynamic losses. These effects are strong and vigorous steps are taken to minimize them by minimizing the quantity of cooling air. Detailed heat transfer information is essential for the effective design of hot section components which experience extreme thermal stress variations. But because the complete nature of the complex three dimensional flow in the turbine section is difficult to model and currently not fully understood, a comprehensive theoretical solution to the problem is not available. Consequently, heat transfer information for the designer and for developing design models, must come from experimentation.

Table 1.1 (Oates, 1985) lists the cooling air supply system requirements for a typical two stage gas turbine hot section. Noteworthy with respect to the work documented in this study, is that the first stage vanes require the largest percentage of mainstream air for cooling.

Table 1.1 Percentage of Mainstream Air
Used in Cooling Turbine Section

Turbine Component	% of Mainstream Air Bled from Compressor for Cooling
1st Stage Stator Vanes	6.3
1st Stage Stator End Walls	3.1
1st Stage Rotor	2.7
1st Stage Rotor End Walls	0.8
1st Stage Rotor Disk	4.4
2nd Stage Stator Vanes	1.7
2nd Stage Rotor	1.1
2nd Stage Rotor Disk	1.3

The stagnation temperature and free stream temperature potential associated with the first vane are much higher than those of the subsequent blade rows. While the first stage rotor must also contend with high centrifugal forces in addition to the high thermal stresses, the combined effect , termed creep, is limited by two factors. First, gas temperatures are reduced and hot spots diluted by cooling air mixed with the flow in the first vane. Also, because the rotor is retreating from the high velocity flow, the stagnation temperatures are significantly lower than would otherwise be the case. The first stage vane is the focus of this work even though the results have implications for each hot section component.

As mentioned earlier, several methods of cooling turbine blades are available including internal convection and impingement cooling. In these processes, cooling air is brought in at the root or tip of the airfoil and then discharged most often through the trailing edge. This method of cooling is quite efficient and is used when a cooling effectiveness below 0.5 is required. The average cooling effectiveness (Φ) for an airfoil is defined by

$$\Phi = \frac{T_\infty - T_m}{T_\infty - T_f}$$

where T_m is the average metal temperature of the blade and T_f is the temperature of the cooling air flow . Cooling by these methods is limited because the air supply pressure is limited and an effectiveness above 0.5 requires an extremely high pressure above that available from the compressor. In addition, with high cooling effectiveness levels from only internal cooling, the temperature gradients become very large and aggravate thermal stress problems. With the levels of cooling supply pressures generally available in turbines and because allowable metal temperatures require a higher effectiveness, film cooling is used in all modern aircraft gas turbine engines (Figure 1.2). This method of cooling provides a layer of coolant air over the airfoil, which insulates the airfoil from the hot turbine gases. When combined with internal convection cooling, film cooling is a very effective method of maintaining acceptable metal temperatures.

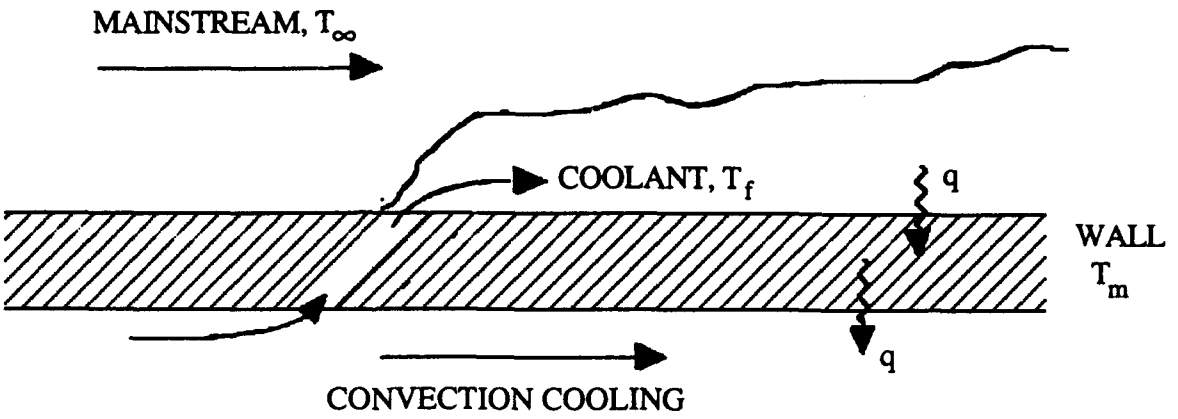

Figure 1.1 Film cooling

With few exceptions, past analytical and experimental studies have assumed a smooth wall surface. In operation, however, the surface often becomes rough through surface oxidation and foreign object deposition. A recent surface roughness investigation (Tabbita,1993) conducted by Pratt & Whitney Engine Company (P&W) dealt with the surface profile of two F100-PW229 high pressure turbine vanes. The two vanes taken from flight test engines in use at Nellis Air Force Base (AFB) and Edwards Air Force Base were examined using profilometry and microscopy to determine surface profile characteristics. Although surface roughness (Ra) of a new vane is approximately 0.06 mils, the study found surface axial Ra to vary from 0.326 mils to 1.690 mils. This increase in roughness affects both the convective heat transfer coefficient and the film cooling effectiveness. Specifically, heat transfer coefficients will increase. Film cooling effectiveness, however, is another matter and its variation depends upon both surface geometry and flow fields parameters. P&W has measured a loss in overall cooling

effectiveness (Φ) resulting from an increase in average surface roughness from 0.06 to 0.35 mils.

Likewise, work at the University of Minnesota [Goldstein, Eckert, et al. (1985)] has found that at low blowing rates (M) less than 0.6 there is a decrease in the adiabatic wall film cooling effectiveness (η) of 10-to-20 percent over that compared to a smooth surface under similar conditions. But to the contrary, at higher blowing rates (M>0.6), the film cooling performance is improved by as much as 40-50 percent under the same conditions. Here, adiabatic wall film cooling effectiveness is defined in non-dimensional form, relating the adiabatic wall temperature (T_{aw}), the free stream temperature (T_∞) and the film temperature (T_f), as

$$\eta = \frac{T_{aw} - T_\infty}{T_f - T_\infty}$$

The authors attribute this improvement to an increase in turbulence and mixing with the rough surface, which tends to dissipate the injected flow and prevent it from penetrating as far into the mainstream. This work relied on mass transfer techniques with helium as a tracer gas to obtain the analogue of the adiabatic wall temperature. This technique provides laterally averaged cooling effectiveness at discrete downstream locations and area averaged film cooling performance. It unfortunately did not provide spatially continuous effectiveness values or heat transfer coefficients. Since the magnitude of the heat transfer coefficient is expected to be larger than that of a smooth surface, the specific impact is not fully known by evaluating cooling effectiveness alone.

This study extends the encapsulated chiral nematic thermochromic liquid crystal (TLC) methods already in use at Arizona State University (ASU) to the case of a roughened surface. Using the roughness characterization data, boundary layer thickness, and Reynolds number information for the F100-PW229 1st vane provided by P&W, the focus of this study is a test plan which will, for a Reynolds number appropriate for the 1st vane environment, determine local film cooling effectiveness and heat transfer coefficients for two appropriately rough surfaces.

In addition to past studies focusing on smooth surfaces, the majority of studies have focused on flows with relatively low turbulence levels (<1%). In reality however, the turbulence intensity at the leading edge of the first vane stator can be as high as 15% or more in engine operating conditions (Mehendale and Han, 1992). This turbulence level decreases through the first stage vane, but would be expected to remain as high as 10%. This study uses flows at 6.5% and 8.5% turbulence levels. Rough surface film cooling tests are accomplished at the 8.5% turbulence level.

As is discussed more fully in the sections to follow, the accuracy of the TLC methods in use at ASU depends heavily upon accurate temperature calibration of the liquid crystals under varying lighting conditions. Methods employed in the past have included a possible uncertainty in the wall temperature (T_w) as high as $\pm 1^\circ F$ when determined using the TLC. This in itself can produce uncertainties of $\pm 4\%$ in heat transfer coefficient and film cooling effectiveness values determined by this method. This study introduces the methodology and experimental work to reduce the TLC calibration uncertainty to $\pm 0.2^\circ F$ and thus improving greatly the accuracy of the TLC method employed at ASU.

1.2 Prior Studies

As discussed in the previous section, the use of film cooling has been around since the beginning of gas turbine engines. There is a vast library of works which attempt to quantify the effect of film cooling on the heat flux at the surface and the temperature potential which drives that heat flux. A comprehensive review of the experimental findings and theoretical models for two-dimensional film cooling has been accomplished by Goldstein (1971). These studies have concentrated on three methods of introducing a secondary fluid into the boundary layer of the hot mainstream gases. In all three cases the object is to create a film of coolant downstream of the injection zone. The coolant can be injected into the mainstream through a porous wall (e.g., Goldstein et al., 1968 and Nishiwaki et al., 1961). While this results in a uniform distribution of cooling fluid, the clogging of the minute pores along with the difficulty of designing porous materials to withstand high stresses has rendered this method unusable in gas turbine designs. The next best possibility, from a uniform film standpoint, is the use of slotted configurations.

These slots can be either parallel to, as in Figure 1.3, or at angle to the mainstream flow. The earlier works (e.g. Wieghardt, 1943 and Scesca, 1943) were investigations of the effects of tangential and normal injection on downstream film cooling effectiveness. As with the porous wall approach, stress considerations as well as aerodynamic design have precluded the use of slots in gas turbine airfoil designs. A form of this type of cooling is however used extensively in combustor liner designs. By far, the use of injection through holes is the most common configuration for components experiencing high stress loads.

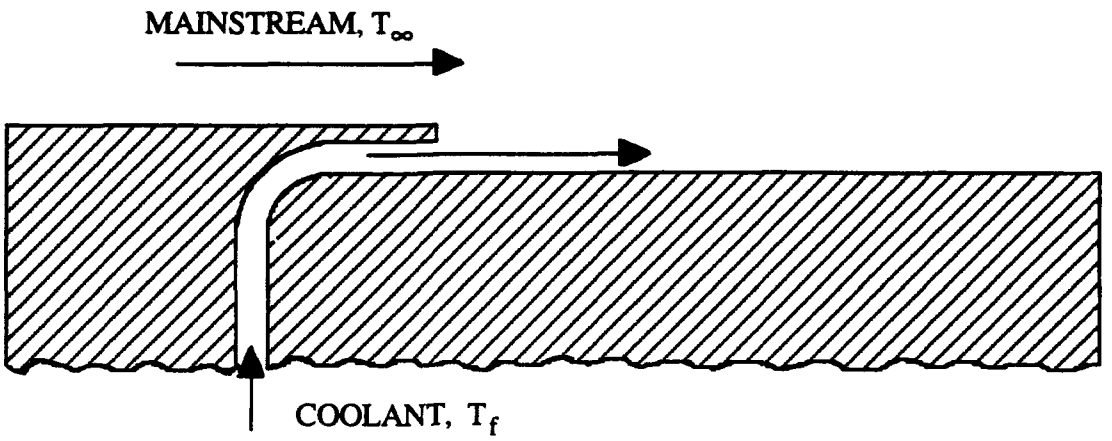

Figure 1.2 Slot film cooling

Three-dimensional film cooling (film cooling through discrete holes) has not been studied as extensively as two-dimensional film cooling. Most of the earliest research was concerned with determination of the film cooling effectiveness and is reviewed by Eckert (1971). The interaction between the cooling jets and the mainstream is highly three-dimensional and unlike the slot configuration, local heat transfer characteristics rather than spatially averaged information is essential. The difficulty of the problem is even more complex because no obvious temperature potential exists. When injection is absent the temperature potential is simply the difference between the wall and mainstream temperatures. However, with injection there is mixing of the two streams. The temperature potential is therefore the wall temperature and some temperature between the film and mainstream temperatures. For constant property flows, the heat flux is expressed as

$$q = h\,(T_w - T_r)$$

Typically in these studies, a surface approximating an adiabatic wall is fabricated and the surface temperature distribution in thermal equilibrium is measured. Under these conditions the local reference temperature (T_r) can be defined as the adiabatic wall temperature and the is equation written as

$$q = h\,(T_w - T_{aw})$$

Experimentally, T_{aw}, the adiabatic wall temperature is a convenient temperature for expressing the heat transfer potential. For flow with constant properties, the heat transfer coefficient (h) expressed in this way is independent of temperature.

The adiabatic wall temperature is often presented in dimensionless form as the film cooling effectiveness as

$$\eta = \frac{T_{aw} - T_\infty}{T_f - T_\infty}$$

η is a measure of how effective the film is in protecting the surface from the hot mainstream gases.

The many investigators of these types of flows have found that numerous parameters influence the film cooling effectiveness and heat transfer coefficient, including: angle of injection, spacing between cooling holes, shape of holes, ratio of mainstream and coolant specific mass flows ($M = \rho_f U_f / \rho_\infty U_\infty$, blowing ratio), Reynolds number of each flow, turbulence intensity, mainstream boundary layer thickness, and most recently added to the list, the presence of roughness on the wall surface.

The majority of research into film cooling has concentrated on the behavior of the adiabatic film cooling effectiveness since it varies over a wide

range on film cooling surfaces with the list of parameters mentioned above. It has been common practice with many early studies to assume that the heat transfer coefficient is not significantly modified by the injection. This assumption, as this work and the work of others has shown is valid for locations some distance downstream and for low blowing ratios, but it is certainly not valid for locations near the holes and for blowing ratios on the order of one or greater. In this region, the injection of the secondary fluid significantly alters the flow pattern from that of the primary fluid alone, and the heat transfer coefficient may be either increased or decreased depending on the amount and nature of the injection (Metzger et al., 1968). This has motivated some researches to investigate the heat transfer coefficient. This information, however, is far more limited than cooling effectiveness data. Liess (1975) reported heat transfer measurements for injection through a row of 35° holes with a lateral spacing of 3.0 diameters (3D). He found that close to the injection holes, the heat transfer coefficient increased by up to 60 percent above the no-injection value and further downstream, the increase was up to 25%. With a geometry similar to Liess', Eriksen and Goldstein (1974) showed at low blowing parameters, the heat transfer coefficient with film injection was approximately equal to the heat transfer coefficient with no film injection. Above a blowing ratio of 0.5, however, h became progressively greater with blowing ratio. In addition, the effectiveness data which accompanied the work reported by Eriksen and Goldstein (1974) was published by Goldstein, Eckert, Eriksen and Ramsey (1970). The compilation of these two works is the most complete works with direct application to current gas turbine discrete hole injection angles and blowing ratios. The results of this work are used to validate the TLC methods employed in this

study. In addition to the values reported for h and η, replotted in detail in chapter 3 of this study, Goldstein et al. (1970) and work by Liess (1975) report boundary layer thickness at the point of cooling injection plays an important part in determining the film cooling effectiveness. In short, they found when the boundary layer displacement thickness at the point of injection is thin, the jet encounters a greater force, due to higher fluid momentum close to the wall, upon leaving the injection hole than for a thicker boundary layer and is turned more, remaining closer to the wall and increasing the film cooling effectiveness. This effect is also investigated in Chapter 11 of this study. Unfortunately, the work by Goldstein et al. (1970) dealt with turbulence levels on the order of 0.5%. As mentioned in the previous section, turbulence levels in gas turbine engine hot section is typically at least an order of magnitude greater. There are about a dozen published works on the effect of free-stream turbulence on film cooling effectiveness. Most of these look at slot injection or 2-D heat transfer. There are, however, several works (e.g., Jumper, 1987 and Ou et al., 1992) which do consider angled discrete holes. Ou et al. (1992) investigated turbulence levels of 5,10, and 13% turbulence for film flow over a blunt body with a semicylinder leading edge for blowing ratios of 0.4, 0.8, and 1.2. They found that progressively higher mainstream turbulence causes progressively lower film effectiveness and caused the effectiveness to drop off more quickly with distance downstream of the injection hole. In addition to Eriksen and Goldstein (1974) and Goldstein et al. (1970), Metzger and Fletcher (1971) investigated the variation of the laterally averaged heat transfer coefficient downstream of a row of holes on a flat plate. They found significant increases

(up to 50%) in the heat transfer coefficient close to the injection hole for large blowing rates.

Most of heat transfer data available in the literature is for 35° injection. This was appropriate since this was a typical injection angle for gas turbine engine airfoil designs until the last decade. In an effort to improve cooling effectiveness, 30° injection is more common in present engines. Work in this study uses 35° injection for comparison purposes and 30° injection for the rough plate injection in order to match that of the P&W F-100 turbine vanes.

As mentioned in the previous background section, the investigation by Tabbita (1993) found axial surface roughness (Ra) to vary from 0.326 mils to 1.690 mils on the pressure side of the first stage turbine vanes. This increase in roughness affects both the convective heat transfer coefficient and the film cooling effectiveness. The only published study dealing with the effect of surface roughness on film cooling is the study by Goldstein et al. (1985). In this study, film cooling effectivenesses were determined for two roughness heights over a range of blowing ratios from 0.5 to 1.5 for an injection angle of 35°. This work found at low blowing rates, less than 0.6, there was a decrease in the film cooling effectiveness of 10 to 20 percent over that of a smooth surface under similar conditions. But surprisingly, at higher blowing rates (M> 0.6), the film cooling performance improved as much as 40 to 50 percent over a smooth surface under similar conditions. This work relied on mass transfer techniques with helium as a tracer gas to obtain the analogue of the adiabatic wall temperature. This technique provides laterally averaged cooling effectiveness at discrete downstream locations and area averaged film cooling performance.

Such methods are commonly used where fabrication of a truly adiabatic surface is difficult or when the study is content to determine effectiveness without determination of heat transfer coefficients. Since the magnitude of the heat transfer coefficient is expected to be larger than that of a smooth surface, the specific impact is not fully known by evaluating cooling effectiveness alone. In addition to the lack of heat transfer data from this study, it was also conducted at boundary layer thicknesses to cooling hole ratios much larger than found in actual engines. As mentioned earlier, the work by Goldstein et al. (1970) and Eriksen and Goldstein (1974) found the boundary layer thickness to cooling hole diameter to be an important factor in film cooling effectiveness. In Chapter 9, this study does, however, use Goldstein et al.'s (1985) work for qualitative comparison.

The only applicable analytical relationship available for predicting convective heat transfer for a rough surface is developed by Kays and Crawford (1980) using a thermal law of the wall approach. Constants in the developments are assigned values based on the work of Dipprey and Sabersky (1963) and Pimenta et al. (1975). In order to use this relationship the equivalent sand roughness of the surface under investigation must be determined. Very extensive measurements of rough pipes were carried out by Nikuradse (1933) who used circular pipes covered on the inside as tightly as possible with sand of a specific grain size glued to the wall. Schlichting (1936) developed the concept of equivalent sand-grain roughness (k_S) as a means of characterizing other types of roughness elements by comparing the equivalent net effect produced by Nikuradse's experiments. k_S is a length dimension to describe element size, and corresponds to the actual sieve size used by Nikuradse to sift sand. Schlichting (1936), using a law of the wall

development, determines the k_s for a variety of surfaces in a channel under fully developed flow conditions. The results indicate that k_s is often larger than the actual element height when the elements are closely packed. Using a law of the wall development for a flat surface Pimenta et al. (1975) develop a relationship between k_s, boundary layer thickness and the coefficient of friction for the surface. In this study, Pimenta et al. (1975) work is used along with the appropriate momentum integral equation to determine k_s and a Stanton number from Kays and Crawford's work (1980). This result is compared to the flat plate, no film flow, experimental results reported in Chapter 8.

Metzger and Larson (1986) also outline prominent experimental methods for obtaining heat transfer information. They point out that the majority of these experimental methods produce averaged coefficients over segment areas and provide accurate information at only discrete locations. If detailed resolution is desired, the fabrication of the test section becomes complex and expensive. Metzger and Larson (1986) describe an alternative approach along with the theory and experimental method. This method uses melting point coatings to determine local heat transfer values. Using commercially available encapsulated chiral nematic thermochromic liquid crystals (TLC), this technique has been further developed to obtain both heat transfer coefficients and effectiveness values for the film flow situation (Vedula, 1989, Kim, 1992 and Metzger et al., 1992). There are advantages to this technique. First, spatially continuous values may be obtained, the resolution of which is based to a large extent on the experimenters' willingness to reduce data. Secondly, this technique may be applied to new configurations without the complex and often expensive fabrication

requirements of other techniques. This transient experimental method uses a video camera/frame grabber combination to determine the intensity of colored light being emitted by the liquid crystal surface coating at each video pixel location. This intensity is compared to known intensity values for the crystal at a calibration temperature. In this way, a time to reach a known temperature may be determined for each pixel of the test section captured by the camera/frame grabber combination.

The clear advantage of the transient test method used in this work using TLC, is that both h and η are simultaneously determined. The accuracy of this technique has been improved during the last year by introduction of a normalized threshold method (Chapter 3). This method permits accurate convective heat transfer coefficients to be obtained visually even when the background intensity of the surface varies greatly from one area of the test section to another. This is an important feature for complex test arrangements.

1.3 Current Investigation

The investigation of roughness by Tabbita (1993) indicates that the surfaces of turbine airfoils become rough during service. It is clear from previous work, that this affects both the film cooling effectiveness and the convective heat transfer coefficients of the airfoils. This in-service change in the airfoil surfaces needs to be taken into account when designing the turbine blade cooling system. This investigation provides information on the effects of roughness on film cooling heat transfer for a configuration which matches conditions applicable to the pressure side of the first stage turbine vane of the P&W F100-PW229 engine.

In order to use the semi-infinite solid approach used by Dr. Metzger and his students in the past at ASU, it was necessary to develop a different type of test model which could be roughened to a particular specification and still provide a surface which when optically viewed provides an accurate measurement of the film cooling performance.

This work includes comparing the results to an aerodynamically smooth surface where roughness Reynolds number (Re_k) is the determining parameter. Prandtl Mixing Length theory will be used to characterize the test surfaces under investigation as being fully rough (Re_k>70). Scaling of the test surface geometry will be based on the momentum boundary layer thickness (δ_2) from a point on the pressure side of the F-100-PW229 vane at approximately 0.5 inches from the leading edge. δ_2 is used for several reasons. In deciding upon a convenient parameter for a turbulent transition criterion, a local Reynolds number criterion is often more useful than a length Reynolds number. Either the displacement or momentum thickness Reynolds number might be used, but since the momentum thickness Reynolds number is evaluated anyway in evaluating the Re_k it is convenient to use for scaling also. Since the roughness in the fully turbulent region under investigation causes an increase in the drag (virtual shear of the surface), using δ_2 (which is a measure of the momentum loss due to the fluid/surface interaction) makes sense from a physical understanding viewpoint. As the momentum analysis in chapter 8 indicates, the coefficient of friction for a rough surface is a function of the rate at which δ_2 changes along the surface. Since the roughness in the fully turbulent region has a direct effect upon the turbulent boundary later velocity profile primarily very near the surface (Schlichting, 1979), the momentum boundary layer thickness is more appropriate than the

standard boundary layer thickness (δ) for scaling when roughness is involved. Likewise, because the cooling effectiveness on a flat plate is primarily a function of blowing rate (Kays et al., 1980) which in turn is a measure of momentum ratio between the primary and cooling flows, the momentum thickness would again seem the appropriate local scaling length. A boundary layer probe is used to determine the momentum thickness at a location just prior to the film holes. This information will be used to scale the film hole diameter based on F-100 engine information.

A brief outline of the chapters follows:

Drawing upon the ideas of Metzger and Larson (1986), Vendala (1989) and Kim (1992) the experimental apparatus and test model necessary to successfully apply the TLC techniques in use at ASU to a rough composite surface are presented in Chapter 2.

In chapter 3, the method termed normalized threshold method along with a general investigation of TLC calibration is presented. The normalized threshold concept improves dramatically the calibration uncertainty employed in the study. In addition, as a basis for future work beyond this study, calibration of the red and green responses of the TLC is investigated. Finally, a try at understanding the elusive single-test method is made.

In Chapter 4, the results of flat plate (aerodynamically smooth) boundary layer measurements are presented. These results form a basis for the film hole placement and film hole diameters used in chapter 6 and in determining the appropriate design for the rough plates used to investigate film cooling in Chapter 9.

While the semi-infinite solid/TLC approach has been used since 1989 to obtain 3-temperature (film cooling) heat transfer information there has been

concern about the values of h and η obtained in comparison to adiabatic wall and mass transfer methods used by prior investigators. In general, this concern should be laid to rest by film cooling work presented here for an aerodynamically smooth surface and its comparison to the work of Goldstein et al. (1970) and Eriksen and Goldstein (1974). The present work presented in Chapter 4, recognizes the importance of matching the dimensionless boundary layer momentum thickness (δ_2/D) when comparing data and its strong effect on heat transfer data.

In Chapter 6, a finite difference conduction heat transfer computation is carried out for the composite test plate to show the feasibility of the data reduction model utilized (semi-infinite lumped capacitance) and to help ascertain the uncertainty in heat transfer coefficients and effectiveness caused by the data reduction method.

With the reliability of the TLC method demonstrated in Chapter 6, a comparison of an aerodynamically smooth stainless steel composite plate is compared to the results from tests using the more conventional Plexiglas test plate. The methods used to produce the composite test plate are described along with the novel approach used to determine the thermal properties of the epoxy used in the manufacture of the smooth and rough composite test plates. These tests indicate the value of this experimental approach and the limitation of the heat transfer information obtained.

In Chapter 8, the results of heat transfer experiments using the two rough composite plates are analyzed and compared to the relationship for Stanton number proposed by Kays and Crawford (1980).

In Chapter 9, the focus of this work is presented. Convective heat transfer coefficients and film cooling effectiveness for blowing ratios from 0.4

to 1.25 are presented for two rough composite plates. A Reynolds number of 1.61×10^5 matches the Reynolds number at approximately 0.44 inches from the leading edge of pressure side of the first stage turbine vane of the F-100 engine. The ratio of δ_2/D is matched with that of the F-100 engine. Results are compared qualitatively with those of Goldstein et al. (1985).

Turbulence data for the two mainstream velocities used in this study are presented in Chapter 10 and in Chapter 11. Turbulence levels have a clear impact upon heat transfer performance. In addition, the effect of boundary layer thickness on heat transfer characteristics is presented for the lower Reynolds number flow investigated in this study.

CHAPTER 2
THEORY OF OPERATION
AND
EXPERIMENTAL APPARATUS

2.1 Introduction

During the course of this investigation, three experimental setups were used to gather the needed data. First, a test rig (section 2.3), which was designed for investigation of turbine tip flow by previous heat transfer students at ASU, was used to investigate calibration techniques and to develop the normalized threshold method presented in chapter 3.

For the smooth and rough surface experiments a new apparatus was designed which permits visual access to the TLC layer and boundary layer removal for control of the boundary layer thickness. The apparatus and experimental procedures are presented in sections 2.4 and 2.5. The basic equations for tests conducted with a Plexiglas surface are presented in section 2.2. These relationships are the same as those presented in the work of Vedula (1989) and Kim (1992) and the details of the software used to convert the TLC response times to convective heat transfer coefficients and film cooling effectivenesses are presented in those works. Here, only the necessary relationships are presented to gain an understanding of the method and not the flow charts or lengthy programs necessary for this process. In order to apply the semi-infinite solid approach to the composite rough plate apparatus, illustrated in section 2.5, it was necessary to include a lumped capacitance model to account for the energy stored in the stainless steel portion of the composite plate. This lumped capacitance model is presented

in section 2.6. Experimental and finite difference results which demonstrate the success of this model are presented in chapters 6 and 7. The data reduction program written to handle the lumped capacitance/semi-infinite solid model, used to reduce the composite plate heat transfer data, is documented in Appendix A.

2.2 Basic Equations

In forced convection, the local surface heat flux is conventionally expressed as:

$$q = h\,(T_r - T_w) \qquad (2.1)$$

where T_w is the local surface temperature and T_r is an appropriate reference, or driving, temperature that renders h independent of the temperatures. Such a choice of T_r reduces the convection coefficient h to a function of the aerodynamic character of the flow field alone, and allows local surface convection behavior to be condensed into a constant of proportionality (h) for a given flow field. Here, and in the following discussion, linear convection behavior is assumed, with temperature differences sufficiently small to allow fluid properties to be represented by values independent of temperature.

In two-temperature convection situations, with a single fluid at temperature T_∞, the reference temperature is simply T_∞, and convection experimentation consists of measuring q together with T_w and T_∞, and from them determining h. In three-temperature convection situations like film cooling, the reference temperature is at some generally unknown level that depends on the supply temperatures of the two interacting streams and the

degree of mixing that has occurred between them before they arrive at the various locations on the surface. For these situations, both h and T_r must be considered unknowns to be determined by experiment. Since T_r must be equal to the wall temperature when q = 0, T_r is often termed the adiabatic wall temperature, and can be determined from measurements on an adiabatic surface. It must be recognized that such measurements on an adiabatic surface provide no information on convection coefficients, and additionally it is often difficult in practice to make the surface locally adiabatic, particularly in regions where T_r is varying rapidly.

In this work, local determination of both T_r and h is made by suddenly exposing the test surface to steady mainstream and secondary flows and observing the transient response of the test surface as indicated by the TLC color display. The wall material, including the test surface, is initially at a uniform temperature at all depths, and the initial response near the surface is governed by a semi-infinite formulation of the transient heat conduction with the convection boundary condition stated as in equation 2.1:

$$k\frac{\partial^2 T}{\partial z^2} = \rho C_p \frac{\partial T}{\partial t} \tag{2.2}$$

$$\left[-k\frac{\partial T}{\partial z}\right]_{z=0} = [h\,(T_w - T_r)] \tag{2.3}$$

$$[T]_{z=\infty} = T_i \tag{2.4}$$

$$[T]_{t=0} = T_i \tag{2.5}$$

Here the z direction is normal to the surface with zero at the convection surface. The semi-infinite description is appropriate as long as the transient temperature penetration does not exceed the thickness of the wall material being used, and thus the penetration time becomes the criteria for deciding test wall thickness and subsequent allowable transient test duration. In the above equation, set for three-temperature situations, the convection coefficient and reference temperature are both unknown. However, the convection coefficient is constant with time and for situations where T_r is known the solution is given by (Meyers , 1971):

$$\frac{T_w - T_i}{T_r - T_i} = 1 - \exp\left[\frac{h^2 \alpha t}{k^2}\right] \operatorname{erfc}\left[\frac{h\sqrt{\alpha t}}{k}\right] \qquad (2.6)$$

By measuring the time (t) required for the surface temperature to reach a prescribed value displayed by an indicating coating, h can be determined (Metzger and Larson, 1986) from equation 2.6.

This method has been extended to three-temperature situations (Vedula, 1989) by noting that h and T_r can be obtained as the simultaneous solution of two equations of the form of equation 2.6 obtained either from a single transient test with two surface temperature indications at different times during the transient, or from two separate related transient tests. For example, if during the transient a liquid crystal surface coating indicates one surface temperature T_{wg} at time t_g corresponding to the green display of the TLC and another T_{wb} corresponding to the blue display at t_b, then h and T_r are determined from the simultaneous solution of:

$$\frac{T_{wg} - T_i}{T_r - T_i} = 1 - \exp\left[\frac{h^2 \alpha t_g}{k^2}\right] \operatorname{erfc}\left[\frac{h\sqrt{\alpha t_g}}{k}\right] \qquad (2.7)$$

$$\frac{T_{wb} - T_i}{T_r - T_i} = 1 - \exp\left[\frac{h^2 \alpha t_b}{k^2}\right] \operatorname{erfc}\left[\frac{h\sqrt{\alpha t_b}}{k}\right] \qquad (2.8)$$

Alternatively, two separate tests, 1 and 2, with the same flows but different flow temperatures can be conducted, with indication in both cases given by a single color display.

In the experiments, for both two- and three-temperature situations, an additional complication is introduced, since true step changes in the applied fluid temperatures are usually not possible and the reference temperatures are thus functions of time. This complication is accounted for by modifying Equations (7) and (8) through use of superposition and Duhamel's theorem (Metzger and Larson, 1986). The actual gradual change is obtained by using a series of steps. The solution is represented as:

$$T - T_i = \sum_{i=1}^{N} U(t-\tau_i)\Delta T_r \qquad (2.9)$$

where

$$U(t - \tau_i) = 1 - \exp\left(\frac{h^2}{k^2}\alpha(t-\tau_i)\right) \operatorname{erfc}\left(\frac{h}{k}\sqrt{\alpha(t-\tau_i)}\right) \qquad (2.10)$$

Here, T_r is time-varying and unknown but related to the time variation in T_∞ and T_f and to the value of η such that:

$$\Delta T_r = (1-\eta)\Delta T_\infty + \eta \Delta T_f \qquad (2.11)$$

So:

$$T - T_i = \sum_{i=1}^{N} U(t-\tau_i)((1-\eta)\Delta T_m+\eta\Delta T_f) \qquad (2.12)$$

Two equations need to be solved in the form of equation. 2.12 to obtain the two unknowns, h and η. The two equations can come either from a single transient or two closely related transient tests. The two equations are solved iteratively for the two unknowns.

In the technique used, the transient surface temperature information is provided by the application of a temperature indicating coating material and a Sun workstation-based image processing system employing a 24-bit frame grabber. The coating material used for this study is a commercially available encapsulated chiral nematic thermochromic liquid crystal (TLC), applied to the test surface and the calibration copper bar using an airbrush. The TLC displays colors in response to temperature changes as a result of lattice reorientation of the crystal. When sprayed as a thin layer, the TLC is essentially clear and displays color with increasing temperature in sequence of red, green, blue, and back to clear. The nominal temperatures for red, green, and blue displays of the present chiral nematic TLC are 38.4°C, 39.8°C, and 43.5°C, respectively. The process is reversible such that the calibration of temperature remains unchanged for a large number of cycles under laboratory conditions. While all TLC type coatings assume a finite time response for the lattice rotations, Ireland and Jones (1987) have shown that micro-encapsulated chiral nematic coatings on the order of 10^{-3} cm thick

require only a few milliseconds for this action. This time lag is negligible in comparison with the thermal transients of the present study.

2.3 Experimental Apparatus and Procedures for Calibration

Figure 2.1 shows a schematic of the experimental apparatus used in the calibration tests. Compressed air from a dedicated air supply is filtered and dried and orifice metered for both the main and film flows. After metering, both flows are routed to autotransformer controlled tubular heaters where their temperatures can be accurately set to desired levels. The two flows are each initially diverted away from the test section by three-way ball valves until both flow rates and temperatures reach steady-state values.

Although not important to this particular study, the test section is a Plexiglas model, designed to simulate the clearance gap leakage flow from the pressure side to the suction side of a turbine blade. The main flow inlet tube opens into a rectangular plenum 4" by 2.5". The plenum contains a wire mesh enclosed by a flow straightener to provide uniform flow into the clearance gap. The main flow then passes through the clearance gap and across the test surface. The test section, Fig 2.2, simulates a turbine tip with an embedded 3/8" cavity. Such a cavity will affect the turbine tip's heat transfer characteristics. Four 3/16" diameter injection holes 1/4" from the trailing edge of the cavity provide cooling air to the turbine tip cavity. Since the purpose of this work was to validate the technique presented, rather than the turbine tip heat transfer characteristics, only a single blowing ratio is used. The clearance gap exists between the test surface, simulating the turbine tip, and the viewing plate which acts as the shroud. The test surface, coated with liquid crystals, is viewed through the viewing plate using a video camera.

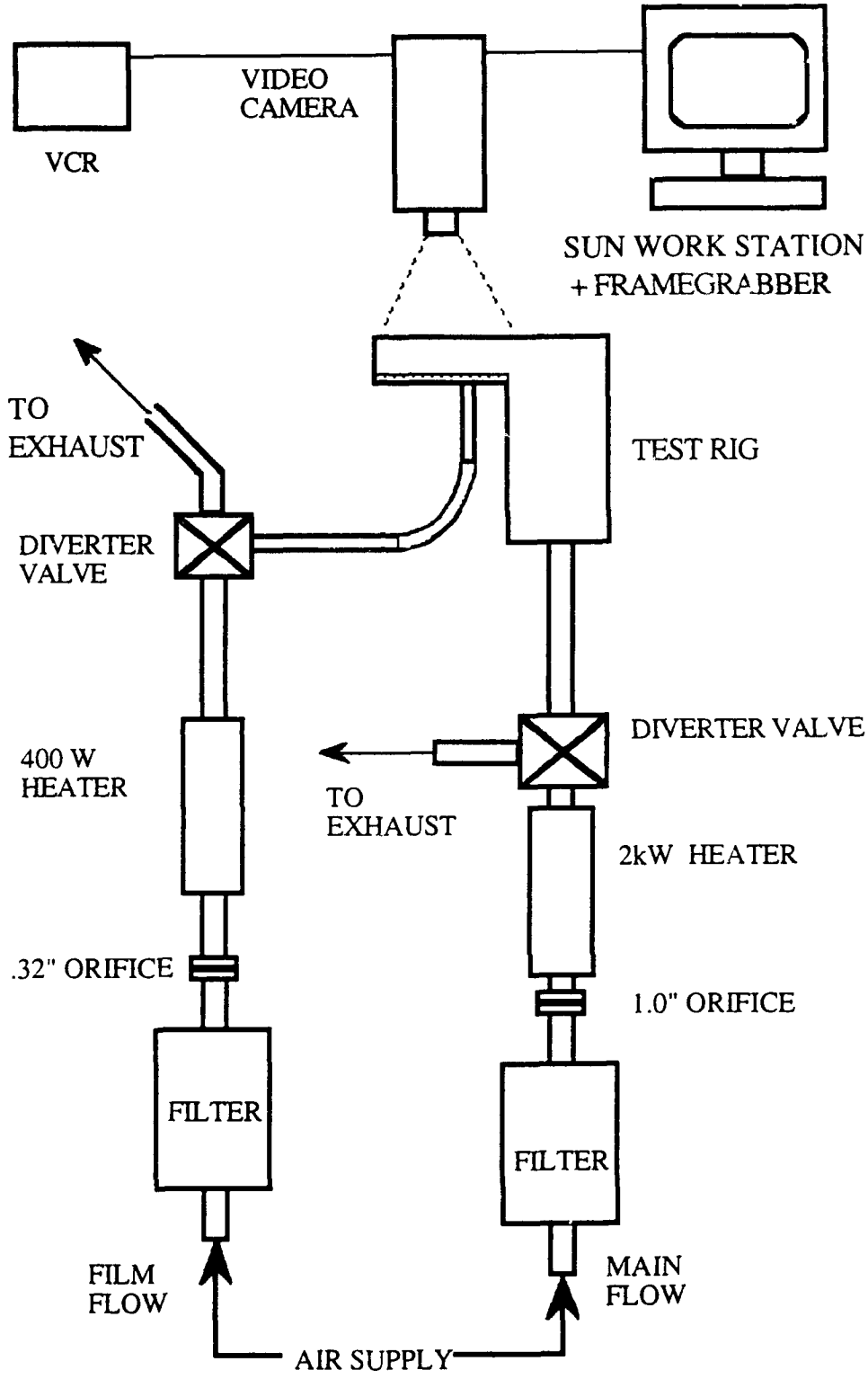

Figure 2.1 Calibration apparatus

At the end of the test section, Figure 2.2, a copper bar with an embedded thermocouple is used to calibrate the TLC. Main flow temperature is determined from a thermocouple placed in the center of the inlet plenum. An additional thermocouple placed in one of the tubes carrying injection flow to the test section, measures the secondary flow. All thermocouples were type K (Chromel-Alumel) with a wire diameter of 0.00314". The transient responses of the three thermocouples monitoring the copper calibration bar, the main flow, and the injection flow were recorded through a data log unit (Fluke 2400 B Intelligent Computer Front End) with a 0.16 second sampling interval for each thermocouple.

The computer-vision system employs the following three major components: (i) SUN SPARC II workstation with ethernet mainframe connection, (ii) RasterOps RGB color frame grabber, and (iii) Sony 8mm color video camera.

A typical experimental run begins with heating laboratory compressed air up to a desired temperature while the test section is maintained at room temperature. A three-way ball diverter valve is used to route the heated air away from the test section until the air temperature reaches preselected steady-state value indicated by a monitoring thermocouple in the diversion line. The diverted air passes through a balancing valve which is preadjusted to equalize the flow resistance between the test section and bypass circuit so that the flow rate is unchanged when the flow is re-routed to the test section. When stabilized at the desired conditions, the heated air is suddenly re-routed to the test section as the frame grabber and data log system for air temperature measurements are initiated simultaneously. For tests with injection flow, the secondary air flow is also heated as desired and initially

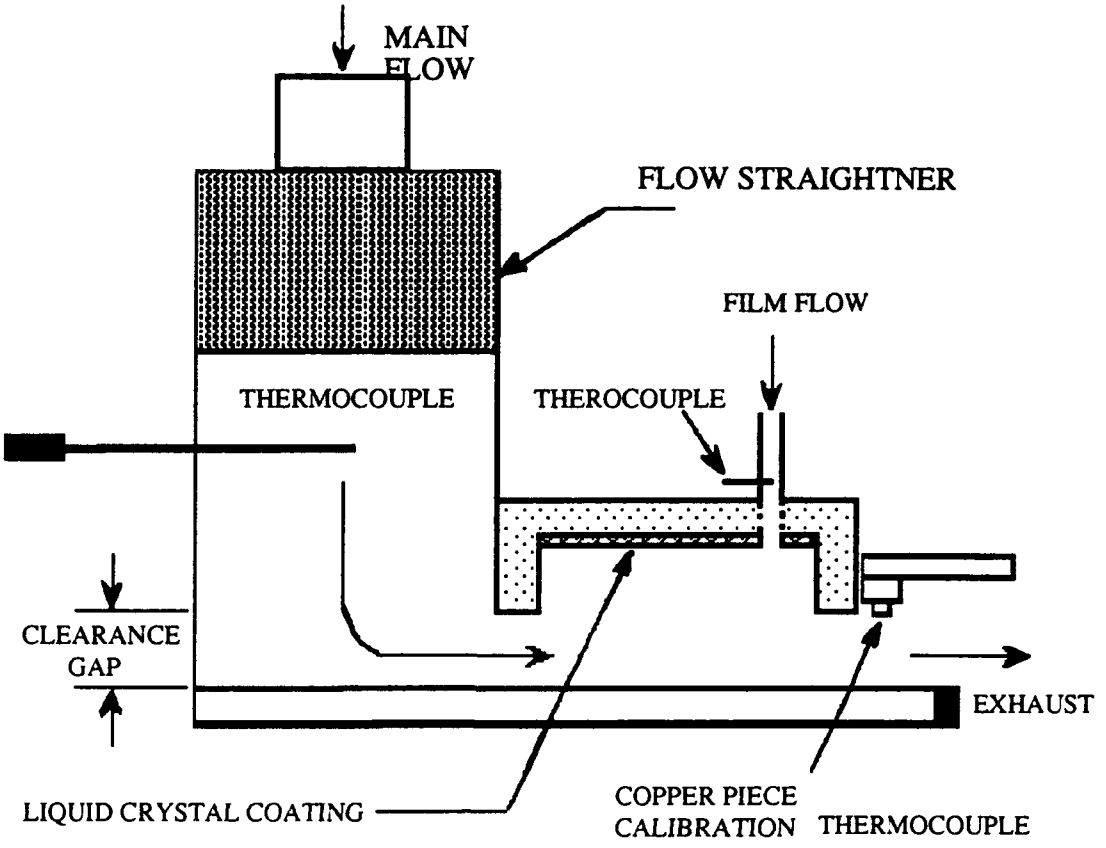

Figure 2.2 Calibration test section

passed away from the test section by a second diverter valve and re-routed simultaneously with the main flow.

As the test surface is heated by introduction of flow at elevated temperature, the local color information from TLC captured by a color video camera is digitized pixel by pixel with the frame grabber in reference to a preset threshold corresponding to the calibrated color intensity. The outcome of this image digitization process is a pixel time-temperature matrix covering the entire test region monitored by the video camera. This information together with the transient reference temperature data suffices to obtain the

local heat transfer coefficients with a relatively high resolution using equation. 2.12.

The pre-set threshold for the desired color is determined by calibrating the image processing system against the TLC coated copper bar. The temperature response of the copper bar to a heat input load is monitored by the thermocouple embedded in the bar.

To minimize experimental uncertainties, the temperature of the supplied flow is chosen so the color threshold is not reached until sufficient time has elapsed after the start of flow (usually 10 seconds or more) to insure the elapsed time can be determined accurately. Also, the flow temperature is chosen so the elapsed time and corresponding penetration of the temperature pulse into the surface are small enough (usually less than 90 seconds) to insure the test surface can be treated as semi-infinite as assumed in the data reduction.

2.4 Experimental Apparatus for Smooth Surface Testing

In chapters 4, 5, and 7 heat transfer data is presented for aerodynamically smooth flat plates. Figure 2.3 shows a schematic of the experimental apparatus to be used for this work. Compressed air from a 100hp air supply solely dedicated to the heat transfer lab is filtered and dried and orifice metered for the main flow. As is the case for the test apparatus illustrated in section 2.3, the film flow is supplied by a separate compressed air system common to several labs at ASU. After metering, both flows are routed to autotransformer controlled tubular heaters where their temperatures can be accurately set to desired levels. The two flows are each initially diverted away from the test section by three-way ball valves until both flow

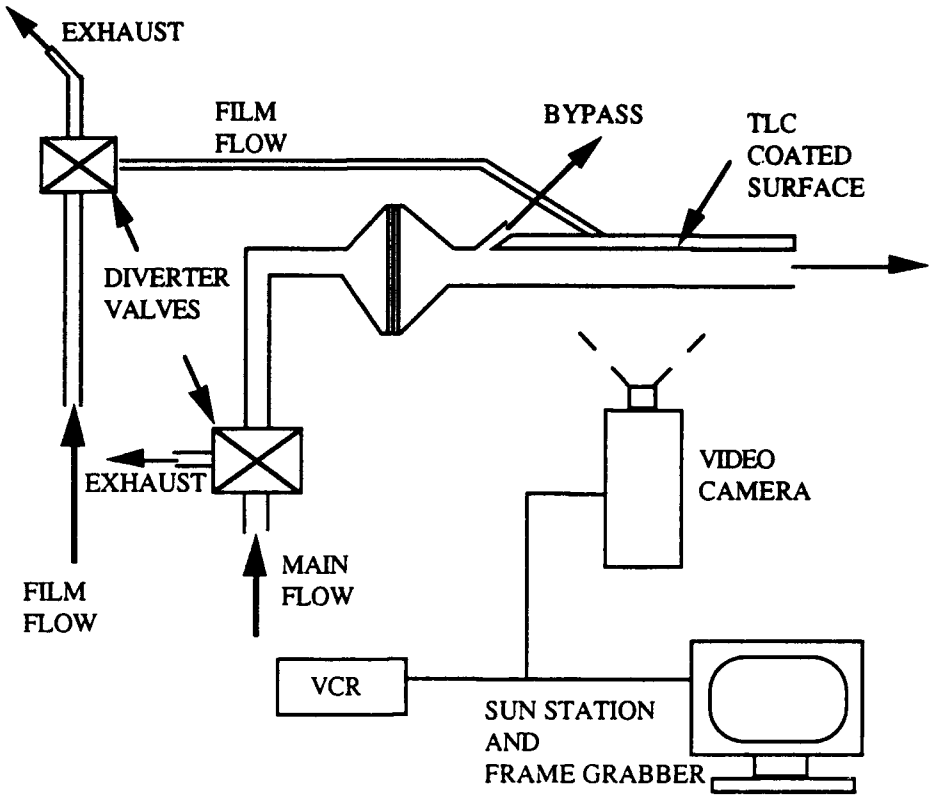

Figure 2.3 Plexiglas flat plate test apparatus

rates and temperatures reach steady-state values. The test section is a Plexiglas model designed to simulate the pressure side of a turbine blade. The main flow inlet tube opens into a rectangular plenum 6" by 5". The main flow then converges to an opening of 1.5" by 3". The flow passes by a splitter plate where a 0.25" bypass occurs. The main flow then passes over the test section, 3" by 8" flat plate, providing a boundary layer and Reynolds number appropriate for the pressure side turbine vane cases investigated in this work. The film cooling holes are located at 2.25" from the splitter plate and in combination with the air supply system capability of 170 grams/sec

provides a Reynolds number ($U_\infty X/\nu$) at the film holes of 1.61×10^5. As mentioned earlier, this corresponds to a location of approximately 0.44 inches along the pressure side of the F-100 first vane. The corresponding momentum thickness (δ_2) for the vane is estimated by P&W to be 0.0008". The boundary layer measurement work presented in chapter 4 found that for a Reynolds number of 1.61×10^5 the δ_2 at 2.25" is 0.0080". Prediction using the Prandtl mixing length theory (Chapter 4) for a turbulent boundary layer estimates the δ_2 at 2.25" on a turbulent flat plate to be approximately 0.0071". The two values compare quite well. With our work being scaled to δ_2, our scaling value is then approximately a factor of 10. Up scaling the film holes from the F-100 vane results in film hole diameters of approximately 0.21". The ratio δ_2/D is then 0.037 and approximately the same as the F-100 first vane at 0.44 inches from the leading edge on the pressure side. A turbulent boundary layer is ensured with use of a trip wire at the beginning of the plate sized as recommended by Schlichting (1979).

Experimental procedures are the same as those outlined in the previous section for calibration tests. In this case the video camera captures the TLC response over the entire flat plate surface pixel by pixel.

2.5 Experimental Apparatus for Rough Surface Testing

The test surface is the key to being able to use the TLC techniques already developed in ASU's laboratories. In the past, as in the last section, the TLC has been applied to the surface directly exposed to the test flow gases. This has been possible because the liquid crystal did not add enough roughness to extend out of the viscous sublayer and the surface could

continue to be considered aerodynamically smooth. The surface is then viewed through the flow field and through an adjacent Plexiglas surface.

For a rough surface, this technique is not appropriate for several reasons. A TLC layer on the roughened surface will provide a temperature response which sees only the tops of the roughening elements. This analysis would fail to take into account the heat transfer occurring on the sides of the roughening elements and would give an inaccurate description of the true heat transfer occurring to the surface. In addition, with any portion of the roughened surface viewed which is not perpendicular to the camera errors in the calibration of the TLC occur (Jones, 1991).

Figure 2.4 shows the composite plate developed for the rough surface model. The composite consists of a stainless steel roughened surface sprayed on the non-flow side with TLC and backed with a clear epoxy layer. In this set up, rather than the roughened heat transfer surface being viewed from the front side, it will now be viewed from behind. As is discussed in the finite difference chapter of this work, stainless steel was chosen to provide an acceptab small temperature drop across the metal plate but yet limit the lateral conduction. The TLC is then viewed through the epoxy layer which serves as a semi-infinite conduction medium. This approach provides a temperature time response just below the roughened surface which is used to determine heat transfer and film effectiveness coefficients. This method results in local coefficients smoothed on the order of twice the diameter of the roughness columns and in terms of engineering design work should prove valuable. Figure 2.5 is an overall view of the rough testing apparatus. Viewing of the TLC takes place from the rear side of rough composite.

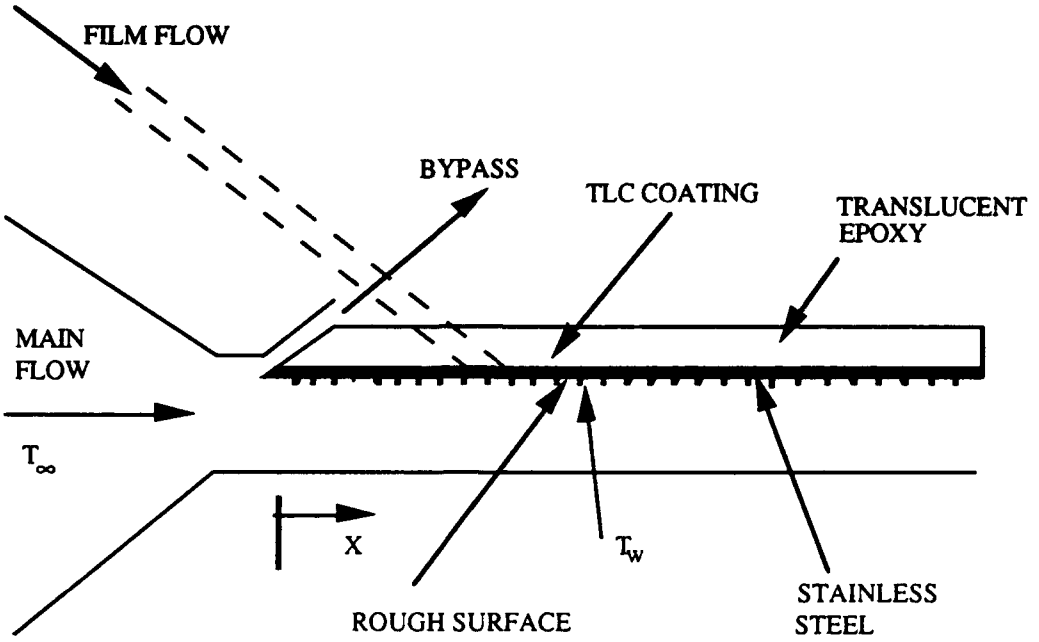

Figure 2.4 Composite plate

An epoxy was chosen which provided excellent translucent and material properties very close to those of Plexiglas. The epoxy is manufactured by Hysol, Dexter Electronic Material Division, and is designated RE2039 (Resin) and HD3561 (Hardener). Thermal properties for this particular epoxy were known only approximately, but were determined more exactly by a simple experimental procedure presented in chapter 7.

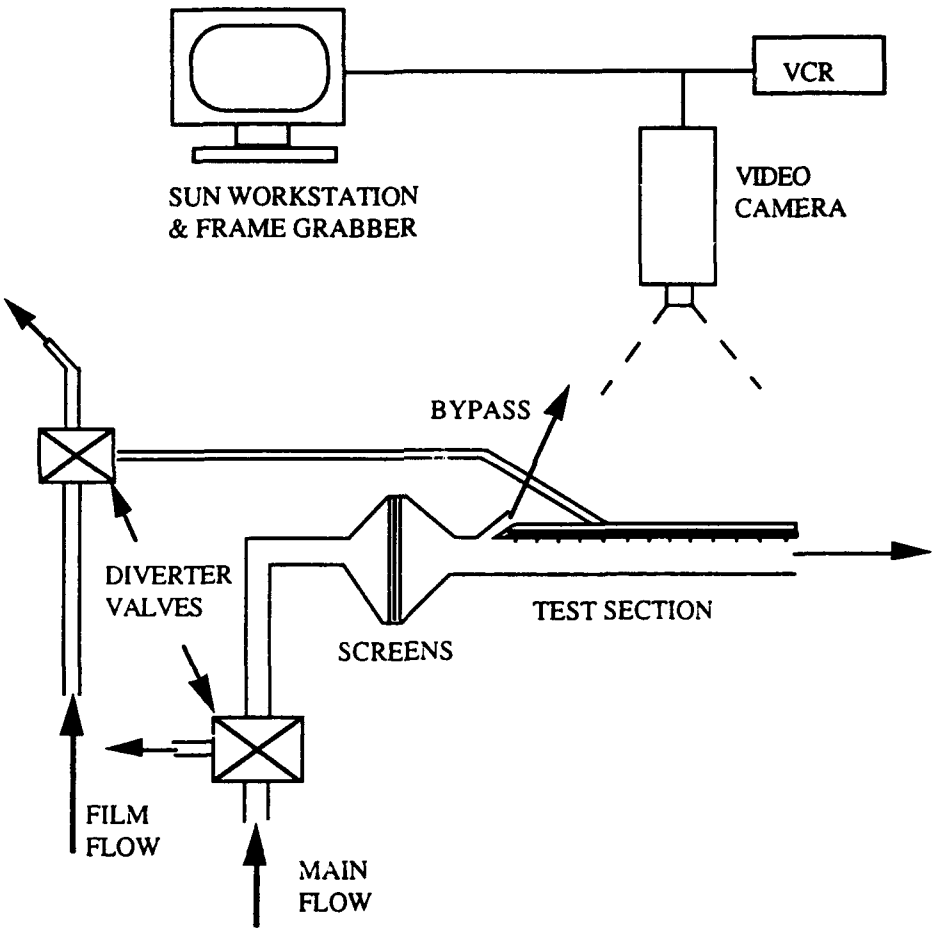

Figure 2.5 Rough surface test apparatus

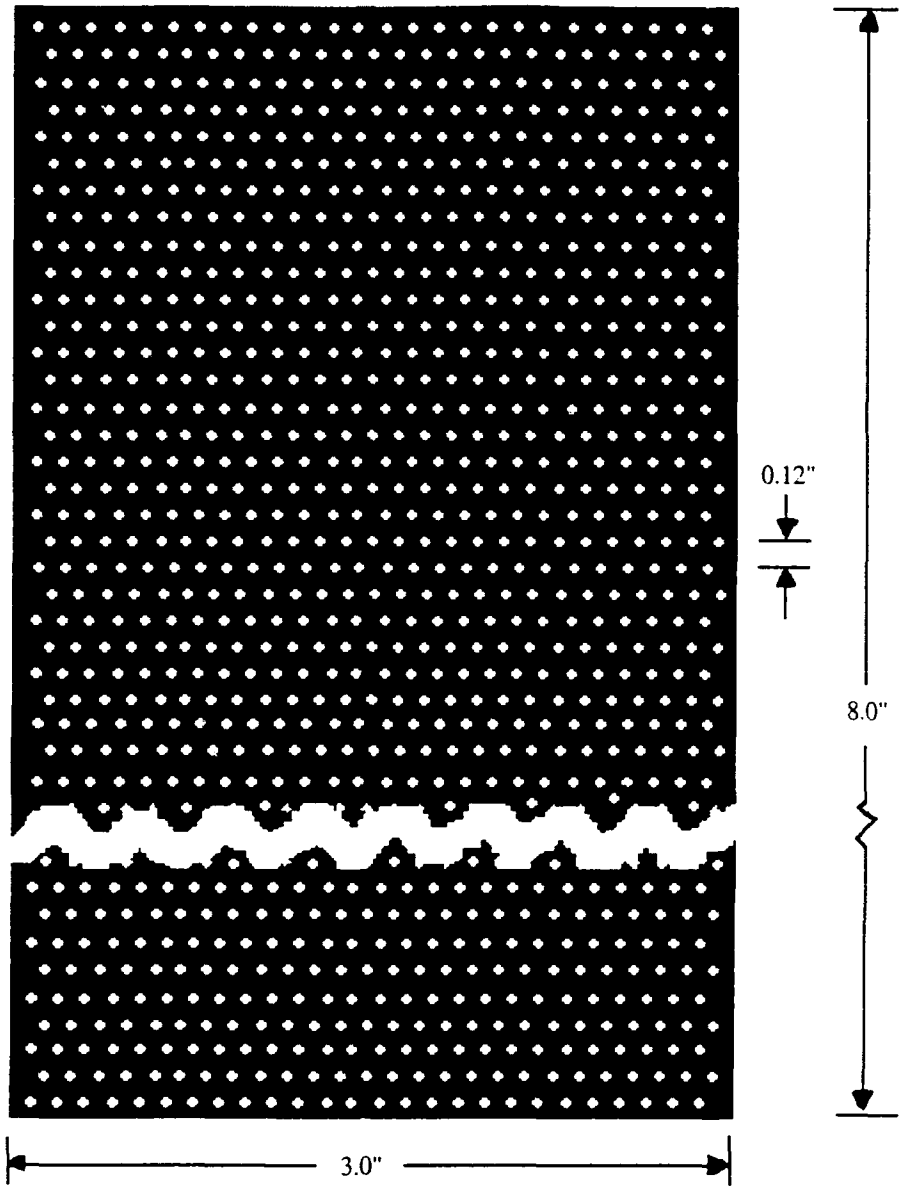

Figure 2.6 Rough surface (top view)

Figure 2.6 is a top view of the flow side of the roughened surface. Several types of surfaces were investigated, as well as manufacturing methods including anisotropic surfaces, electric welding machining, conventional

machining, plate stamping, a copper/graphite composite, and metal etching. After months of investigation, metal etching was chosen.

Metal etching is a patented method of using acids to remove metal from surfaces in a very controlled manner. It provides accurate surface geometries and is capable of leaving a very thin surface on the order of three to four mils between the roughness columns.

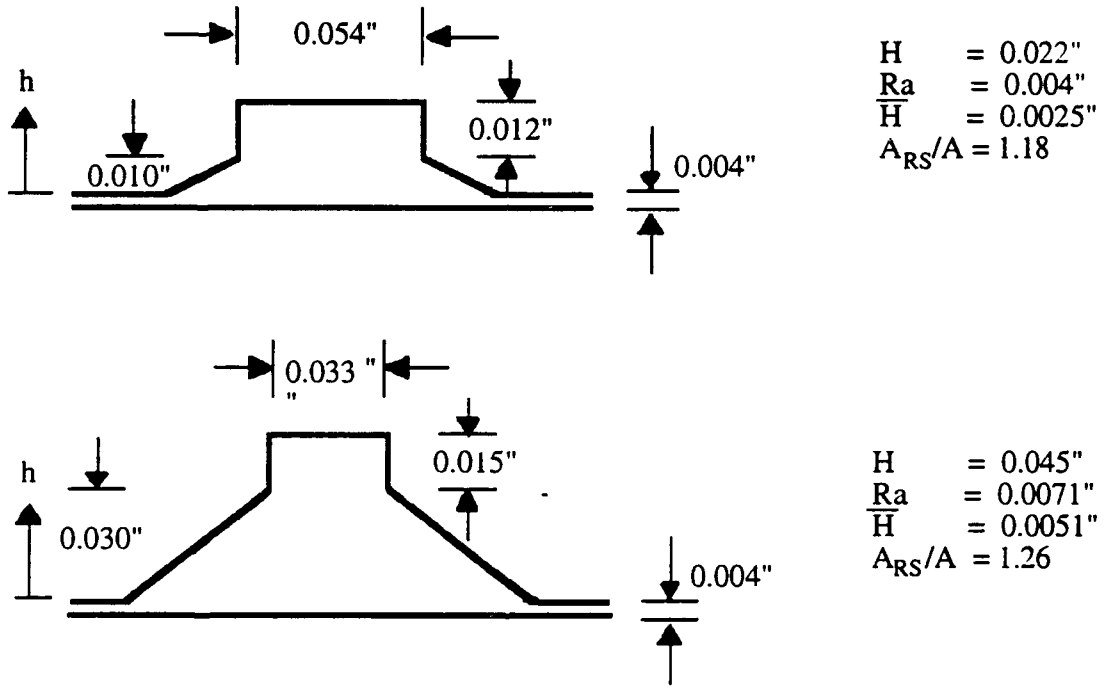

$$\bar{H} = \frac{1}{A}\int H \, dA \qquad Ra = \frac{1}{A}\int |(H - \bar{H})| \, dA$$

Figure 2.7 Profile view of roughness elements

Two rough surfaces are investigated in this study with absolute roughness heights (H) of 0.022" and 0.045" (Figure 2.7). The heights were chosen to match, after scaling, the approximate height of the roughness at 0.44 inches on the pressure side of the F-100 first vane.

The roughness average (Ra) values, when scaled by ten, represent Ra values for the F-100 vane environment of 0.4 mil and .71 mil. A radial trace reported by Tabitta (1993), of the F-100 first vane at about the 0.44 inch span location on the airfoil, found an Ra of 0.9 mil. The roughest surface (Ra=0.0071") provides a rough surface on the right order of the roughness found in operational airfoils under the correct Reynolds number and scaled momentum thickness conditions. The other rough surface (Ra = 0.0040") permits investigation of the trends of increasing roughness on film cooling effectiveness and convective heat transfer coefficients.

Calipers with an accuracy of ±0.0005" were used to determine the rough element dimensions. As a check, the volume of the stainless steel, determined from the rough element dimensions, was used to determine the rough plate mass prior to being bonded to the epoxy. This mass was found to be within ±2.5% of that measured using an accurate gram scale.

As is reported in detail in chapter 8, these rough surfaces provide roughness Reynolds numbers (Re_k) greater than 70 over the entire plate under test conditions. This ensures that the roughness under investigation is in the fully rough region. The effect of roughness on a turbulent boundary layer is primarily at the wall, and shows up as a change in velocity profile near the wall and a corresponding change in the shear stress at the wall. The shear stress is commonly expressed in terms of either a coefficient of friction (c_f) or in terms of a shear velocity (u_τ).

$$\frac{\tau_o}{\rho} = \frac{c_f u_\infty^2}{2} = u_\tau^2$$

Shear velocity is commonly used in the law of the wall developments. Since the effects of a rough surface are primarily right at the wall, shear velocity is a logical choice for characterizing the roughness size. Length Reynolds number is not particularly useful in characterizing the boundary layer of a rough surface and instead a local Reynolds number based on shear velocity is more useful. This leads to a roughness Reynolds number (Re_k) as a nondimensional measure of surface roughness (Kays and Crawford, 1980).

$$Re_k = \frac{u_\tau k_s}{\nu}$$

Here k_s is equivalent sand roughness as discussed in chapter 1.

Using Rek, three regimes have been identified from experimental data. For $Re_k < 5.0$ the surface behaves as aerodynamically smooth. This is the case with the Plexiglas surfaces commonly used in TLC testing at ASU. For Re_k between 5.0 and 70.0 there is an increasing effect of the roughness but some of the smooth characteristics remain. This region is termed the transition region. For $Re_k > 70.0$ the local surface is termed fully rough. A basic characteristic of a fully rough surface is that friction coefficient is independent of Reynolds number, confirming it as a less significant variable (Kays and Crawford, 1980). The mixing-length equations developed for a fully rough surface are given in chapter 8 in order to determine an appropriate k_s for the surfaces used in this study. With increasing Re_k the

viscous sublayer is destabilized and a thinner sublayer results. The viscous sublayer is the thin region close to the surface where viscosity is responsible for the vast majority of momentum transfer into the boundary layer and where turbulent mixing accounts for little of the transfer. At about Rek = 70, the viscous sublayer disappears all together and viscosity is no longer a significant variable (Kays and Crawford, 1980). In this case the shear stress is transferred to the wall by a mechanism, other than viscosity, termed pressure drag. Pressure drag is a result of the dynamic pressure on the upstream side of each element and is often termed form drag. A fully rough mixing length theory is available as outlined in Kays and Crawford (1980). It is the basis for the equations used in chapter 8 of this work to determine k_s and to determine that the rough surfaces used in this work operate in the fully rough regime. Because this is true, the correlations developed by Dipprey and Sabersky (1963) can be used to predict the two temperature Stanton number for the rough surfaces investigated in this study. The comparison between these values and experimentally determined values are also presented in Chapter 8.

The manufacture of the composite plates was a multistep process that took several months to perfect. In the first step, a local metal etcher who does work for local aerospace and electronics companies produced the rough stainless steel surfaces. The stainless steel is then machined to the lateral dimensions required and film cooling holes drilled in one of two plates produced for each roughness. The other plate is left without film holes for the work accomplished in chapters 7 and 8. The backside of the plates are acid washed and TLC coating applied. This coating is on the order of 10^{-3} cm thick and has a response time of only a few milliseconds (Ireland and Jones, 1987). This time is negligible in comparison with the length the

thermal transients present with each run. In addition, the TLC is in a polymer binder whose thermal properties are of the same magnitude of those of the epoxy and Plexiglas used for the test surfaces and is expected to have very little affect on the semi-infinite solid model presented in section 2.6.

After the plate is presized and coated on the non-rough side with TLC, it is placed in a prefabricated form for epoxy pouring. The epoxy is mixed by weight and pored into the form. Drying time is 48 hours. The particular epoxy used is susceptible to what it termed ammine blushing. Ammine blushing is where the ammonia in the resin combines with water molecules in the air to form a white compound on the surface of the epoxy during curing. To prevent this the curing process must take place in a dry environment.

After cured and removed from the form, the composite piece is machined to fit the dimensions of the experimental apparatus. The surface permitting visual access to the TLC is protected to prevent scratching during machining of the lateral dimensions. At this time, film cooling holes are drilled through the epoxy to match up with those predrilled in the stainless steel plate. By having predrilled the steel, very little stress, both mechanical and thermal, is placed on the epoxy-stainless steel interface, which is susceptible to separation if care is not taken.

2.6 Experimental Model for Composite Test Plate

Two concerns exist for this type of composite test plate. First, the temperature drop across the surface perpendicular to the flow should be as small as possible so that the backside temperature response accurately represents the flow side surface temperature. Secondly, lateral conduction

must be limited or the local surface temperature response becomes smoothed and area averaged heat transfer coefficients result. These two requirements oppose each other and any choice for the surface material is a compromise. Copper for example satisfies the first criteria extremely well, but permits too much energy to be conducted laterally, even when thicknesses are on the order of 3 to 4 mils. Plexiglas, on the other hand, limits lateral conduction well, but the temperature drop across the surface becomes unacceptable. Stainless steel is the chosen compromise. Copper has a thermal conductivity (k) of 401 W/(m K), Plexiglas a k of 0.15 W/(m K), and stainless steel a k of 14 W/(m K). It is also worth noting that stainless steel has similar thermal properties to materials such as Inconel currently used in turbine blade manufacturing.

As is evident when the finite difference work in chapter 6 is reviewed, while there is very little temperature drop across the stainless steel plate during a test run, less than 0.02°C for a 0.004" smooth surface and less than 0.25°C for the worst case Ra = 0.0071" rough surface, there is a difference between the time it takes a Plexiglas test model and the composite test model subject to the same flow conditions to reach the TLC calibration temperature. This time difference exists because of the energy stored in the stainless steel and thus a time lag is required to increase the stainless steel to the TLC calibration temperature. This time lag, pixel by pixel, causes a difference in the convective heat transfer coefficients which result at each point in the surface when the method presented in section 2.2 is used. Specifically, the time that it takes the composite plate to reach the TLC calibration temperature is greater than that for the Plexiglas under the same conditions. Unfortunately, an analytical solution does not exist at present for a composite

semi-infinite solid under transient conduction. Therefore, the following model is proposed, the value of which can be judged based on the finite difference work in chapter 6 and the comparison of Plexiglas and composite plates run under the same convective conditions presented in chapter 7.

Since the temperature drop across the stainless steel is very small, the conduction in the epoxy semi-infinite solid beneath it can solved for in the same method as that presented in section 2.2 for the Plexiglas model. Due to the energy that it takes to also raise the stainless steel to the TLC calibration temperature, the temperature time response is lower and this method leads to lower heat transfer coefficients when the semi-infinite solid equations are solved for the epoxy portion of the composite. The time lag, the difference between time that the composite plates reaches the calibration temperature and the time a homogeneous epoxy model under the same conditions reaches the calibration temperature, can be estimated by a lumped capacitance calculation of the stainless steel portion of the composite plate. Since the stainless steel is nearly at a uniform temperature and the Biot number (Bi) is less than 0.03 in all cases, where $Bi < 0.1$ is the standard criteria, a lumped capacitance correction is made to the standard semi-infinite solid solution. Specifically, the transient time response to reach the TLC calibration temperature at each location on the surface is reduced by the time, calculated assuming lumped capacitance for the stainless steel, that it takes for the stainless steel layer to reach that same calibration temperature. In essence, this method tries to keep track of all of the energy that enters the composite model and to determine heat transfer characteristics from the result. As is described in the finite difference chapter, the results are very good, predicting heat transfer coefficients within 1% for a smooth surface and within

approximately 3% and 5.5% for the two rough surfaces. This model under predicts the energy into the surface by about 3% for the Ra = 0.0040" surface and about 5% for the Ra = 0.0071" surface. The results for the film cooling effectiveness are interesting; both the finite difference work in chapter 6 and the comparison between a flat composite plate and a Plexiglas plate reported in chapter 7, indicate, that for a stainless steel thickness of 0.004", η's are under predicted by abo.. ..egardless of the η or h values.

For this case where the driving potential is in terms of the reference temperature, the governing lumped capacitance equation is written as

$$hA_{rs}(T_r - T_w) = \rho V c_p \frac{dT_w}{dt} \tag{2.13}$$

with the initial condition

$$[T]_{t=0} = T_i \tag{2.14}$$

Here A_{rs} is the wetted surface area of the rough stainless steel surface and T_r means that the equation is posed in a three temperature environment. When the situation doesn't involve film flow, T_r is simply replaced by T_∞. The solution is given by

$$\frac{T_w - T_i}{T_r - T_i} = 1 - \exp\left[\frac{-hA_{rs}t}{V\rho c_p}\right] \tag{2.15}$$

As was the case for the semi-infinite solid solution presented in section 2.2, an additional complication is introduced, since true step changes in the applied fluid temperatures are not possible and the reference temperature is a function of time. This is again accounted for by modifying equation 2.15 through the use of superposition and Duhamel's theorem. The actual change is obtained by using a series of steps. The solution is then represented by

$$T - T_i = \sum_{i=1}^{N} U(t-\tau_i)\Delta T_r \qquad (2.16)$$

where

$$U(t - \tau_i) = 1 - \exp\left(\frac{-h}{V\rho c_p} A_{rs}(t-\tau_i)\right) \qquad (2.17)$$

Here, T_r.is time-varying and unknown but related to the time variation in T_∞ and T_f and to the value of h such that:

$$\Delta T_r = (1-\eta)\Delta T_\infty + \eta \Delta T_f \qquad (2.18)$$

So:

$$T - T_i = \sum_{i=1}^{N} U(t-\tau_i)((1-\eta)\Delta T_m + \eta \Delta T_f) \qquad (2.19)$$

The data reduction program with this model is listed in Appendix A. In brief, this program is highly iterative requiring an iterative solution for the time lag

correction to the semi-infinite solid solution each time an η or h is solved for in the data reduction. This is on top of the iterative nature of solving for h and η from equation 2.12 in the program and the iterative process of solving for η or h during each of those iterations.

Again, the results of this model are the basis for the composite surface of this study and its success can be seen in chapters 6 and 7.

CHAPTER 3

LIQUID CRYSTAL CALIBRATION AND THE SINGLE-TEST APPROACH

3.1 Introduction

As described in chapter 2, this study and previous work at ASU by Vedula (1989) and Kim (1992) has pioneered the use of TLC to obtain simultaneously both heat transfer coefficients and film cooling effectiveness value for the three-temperature situation. There are advantages to this technique. First, spatially continuous values may be obtained, the resolution of which is based to a large extent on the experimenter's willingness to reduce data. Secondly, this technique may be applied to new configurations without the complex and often expensive fabrication requirements of other techniques. This experimental method uses a video camera/frame grabber combination to determine the intensity of green light being emitted by the liquid crystal surface coating at each video pixel location. This intensity is compared to known intensity values for the crystal at a calibration temperature. In this way, a time to reach a known temperature may be determined for each pixel of the test section captured by the camera/frame grabber combination. With this knowledge, heat transfer coefficients may be determined as outlined in chapter 2.

Unfortunately, work at Arizona State suggests that the intensity of the colored light at which the calibration temperature is reached, depends heavily on the illumination level of the test surface. Even when great care is taken to

produce uniform illumination on a simple flat surface, background intensity levels of green vary by as much as 20%. For more complex test sections the variation is often 50% or more. This can be handled by recalibrating for various sections which locally have similar background intensities. However, this method is labor intensive and leads to slight discontinuities between the various sectors in terms of heat transfer coefficients on the sector boundaries.

Past work at Arizona State has used two methods to determine when each pixel of the processed test section had reached the desired temperature. The first method assumed a constant threshold that each pixel must reach to be at the calibration temperature (Vedula and Metzger, 1989). This method limited the reliable data to those pixels that had similar illumination levels to the calibration test. The second method used by Kim and Metzger (1993) used an offset threshold to determine when a predetermined calibration temperature was reached. This method measured initial background intensities of each pixel prior to the test run and then added a constant offset to those values to determine the threshold for each pixel. This method produced better results than the constant threshold method, but still did not give reliable results for areas of the test section with low illumination levels. Some pixels with lower illumination levels did not reach the threshold value set and therefore the heat transfer characteristics could not be determined. In addition, as work in this chapter indicates, an additional error is introduced in the coefficients for areas where the background intensity differed greatly from the background intensity level of the calibration area (copper bar with embedded thermocouple coated with liquid crystal).

This work takes a different approach. Since during a test run both the background intensity and the maximum intensity for green, in this case, vary

with the illumination level at each pixel, a normalized percentage offset is tried. Specifically, during calibration, both the nominal background intensity of green and the maximum intensity seen during heating of the liquid crystal are measured at each pixel. Then, a percentage of the difference between the two is added to the nominal background value at each pixel to set the threshold value for that pixel. When that threshold is reached at a given point, the calibration temperature is assumed to be reached and the local heat transfer calculation can be accomplished.

In addition, this study looks at the use of video tape to record the test run, permitting the test to be processed in a delayed fashion. Motivation for this portion of the study lies in the ability to tape complex test sections from various angles, using multiple cameras, during a single test run and to then process the test at a later time. Additionally, because the thermal transient portion is short compared to the entire testing process, limited computer resources are needed for a far shorter period of time.

For completeness of this method and to improve the flexibility of the method for obtaining more than a single transient during each test, work reported in this chapter also considers not only calibration of green for determining surface temperature but also red, blue and what is termed backside green. This work looks for the optimal threshold to be used with each color and considers the effect on the calibration temperature of viewing the test surface through Plexiglas . Results support the use of green and red in running heat transfer tests and indicate the noise levels inherent in processing blue data limits its usefulness in this experimental technique. Independent tests using green and backside green thresholds produce very similar results, both increasing confidence in the experimental method and

limiting concerns of the effect of lateral conduction within the test surface on experimental results.

In addition, this study looks at using the single run approach to determine both convective heat transfer coefficients and effectiveness values for the three-temperature problem. The work in the rest of this study relies upon a two-test scheme in which Reynolds number and blowing ratio of the two tests are matched, but film temperature is varied as described by Vedula (1989). This method provides excellent results, but requires the cumbersome task of running two tests for which the flow parameters must be matched in order to produce valid data. As Vedula discussed, the single-test approach appears theoretically possible and could potentially reduce testing time, cost and reduce error introduced when matching the two-test run approach. Unfortunately, results of this study suggest necessary test conditions for the single-run approach may be experimentally impossible to achieve and, in general, as currently envisioned, should not be considered for future tests.

3.2. Experimental Apparatus and Procedures

The experimental apparatus and test procedures for this chapter are conducted on a turbine tip model used by Kim and Metzger (1993) for detailed heat transfer studies. The details of that study are not discussed here since our concern is the procedure and not the specific results. Details of the experimental apparatus and the test procedures were presented in section 2.3.

3.3 Liquid Crystal Calibration

Figure 3.1 illustrates the RGB color resposes of the TLC versus temperature. Testing was accomplished to better understand the effect of variation of background intensity on calibration temperature. Much of the past work at Arizona State University has calibrated the TLC by first measuring the background intensity of green on a normalized scale from 0 to 255. Then, a constant offset was added to the color background and a threshold set for each pixel of the viewing window matrix. Since the background intensity varies from one pixel to another, so does the threshold for each pixel. The pixels which overlay the thermocouple embedded in the copper bar are used to determine the calibration temperature of that particular offset. In this way, a time matrix for reaching a given calibration temperature for the entire test section may be determined. If the background intensity of the test section is sufficiently uniform, ±5% of the copper bar nominal, then this method yields excellent results with a temperature resolution of ±.5°F.

Unfortunately, on test sections with more complicated geometries the background intensity can vary as much as 50% making the constant-offset method unacceptable for the entire test section. Figure 3.2 shows the results of such a case. Here a TLC coated copper bar was calibrated using a 40 constant offset to a temperature of 102.8°F Then, a series of runs were made in which the background intensity was varied by varying room lighting. As expected, near the background intensity of the original calibration (78), the constant offset threshold provided a good method of determining transient surface temperature responses. On the other hand, at a background intensity

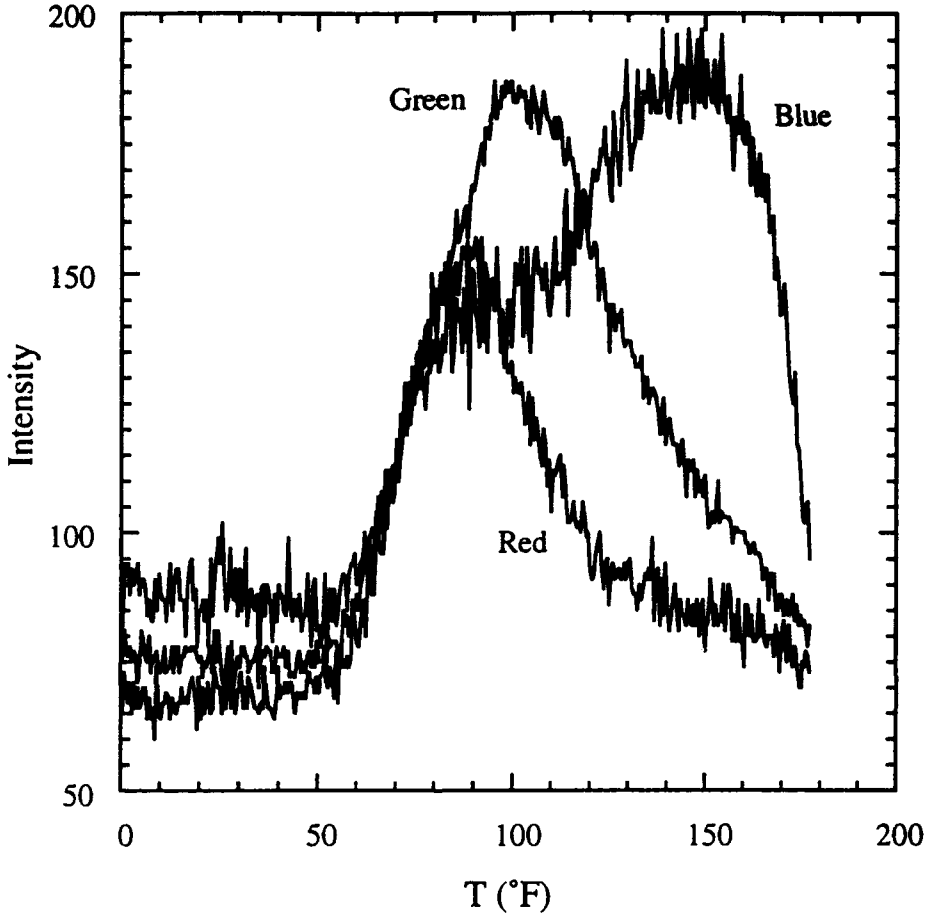

Figure 3.1 TLC intensity response

either much higher or lower than nominal, the error in recording the response became unacceptably high. For example, at a background intensity of 55, Figure 3.2 indicates a temperature error of 1.8°F was introduced. The implication is that an experimenter must recalibrate for various background intensity levels if such variations exist on the test section. An alternative approach for complex test sections is desired.

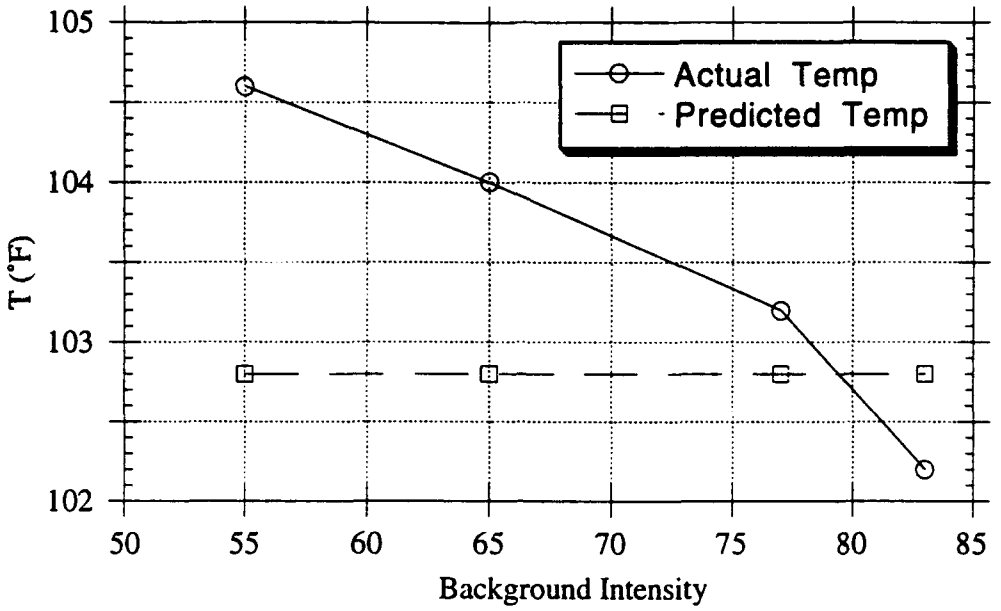

Figure 3.2 Constant threshold - offset of 40

3.4 Normalized Threshold

Experience gained through extensive use of TLC coatings at ASU led to an alternative approach. Observation of the intensity response of the TLC during a transient indicated when background illumination of green, red, or blue changed, so did the maximum intensity of that color seen during a transient response. In addition, this change in maximum intensity is very nearly proportional to the variation in background intensity. This led to a normalized percentage threshold method.

In this technique the background intensity of each pixel is again recorded. A calibration test is then run in which the test section is slowly heated through the TLC's response range. The maximum intensity of each

pixel is determined by either taking the maximum value seen or by averaging the top 2, 3, or 4 values seen at the peak of the intensity response. This is explored to lessen the impact of the approximately .25 second frame grabbing intervals on the maximum intensity value. A percentage of the difference between the background intensity and the maximum intensity is then calculated for each pixel and added to the pixel's background value. In such a way, a threshold is set for each pixel. At the same time, this process is accomplished for the TLC coated thermocouple placed in the flow as shown in Figure 2.2. For a given percentage, the calibration temperature for this method is then determined from the thermocouple's transient response.

To test the accuracy of this method, a series of tests were accomplished using various percentages and averaging either 2, 3, or 4 frames at the top of the intensity response curve. Results showed that the averaging of frames at the top of the intensity curve was not necessary and did not aid in reducing the calibration spread for a given percentage. The results for 4 frames, 3 frames and single frame averaging are shown in Figures 3.3, 3.4, and 3.5. The results show that for a particular percentage, the temperature response can be determined over a wide range of background intensities to an accuracy of ±0.2°F of calibration temperature. In some cases the accuracy was even better.

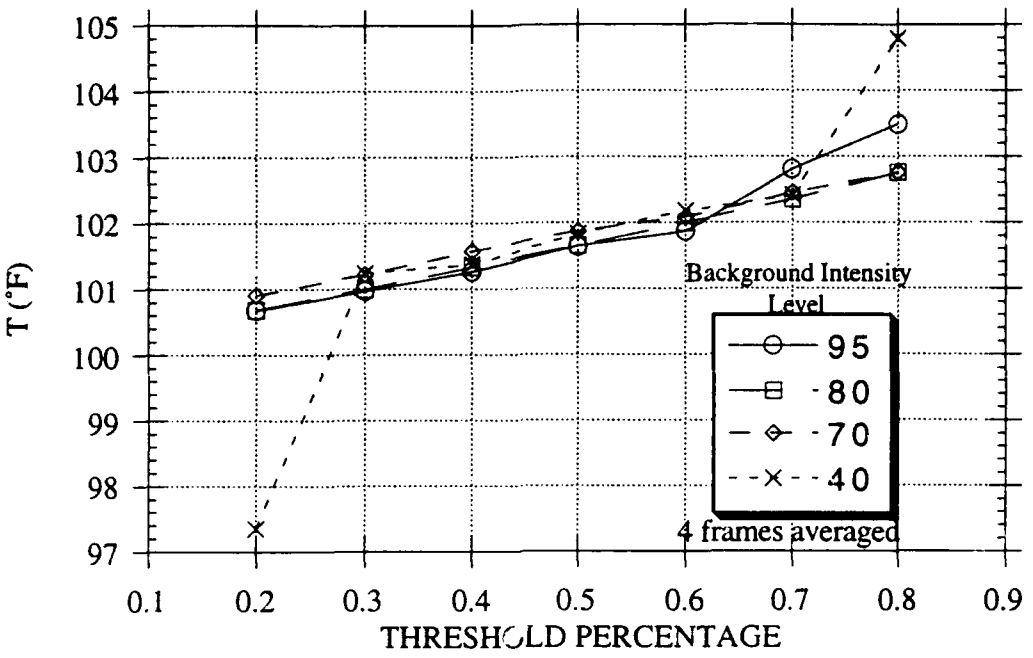

Figure 3.3 Normalized threshold - 4 Frames Averaged

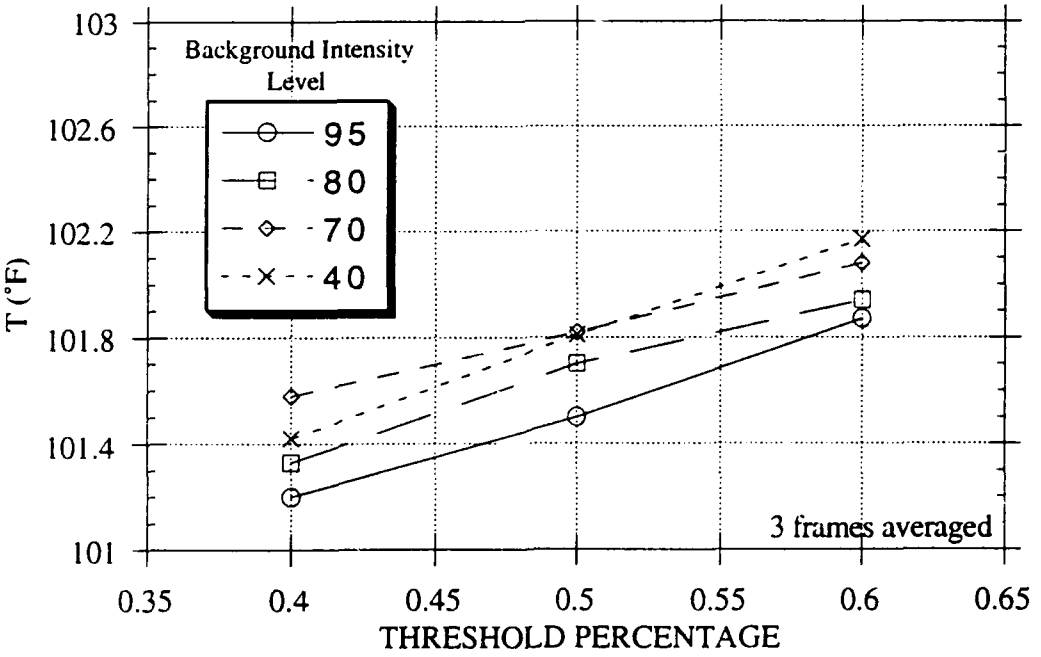

Figure 3.4 Normalized threshold - 3 frames averaged

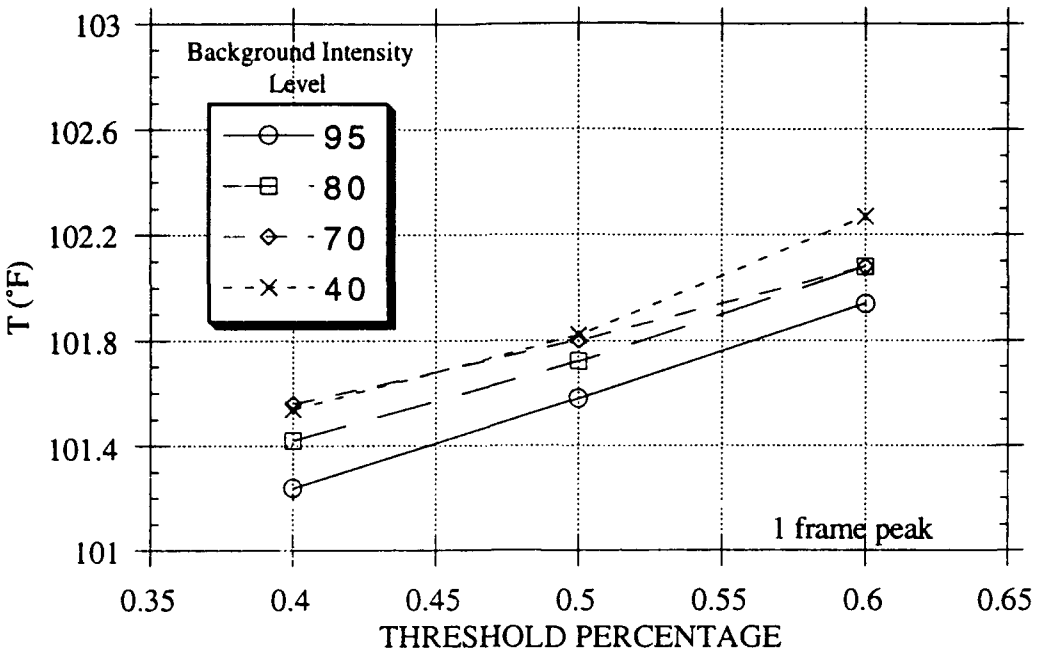

Figure 3.5 Normalized threshold - 1 frame peak

The range of percentages used on each plot ensured good results across the test section even with large variations in background intensity levels. Below the percentages shown, noise from the processing method began to be important enough to affect the results and cause some pixels to give an error in their transient response.

The results of these tests were extremely favorable. The potential now exists, using the normalized threshold method, to get an accurate time matrix for transient surface temperature response even for test sections with complex geometries and nonuniform surface background intensities. Again, even for test sections with varying background intensities, each pixel area of the section has a temperature response error of less than ±0.2°F, when a normalized threshold method is used.

Error analyses carried out by Kim (1992) where the TLC Calibration was taken as ±0.5°F found the uncertainty for h to be -9% to 4% and the uncertainty in η to be from -3% to 7%. Experimental uncertainties, using ±0.2°F for the calibration uncertainty, have been assessed (Appendix A) by the methods of Kline and McClintock (1953). The uncertainty in h is estimated to be between -4.3% and +3.8%. The uncertainty in absolute effectiveness values were found to be within ±0.027.

3.5 Video Taping

As an aside to this work, because of future plans at ASU to analyze complex test sections by simultaneous videoing from several perspectives, video taping was analyzed. In this analysis, a single test run of the flat plate configuration is processed live and also taped and processed from the tape. Figures 3.6 and 3.7 show the results for convective heat transfer coefficient. As a result of the taping process, the calibration temperature shifted slightly from 101.7°F - live to 101.6°F - taped. The copper bar with embedded thermocouple located at the end of the test section is visible at the top left center of each Figure. This slight shift is well within the experimental error of the temperature measurements. In addition, there is a random change in h when each live pixel is compared to the corresponding video-processed pixel. This change was typically about ±1%, but some pixels changed by as much as ±2.5% from live h values.

Figure 3.6 Flat plate, 5/16" clearance gap, live processed

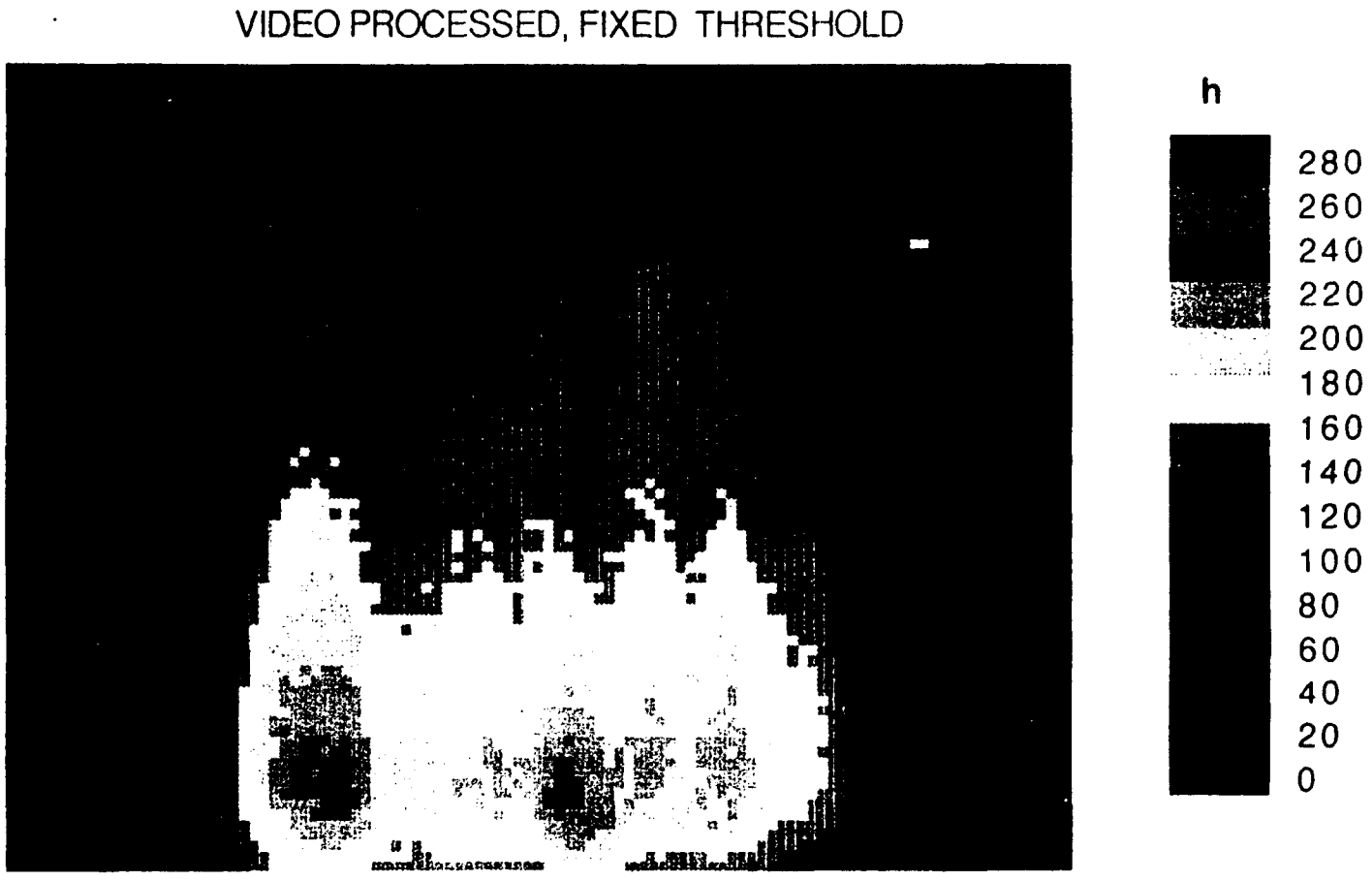

Figure 3.7 Turbine tip, video processed

3.6 Percentage Versus Fixed Threshold

With the video-processing and percentage threshold methods understood, an analysis is conducted of the turbine tip test section with a 3/8" cavity, a blowing ratio of .1 and a Reynolds number of approximately 30,000 based on a gap size of 5/16". Figure 3.8 shows the results of this test using a fixed-threshold analysis. Even though care was taken to ensure uniform lighting, background values on the test section varied from 90 in the center to a low of 65 in the upper left region of the cavity. As pointed out earlier, this means the h values in regions where the background differs from the background value of the copper bar used in calibration are suspect. Because the calibration temperature is in error by as much as 1.8°F in these areas, additional error is introduced in the local h values. Also, the results are not symmetrical when the left and right sides are considered, even though care was taken to provide uniform flow through the clearance gap. Finally, some pixels in the low intensity background region in the upper left portion did not reach the preset threshold and therefore show no h values.

Figure 3.9 shows the results of the same test using the percentage-threshold method. Here a 0.5 percentage was used. As expected, the h values in the center of the section, where the background intensity is uniform, match well between the fixed and percentage-threshold Figures. However, on the sides and top of the test section, where the background intensity varied significantly from the center, a different picture results. The h distribution is much more symmetrical and h values for all pixels, regardless of a severe background intensity variation, are determined.

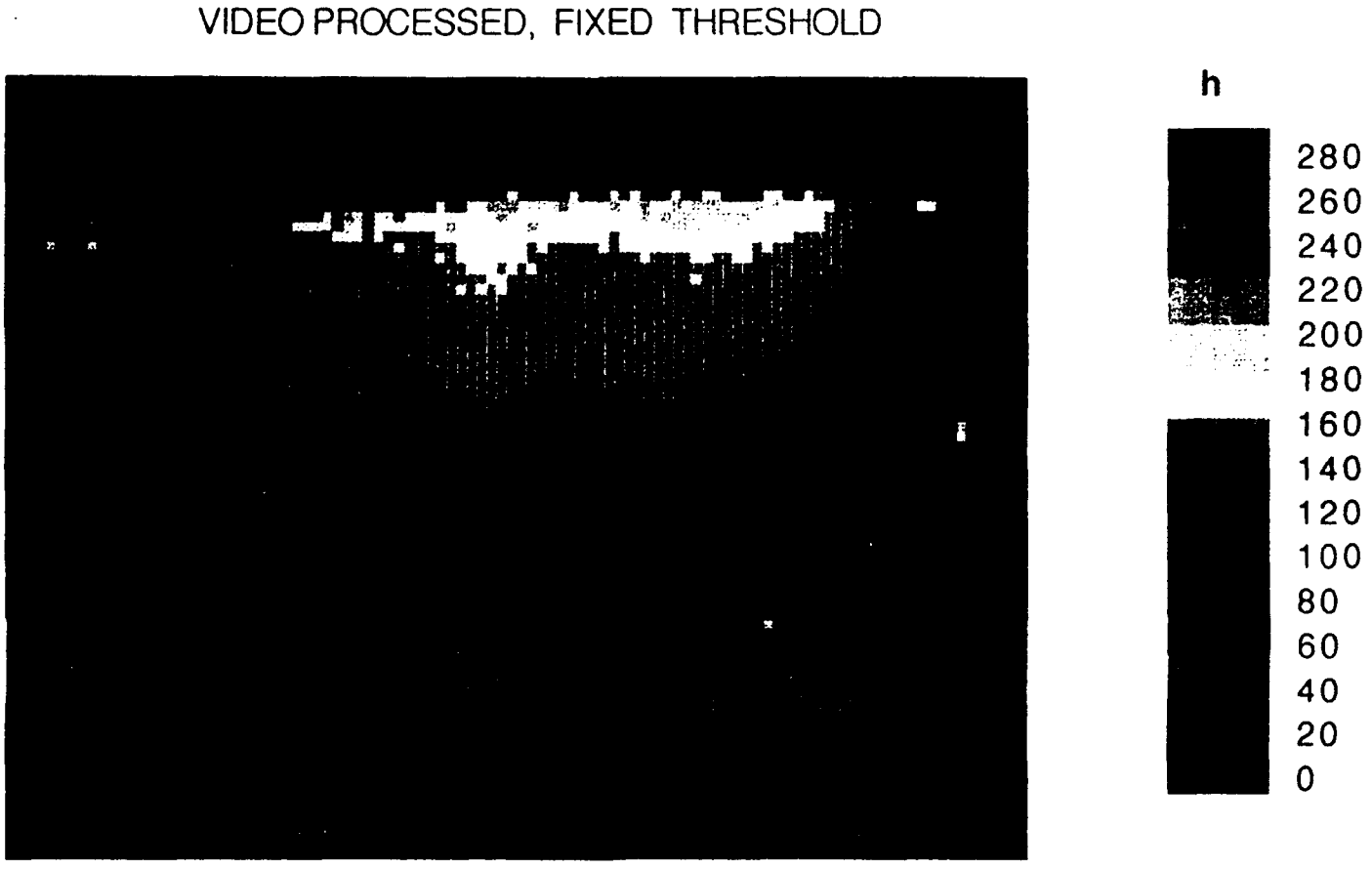

Figure 3.8 Turbine tip flow, fixed threshold

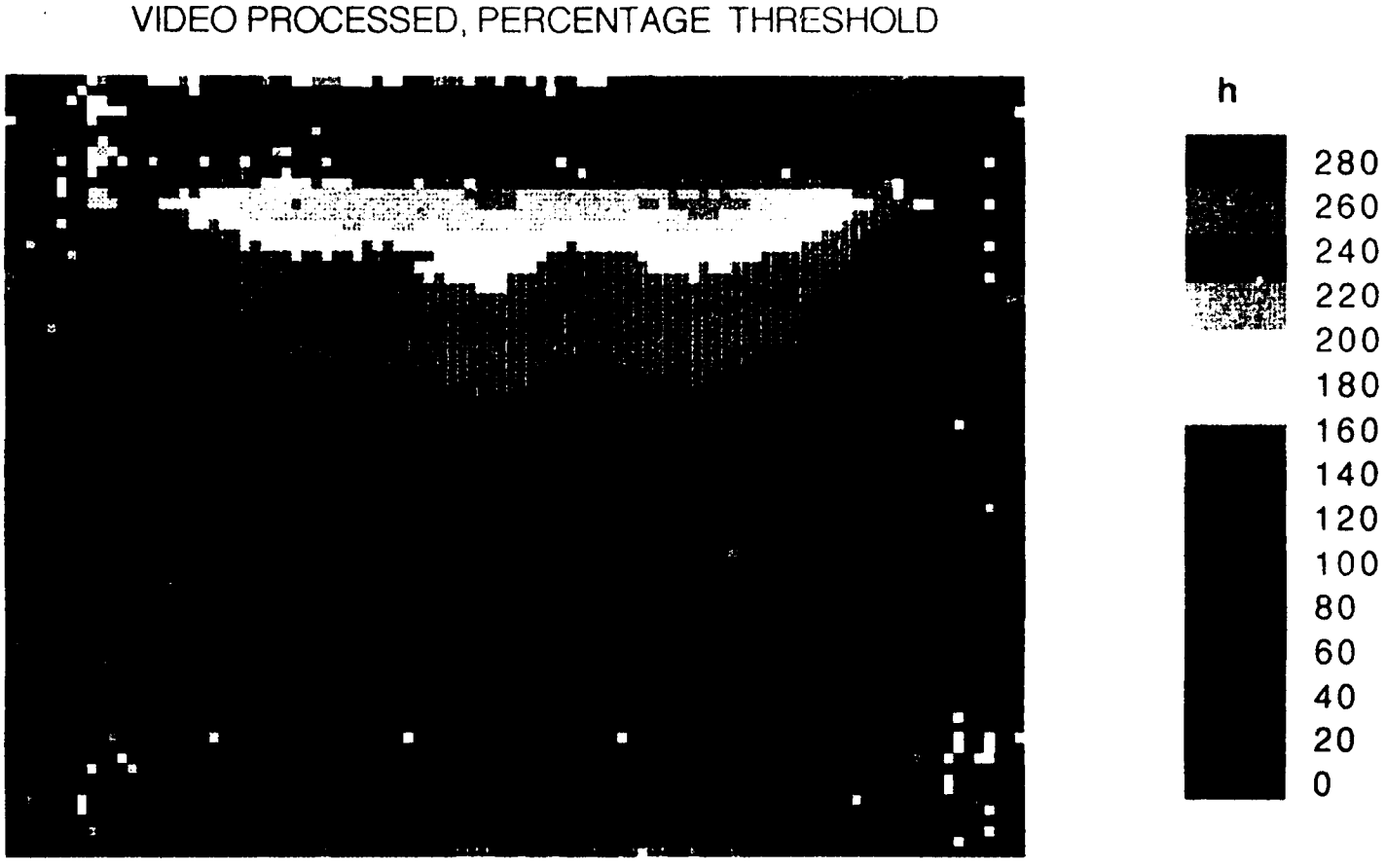

Figure 3.9 Turbine tip, normalized percentage threshold

The calibration temperature for each pixel is now within ±0.2°F of the copper bar calibration temperature.

Figure 3.10 shows a smoothed version of the results using the interpolated image option of University of Illinois' National Center for Supercomputing Applications Data Scope plotting program. This presentation loses the data resolution knowledge available when the unsmoothed data are viewed, but should present a more realistic view of the physics at work on the test section.

3.7 Red, Green and Blue Calibration

In this section, red, green and blue are captured by color video camera to produce a time/temperature matrix of the test region and the copper bar. As mentioned earlier, the normalized-threshold technique is used exclusively here to establish the time matrix for each test case. Previous work indicates a percentage of about 0.5 is optimal for green. When that threshold is reached, the calibration temperature is reached. Since the background intensity varies from pixel to pixel, so does the threshold for each pixel. The pixels which overlay the thermocouple embedded in the copper bar determine the calibration temperature of that particular percentage offset.

In this section, calibration is extended to red, blue, and backside green. In choosing a percentage for calibration, we desire relatively noise-free results where the temperature spread over varying background intensities is minimized. In general, this limits useful percentages to those between 0.3 and 0.7. If the percentage is set too low, noise from the image processing system (camera sensor, TLC, frame grabber) becomes important enough to affect the

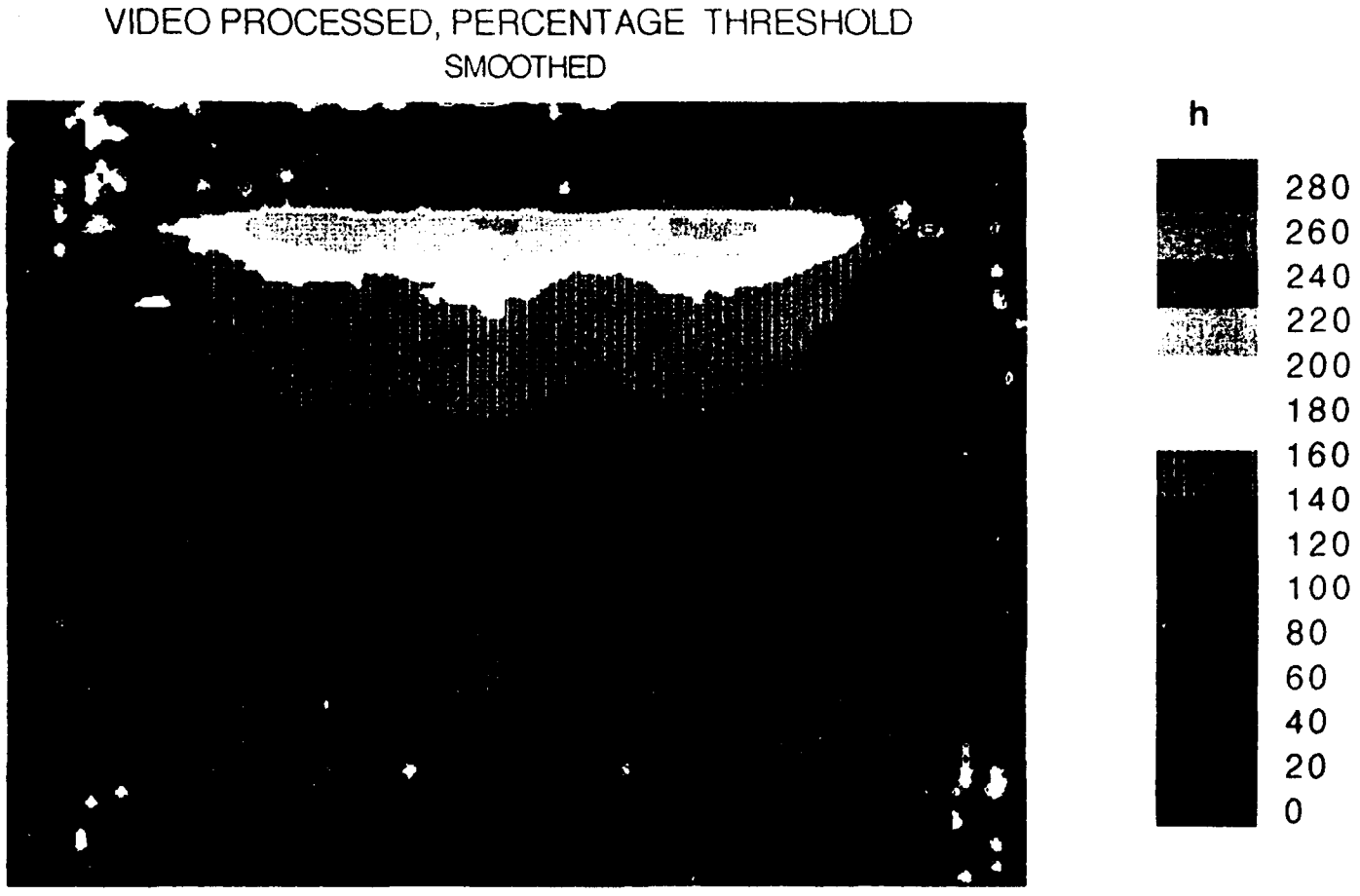

Figure 3.10 Turbine tip, normalized percentage threshold, smoothed

results and cause some pixels to give an error in their transient response. If the percentage is set too high, depending on the time response of the surface, some pixels never show the calibration temperature (color intensity) is reached.

Our desire is to document the advantages of using red, green, or blue and their effect on overall heat transfer calculations. Figures 3.11 and 3.12 are the calibration curves for red and blue. From Figure 3.5, in the last section, the TLC is calibrated to 101.6°F ± .2 for green at 50%.

For red the TLC can be calibrated relatively noise free, although not as noise free as green, for percentages between 40% and 60%. At 40% the TLC calibrated to 101.1°F ±.2 for red and at 50% to 101.5°F ±.2. This correlates well with what is seen by an observer during a test run. Red is visible just prior to the appearance of green.

For blue, the TLC could be calibrated for percentages between 0.4 and 0.6. However, unlike green and red, significant noise was present in the results even in this optimal range. The effects of this noise will clearly be seen later in this section. In addition, at low background intensities (ie. a green background intensity of 40) blue did not calibrate satisfactorily unless the percentage was set above 50%. Below this value, camera sensors seem unable to distinguish between green and blue. At 50% the TLC calibrated to 108.8°F ± .8 for blue and at 55% to 109.6°F ±1.6. If the test surface can be assured to have background intensity values above 70, a calibration of 109.1°F ±.4 can be used for 50%. Again, as we will see shortly, even at 50% significant noise exists in the results. This increased noise level in the blue response is clearly seen in Figure3.1. Whether this is a result of the

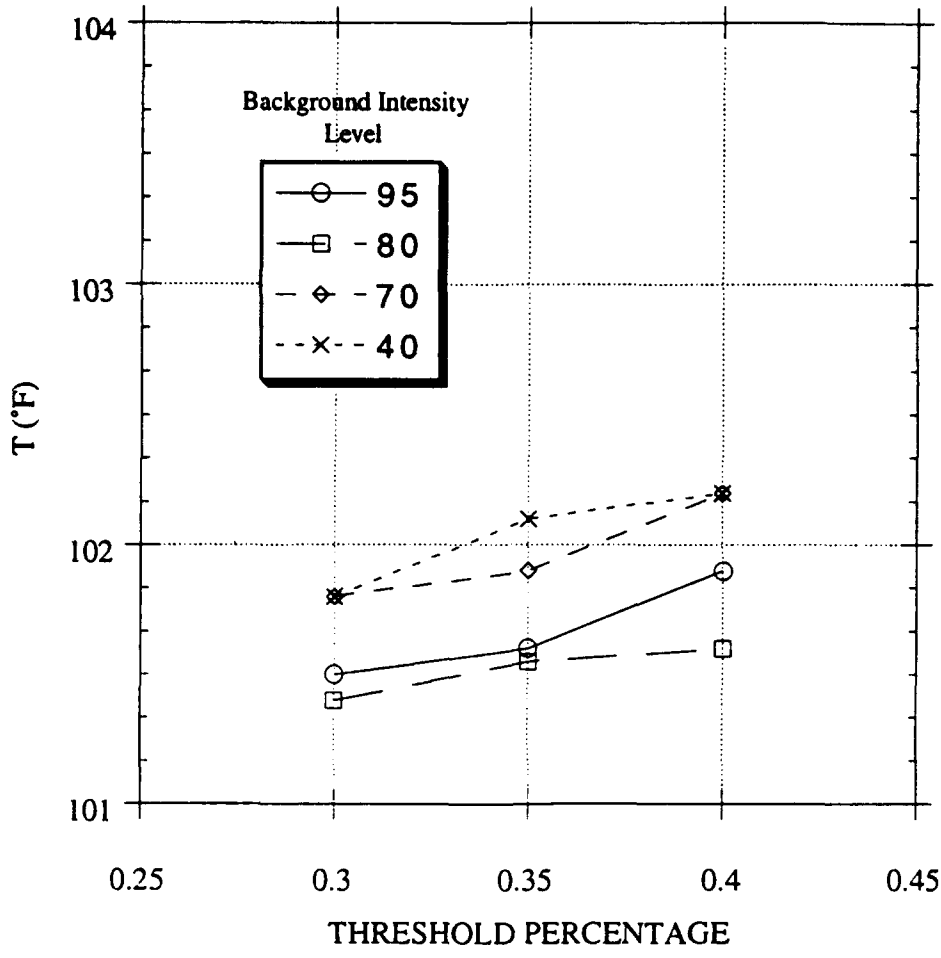

Figure 3.11 Red calibration

fluorescent lighting system used to illuminate the surface or a result of the ability of the charged-coupled device (CCD) chip used in the video camera to convert the various color intensities to electric signals is not currently known.

The next section documents the attempts to obtain h and η in a single test run. To accomplish this, two points with temperature and time are

required at each pixel in order to solve two equations in the form of equations 2.7 and 2.8. These points should be as far apart temperature-wise as possible, as will be discussed later. Because of the noisy results blue gives and the close proximity of red and green calibration temperatures, another approach is tried where the backside of the green intensity curve is calibrated.

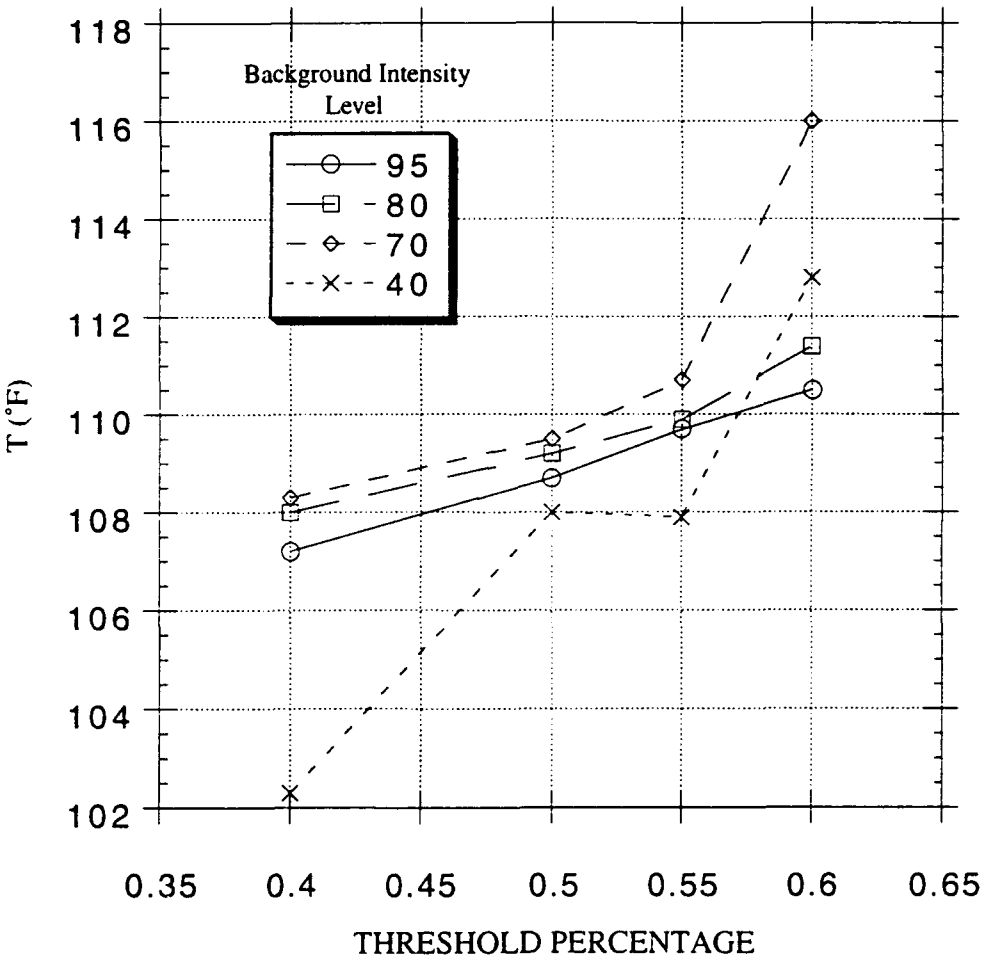

Figure 3.12 Blue calibration

When calibrating the backside of the green calibration curve, a two-step process is required. First, it must be determined whether the intensity response lies on the front or backside of the green intensity curve and if on the backside, when the response drops below a preset percentage threshold. Figure 3.13 helps illustrate the process.

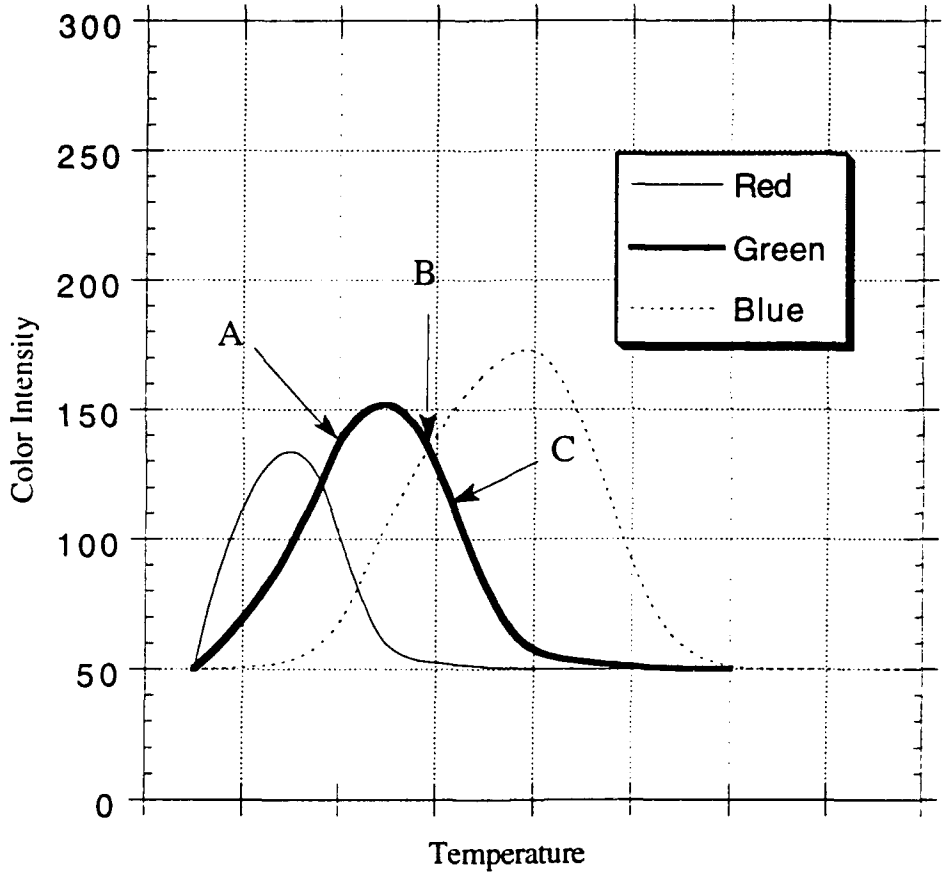

Figure 3.13 Intensity response, backside calibration

A percentage is picked to determine point A. Once the intensity response moves above this point and then drops below it again at point B, we can determine our location on the backside of the response curve. A different percentage threshold is then calibrated to correspond to point C. Although seemingly straightforward, because of the noise inherent in the process, points B and C must be spread by sufficient intensity level to prevent being misidentified. But, because a small window exists for determining a relatively noise-free point A (and thus B), very few combinations of upper percentage (A and B) and lower percentage gave good results. In general, the percentages must be spread by at least 10%. With front side green being limited to values between 40 and 60%, backside green threshold was limited to values less than 50%. However below about 30% , backside green also experienced the same type of noise problems associated with low percentages on the front side of the calibrations curve.

Figure 3.14 indicates the calibration curve for a front side percentage of 45% and a variable backside percentage. Although these calibration curves indicate 40% as good backside percentage, actual results showed a fair amount of noise over the test surface. As a result, the TLC could best be calibrated for a front side percentage of 50% and a backside threshold of 40% to 110.15°F.

In each case reported above, the Plexiglas through which the test section is viewed was 1/4" thick. Prior work at ASU indicated calibration temperature may be affected by Plexiglas thickness. To investigate this effect, calibration of a copper bar coated with TLC was accomplished using resistance heating internal to the copper bar. No Plexiglas was placed between the calibration surface embedded with a thermocouple and the

viewing camera. The results indicated a shift in calibration temperature was present. For example, at a 50% normalized threshold, the calibration temperature is 0.4°F higher when Plexiglas is not present. The experimenter must therefore calibrate the TLC for the appropriate viewing situation. This is important for the composite plate tests accomplished in chapters 7, 8, and 9. In these cases, calibration is accomplished with the same thickness of epoxy on the copper bar as is present for the composite plate.

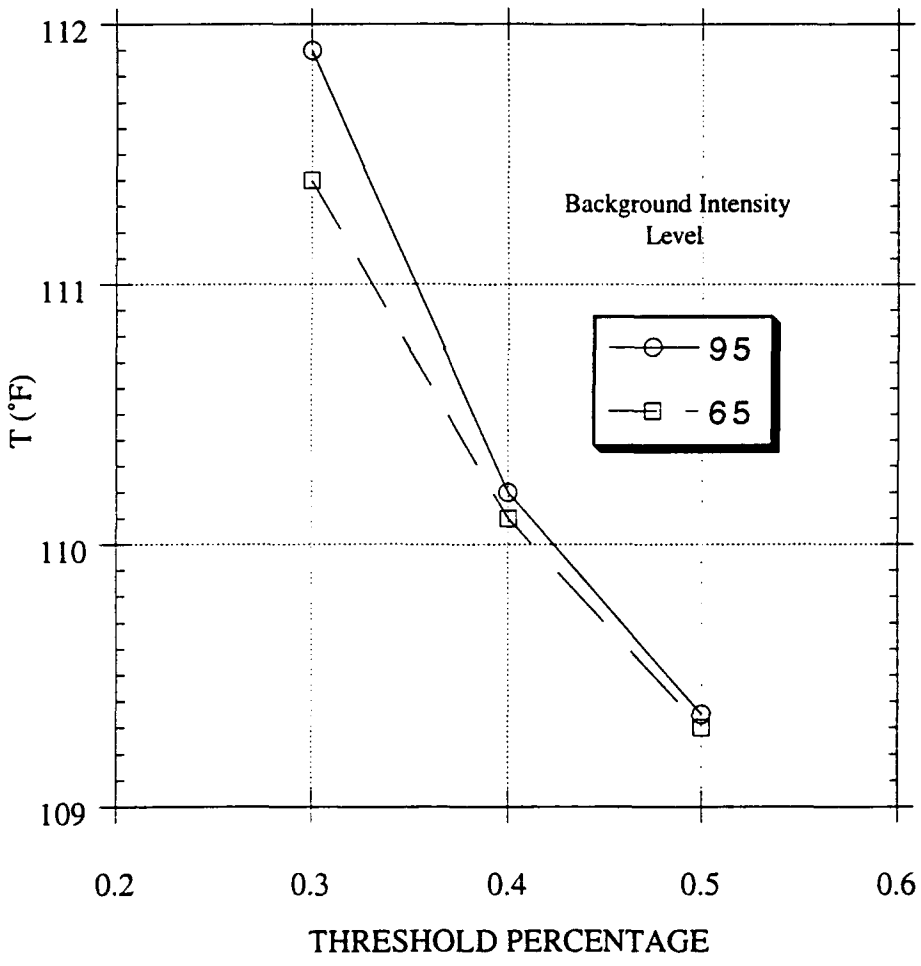

Figure 3.14 Backside green calibration

Using the calibration temperatures determined for green, red, blue, and backside green, it is now possible to accomplish actual test runs to determine heat transfer characteristics. But before looking at heat transfer results, it is useful to view the intermediate time plots which indicate for each pixel the time the chosen calibration temperature is reached. The contour smoothness of each plot, along with the number of bad pixels, those which are black, indicates the relative quality of each time map used in determining heat transfer characteristics. Figures 3.15, 3.16, 3.17, and 3.18 are time plots for green, red, blue, and backside green respectively. These Figures are for a Reynolds number of 30,000 and a blowing ratio of .5. The 3/16" perpendicular film holes are clearly visible in the test section. All edges, approximately 1/2", are exterior to the test section and should be disregarded.

In general, the green and backside green plots are superior. Contours are relatively smooth and almost all pixels indicate a time response on the test surface. Red also provides a relatively smooth plot, but a number of bad points appear in the time matrix. As expected, the red time plot almost exactly matches the front side green plot. The blue time plot, on the other hand, does not have smooth contours and many more bad points appear in the interior of the test section. This difference is not a result of the crystal response, but rather, we believe, from the video camera's ability to accurately sense blue. The camera's output is noisy in blue regardless of the subject being viewed. This is true for not only the camera used in this study, but also other cameras in use in the lab. This difference between green and red, and blue can easily be seen by looking at consecutive frame grabbing values for a subject under constant illumination at a constant temperature.

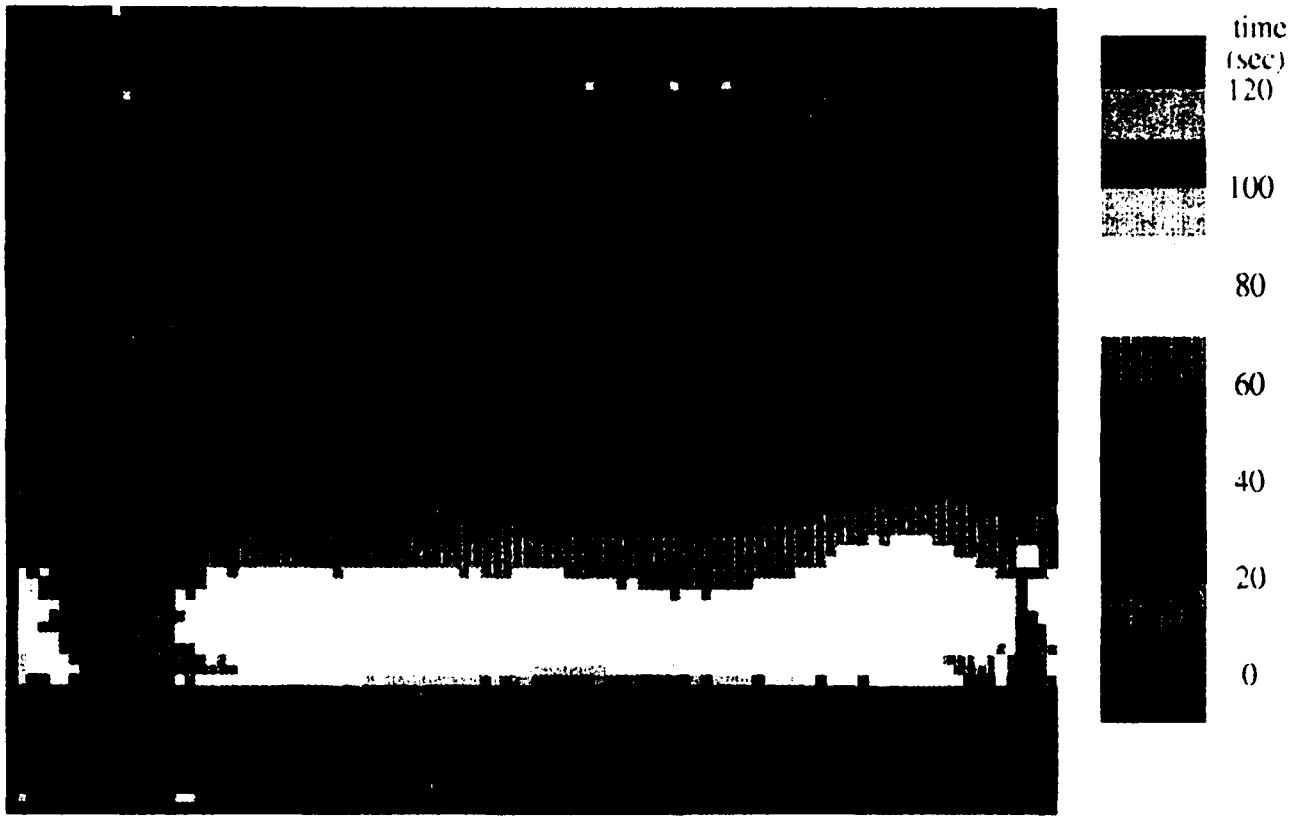

Fig3.15 3/8" cavity, 5/16" clearance gap, suction side injection
Re = 30,000; M = 0.5.
Time plot using green calibration

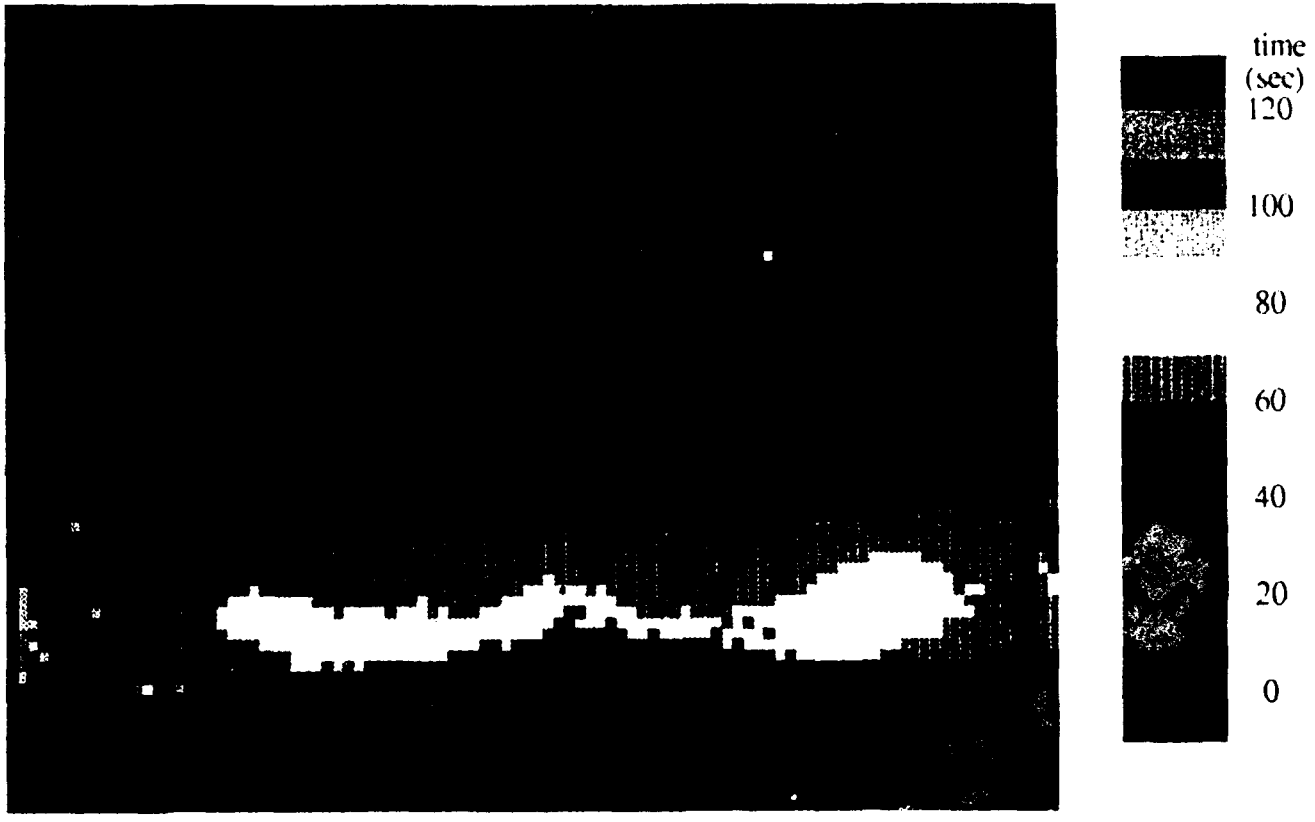

Figure 3.16 3/8" cavity, 5/16" clearance gap, suction side injection,
Re = 30,000, M = 0.5,
Time plot using red calibration

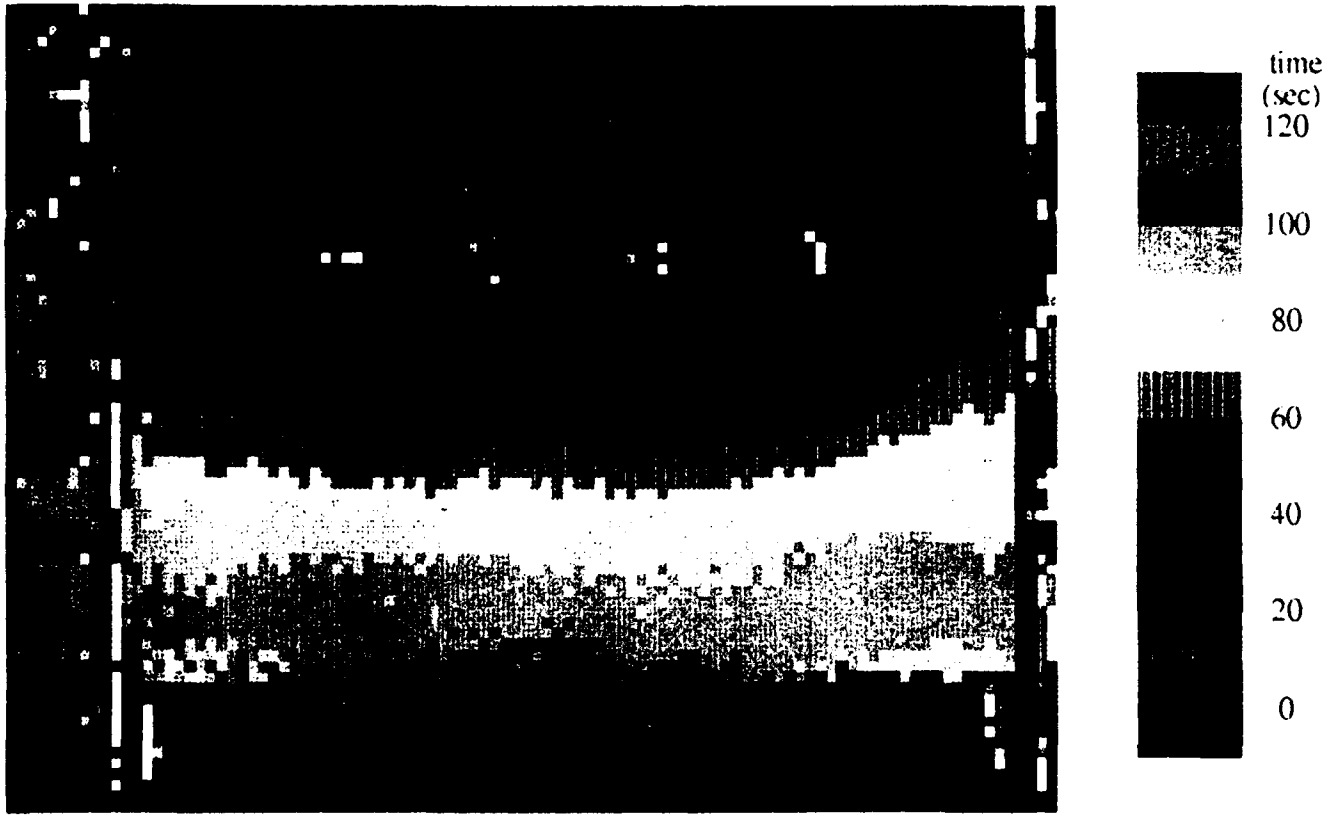

Figure 3.17 3/8" cavity, 5/16" clearance gap, suction side injection,
Re = 30,000, M = 0.5,
Time plot using blue calibration

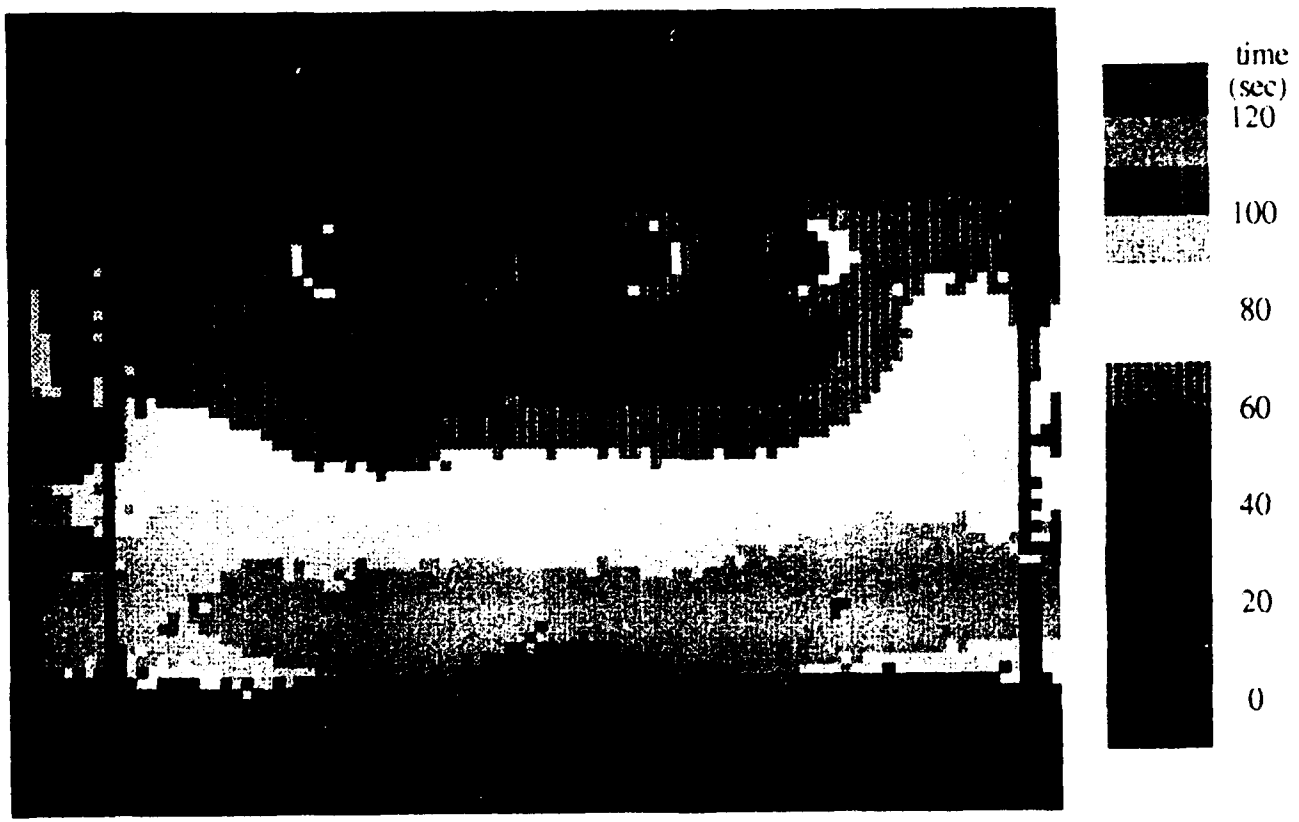

Figure 3.18 3/8" cavity, 5/16" clearance gap, suction side injection,
Re = 30,000; M = 0.5,
Time plot using backside green calibration

Since the intensity of a particular point should not vary with time, the red, green, and blue intensity values should be constant. If one runs the system under constant conditions, the value of green intensity shows very little noise, red only slightly more, but blue shows noise levels several times higher, indicated by a varying blue intensity when none should exist.

The lesson appears to be that green and backside green should be used whenever possible. The real test will be when each color's time responses are used to solve equation 2.2 for heat transfer characteristics.

As described in the measurement theory section, at least two experimental approaches exist for the solution of the three-temperature problem. The method of using two separate tests with different flow temperatures has successfully been used at ASU for the past few years with excellent results. To ensure success, a rigorous test procedure must be followed. Both h and η are functions of the Reynolds numbers of the main and film flows. While it is necessary to have different temperature potentials in order for the two tests to provide a consistent set of equations to be solved, it is also absolutely essential that the Reynolds numbers and blowing ratio are the same for the two tests to insure h and η are the same for both tests. In this study, two independent tests were accomplished by running what is termed a cold test and a hot test. In both tests main flow temperatures are set the same, however film temperatures differ by 20°F to 30°F. Film flow pressures are adjusted to ensure proper blowing ratio is maintained for both tests. During each test both the main flow and film flow vary enough that both main and film flow Reynolds numbers vary by approximately 3% from the early part of the test to the end of the test. As a result, there is some drift in both h and η . Because this drift in Reynolds number is very similar for

both the cold and hot test and is in general small, the consistency of the two nonlinear equations to be solved is not severely affected and solutions may be obtained.

Figures 3.19 through 3.26 are the h and η values for the turbine tip cavity at a Reynolds number of 30,000 and a blowing ratio of .5. The only difference between each pair of plots is the color used to determine the time/temperature matrix for each pixel.

As expected from the time plots presented in the last section, the data produced from using front and backside green calibrations, Figures 3.19, 3.20, 3.25, and 3.26 provide excellent results.

In general, Figure 3.21 and 3.22, using red intensity to determine the solution matrix, show averaged results which compare well to those obtained using green. Unfortunately, due to the noise associated with red seen in the time plots, a number of pixels can not be resolved. For the case of blue intensity, Figures 3.23 and 3.24 indicate a significant shift in h and η. This is most likely due to the larger noise problem blue experiences. As a result, the uncertainty in h and η are higher than for green.

The good news is green and backside green produce very similar results. When rows of each plot are averaged and compared, h values are within 4% and η values are within 7%. This is less than the uncertainties predicted for this experiment. This agreement exists even though green calibration is at 102.0 °F and backside green calibration is at 110.15 °F. As expected, there is some drift in h and η as a test run proceeds, but not enough to destroy the consistency of the problem. This agreement supports the overall technique of obtaining h and η.

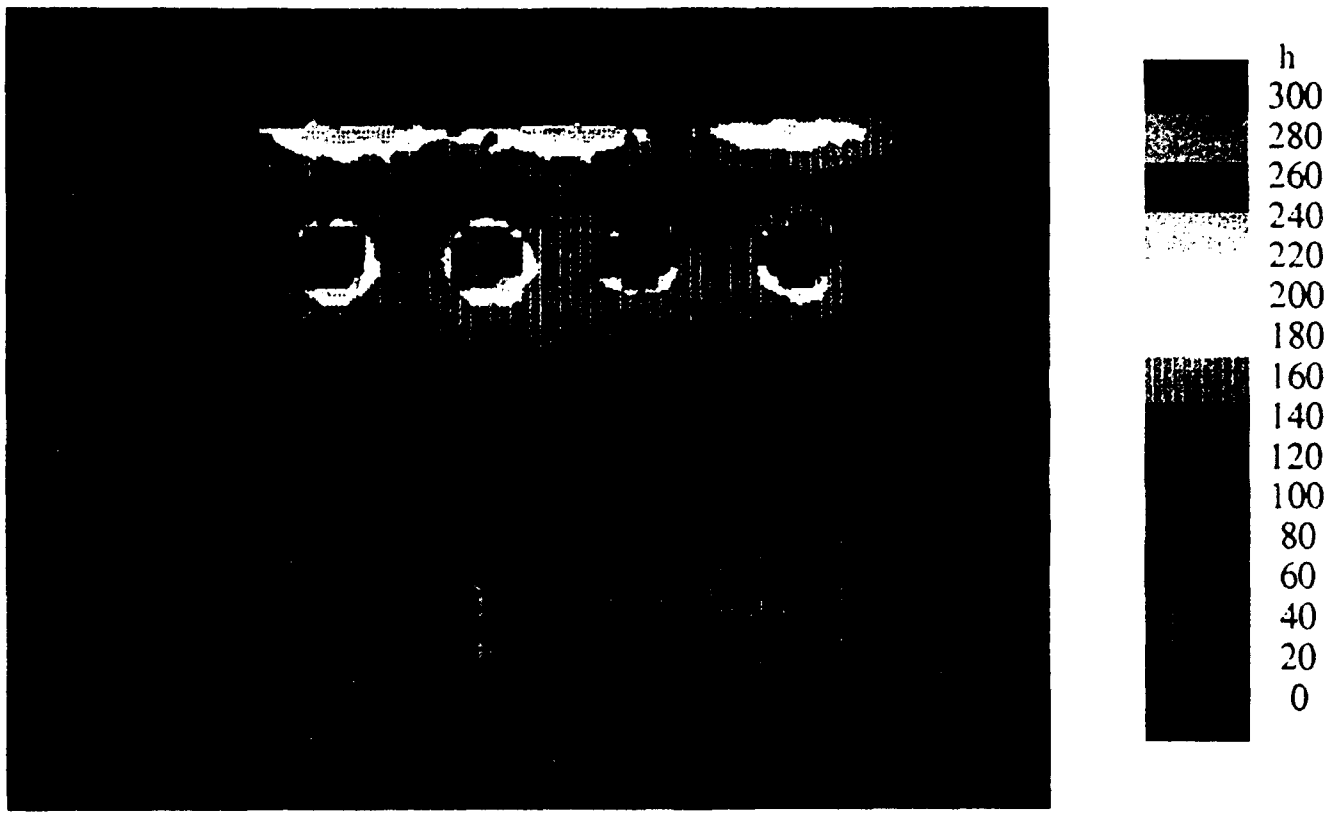

Figure 3.19 3/8" cavity, 5/16" clearance gap, suction side injection.
Re = 30,000; M=0.5.
Front side green calibration - 102.0 F

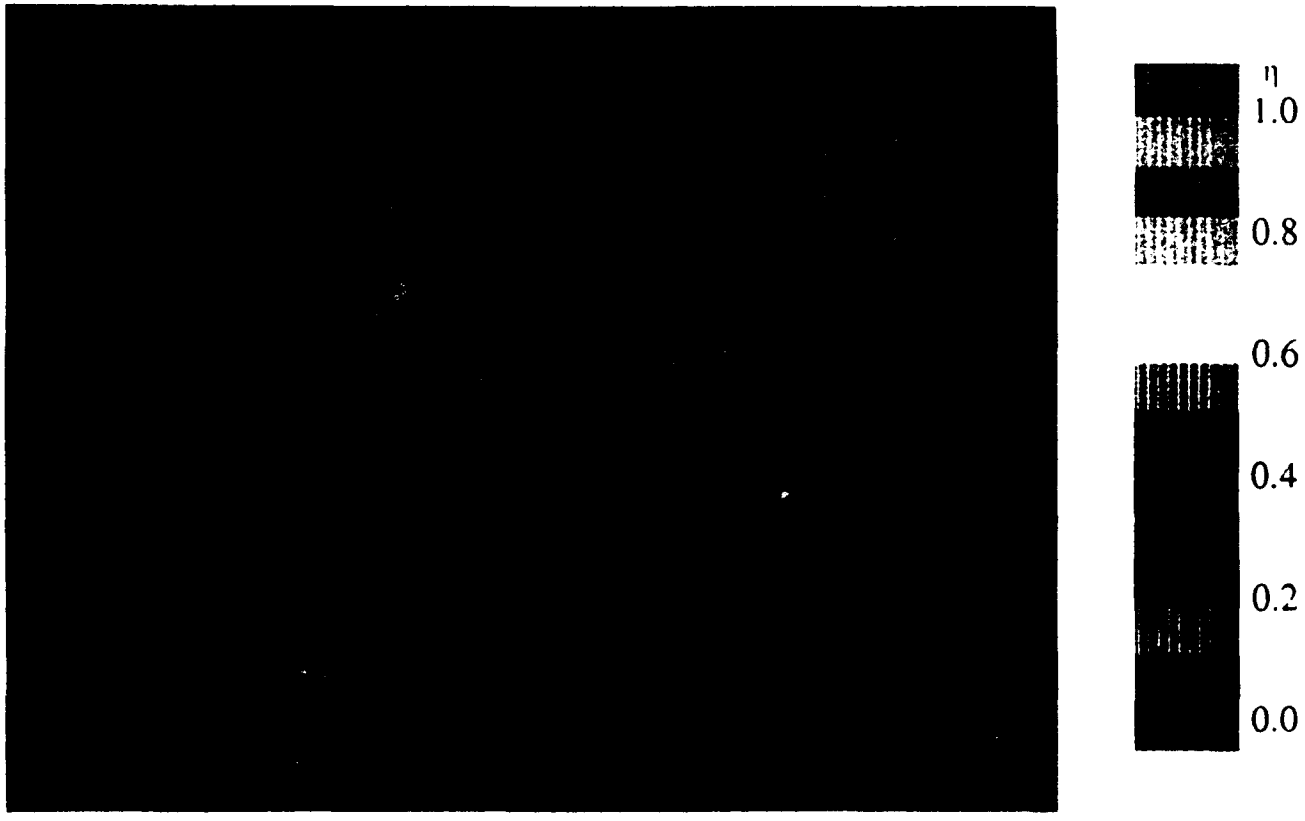

Figure 3.20 3/8" cavity, 5/16" clearance gap, suction side injection,
Re = 30,000, M=0.5.
Front side green calibration - 102 F

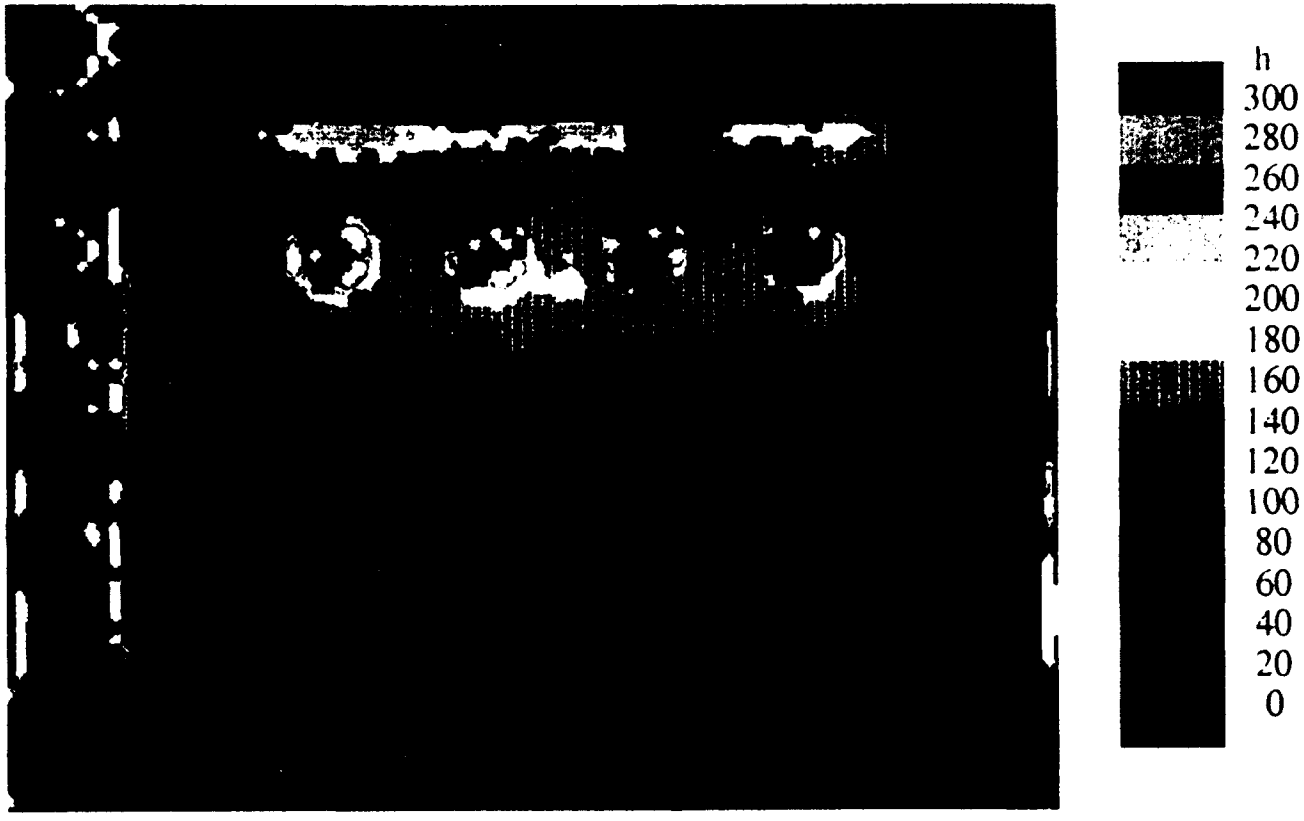

Figure 3.21 3/8" cavity, 5/16" clearance gap, suction side injection,
Re = 30,000, M = 0.5,
Red calibration - 101.6 F

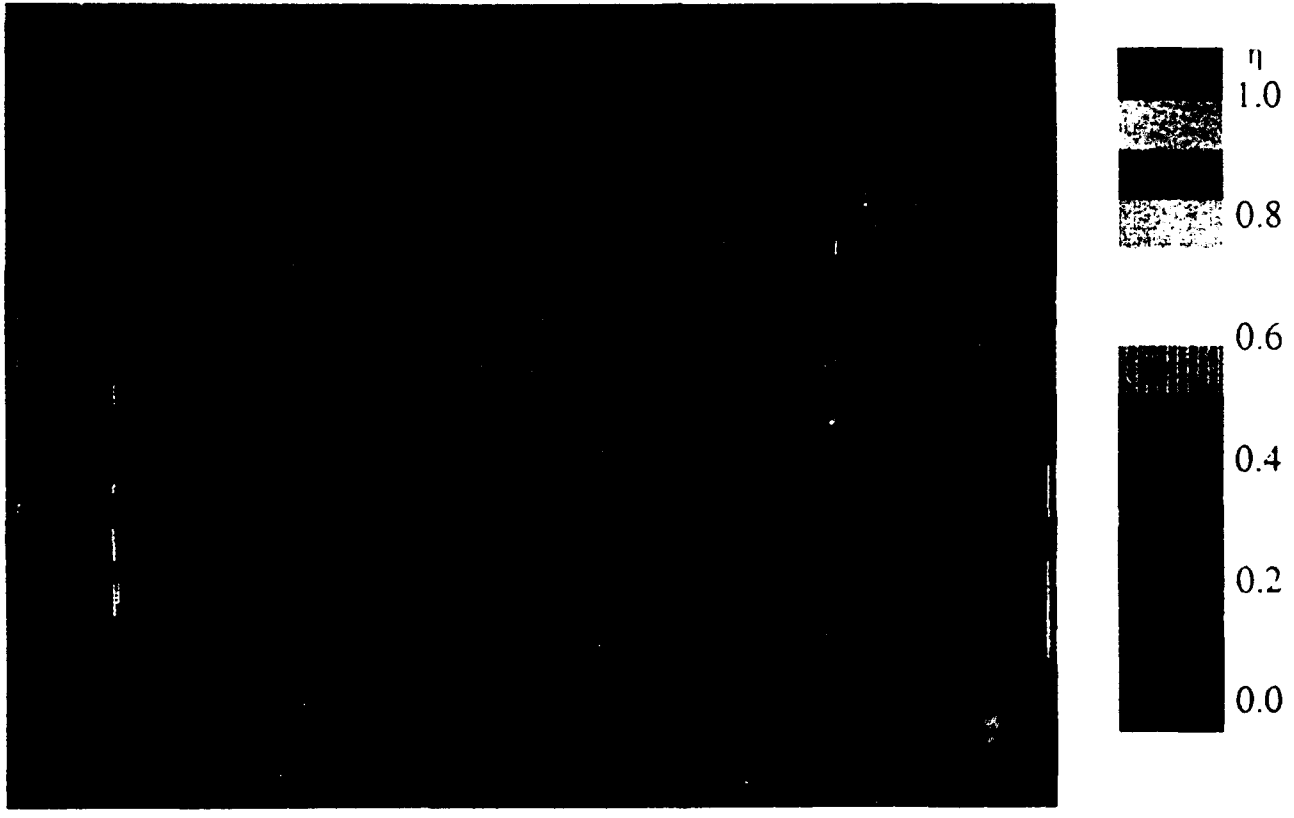

Figure 3.22 3/8" cavity, 5/16" clearance gap, suction side injection,
Re = 30,000, M = 0.5,
Red calibration - 101.6 F

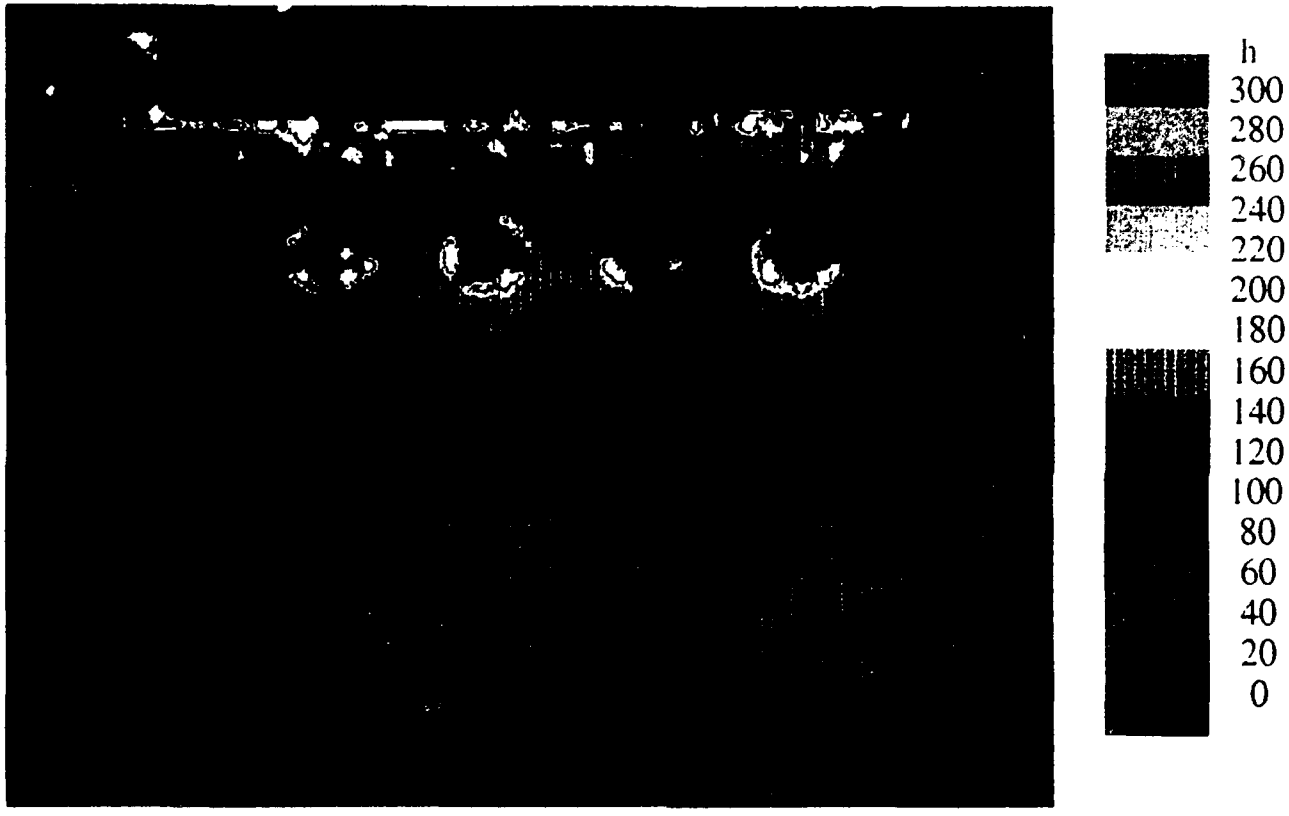

Figure 3.23 3/8" cavity, 5/16" clearance gap, suction side injection,
Re = 30,000, M = 0.5,
Blue calibration - 109.1 F

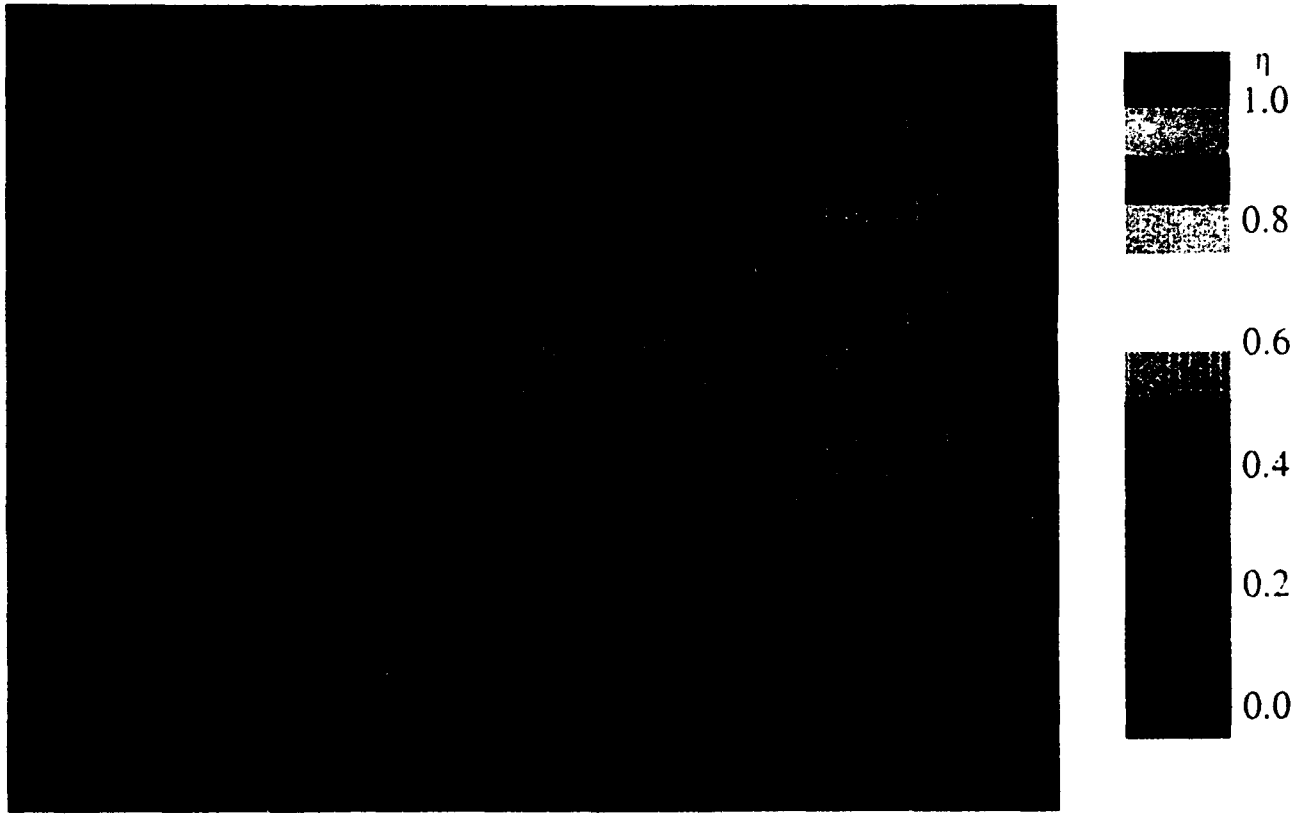

Figure 3.24 3/8" cavity, 5/16" clearance gap, suction side injection,
Re = 30,000, M = 0.5,
Blue calibration - 109.1°F

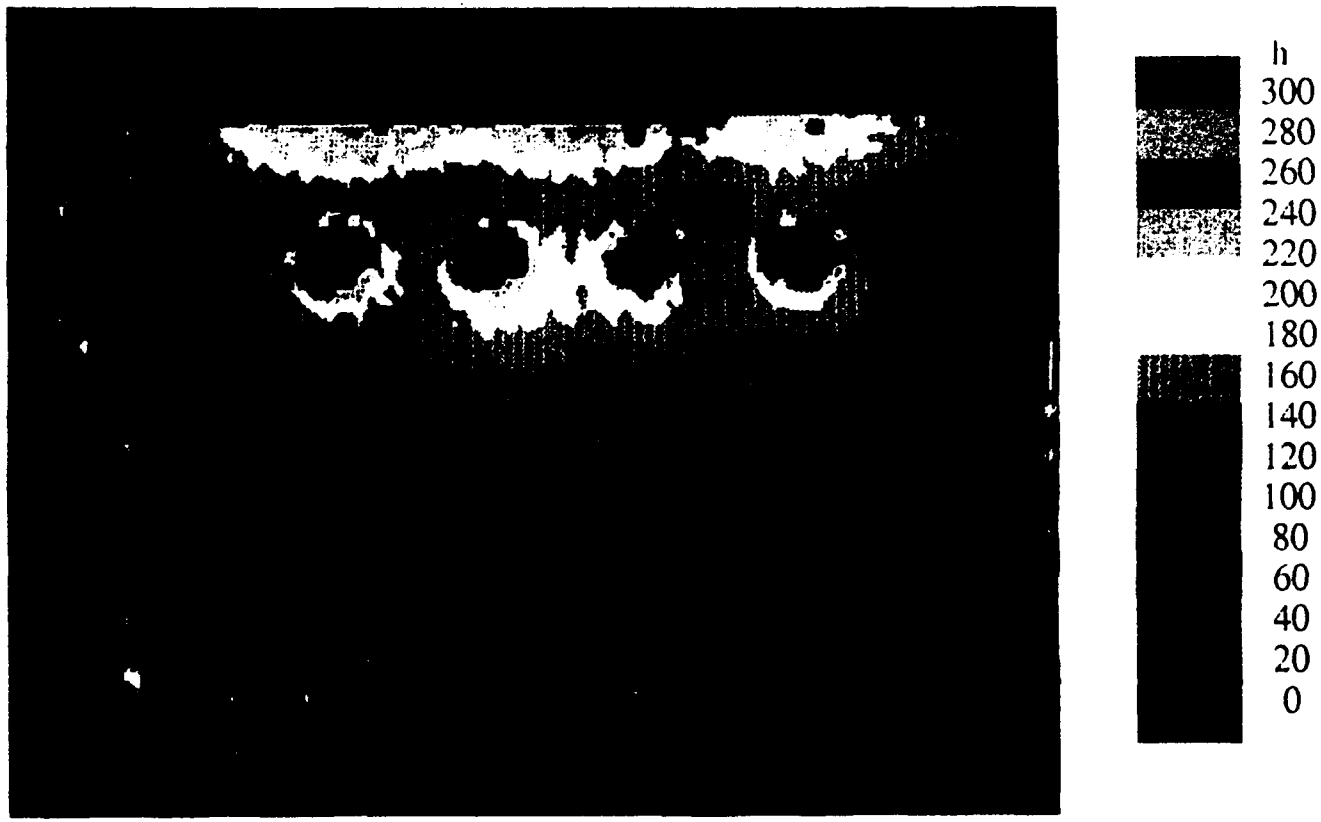

Figure 3.25 3/8" cavity, 5/16" clearance gap, suction side injection,
Re = 30,000, M = 0.5,
Backside green calibration - 110.15 F

Figure 3.26 3/8" cavity, 5/16" clearance gap, suction side injection,
Re = 30,000, M = 0.5,
Backside green calibration - 110.15 F

3.8 Single Test Method

Unlike the success achieved using the two-test approach, the single test approach has been used with extremely limited success. Although theoretically a sound approach to the three-temperature problem, experimentally it appears nearly impossible to achieve good results. Dr. Yufeng Yu, a post doctoral researcher at ASU, has on several occasions produced results which, although noisy, did approach those achieved using the two-test method. With Dr Yu's help we attempted to reproduce those results on a flat plate with round hole film ejection. Those attempts unfortunately failed. As will be described here, the problem of maintaining the consistency of the problem is difficult and not fully understood at this point. Two approaches are taken experimentally to try to achieve an acceptable solution. The methods, results and a discussion of the problems associated with the technique follow.

Before proceeding, a concept used by Vedula (1989) is useful in understanding the single-test approach. As presented in Chapter 1, the local surface heat flux is conventionally expressed as

$$q = h\,(T_r - T_w) \qquad (3.1)$$

Here h is a function of the aerodynamic character of the flow field alone and can be considered a constant of proportionality for a given flow field. If the heat transfer coefficient is instead based on the mean flow temperature and the wall temperature potential, the rate equation can be written as

$$q = h_m\,(T_\infty - T_w) \qquad (3.2)$$

Here h_m is not based on the actual temperature potential and is not a constant quantity as is h in equation 3.1.

At the instant the wall temperature is T_w, the heat fluxes represented by equations 3.1 and 3.2 must be the same.

$$h_m(T_\infty - T_w) = h(T_r - T_w)$$

or

$$h_m(T_\infty - T_w) = h(T_r - T_\infty + T_\infty - T_w)$$

or

$$(h_m - h)(T_\infty - T_w) = h(T_r - T_\infty)$$

or

$$(h_m - h)(T_\infty - T_w)/(T_f - T_\infty) = h(T_r - T_\infty)/(T_f - T_\infty)$$

Let

$$\frac{T_f - T_\infty}{T_w - T_\infty} = \theta^* \quad \text{and} \quad \frac{T_f - T_\infty}{T_r - T_\infty} = \theta^*_o = \frac{1}{\eta} \qquad (3.3)$$

Then

$$\frac{h_m}{h} + \frac{\theta^*}{\theta^*_o} = 1 \qquad (3.4)$$

Equation 3.3 is the equation of a straight line with the quantities of interest, h and θ^*_o being the intersection of this straight line with the ordinate and abscissa. The straight line plot is as shown in Figure 3.27.

To completely define this straight line, two points are needed. If the h_m values for two different values of θ^* can be measured then h and θ^*_o can be calculated. Notice that the reciprocal of θ^*_o is the effectiveness (η) as defined in the theory section.

Experimentally, θ^* can be varied by changing the film temperature (T_f) or the mean stream temperature (T_∞). To obtain the two different points from a single test, two different wall temperatures may be used. This can be accomplished by using front side and backside green indication temperatures of the TLC.

We will use this graphical representation shortly to interpret single-run data.

For the single-test approach, two experimental methods are considered. In the first method, the cold and hot tests from the two-test method are reprocessed. This is possible because each test run is video taped and processed at a later time. This time, however, two points are determined for each pixel from the front side and backside green thresholds corresponding to 102.0°F and 110.15°F. The results from the cold test-single run are shown in Figures 3.28 and 3.29. The results are not good.

The results from the hot test-single run are shown in Figures 3.30 and 3.31. Here we see the right trend in h, but the values are low. η values are zero.

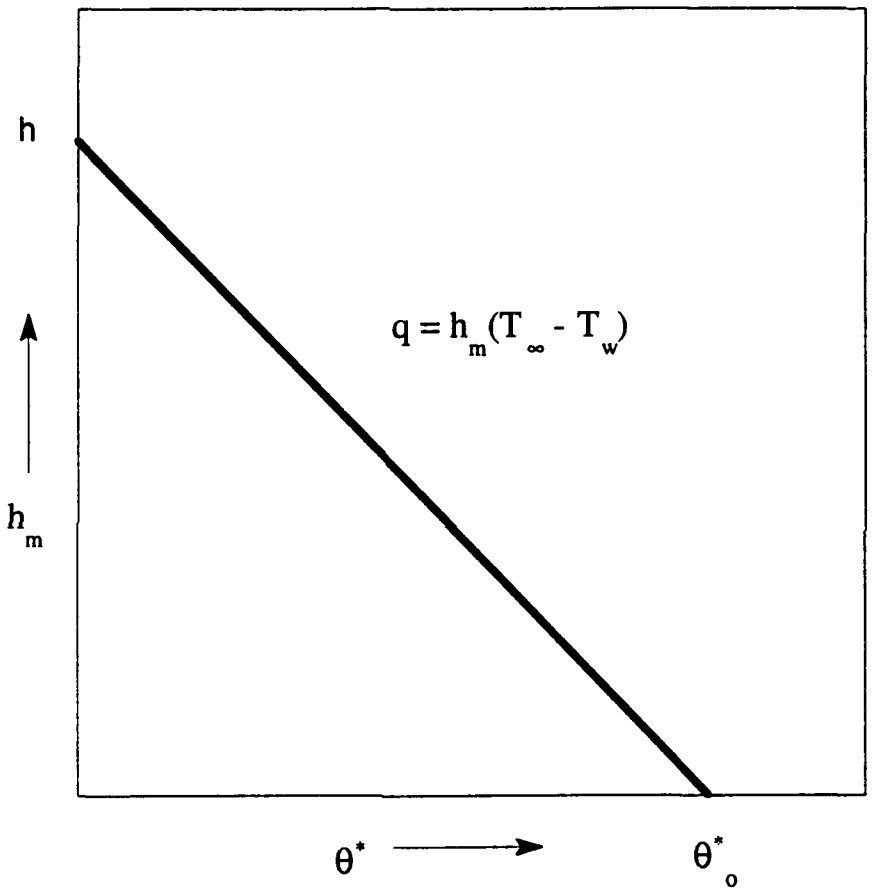

Figure3.27 Variation of h with θ^*

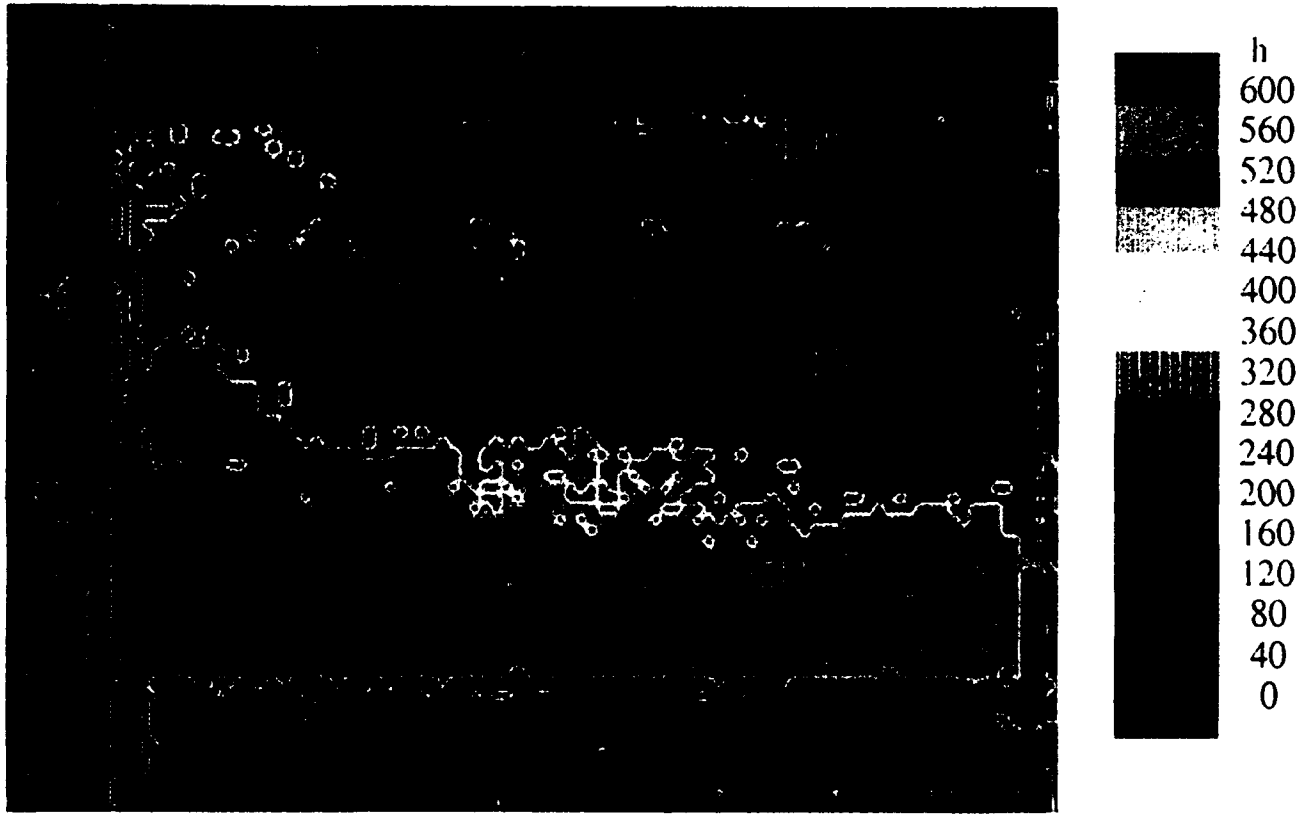

Figure 3.28 3/8" cavity, 5/16" clearance gap, suction side injection,
Re = 30,000, M = 0.5,
Single run - cold test

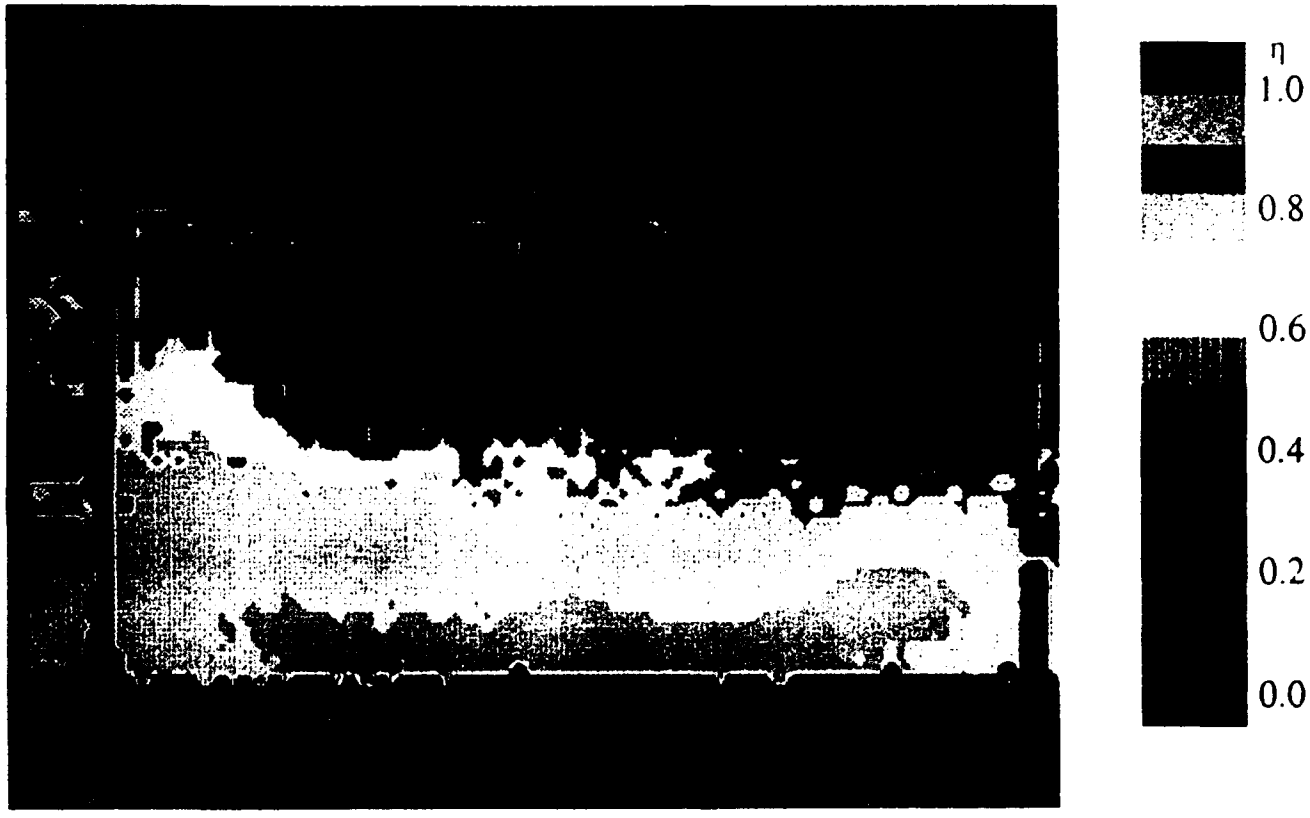

Figure 3.29 3/8" cavity, 5/16" clearance gap, suction side injection,
Re = 30,000, M = 0.5,
Single run - cold test

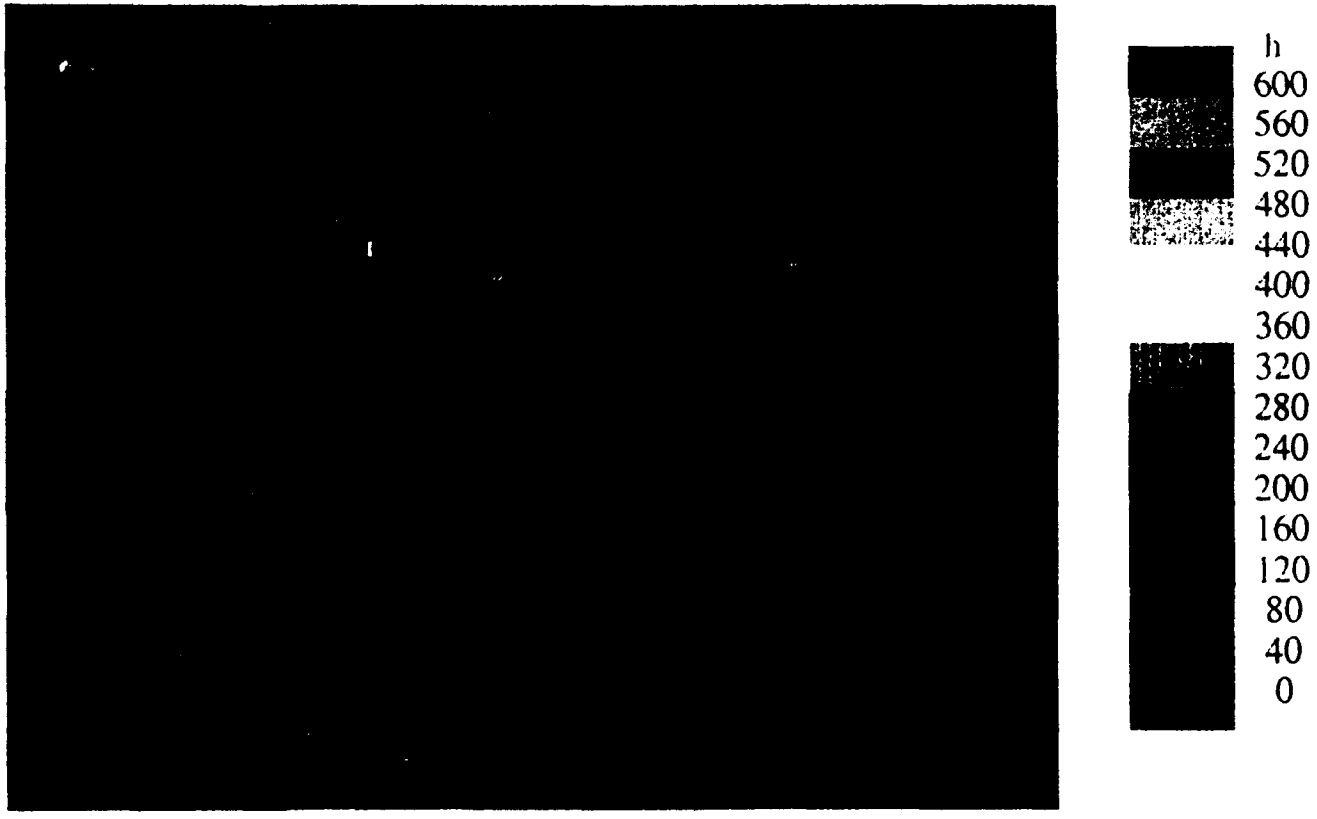

Figure 3.30 3/8" cavity, 5/16" clearance gap, suction side injection,
Re = 30,000,M = 0.5,
Single run - hot test

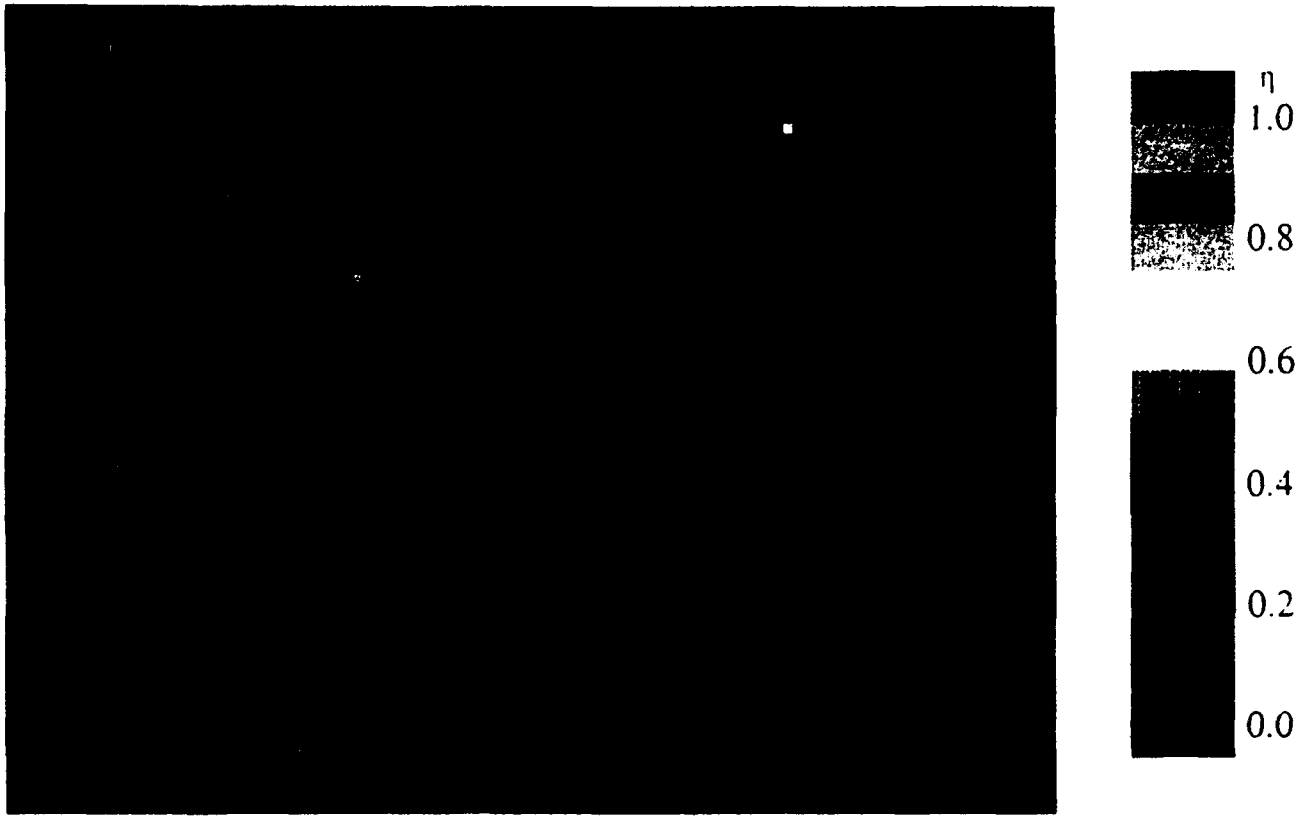

Figure 3.31 3/8" cavity, 5/16" clearance gap, suction side injection,
Re = 30,000, M = 0.5,
Single run - hot test

Although not exact, returning to the graphical representation suggested earlier helps understand the results. With results presented in Figures 3.19 and 3.20, two-test solution using front side green, it is possible to pick any pixel on the test surface and to approximately fix a graphical straight line to the h vs θ^* chart. Likewise, the same process can be accomplished with Figures 3.25 and 3.26, two-test solution using backside green. Picking a point 1/4" below the second-from-the-right hole (designated R2), specific values for h and η are picked for both the green and backside green solutions. The lines that result are plotted in Figure 3.32. Corresponding to Figures 3.19, 3.20, 3.25 and 3.26, for a point 1/4" below hole R2 the h for the backside green is slightly higher than for front side green and the η is slightly lower. As was discussed in the two-tests section, this difference between the two is within experimental error and may occur because of a 3% variation in Reynolds number from the beginning of each test to the end. In addition, since the front-side green results occur earlier in the test run than backside green results, some drift in both h and η may occur because of the effects of lateral conduction. Finally, the experimental uncertainties may play a part.

The problem in trying to arrive at h and η from a single run now becomes evident. When accomplishing a single-run test using either the hot test or the cold test we are picking off a point using front-side green which lies on one of these lines and a point using backside green which lies on the other line. Our iterative solution method to find h and η in essence fits a line to these two points. Although we are not able to exactly decide where those points are located on each line, we can get approximate the answer.

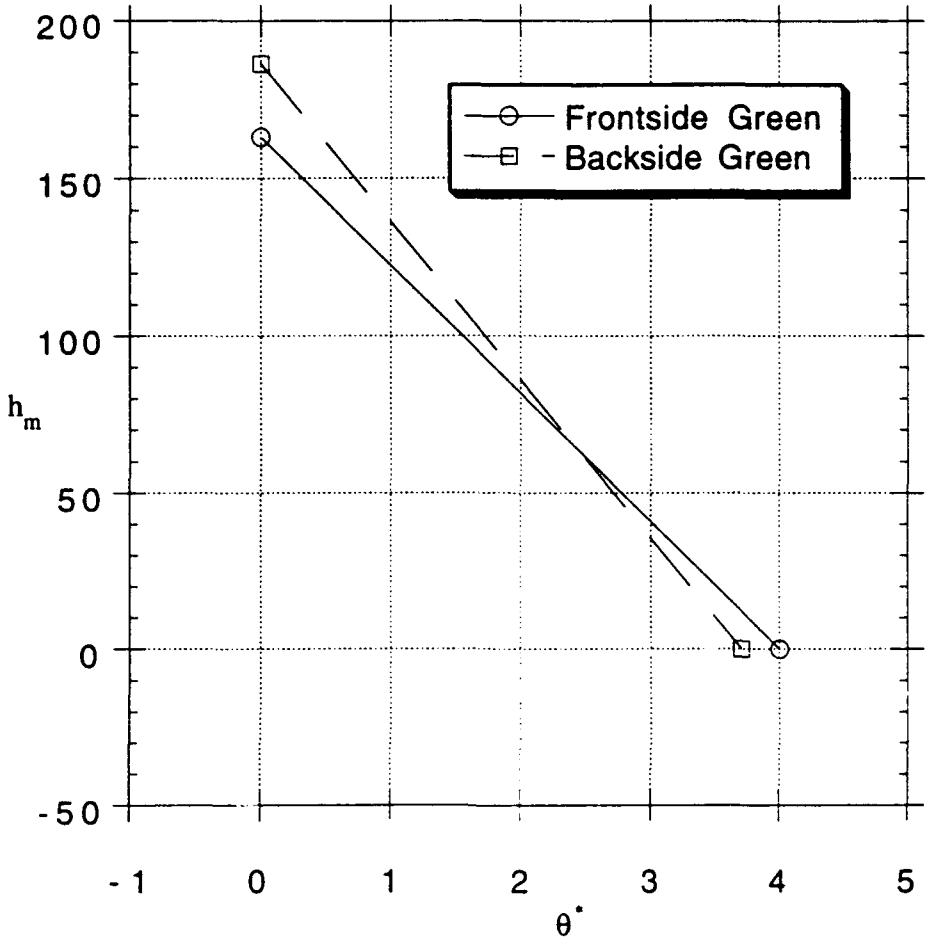

Figure3.32 Two test graphical representation

If we assume the largest changes in the main and film flow temperature occur in the first few seconds of each run and then only slowly increase from there, we can find from the time/temperature data the temperature of the main flow at wall temperatures of 102.0°F and 110.15°F. If we then assume a perfect step change occurred to arrive at these flow temperatures, we can place a point near the location on each line which is used to solve the simultaneous equations for the single test method. Again, remembering that

this is just an approximation, we can use equations 3.3 and 3.4 to calculate θ^* and h_m and approximately fix the points used on the front side green line and the backside green line used in arriving at the single test solution. This can be accomplished for both the single test using the cold test run and the single test using the hot test run. The results are shown in Figure 3.33.

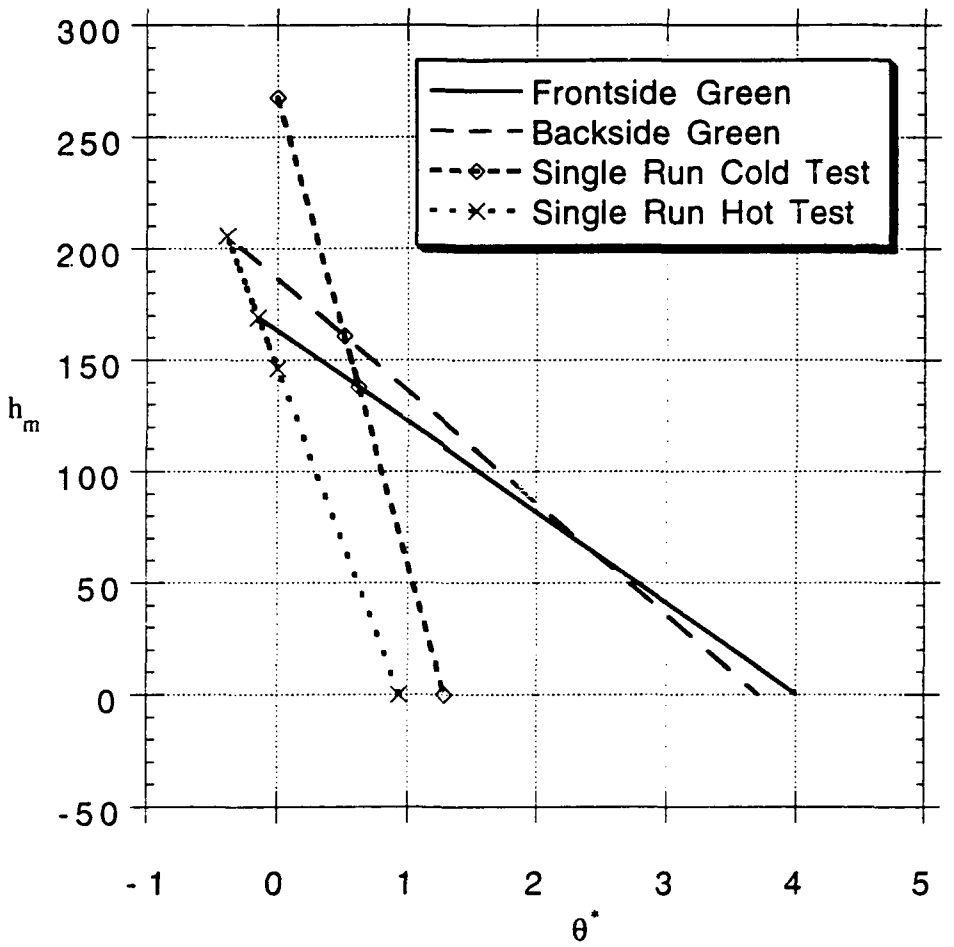

Figure3.33 Single test graphical representation

The solid lines are the same as seen in Figure 3.32 for the two test methods. The dash lines represent the linear solution produced by fitting the

approximate location for the front-side and backside green temperature response during a single-test solution method. Surprisingly, the results give the correct trends we see in Figures 3.28, 3.29, 3.30, and 3.31. For the point 1/4" below hole R2, the single run-cold test shows a higher value of h and a higher value of η than do the h and η of the two-test method, Figures 3.19, 3.20, 3.25 and 3.26. This corresponds well with the predicted linear fit for the single-test runs pictured in Figure 3.33. It must be kept in mind that the abscissa is the inverse of η and lower ordinate values correspond to higher η's.

Likewise, the single-run-hot test shows a lower value of h and a value of zero for η at the same point. The iterative program used to solve the simultaneous equations involved, has limits of zero and one on η. Once η reaches zero, as in the case being considered, the next calculation of h is the final one. In terms of solving the equations, the problem becomes a two-temperature problem, $\eta = 0$, and h can directly be calculated. This again corresponds well with the predicted linear fit for the single-test run predicted in Figure 3.33. Because the points on the front and backside green temperature response lie so close to the ordinate, h will be similar, in this case slightly lower, than the h's found using the two-test method. Previous work at ASU provided many examples of a hot test providing a solution for h even though accurate η's could not be found. Looking again at Figure 3.33, the linear fit for the single-test-hot run predicts an $\theta_o{}^*$ less than 1. This would correspond to a meaningless inverse, out of the η range from zero to one. Again, surprisingly, there is a good match. While this is far from an exact solution, it does give us insight into why the single test method provided us with poor results. Because of the small Reynolds number

changes that occur during a test run and lateral conduction, h and η drift during a test run. When we attempt to use either the cold run or hot run to accomplish the single-test method, the two points used to solve for a solution lie so close in the h versus θ^* plane that the small drift in θ^* and h_m during the test causes large changes in h and η. In mathematical terms, this problem is ill-conditioned.

This method of viewing the single-test run was accomplished for several other pixels with similar results. The actual results of Figures 3.28, 3.29, 3.30 and 3.31 along with the insight developed from Figure 3.33, lead us to the conclusion that a single-test run using either a cold test or hot test will not solve the heat transfer problem.

In an attempt to spread the points used for the single-test solution, an alternate test method was proposed by Dr. Yufeng Yu and Dr. Yong Kim, also of ASU. Initially, the test is set up exactly as a cold test. The experiment begins and after 20 to 30 seconds, the film temperature is raised quickly to temperatures similar to those of a hot test.

Experimentally, the approach sounds appealing. Front-side green is used to pick up the early change exposed primarily, if not totally, to a cold test environment. Subsequently, backside green picks up the wall response later in the run after being exposed to a hot test environment. Different hot-test temperatures, along with different temperature rise times were attempted. Unfortunately, not a single attempt resulted in a successful solution. The results from each attempt were clearly bad with η being either zero for most pixel solutions or one for the rest.

Again the failure with this approach lies with maintaining the consistency of the nonlinear equations used to determine h and η . During

this type of approach the Reynolds number of the entering main flow experiences a drift of about 3% as it did with the two-test method. The film flow, on the other hand, experiences Reynolds number changes on the order of 10%. This makes it difficult to maintain the blowing ratio a constant during the test run. As comparisons of the two-test method for front and backside green showed, there is a definite drift in h and η even when main flow and blowing ratio are held constant. With the additional difficulty in maintaining the film flow Reynolds number the uncertainty in h and η increase further.

It appears, as was discussed in the two-test method section, the drift in h and η for the cold and hot tests are similar enough and the values for θ^* and h_m spread enough in the h_m vs θ^* solution space that the governing nonlinear equations remain consistent. In this case, convergence to an appropriate solution is possible.

In the single-test method, the full impact of the drifting h and η are seen. Unlike the two-test method, in the single test case the two time/temperature responses from front and backside green are separated by 20 to 30 seconds of test time and values for θ^* and h_m are spread very little in the h_m vs θ^* solution space . The result appears to be that due to the slight drift in Reynolds number, the lateral conduction inherent in the test method and the experimental uncertainties present, the problem becomes ill-conditioned and convergence to an appropriate solution is not guaranteed.

From this work it appears the single-test method, as now envisioned, is not a viable experimental method. The problem is ill conditioned and even small changes in the independent parameters cause large changes in the solution or a total failure in convergence.

3.9 Chapter Summary

The work presented in this chapter can be summarized as follows:

- Use of liquid crystals to determine local heat transfer characteristics is well documented in previous work and provides a relatively inexpensive method of determining h and η in detailed resolution for simple and complex test sections.

- Use of a two-test method in which two very similar tests are run with only a variation in film temperature, provides reliable, repeatable results for the three-temperature problem.

- In conducting liquid crystal response measurements, green is the clear color of choice. It provides superior results when compared to either red or blue. Blue in general provides unacceptable results.

- A fixed-threshold method, to determine transient TLC temperature response, provides reliable heat transfer information only in areas of the test section where background intensity is similar to that of the calibration area.

- Percentage-threshold methods provide temperature accuracies for the TLC green response on the order of $\pm 0.2^{\circ}F$ over widely varying background intensities.

- The video-taping process provides an excellent system to extend this visual method without significant degradation of the acquired convective heat transfer information.

- The thickness of Plexiglas or epoxy between the camera and test section TLC surface affects the calibration temperature of the liquid crystal and must be accounted for during TLC calibration.

- The single-test transient method, as currently envisioned, is not viable.

CHAPTER 4

SMOOTH FLAT PLATE MEASUREMENTS AND FILM HOLE SIZING

4.1 Introduction

As described in section 1.2, previous work by several researchers has demonstrated heat transfer characteristics in a film-cooled surface are influenced greatly by the local boundary layer thickness. The conclusion being, in addition to matching Reynolds number and blowing ratio when comparing two film cooling situations on a flat plate, it is also important to match either the dimensionless boundary layer displacement thickness or momentum thickness. These dimensionless parameters are the ratio of boundary layer thickness, using either the displacement thickness or momentum thickness, to the film cooling hole diameter (δ_1/D or δ_2/D). Experimental results presented in Chapter 11 illustrate the affect a variation in this parameter has on heat transfer characteristics.

As validation of this work, it is important to compare the convective cooling heat transfer coefficients and film cooling effectiveness values of prior research with those determined by the transient method used in this study. In Chapter 5, film cooling on a flat plate is compared to the work of Goldstein et al. (1970) and Eriksen et al. (1974). In these works, the ratio δ_1/D is reported to be 0.124 at the point of film injection for a free stream velocity of 30.5 m/s. By matching δ_2/D along with the free stream velocity and blowing ratios, a fair comparison of results for the transient method employed here

and the steady-state method using an adiabatic wall model used by Goldstein is made in Chapter 5.

In addition, the main focus of this work is to determine the effect surface roughness has on heat transfer characteristics for film cooling conditions matching those appropriate for the P&W first stage vane turbine blade. As described in Chapter 1, this study matches the Reynolds number and scales the diameter of the film holes such that the δ_2/D is matched 0.44 inches from the leading edge of the pressure side of the first stage vane. At this point, the Reynolds number is approximately 1.61×10^5 (Tabbita, 1993) and δ_2/D is on the order of 0.037. This corresponds to a free stream velocity of 50 m/s at 2.25 inches downstream from the leading edge of the Plexiglas flat test plate. 2.25 inches was chosen to ensure that the film holes could be included in the plate without disrupting the bypass flow. Once the momentum thickness of the flow at 2.25 inches is determined, the film hole diameter is set for the work accomplished in Chapters 7,8, and 9.

With the two test conditions set for the plate at 30 and 50 m/s, boundary layer tests are accomplished. The test apparatus illustrated in Figure 2.3 is used with inclusion of a 3" by 5" flat Plexiglas plate. Four holes in the Plexiglas wall, adjacent to the test surface, provide access for a static pressure probe and a boundary layer probe manufactured by United Sensors. The probes are mounted on a United Sensors manual traversing unit graduated to units of 0.01 inches with the ability to read to ± 0.005 inches.

Velocity distributions are taken at four downstream locations (X) of 0.875", 3.44", 4.44", and at the point for film injection of 2.25". From the velocity distributions, the displacement thickness and momentum thickness are determined for each free-stream velocity at each downstream location.

For the case where the flow is considered incompressible and the flow properties constant the following definitions hold:

$$\delta_1 = \int_0^\infty (1 - \frac{U}{U_\infty})\, dy \qquad (4.1)$$

$$\delta_2 = \int_0^\infty \frac{U}{U_\infty}(1 - \frac{U}{U_\infty})\, dy \qquad (4.2)$$

While only the thickness at 2.25" is required to scale the film holes for the two sets of tests, the other locations are determined so that the growth of the boundary layer can be compared to the standard empirical correlation reported for turbulent boundary layer growth on a smooth flat plate (Schlichting, 1979).

$$\frac{\delta}{x} = 0.37\, Re_x^{-0.2} \qquad (4.3)$$

This relationship is obtained by solving the momentum integral equation assuming a 1/7 power law velocity profile in the boundary layer, and an empirical correlation for shear stress at the wall.

$$\frac{U}{U_\infty} = (\frac{y}{\delta})^{1/7} \qquad (4.4)$$

It must be remembered, however, this development and the use of equation 4.3 assumes a constant free-stream velocity.

In addition, as the first confirmation of the validity of the heat transfer coefficients determined using the experimental method and apparatus (Figure 2.3) outlined in Chapter 1, the heat transfer coefficients for this flat plate are reported in section 4.3. These values are compared to the well accepted empirical relationship for heat transfer on a smooth flat plate developed from the Chilton-Coburn analogy (Incropera and Dewitt, 1985).

$$Nu_x = \frac{h_x x}{k} = 0.0296\, Re_x^{4/5}\, Pr^{1/3} \qquad (4.5)$$

As with equation 4.3 this correlation is for the case where the free-stream velocity is constant. As is shown in the next section, the experimental approach taken in this work appears to be extremely appropriate for the two-temperature problem.

4.2 Boundary Layer Velocity Profiles and Thicknesses

Velocity profiles for each of the four downstream locations for both 30 m/s and 50 m/s are illustrated in figures 4.1 through 4.7. As expected, a 1/7 power law fits the experimental data fairly well. In reality, the curve-fit varied in a narrow band from 1/6.98 to 1/7.01. The specific curve fit for each location was used to determine the displacement and momentum thicknesses. The boundary layer thicknesses are labeled on each figure. Figure 4.8 and 4.9 indicate the boundary layer thicknesses a function of downstream location.

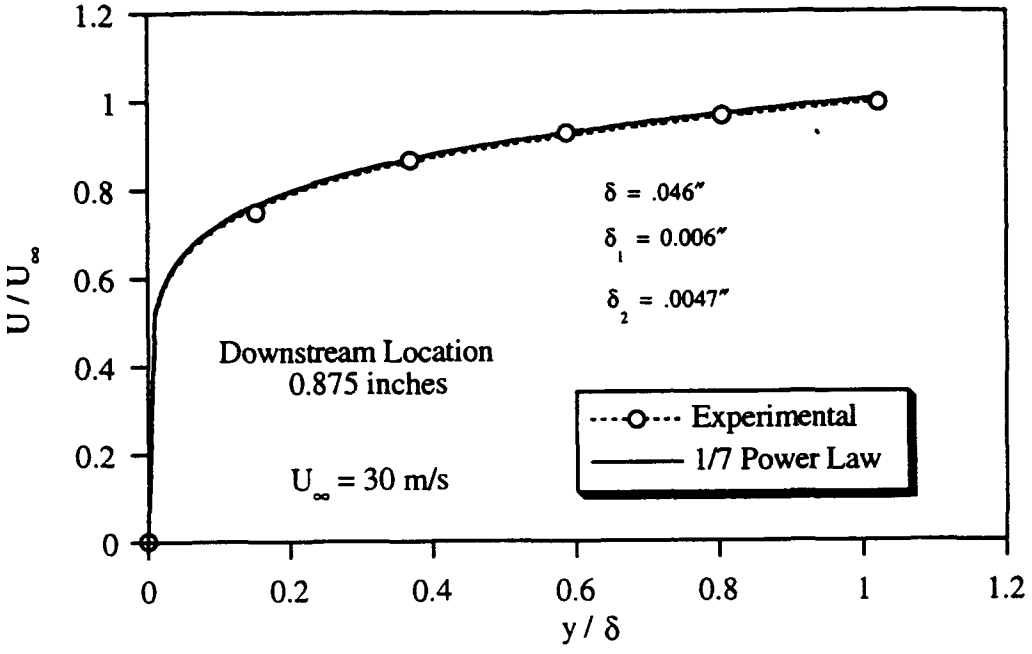

Figure 4.1 Velocity profile, U_∞ = 30m/s, x=0.875 inches

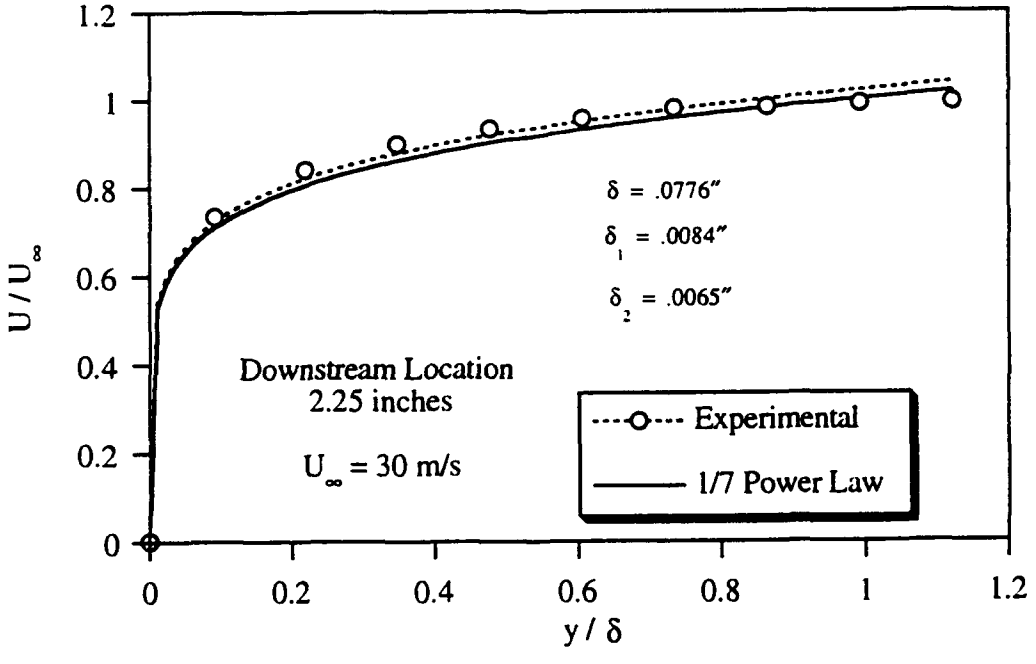

Figure 4.2 Velocity profile, U_∞ = 30m/s, x=2.25 inches

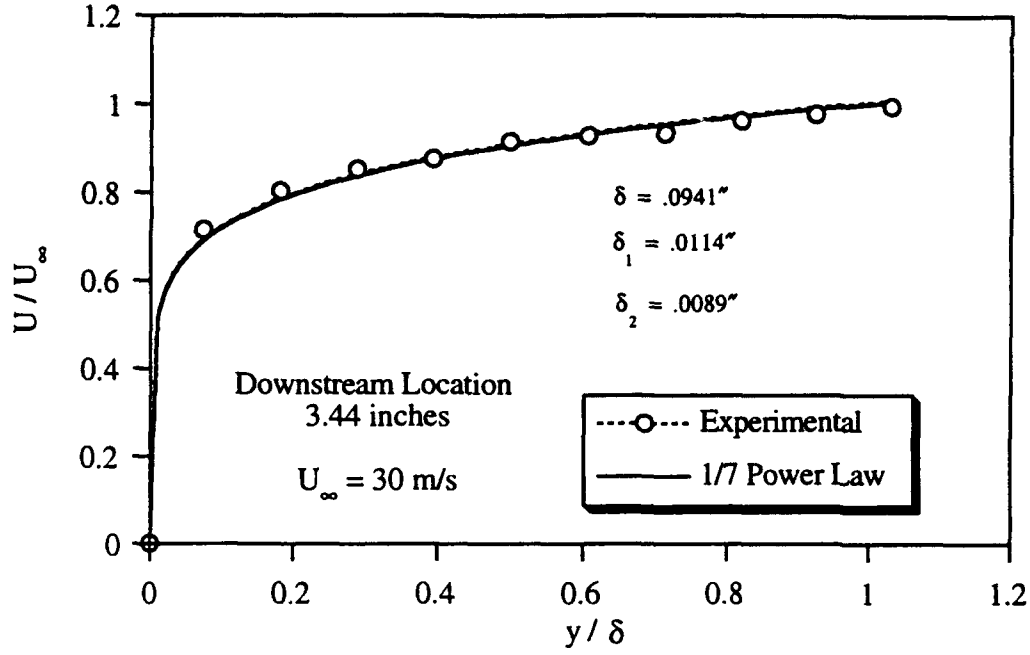

Figure 4.3 Velocity profile, U_∞ = 30m/s, x=3.44 inches

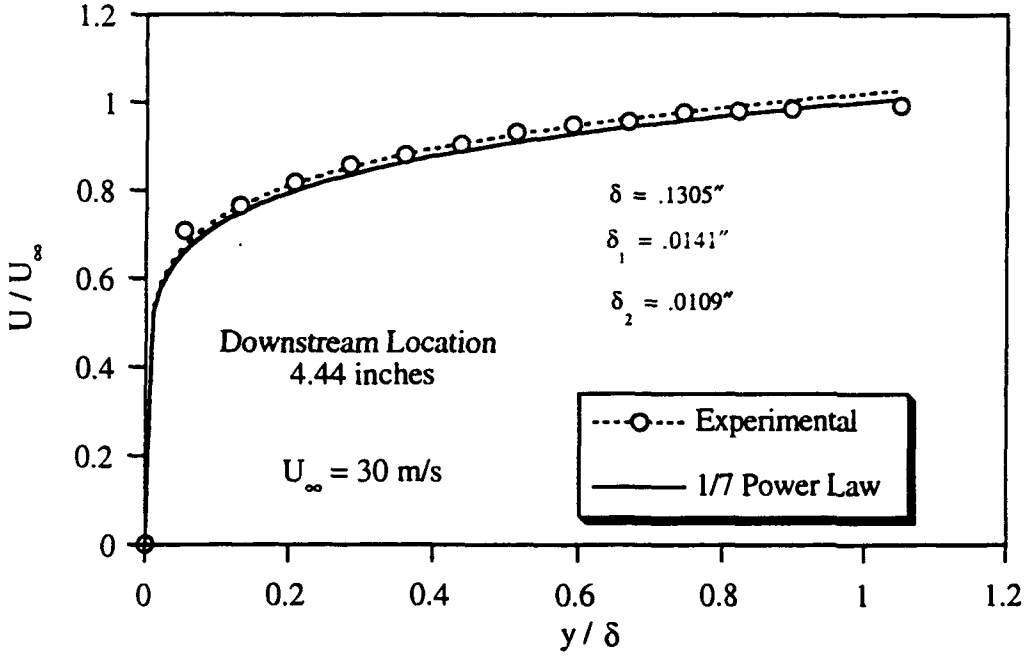

Figure 4.4 Velocity profile, U_∞ = 30m/s, x=4.44 inches

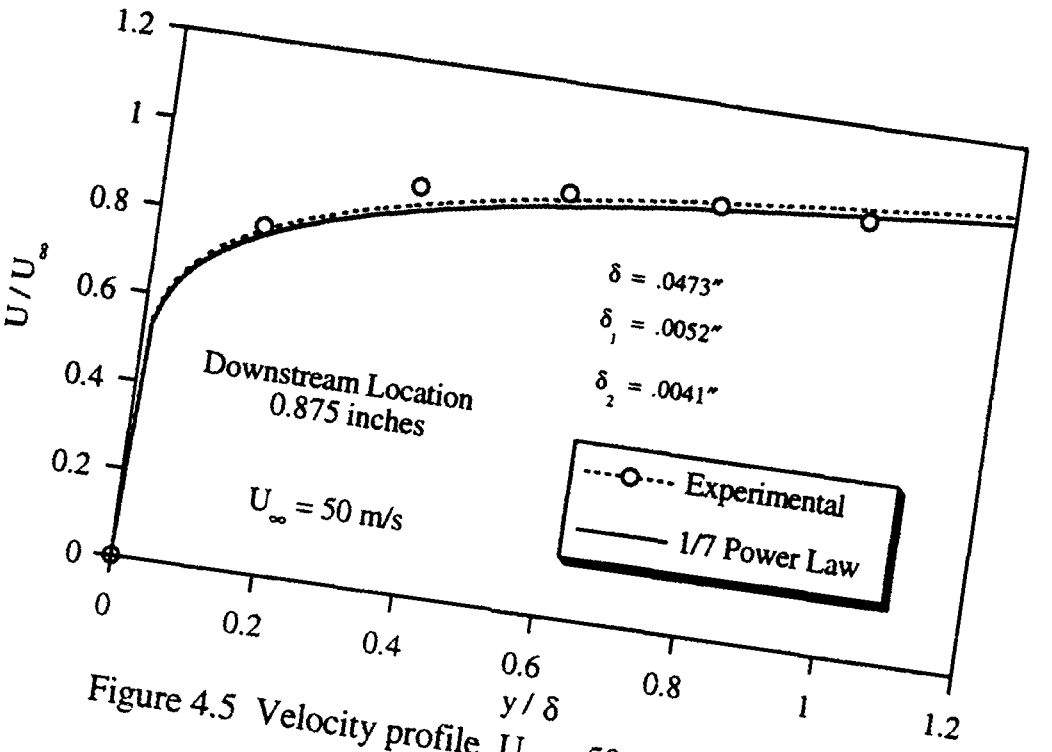

Figure 4.5 Velocity profile, U_∞ = 50m/s, x=0.875 inches

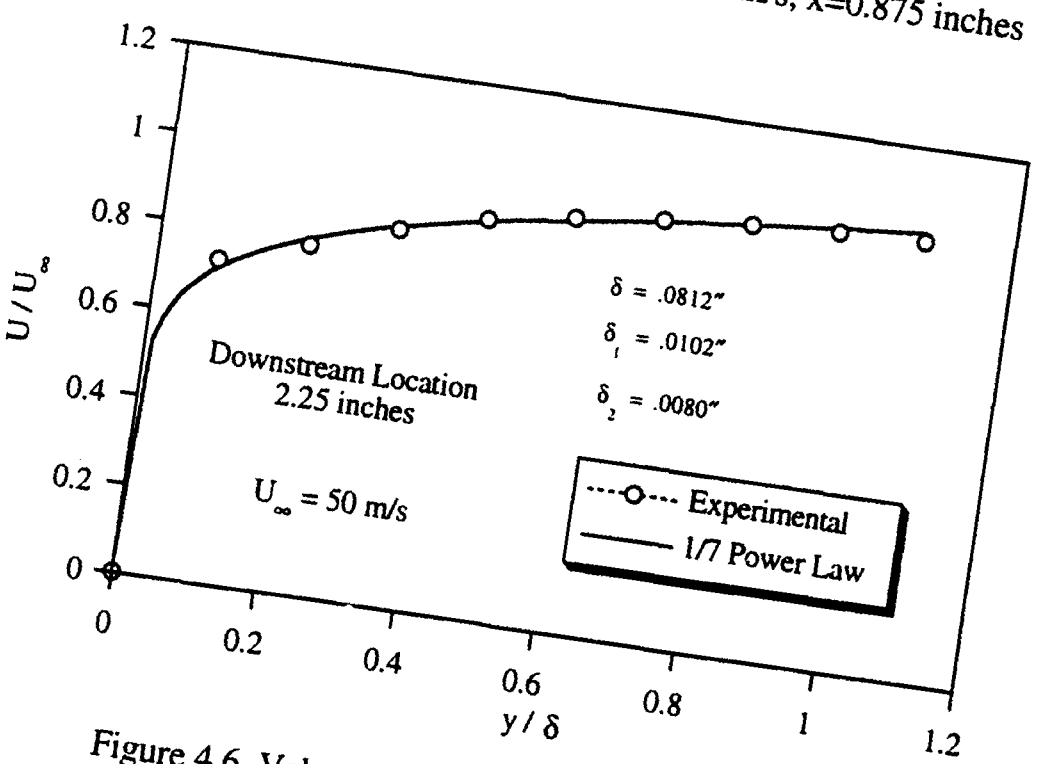

Figure 4.6 Velocity profile, U_∞ = 50m/s, x=2.25 inches

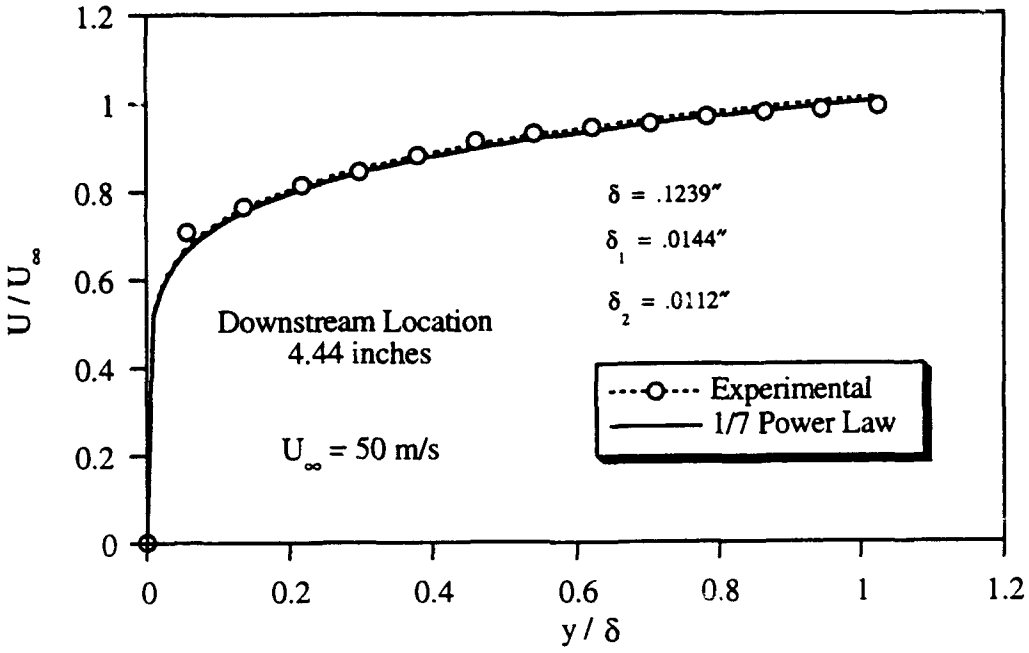

Figure 4.7 Velocity profile, U_∞ = 50m/s, x=4.44 inches

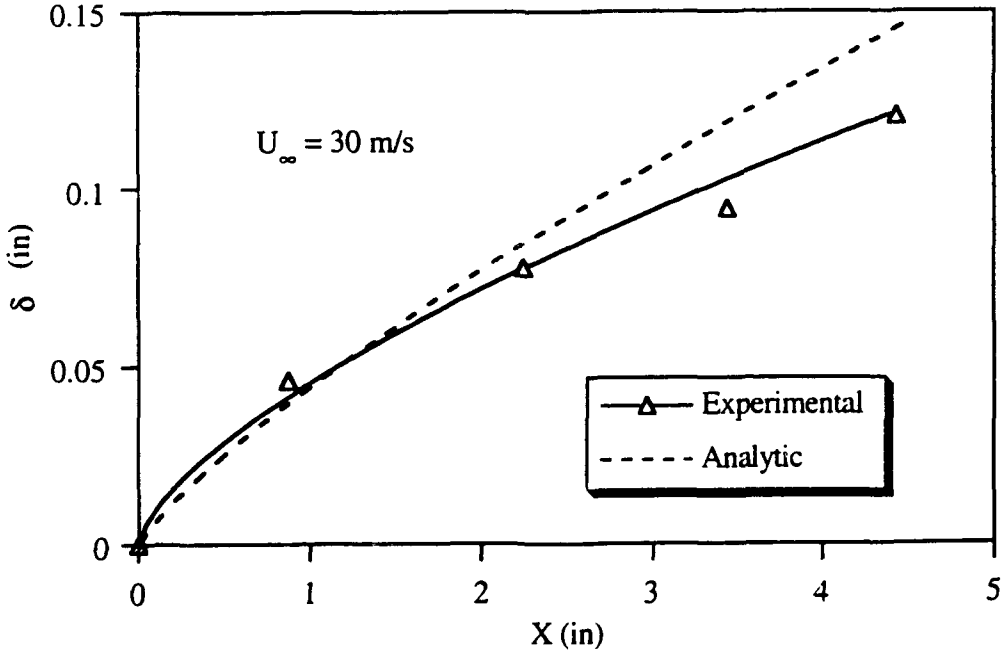

Figure 4.8 Boundary Layer thickness, U_∞ = 30 m/s

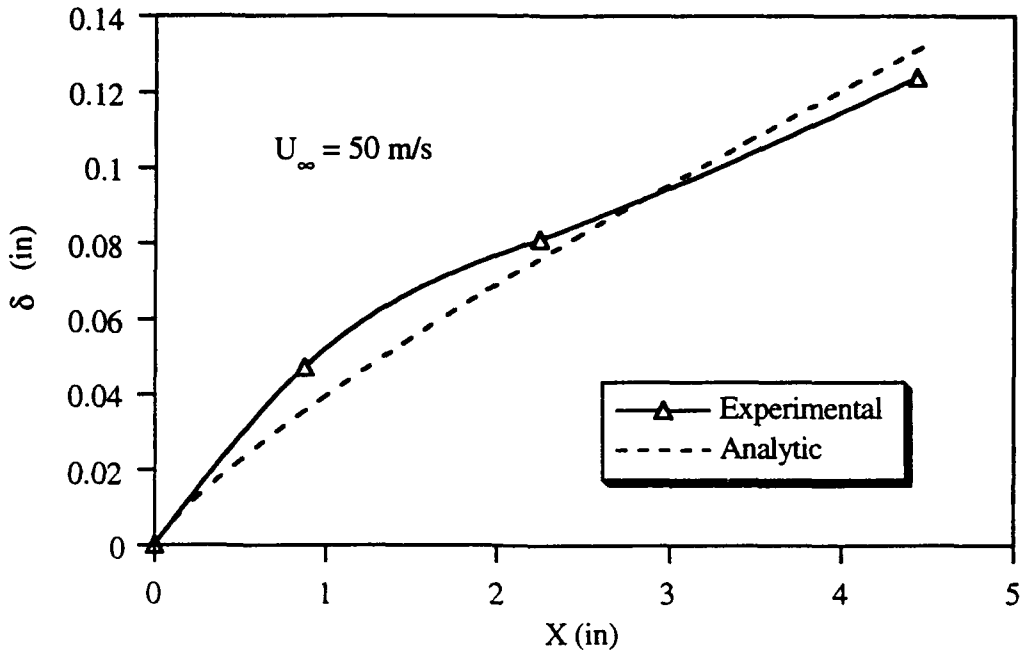

Figure 4.9 Boundary Layer thickness, U_∞ = 50 m/s

Several points can be made about the character of the flow. First, there is not a constant area passage prior to the splitter plate and the beginning of the flat-plate test surface. As can be seen in Figure 2.3, the convergent section ends just prior to the bypass or splitter plate. The test rig was designed short to ensure a minimum energy loss from the heaters to the test section and to achieve as close as possible a step change in temperature at the start of the test run. As a result, the flat plate is actually at a slightly positive angle of attack. With the film holes 2.25" downstream, a slight angle of attack at the beginning was accepted in the design. The resulting slight separation at the leading edge causes an initial boundary growth rate larger than predicted by equation 4.3 for both flow velocities. This is followed by a lower than predicted boundary layer growth rate. As pointed out in the

introduction to this section, the analytic solution assumes the free-stream velocity is constant. In reality, because of the growth of boundary layers on the test section walls, the flow actually experiences a slight acceleration.

For the 30 m/s case, the main flow is at 30.5 m/s at the 2.25" location and 31.7 m/s at the exit of the rig at approximately 8.0". This is a 4% acceleration through the test region. For the 50m/s case, the main flow accelerates from 51.3 m/s at 2.25" to 53.0 m/s at the exit. This is a 3% acceleration through the test region. The effect in both cases is to reduce the boundary layer growth rate compared to the non-accelerating case. By 4.44" downstream, the boundary layer thickness is thinner than predicted by equation 4.3. In the next section, we see this translates into higher heat transfer coefficients than would be predicted for a constant velocity flat plate.

4.3 Flat Plate Heat Transfer Coefficients

Using the set up illustrated in Figure 2.3, the local convective heat transfer coefficients were determined at free-stream inlet velocities of 30 and 50 m/s. The results are shown in Figure 4.10 and Figure 4.11. Growth of the boundary layer is evident along the side walls. As will be the case for the film cooling analysis in later chapters, only the middle lateral portion of the plates is considered in the line plots, Figure 4.12 and Figure 4.13. In these figures, the prediction for h from equation 4.5 is included.

It is evident the heat transfer coefficients match those found by previous investigation for a turbulent flat plate extremely well. Present, however, are lower heat transfer coefficients in the early part of plate,

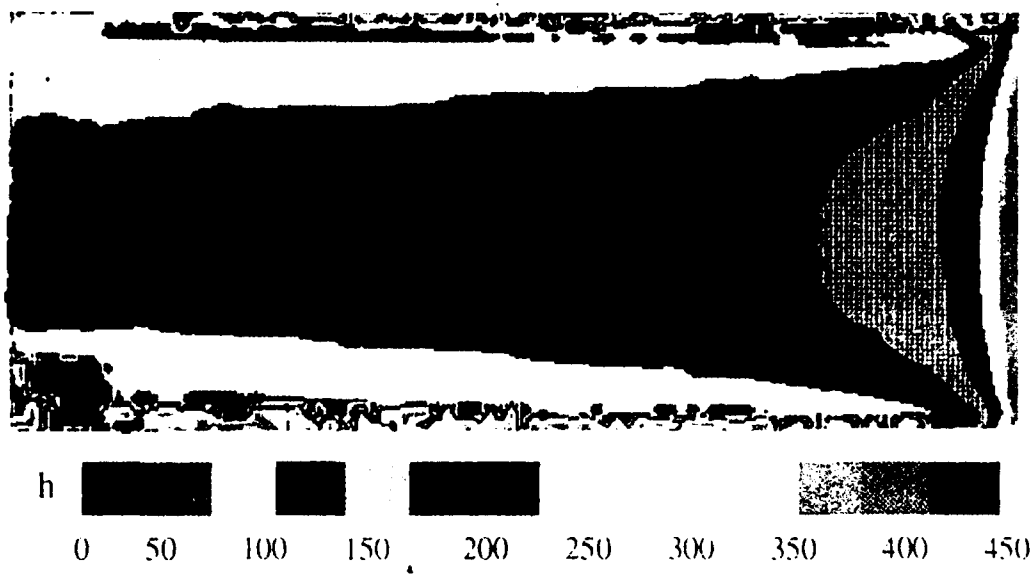

Figure 4.10 Flat plate convective heat transfer coefficients, U_∞ =30 m/s

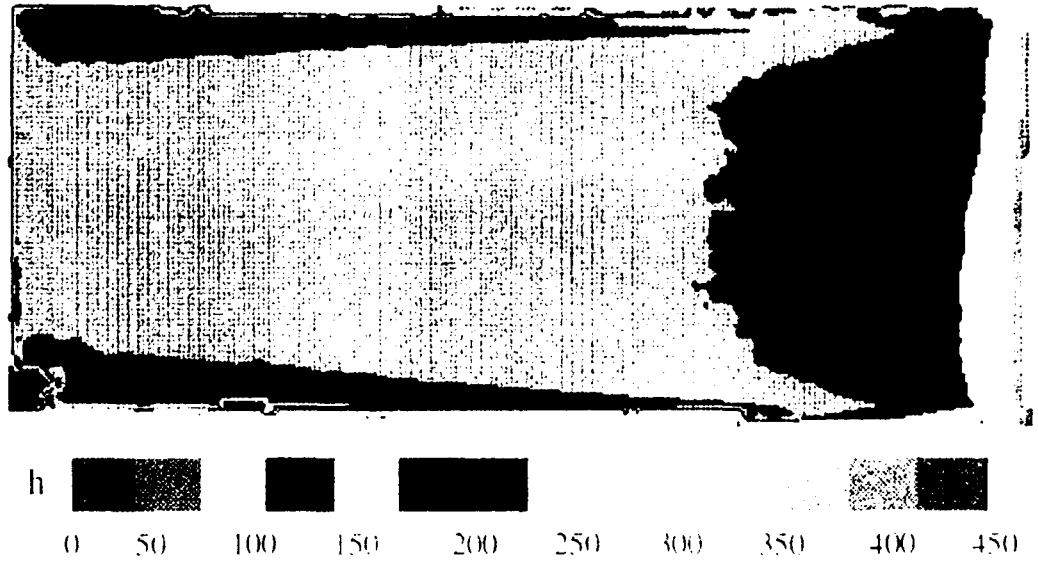

Figure 4.11 Flat plate convective heat transfer coefficients, U_∞ =50 m/s

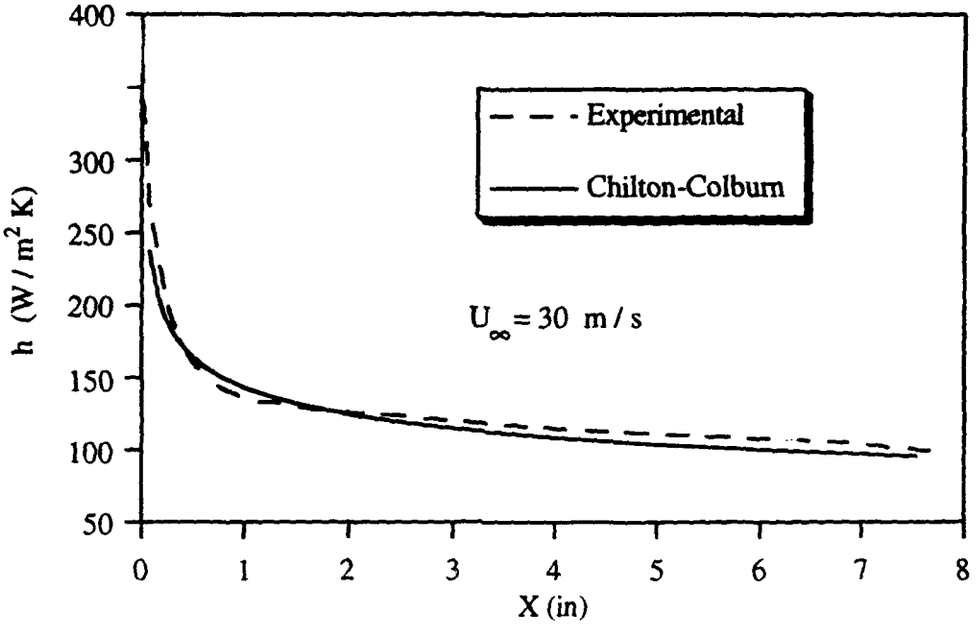

Figure 4.12 Heat transfer coefficients along a flat plate, $U_\infty = 30$ m/s

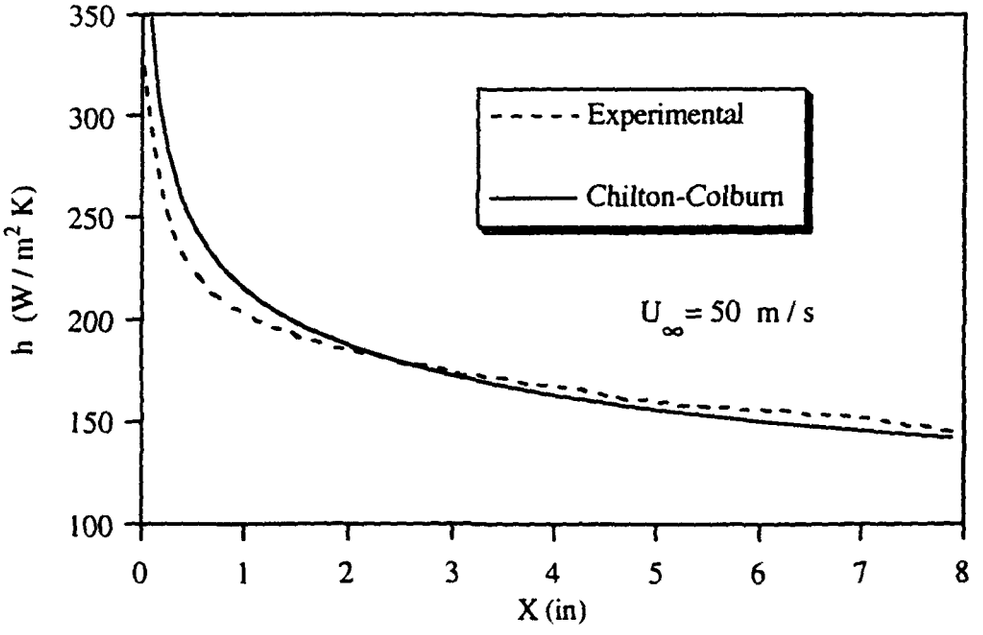

Figure 4.13 Heat transfer coefficients along a flat plate, $U_\infty = 50$ m/s

corresponding to the greater-than-predicted boundary layer thicknesses shown in Figures 4.8 and 4.9. As the flow accelerates slightly downstream, h values increase above those predicted by equation 4.5. This matches the thinner-than-predicted boundary layer thickness in this area.

The primary purpose of boundary layer measurements was to find δ_1 and δ_2 at 2.25" downstream, so hole diameters could be determined for the film cooling experiments to follow. For the 30 m/s case the desired ratio to match is δ_1/D at 0.124 (Goldstein, 1970). For a displacement thickness at 2.25" of 0.0084", the film hole diameter is set at 0.0674". The resulting eight hole film cooled flat plate is investigated in Chapter 5.

For the investigation of the conditions appropriate for the P&W first stage turbine vane, the desired δ_2/D is 0.037, resulting in a 0.213" diameter film hole. The three-hole film-cooled flat plate used to model the turbine blade conditions is investigated in Chapter 9.

CHAPTER 5

VALIDATION OF THE TRANSIENT LIQUID CRYSTAL TECHNIQUE

5.1 Introduction

In Chapter 4, a comparison of heat transfer coefficients for a turbulent flat plate determined with the combination of the semi-infinite solid model and TLC acquisition method, introduced in Chapter 2, compared extremely well with those determined using the Chilton-Colburn analogy. This comparison leaves no doubt the method of this study provides excellent results for two-temperature convective heat transfer. For the three-temperature problem, validation is more difficult. In general, the film cooling effectiveness in a film cooling set up is a function of not only main and film flow conditions, but also the geometry of the film holes and their inclination to the cooled surface. In addition, as discussed in chapter 1, the boundary layer thickness at the point of injection has a tremendous effect on the heat transfer characteristics.

In searching for research to conduct this comparison, several criteria existed. First, the work needed to be discrete hole injection and provide both film cooling effectiveness and convective heat transfer coefficients for a range of blowing ratios. In addition, enough information had to be provided so the boundary layer thickness to hole diameter could be matched. To make the comparison feasible, the flow parameters had to be within the 170 grams/sec ability of the heat transfer lab's air supply system. Finally, it would be best to match the turbulence level of the two sets of test results. This last desire was

not attainable. The majority of work in this area has been with turbulence intensities below 1%. The only discrete-hole experiments in a higher turbulence environment have been conducted by Ou et al. (1992) and they are unfortunately not on a flat plate, but rather a blunt body with a semicylinder leading edge.

However, the very complete work by Goldstein et al. (1970) and Eriksen et al. (1974) do provide an excellent basis to make a comparison other than the turbulence level. In the works by Goldstein et al. (1970), film cooling effectiveness and heat transfer coefficients are determined for discrete 35° inclined circular tubes at a free-stream velocity of 30.5 m/s and 61.0 m/s. In this chapter, a comparison is made with the 30.5 m/s data. Blowing ratios of 0.5, 1.0, 1.5, and 2.0 were investigated by Goldstein. Here blowing ratios of 0.5, 1.0, and 2.0 are considered. Finally, as discussed in Chapter 3, the test confirmation used in this chapter matches the dimensionless boundary layer displacement thickness at (δ_1/D) at the point of film injection with a value of 0.124. A spacing of three hole diameters between film cooling holes is used in both works. The turbulence level for the work reported here, however, is 6.5% (Chapter 10), much higher than the 0.5% reported by Goldstein. Based on the work by Ou et al. (1992) and Shao-Penko and Deng-Ying-Ying Liu (1980), the larger turbulence level used in this work will cause an increased rate of effectiveness drop downstream of the hole as compared to lower turbulence intensity data. One would hope, however, that near-hole effectiveness would compare favorably.

5.2 Test Parameters

Figure 5.1 is a diagram for the eight-hole flat plate used for testing presented in this chapter. The complete apparatus is illustrated in Figure 2.3. As determined by the boundary layer testing in Chapter 4 and in order to match the work of Goldstein et al. (1970) and Eriksen and Goldstein (1974), the film flow round hole diameter is set at 0.0674 inches. As described in the last section, the main flow velocity is set at 30 m/s at the entrance to the flat plate test section and is 30.5 m/s at the injection of the film flow. This matches Goldstein's free-stream velocity. Blowing ratios of 0.5, 1.0, and 2.0 are investigated for 35° inclined film jets along with the no film-cooling injection case (M=0.0). Results are presented in the next section.

5.3 Results

As examples, heat transfer maps of the film-cooled surfaces for M=0.0 and M=1.0 are shown in Figures 5.2 through 5.4. For the line plots that follow, averaged values from holes 3, 4, 5, and 6 is presented. The bottom hole did not provide reliable data due to a manufacturing error and was disregarded. Figures 5.5, 5.6 and 5.7 show the corresponding centerline (Z/D=0.0) and mid-hole (Z/D=1.5) effectiveness values for all three blowing ratios investigated. Included in the plots are the corresponding data from Goldstein et al. (1970) and Eriksen et al. (1974). Figure 5.8 illustrates the effect of blowing ratio on film cooling effectiveness. The effectiveness lateral (perpendicular to the flow direction) profiles are very steep close to the holes and flatten out as one moves downstream due to the spreading of the jets. As is the case for both Goldstein's work and the results presented here, the film-cooling effectiveness, at downstream locations

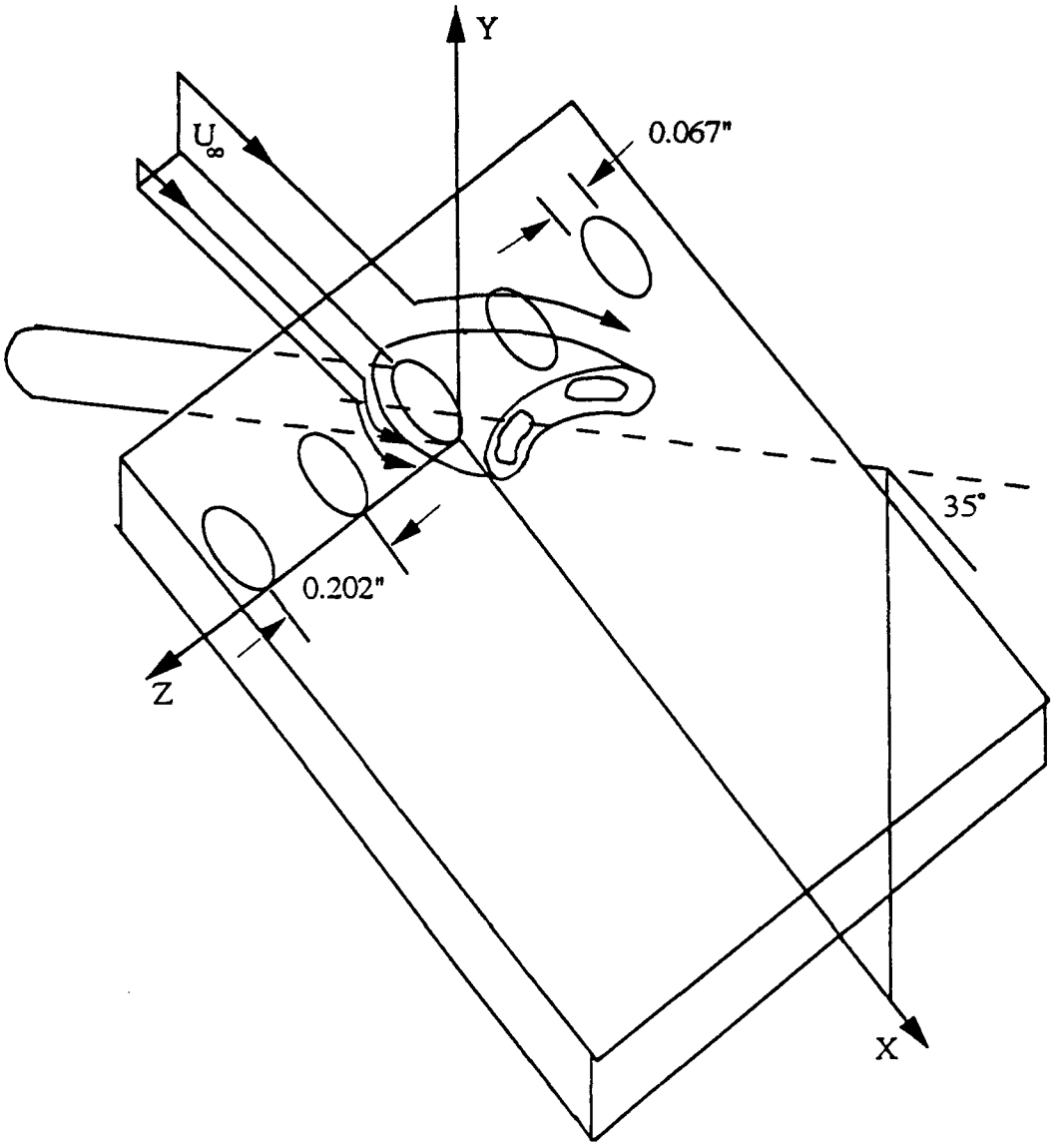

Figure 5.1 Film cooling configuration

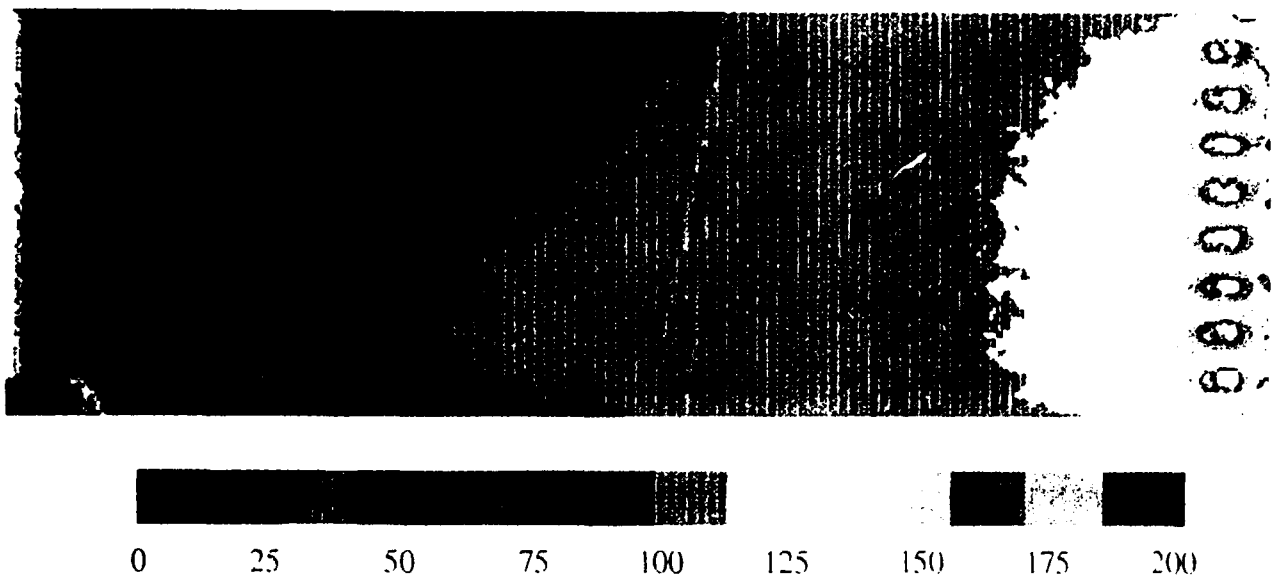

Figure 5.2 Convective heat transfer coefficient map, M=0.0, δ_1/D=0.124

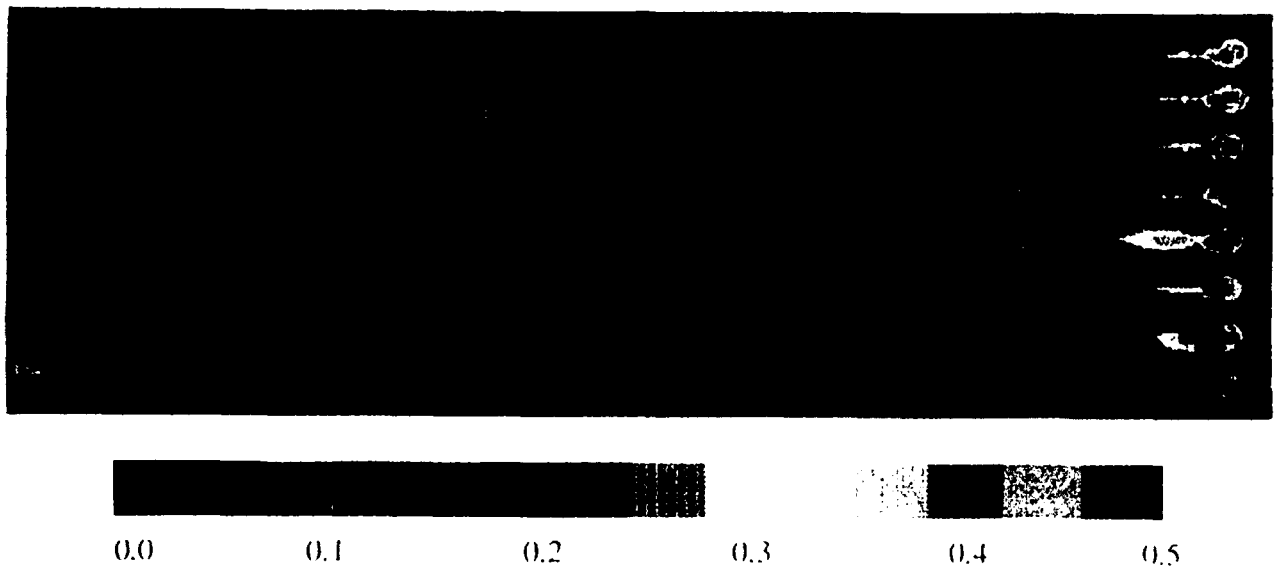

Figure 5.3 Convective film cooling effectiveness map, M=1.0, δ_1/D=0.124

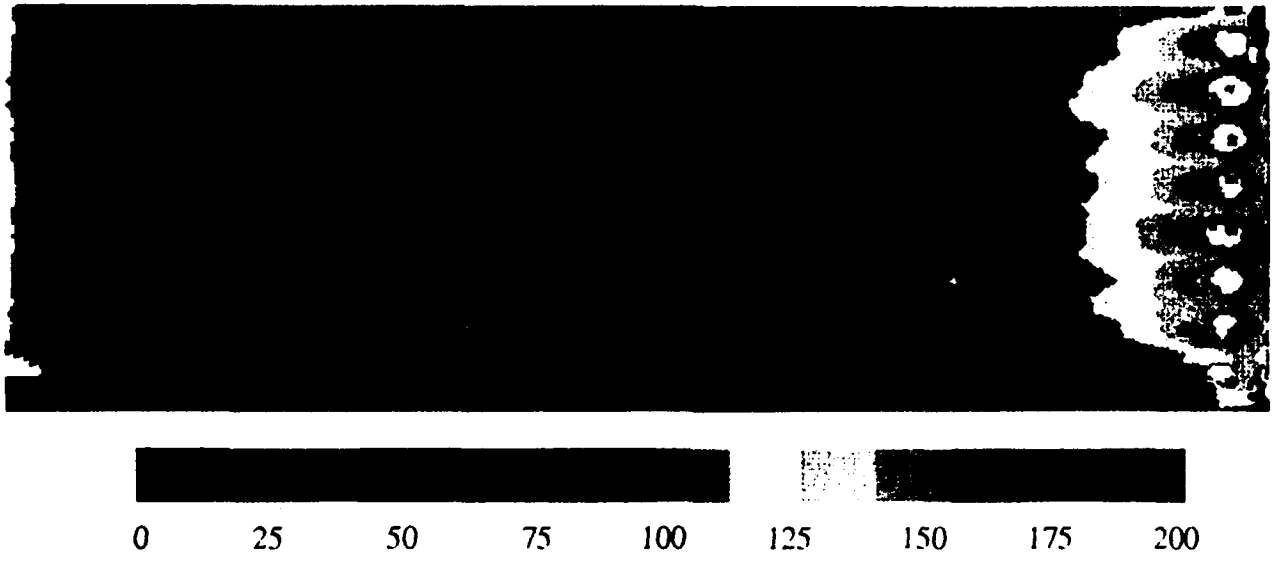

Figure 5.4 Convective heat transfer coefficient map, M=1.0, δ_1/D=0.124

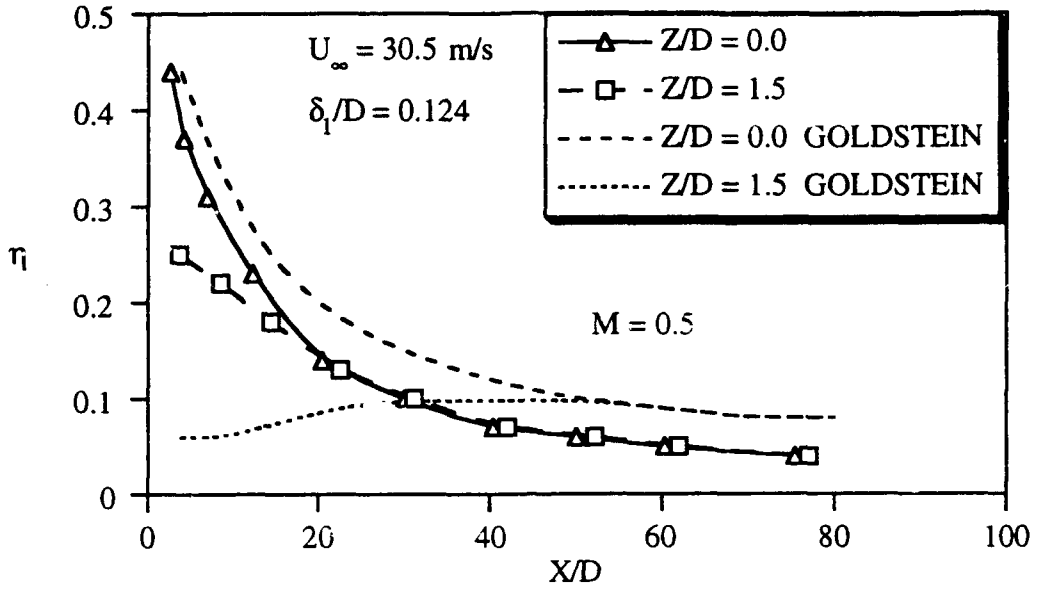

Figure 5.5 Film cooling effectiveness, M = 0.5, δ_1/D = 0.124

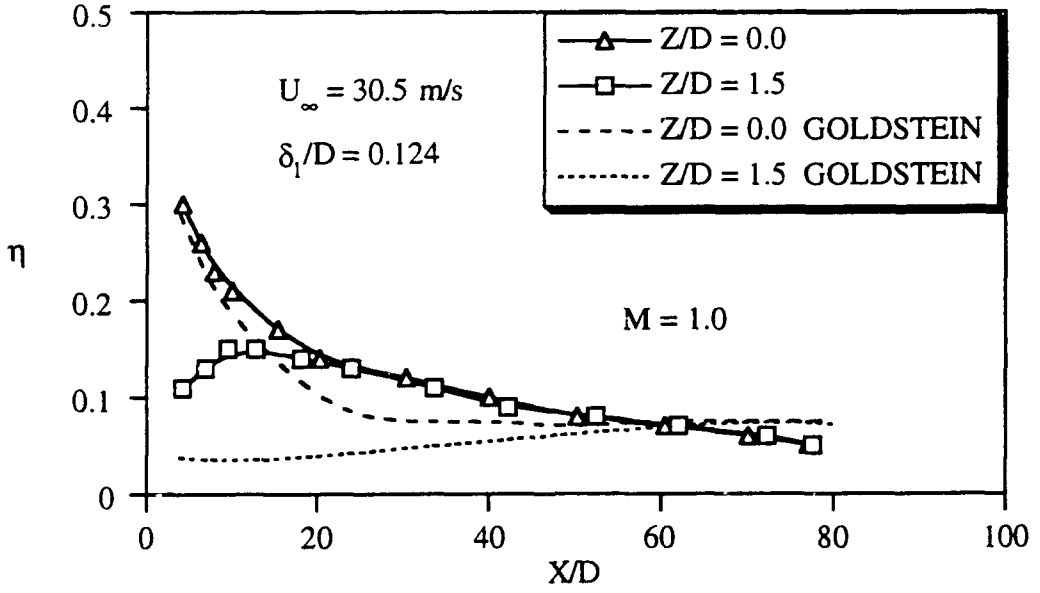

Figure 5.6 Film cooling effectiveness, M = 1.0, δ_1/D = 0.124

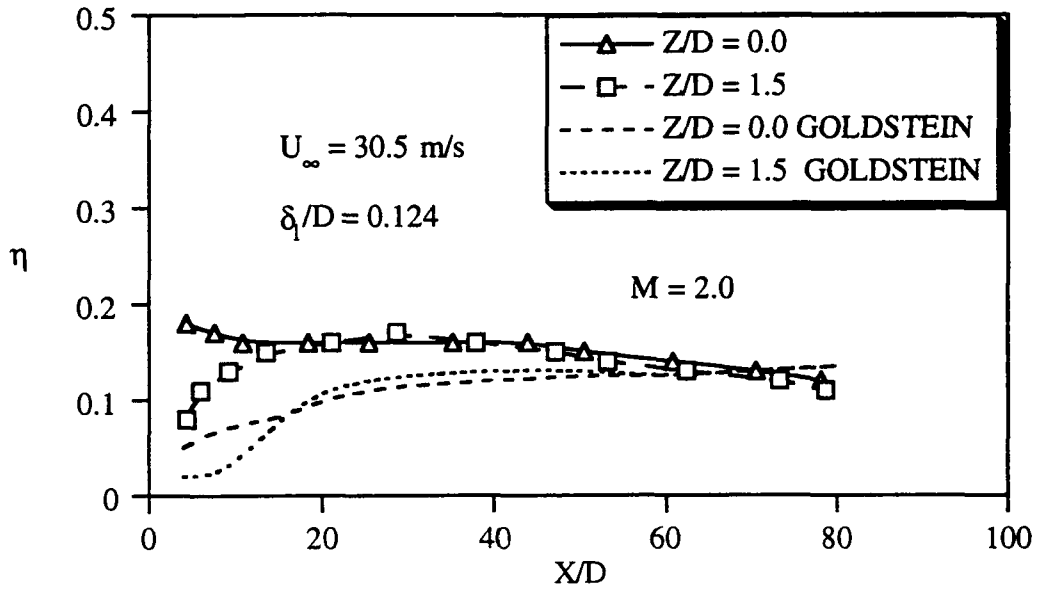

Figure 5.7 Film cooling effectiveness, M = 2.0, δ_1/D = 0.124

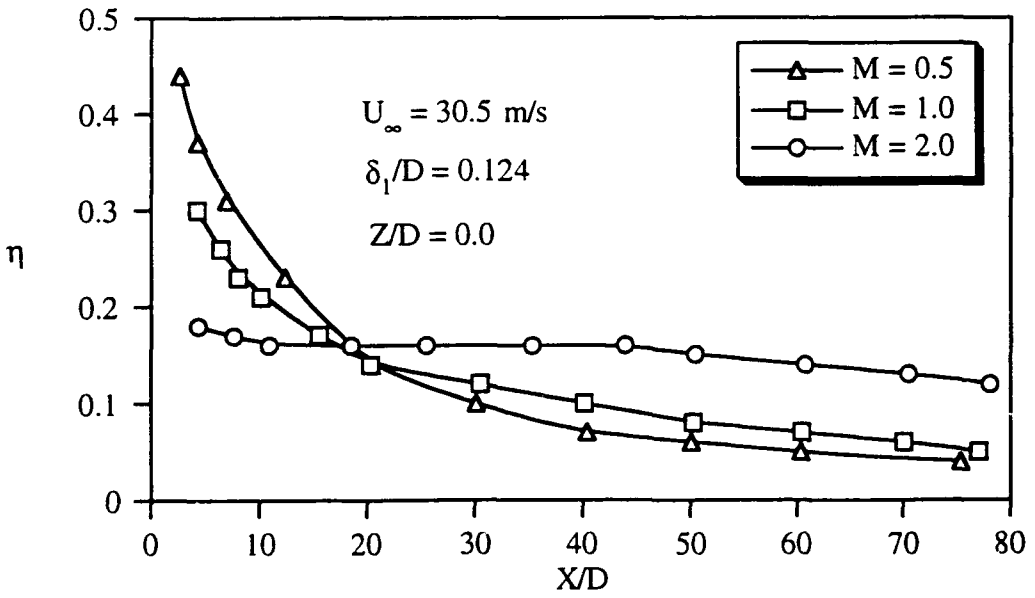

Figure 5.8 Centerline film cooling effectiveness comparison

less than twenty hole diameters is highest for the blowing rate M=0.5. The lowest effectiveness within twenty hole diameters is for a blowing ratio of 2.0. This trend in effectiveness is confirmed by both Goldstein's work and Liess (1975). Both researchers found the maximum effectiveness to occur at M≈0.5 near the point of injection.

Downstream of twenty hole diameters, the effectiveness for all three blowing ratios levels out and is not tremendously different. In this area, the larger blowing ratios, M=2.0, has the highest effectiveness. This trend is confirmed by Goldstein et al. (1970) who, for M=2.0, also found the highest effectivenesses in this region of the plate. Likewise Liess' work found effectiveness in this region to be flat and to improve with blowing ratio. Liess, however, reports a maximum in the area of M≈1.0. In any case, the centerline effectiveness values of this work and of Goldstein's work compares very well.

In between the film holes, the comparison is not as good. This is believed to be the case for two reasons. Near the film holes where gradients in heat transfer are the greatest, lateral conduction in the Plexiglas becomes important. As work in Chapter 6 and 7 will indicate, lateral conduction results in higher-than-actual values of effectiveness between the hole centerlines near the point of injection (X/D=0.0). In general, heat transfer data for the present test plate geometry, where the holes are separated by only 0.2 inches, must be considered suspect within 5 hole diameters. The other factor affecting the effectiveness values between the holes is the turbulence levels of the two studies. As mentioned in section 5.1, the work in Ou et al. (1992) and Shao-Yen Ko et al. (1985) indicates mainstream turbulence reduces the effectiveness, especially at lower blowing ratios. In

this study, it is believed the turbulence of 6.5% results in a greater rate of destruction of the integrity of film jet causing downstream effectiveness levels to smooth out sooner than in the low turbulence case reported by Goldstein. Vedula (1989) also found this same trend in effectiveness. Like the work presented here, the effectiveness between the holes worsened with increasing blowing ratio, but the increased blowing ratios provided increased effectiveness for locations further downstream.

The flow near the point of injection is known to resemble a horseshoe (Goldstein et al., 1970), as illustrated in Figure 5.1. As blowing ratios increase, the film jet retains its structure longer, permitting less cooling air to be taken by this horseshoe circulation down to the surface and lower effectiveness results. Near the holes, at a blowing ratio of M=2.0, the phenomenon called blow off is clearly present (Figure 5.9). The film flow jets penetrate into the main flow away from the surface. The jet then encounters the force of the main flow (Goldstein et al., 1970) and is turned back toward the surface. With higher blowing ratios and higher film-flow momentum the penetration of the film flow is greater resulting in overall lower effectivenesses near the hole. Mainstream air is able to flow around the jet and into the area just after injection. Even though effectivenesses are higher downstream for the M=2.0 case, a penalty is paid near the film hole.

In order to keep this work in perspective, it is worth pointing out that in turbine vane designs, rows of holes are staggered and usually not more than 10 hole diameters apart in the downstream direction. Since the holes are staggered, holes along a particular line will be about twice as far apart , but normally

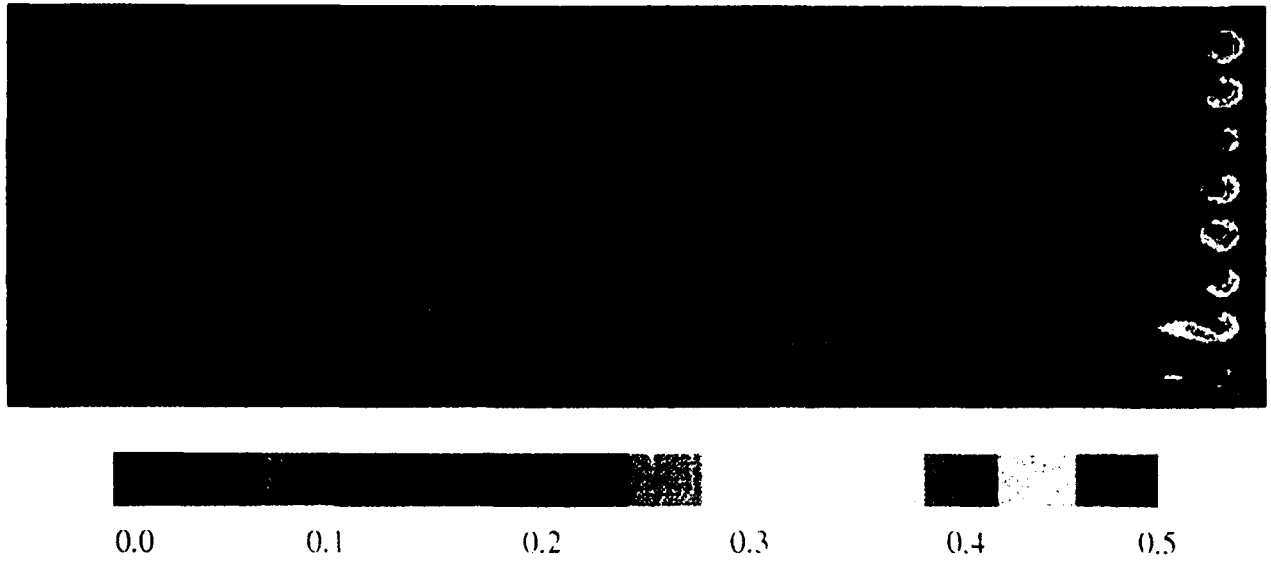

Figure 5.9 Convective film cooling effectiveness map, M=2.0, δ_1/D=0.124

not more than 20 hole diameters downstream. This clearly points to the blowing ratios on the order of 0.5 being most appealing in terms of film-cooling effectiveness.

Overall, there appears to be very good comparison with the effectiveness values found by Goldstein et al. (1970) for similar flow conditions. Prior attempts by Vendula (1989) to compare with Goldstein were not as successful. In those attempts, Vendula had not matched the dimensionless boundary layer displacement thickness. Vendula had lower centerline effectiveness than did Goldstein. Vendula recognized that failure to watch δ_1/D may explain this difference. The heat transfer coefficients downstream of injection are presented in Figures 5.10 through 5.12. Here the values are normalized by the heat transfer values present without film cooling found in Figure 5.2. For blowing ratios of 0.5 and 1.0 the values are within 5% of those present without film cooling. For the M= 2.0 case, the detrimental effect of large blowing ratios is clearly present . Heat transfer coefficients increase on the order of 40% within ten hole diameters and are still 20% higher twenty hole diameters downstream. These increased values of heat transfer have been attributed to the turbulence that results from interaction between the jets and the main flow (Goldstein et al., 1970). For M=0.5, Goldstein attributes lower values of h near the hole in his work to the injected mass thickening the boundary layer, thus decreasing the heat transfer coefficient. Goldstein finds, at all three blowing ratios, the interaction at the edge of the jets and the accompanying increase in turbulence near the surface results in higher values at the edges of the jet (Z/D=1.5) than along the centerline (Z/D=0.0). This differentiation does not appear in the results presented for this work.

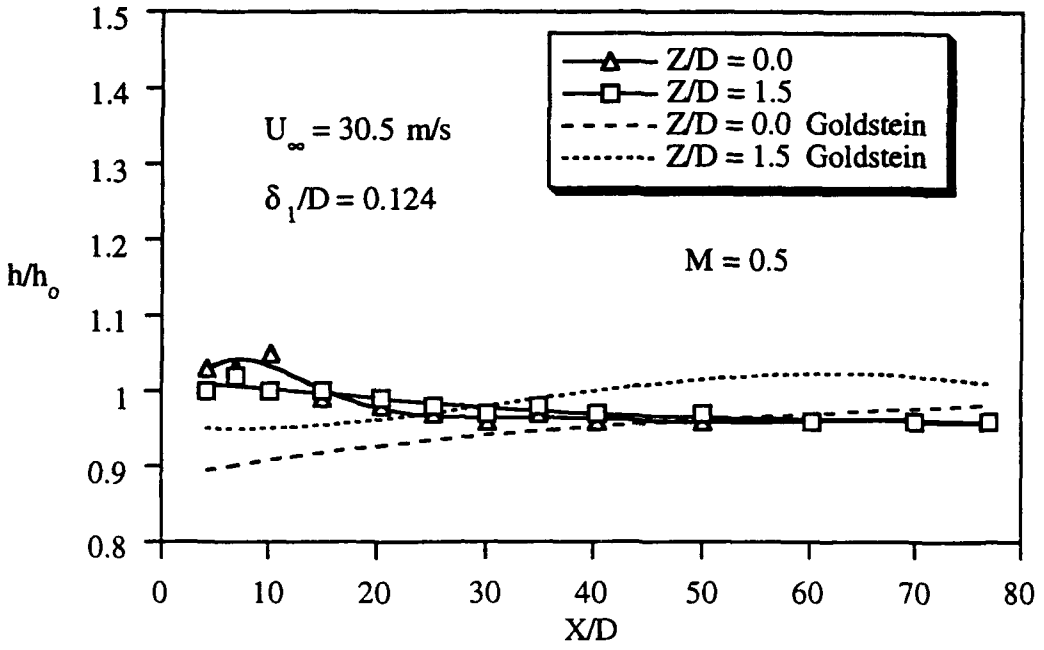

Figure 5.10 Convective heat transfer coefficient, M=0.5, δ_1/D=0.124

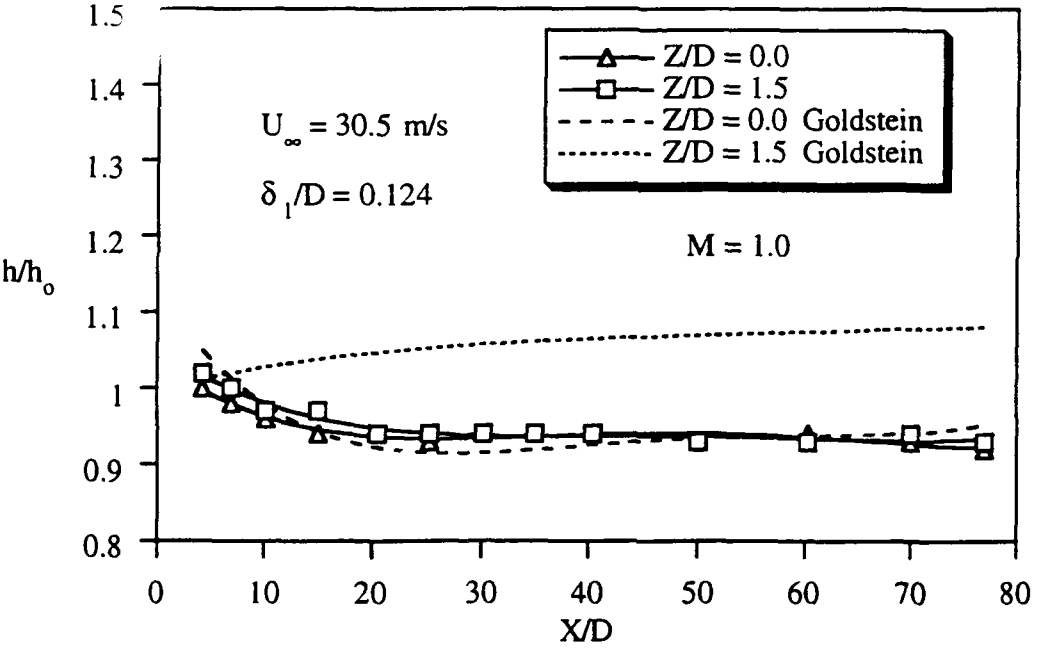

Figure 5.11 Convective heat transfer coefficient, M=1.0, δ_1/D=0.124

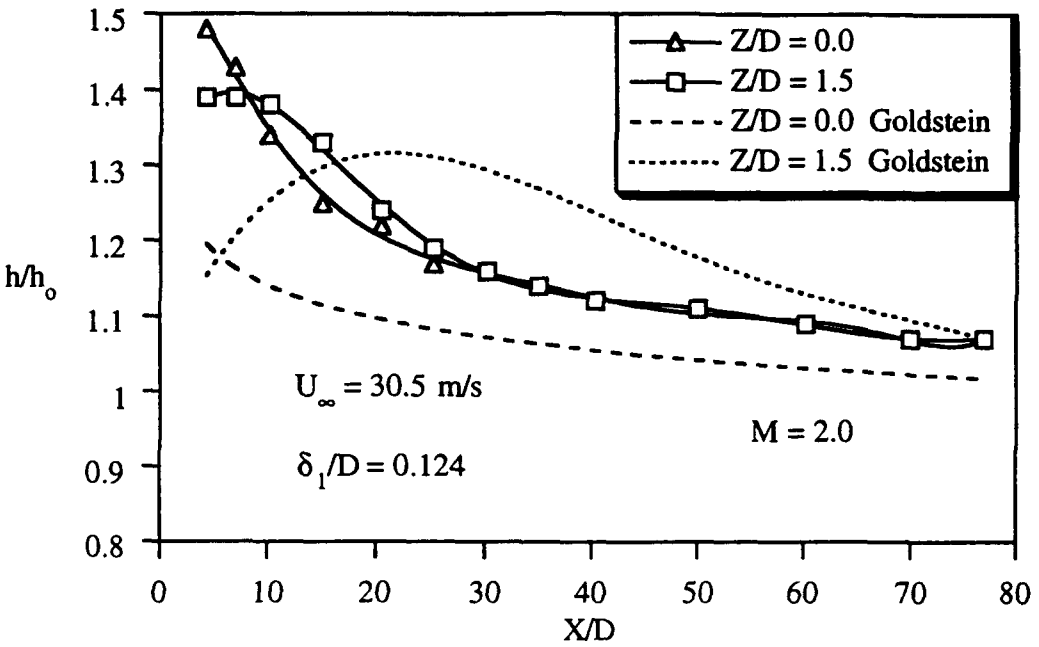

Figure 5.12 Convective heat transfer coefficient, M=2.0, δ_1/D=0.124

This may be because turbulence levels are much higher in this work than in Goldstein's and the interaction along the edge of the film jet and the main flow is not as dramatic a change from the already turbulent main flow environment.

In turbine applications, where the surface to be cooled is a good heat conductor, conduction within the wall decreases lateral variations in wall temperature. Often, a laterally averaged heat transfer ($\bar{h}$) for these applications is of value. Figure 5.13 is a comparison of laterally averaged convective heat transfer coefficients for the three blowing ratios. It is again clear that a high penalty is present for the blowing ratio of two.

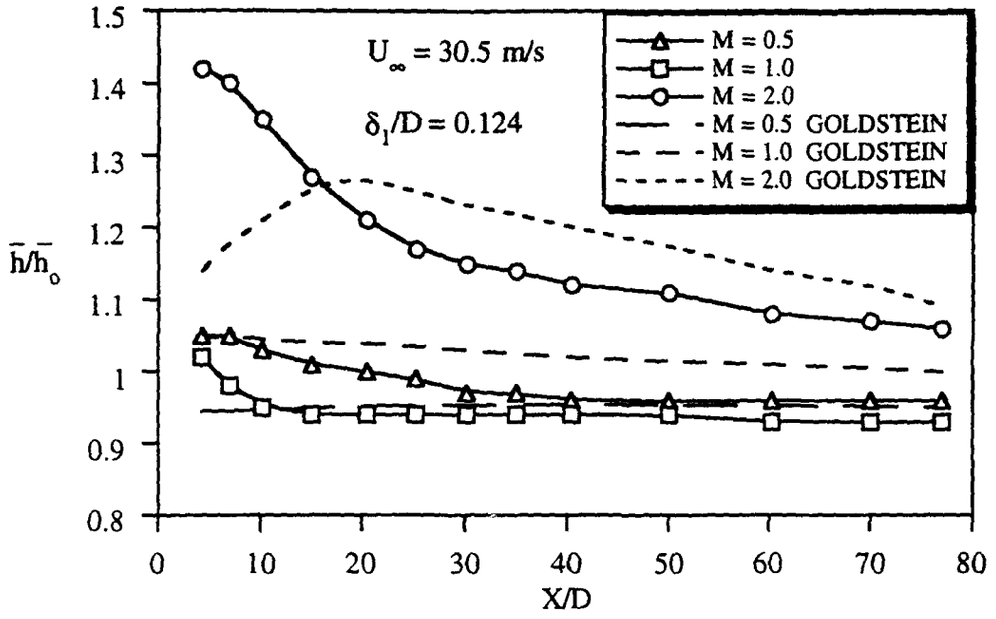

Figure 5.13 Laterally averaged heat transfer coefficient, $\delta_1/D=0.124$

In the results given in Eriksen and Goldstein (1974), $(\bar{h})$ is defined as

$$\bar{h}(X/D) = \frac{\bar{q}}{\bar{T}_w(X/D) - \bar{T}_{aw}(X/D)}$$

In this work, where local data are available, $\bar{h}$ is determined by

$$\bar{h}(X/D) = \frac{1}{3}\int_{-1.5}^{1.5} h(X/D,Z/D)\, d(Z/D)$$

5.4 Discussion

The results of this study when compared to the work of Goldstein et al. (1970) and Eriksen and Goldstein (1974), in general, compare very well. Film cooling effectiveness and the change in heat-transfer coefficients due to 35° injection show the same general magnitudes and trends. It has been the belief of researchers at ASU that effectiveness values obtained by methods using the adiabatic wall method (e.g., Eriksen and Goldstein, 1974) should match the effectiveness values determined using the transient method of this work. This belief is best explained by referring back to Figure 3.27 in Chapter 3. As outlined in Chapter 3, the two-test method used in this work, determines two points in the h_m - θ^* plane. A straight line through these points determines h and η at the intersections of that line with the ordinate and abscissa. The solution for $1/\eta$ lies on the abscissa and corresponds to an h_m of zero. With h_m equal to zero, this point corresponds to a heat flux of zero, or to the adiabatic wall situation. This argument leads to the believe that the ηs, determined by the transient method should compare well with the ηs determined by adiabatic wall techniques. The results of this chapter tend to confirm this hypothesis and provide increased confidence in the transient techniques used in this study.

CHAPTER 6

FINITE DIFFERENCE FOR COMPOSITE TEST PLATE

6.1 Introduction

The experimental method discussed in Chapter 2 and applied in Chapters 3, 4 and 5 to obtain heat transfer and effectiveness information have shown excellent agreement with other experimental methods for obtaining local convection coefficients. In reality, however, lateral conduction effects are present and must be assessed. The greater the gradients in heat transfer coefficient, the greater the significance of the lateral conduction. Lateral conduction in the solid surface smooths the surface temperature distribution and can potentially reduce the ability of the experimental method to resolve steep variations in heat transfer at the surface. Vedula, Bickford and Metzger (1988) used a finite element analysis to assess the effect of lateral conduction. In this work, heat transfer coefficients are imposed on a two-dimensional convective surface and then the transient solution methods of Chapter 2 are used to back out the approximate heat transfer coefficient. The imposed solution and the solution obtained match exactly only in the absence of convection heat transfer gradients. In the absence of heat transfer gradients, the surface temperature is spatially uniform and the situation is reduced to a one-dimensional (1-D) problem. The authors then imposed spikes of heat transfer coefficients on the surface and were able to assess the error of evaluating the local heat transfer coefficient using the 1-D semi-infinite solid

solution. The error is the difference between the computed and imposed coefficients. As one would expect, their results show a spreading of the imposed spike occurs. The error involved increases as the spike is intensified. The largest errors occurring at the base of the spike. For a Plexiglas surface with an imposed 400 W/m^2K convective heat transfer coefficient and a 3-mm wide spike to 600 W/m^2K, the maximum error in the 1-D approximation was 3.5% at the spike base. Since this drastic spike is more severe than is seen in actual testing, the effects of lateral conduction on test results are very reasonable.

In this work, a finite difference code is written to assess the effects of lateral conduction in the composite surface and to evaluate the ability of the lumped capacitance model, outlined in Chapter 2, to account for the energy accumulated in the stainless steel during a transient test. As described in Chapter 2, the semi-infinite solution is still applied to the epoxy solid with a lumped capacitance correction for the time response lag caused by the accumulation of energy in the stainless steel portion of the composite plate. Because of the thin stainless steel layer over the entire composite plate, the effects of lateral conduction will be more significant than is the case for a solid Plexiglas model.

The finite difference code written for this numerical analysis is listed in Appendix B. The code is a central differencing implicit code solved using an alternating direction scheme as presented by Patankar (1980). A harmonic mean is employed to model the conductivity at the epoxy stainless steel interface. The governing equation for this situation is given by the transient conduction equation with constant material properties.

Governing equation:

$$k \frac{\partial}{\partial X}\left(\frac{\partial T}{\partial X}\right) + k \frac{\partial}{\partial Y}\left(\frac{\partial T}{\partial Y}\right) = \rho c_p \frac{\partial T}{\partial t}$$

Boundary conditions:

$$[h]_{x=0} = f(Y)$$

Initial condition:

$$[T]_{X,Y} = T_i$$

This technique is covered well in the literature and need not be repeated here. The two-dimensional code was written to permit evaluation of a flat surface or a rough surface. For the rough surface, the ratio of the wetted surface area to planar matches the rough composite plate used for testing in Chapter 9. In this way both the effects of lateral conduction and the results of incorporating the lumped capacitance model can be assessed. In the next section, the code is validated in the manner used by Vedula et al. (1988) on a Plexiglas surface. In Sections 6.3 and 6.4, the code is used to evaluate the model on a composite plate, both for a smooth and rough surface. By running the code twice, simulating the two-test experimental approach described in Chapter 2, the test model can be assessed in terms of both h and η. convection coefficient distributions on a surface are typically h-isopleths like those shown by the contours in Figure 6.1. Because the surface convection coefficient

distribution is two-dimensional, the transient conduction below the surface is generally three-dimensional. However, the largest gradient in temperature will be normal to the contours and the effects of lateral conduction should be adequately described with a two -dimensional analysis correctly oriented. For the composite two-temperature case considered in section 6.3 the normal runs in the x direction. For the three temperature film-cooled case considered in Section 6.4 the greatest gradients are in the Z or lateral direction and thus, is the orientation of the finite difference grid.

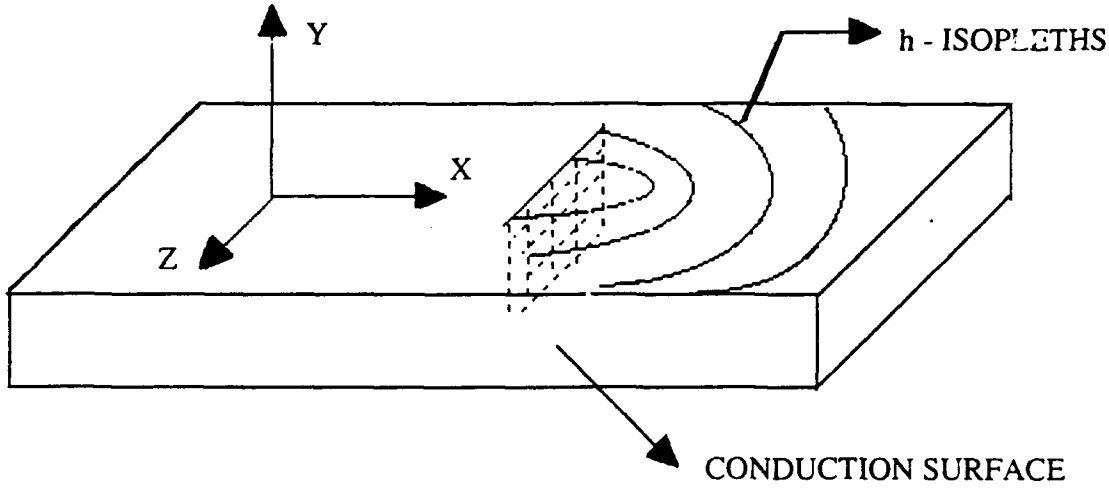

Figure 6.1 Numerical model

6.2 Code Validation

In the same approach as that of Vedula et al. (1988), Figure 6.2 shows a test of the finite difference code. In this test, the code computes values of surface temperature response (T_w) to a step application of convection at the surface. The computed results are compared with those given by equation

2.6, the classical one-dimensional solution, for a Plexiglas isotropic medium. Figure 6.3, displays another numerical experiment with the convection coefficients backed out of the one-dimensional response and compared with the initially imposed values. Both figures show excellent agreement.

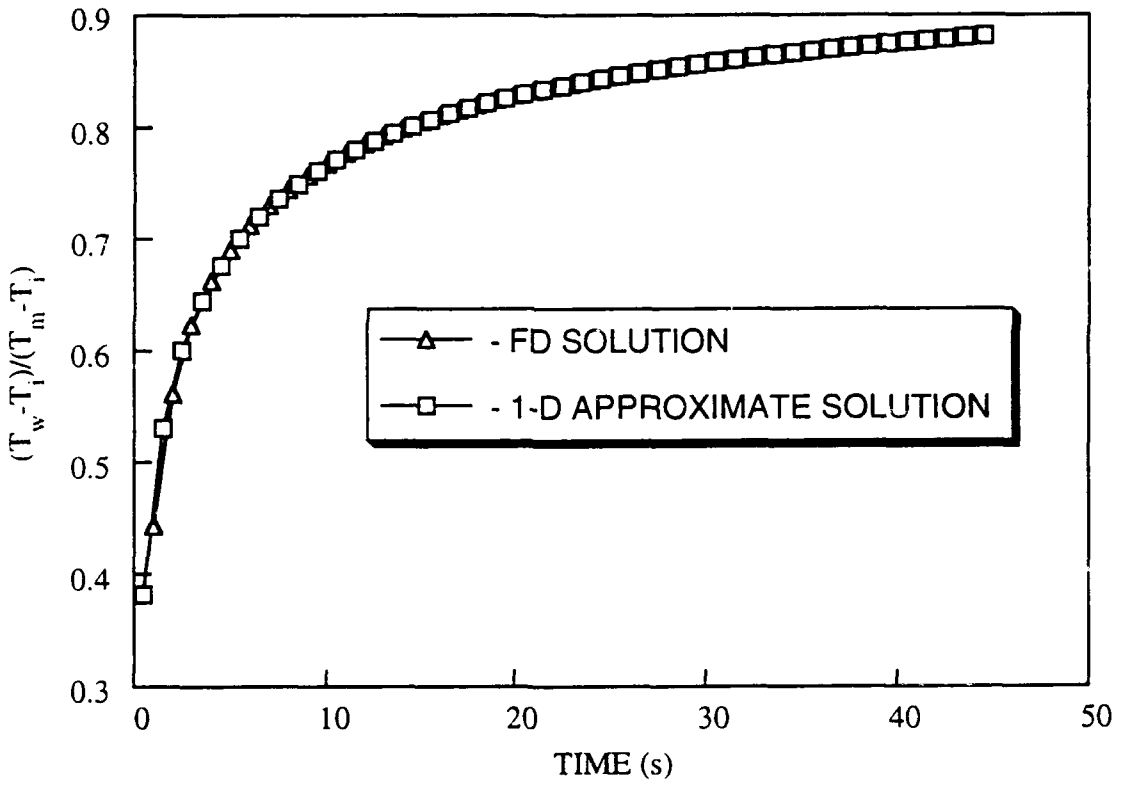

Figure 6.2. Comparison of 1-D and 2-D responses for uniform imposed h

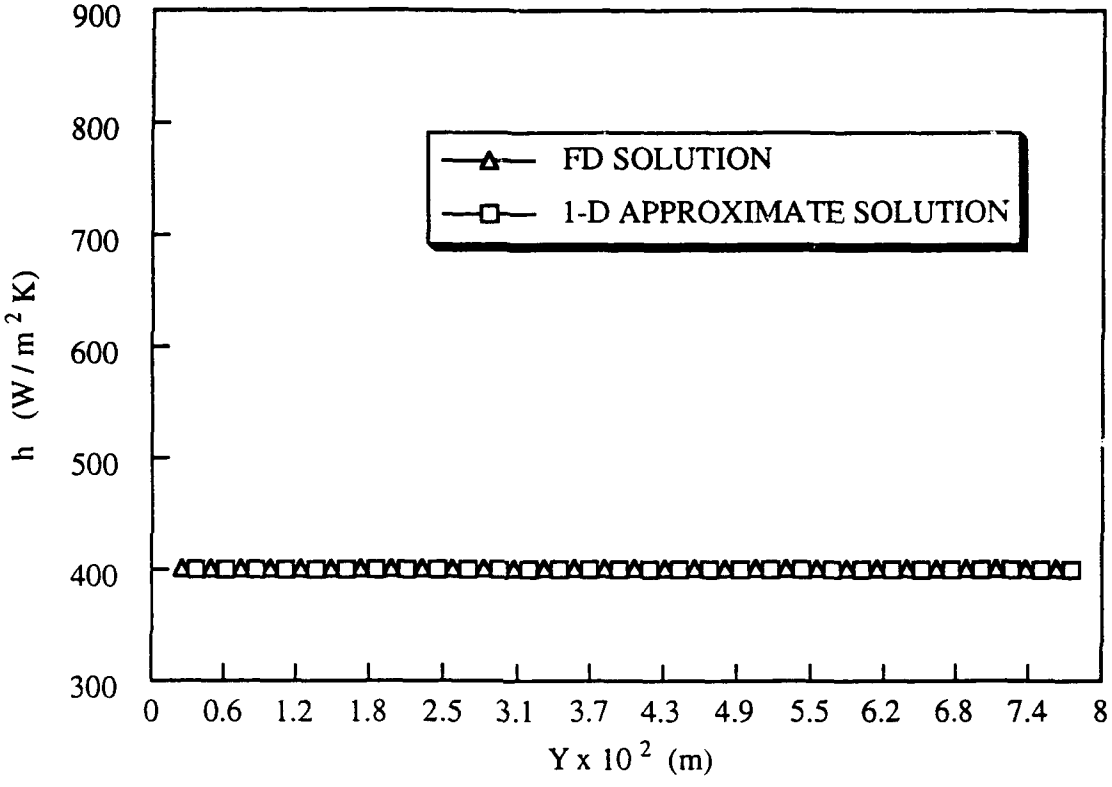

Figure 6.3 Comparison of imposed and 1-D calculated h for uniform h

As a final test of the code, and to demonstrate the good results achieved with using a Plexiglas model, Figure 6.4 shows the backed-out convection coefficients compared with an imposed severe spike. As Vedula et al. (1989) found, the largest errors occur at the base of the spike at about 4%.

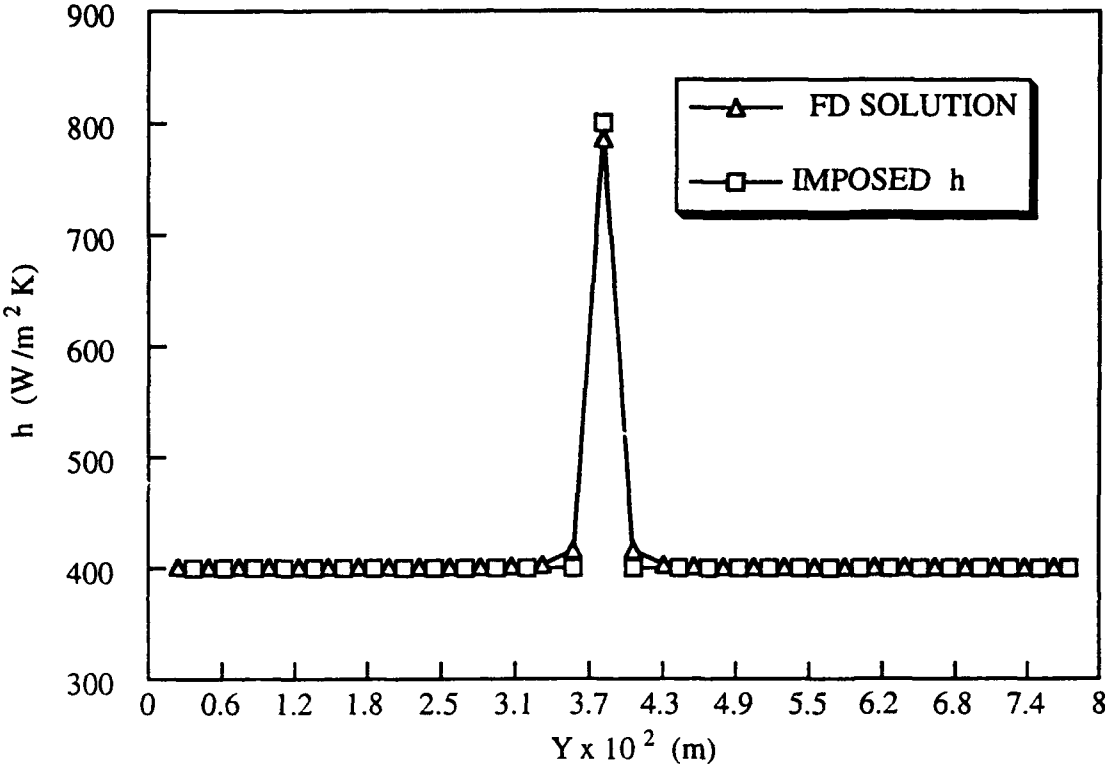

Figure 6.4 Comparison of imposed and calculated h for Plexiglas

6.3 Time Lag Solution for the Two -Temperature Problem

For a smooth plate, an h is imposed on the surface which matches that of a turbulent flat plate. The temperature response on the backside of the stainless steel, the location of the TLC layer in actual experiments, is used to back out h using the semi-infinite solid solution with and without the time lag (lumped capacitance) correction. This numerical experiment is carried out for 30 m/s and 50 m/s using two thicknesses of stainless steel, 0.003" and 0.005".

The results are shown in Figures 6.5 through 6.8. In each case, the addition of the lumped capacitance correction to the time that the TLC reaches its calibration temperature improves the model greatly. Even for the worst case, Figure 6.8, at an imposed h corresponding to ..am velocity of 50 m/s, the backed out h with a stainless steel thickness of 0.005" is within 4% of the imposed values. The smooth composite surfaces, which are compared to the results from Plexiglas in Chapter 7, are 0.004" thick.

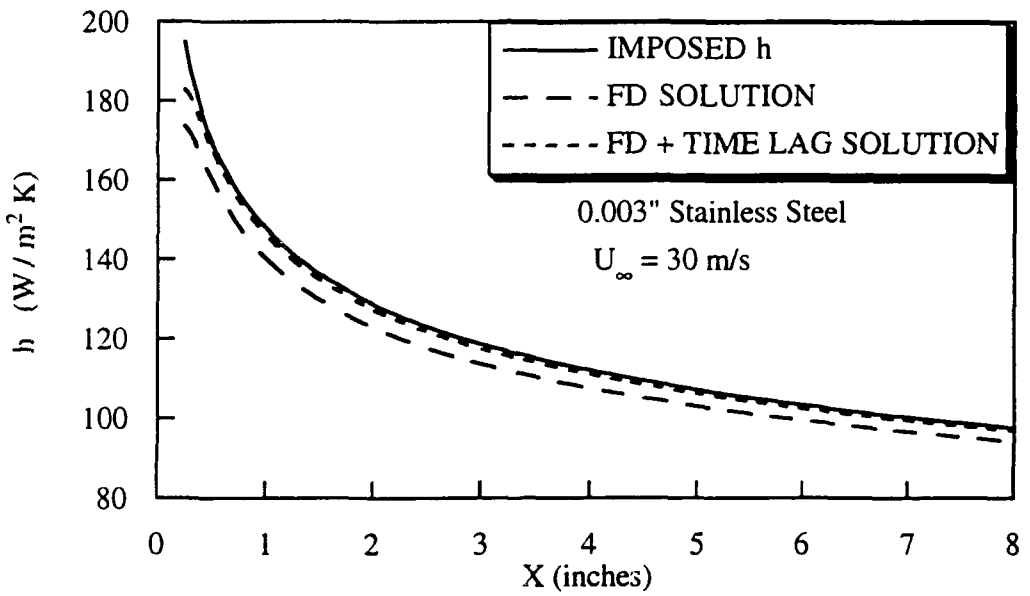

Figure 6.5 Finite difference, 0.003" stainless steel, U_∞=30m/s

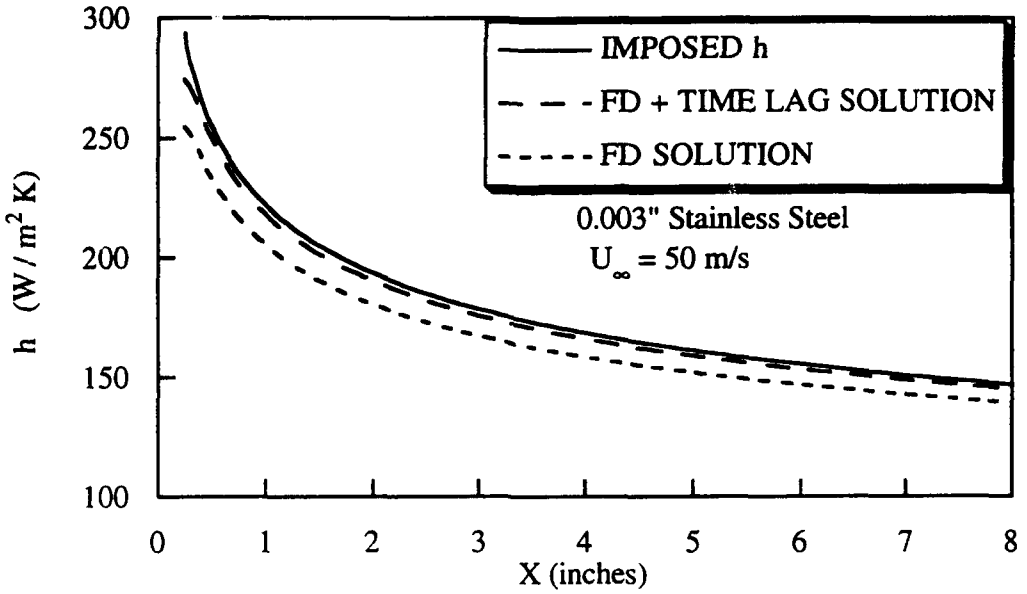

Figure 6.6 Finite difference, 0.003" stainless steel, U_∞=50m/s

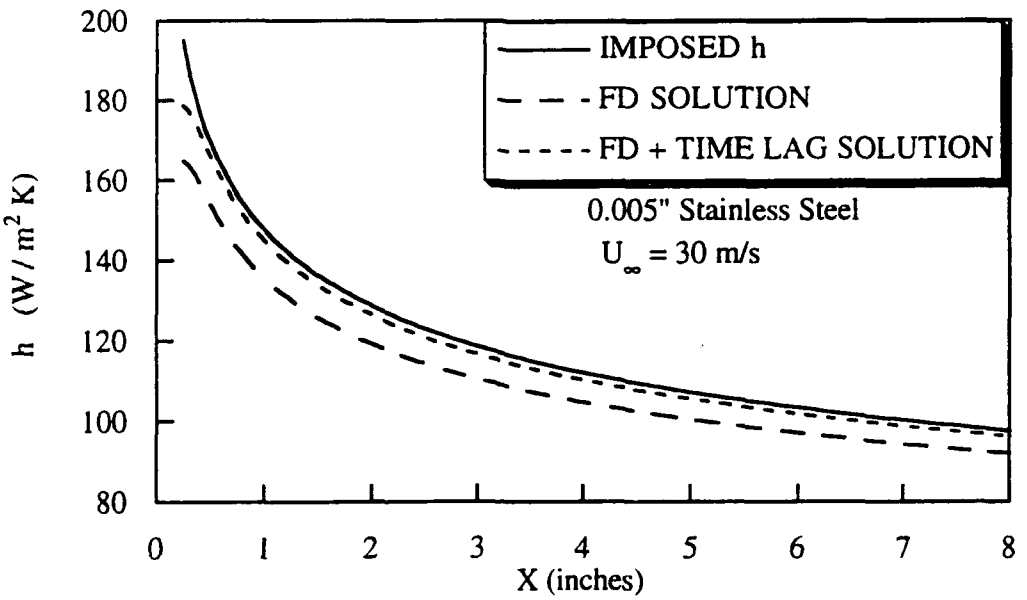

Figure 6.7 Finite difference, 0.005" stainless steel, U_∞=30m/s

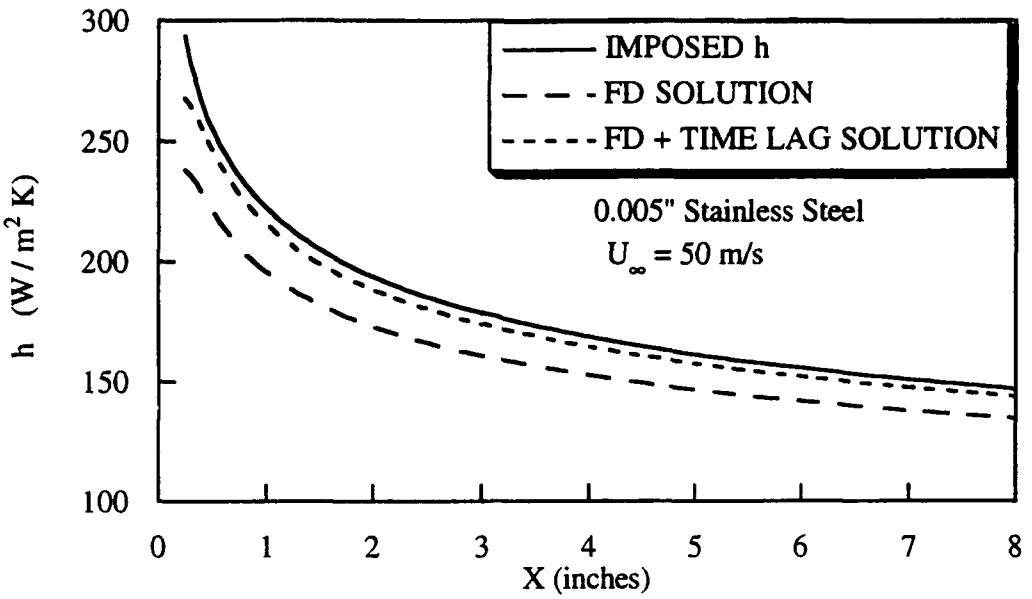

Figure 6.8 Finite difference, 0.005" stainless steel, U_∞=50m/s

6.4 Time Lag Solution for the Three Temperature Problem

To assess the effect of the composite test approach in determining both h and η in a two test scheme, a finite difference experiment is accomplished where both a simulated cold test and hot test are run. The imposed h and η profiles are taken from an actual experimental test on Plexiglas model with a blowing ratio of 0.5. The M=0.5 case at a free-stream velocity of 50 m/s is used, because the gradients encountered are the most severe of the test conditions seen in this testing program. Unlike the actual experiment, where the surface experiences is a gradual free stream temperature rise, the numerical experiment is conducted with a true step in boundary conditions.

Flow temperatures are set to approximate the temperatures of the M=0.5 actual test run in Chapter 7, T_∞=114°F, $T_{f(cold)}$=95°F, and $T_{f(hot)}$=130°F.

Using the h and η profiles along with the appropriate temperatures, both a hot and cold numerical experiments are run. The transient temperature response on the backside of the stainless steel from the two experiments are used to back out the h and η using the semi-infinite solid solution, with and without the time lag correction. The results for composite plates with a 0.003" and a 0.005" smooth surface are shown for four downstream locations X/D=1.5, 5.0, 10.0, 20.0 in Figures 6.9 through 6.24. Indicated on the plots at each location are the laterally averaged convective heat transfer coefficient ($\bar{h}$) and laterally averaged film cooling effectiveness ($\bar{\eta}$) for the imposed h and η along with the ($\bar{h}$) and ($\bar{\eta}$) for the backed out composite surface values. Several factors can be assessed from this work. First, as expected, the effects of lateral conduction are much enhanced over that seen for a Plexiglas test model. As expected, the backed out values match better for the composite plate with the thinner stainless steel surface. Secondly, the results with the time lag solution model the actual imposed values match better than the semi-infinite solution without the lumped capacitance correction. In general, the resulting h and η values are too high in between the film holes and too low at the film hole centerline. In addition, the error associated with the experimental model increases closer to the point of film injection (X/D=0.0). This corresponds to greater surface temperature gradients and greater lateral conduction. At a downstream location of X/D=1.5 the h and η values between the holes are susp[illegible]y X/D=10 the comparisons

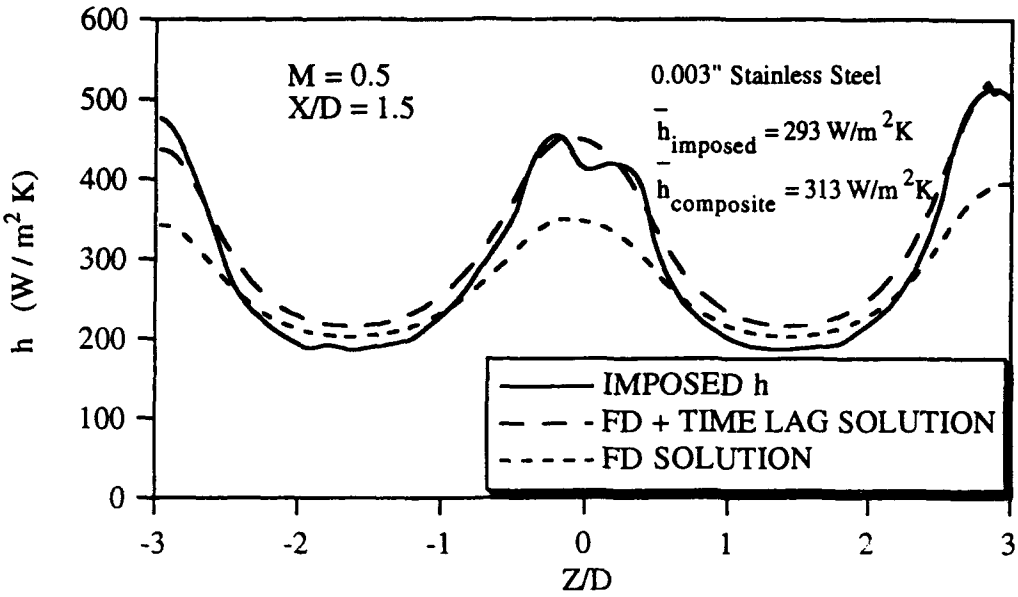

Figure 6.9 h, finite difference, M=0.5, X/D=1.5, 0.003" stainless steel

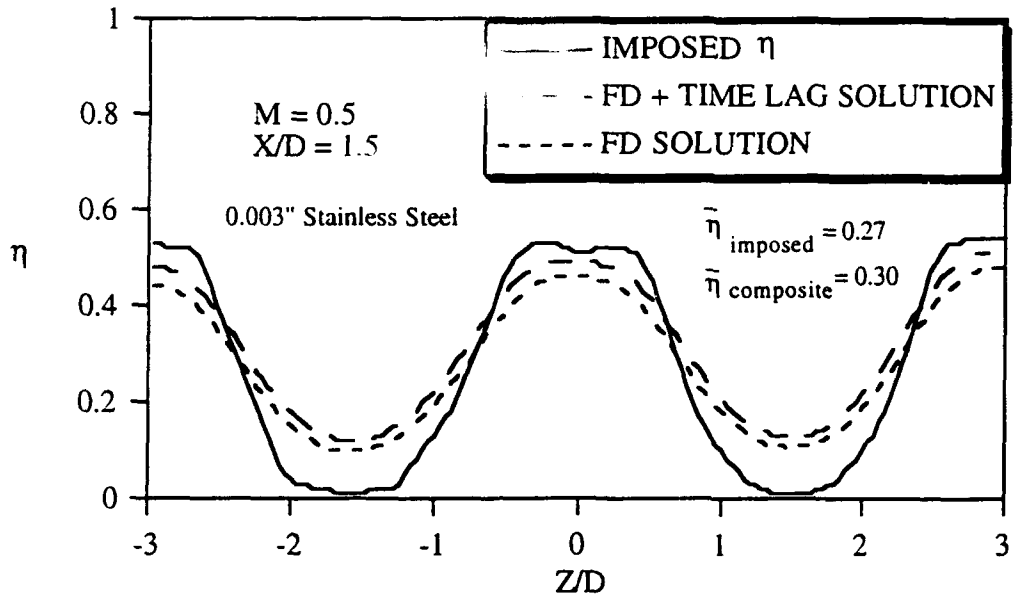

Figure 6.10 η, finite difference, M=0.5, X/D=1.5, 0.003" stainless steel

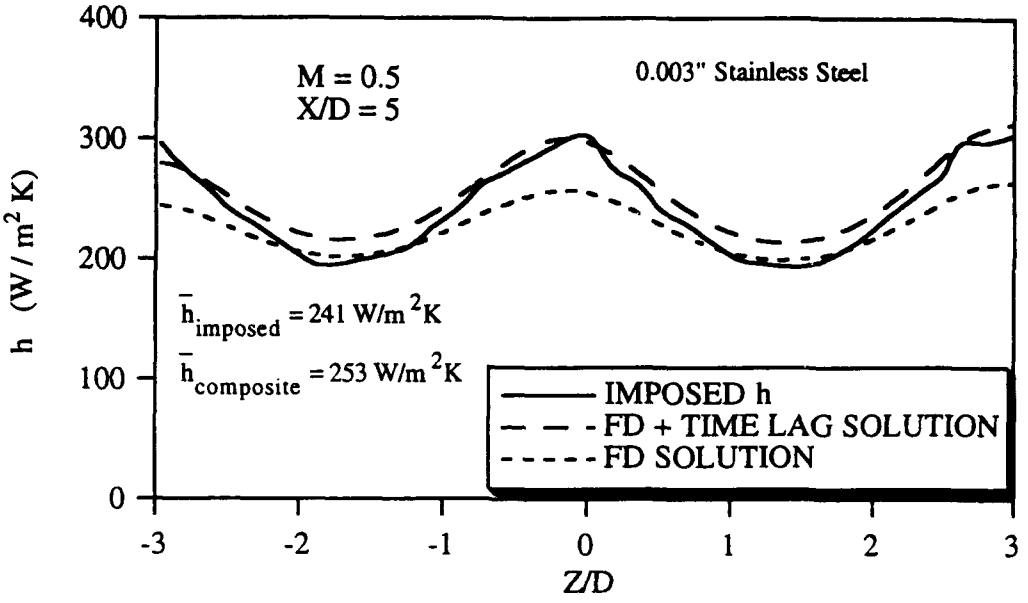

Figure 6.11 h, finite difference, M=0.5, X/D=1.5, 0.003" stainless steel

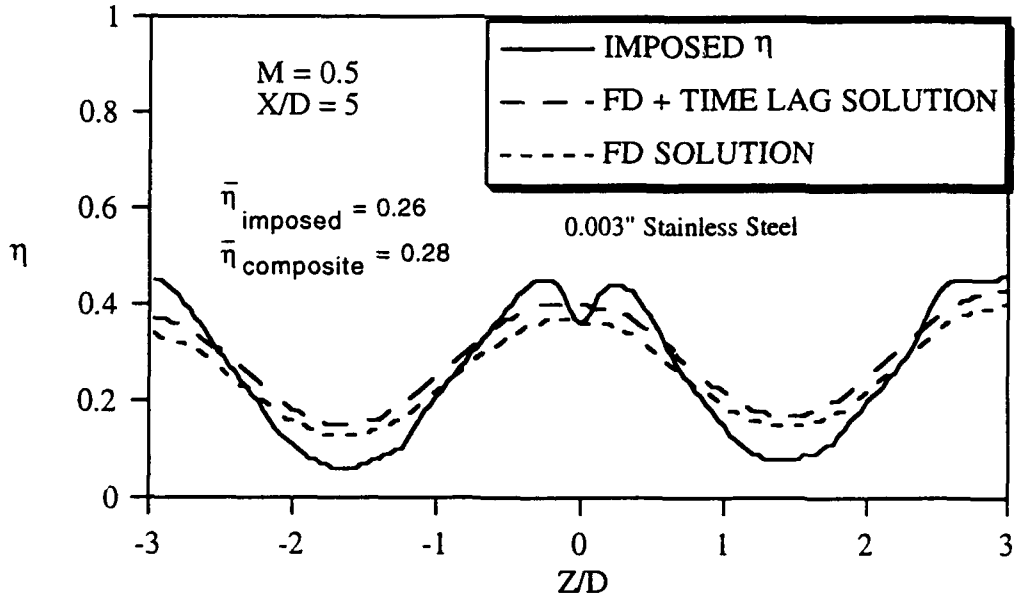

Figure 6.12 η, finite difference, M=0.5, X/D=5.0, 0.003" stainless steel

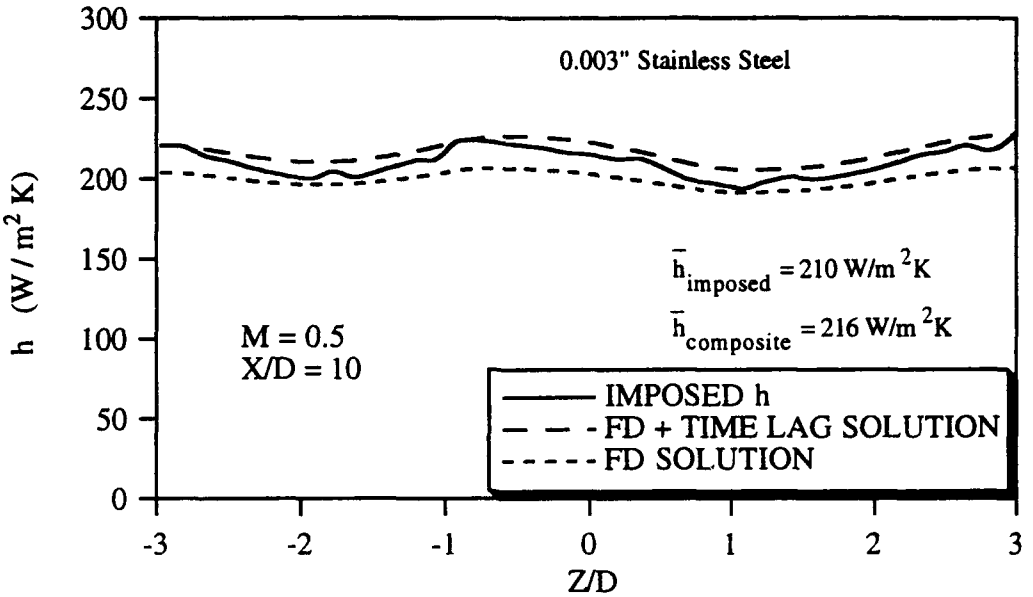

Figure 6.13 h, finite difference, M=0.5, X/D=10.0, 0.003" stainless steel

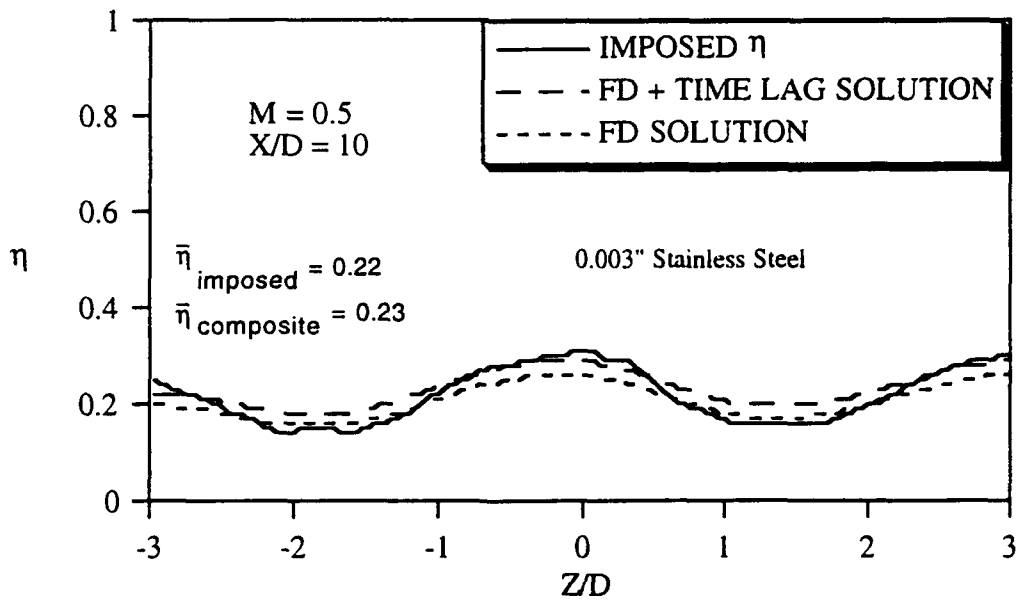

Figure 6.14 η, finite difference, M=0.5, X/D=10.0, 0.003" stainless steel

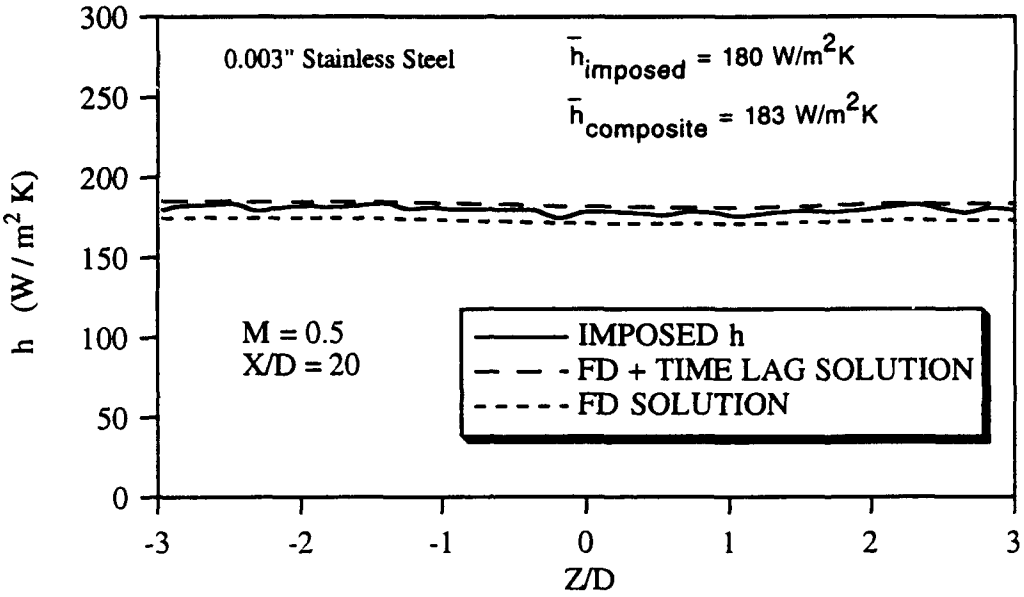

Figure 6.15 h, finite difference, M=0.5, X/D=20.0, 0.003" stainless steel

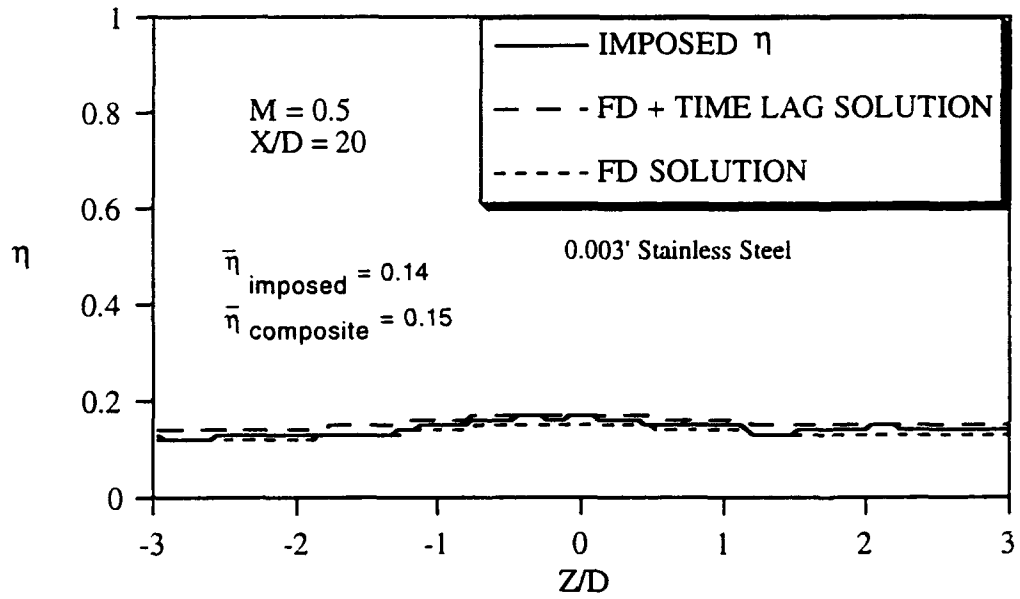

Figure 6.16 η, finite difference, M=0.5, X/D=20.0, 0.003" stainless steel

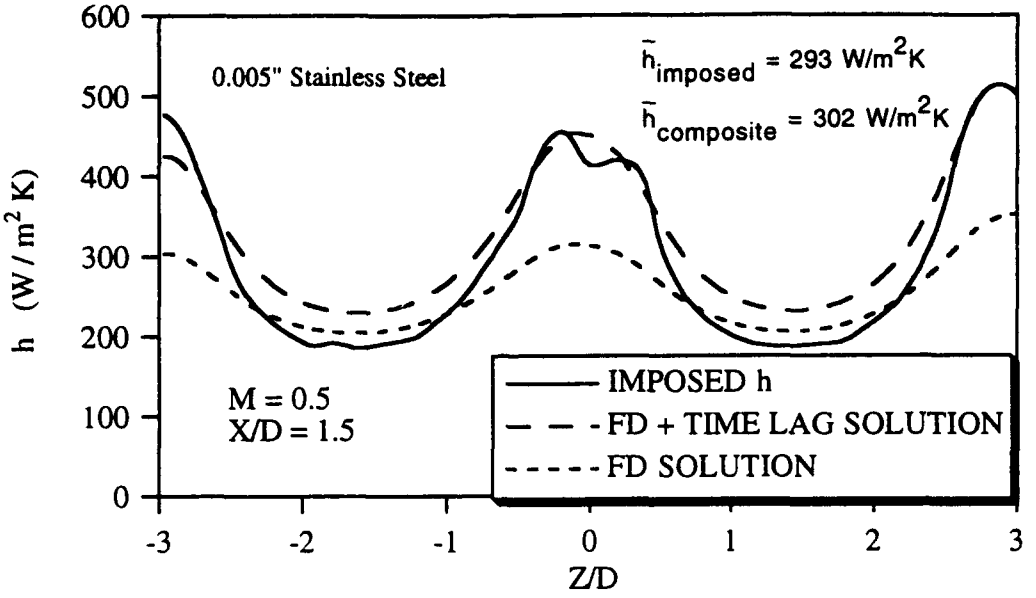

Figure 6.17 h, finite difference, M=0.5, X/D=1.5, 0.005" stainless steel

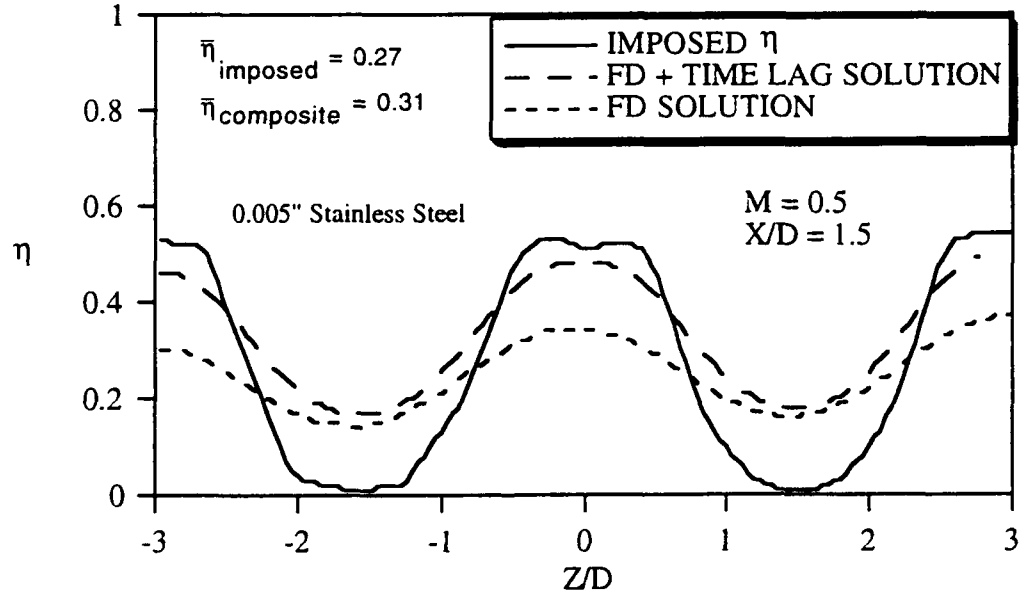

Figure 6.18 η, finite difference, M=0.5, X/D=1.5, 0.005" stainless steel

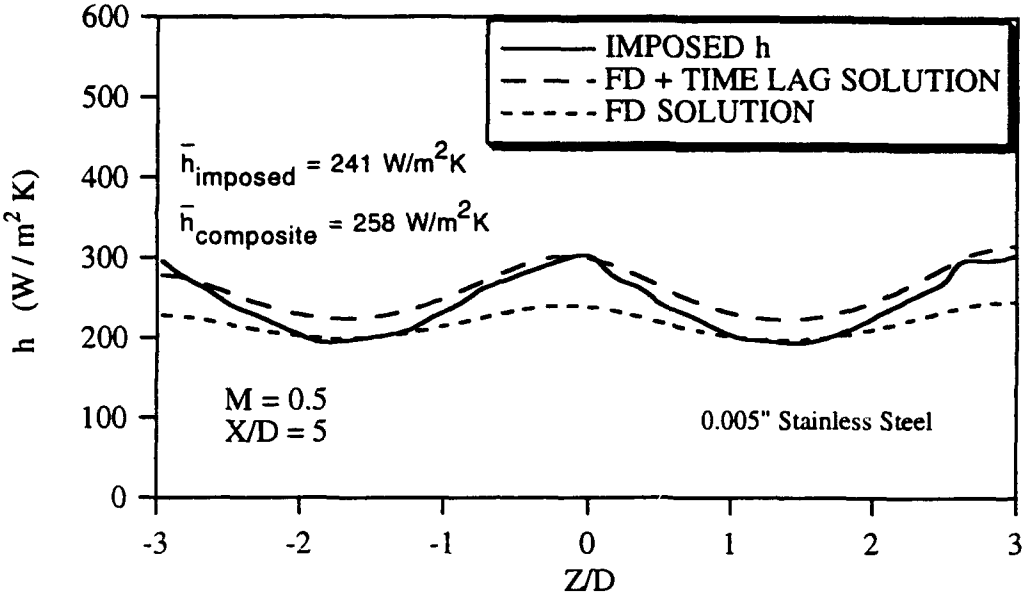

Figure 6.19 h, finite difference, M=0.5, X/D=5.0, 0.005" stainless steel

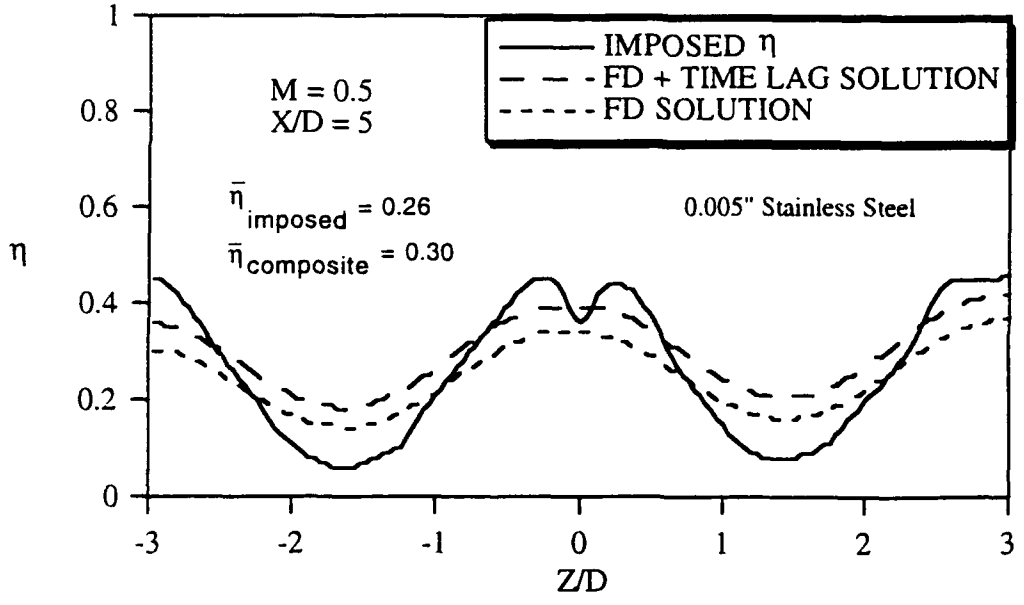

Figure 6.20 η, finite difference, M=0.5, X/D=5.0, 0.005" stainless steel

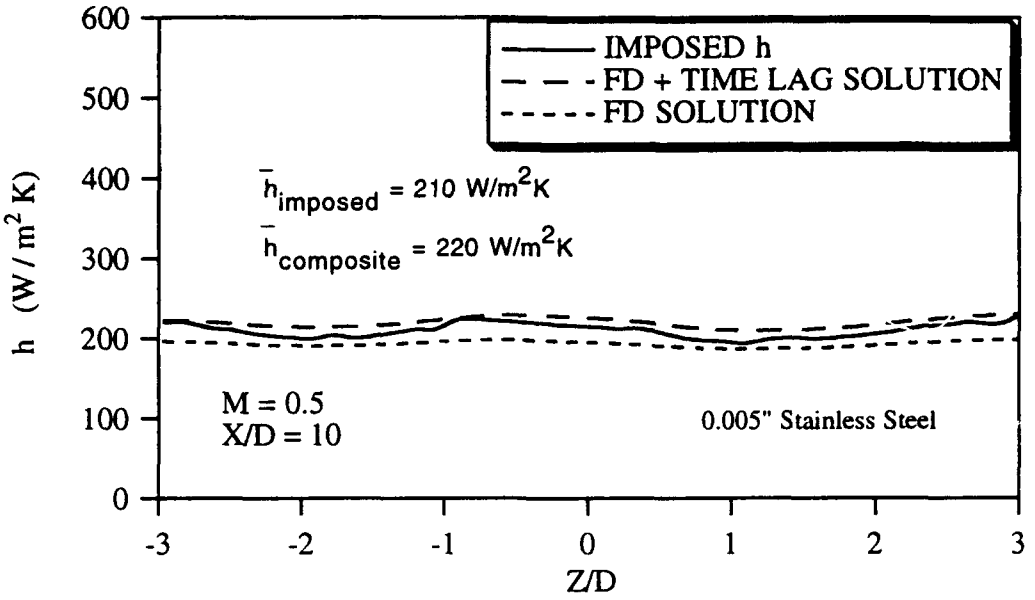

Figure 6.21 h, finite difference, M=0.5, X/D=10.0, 0.005" stainless steel

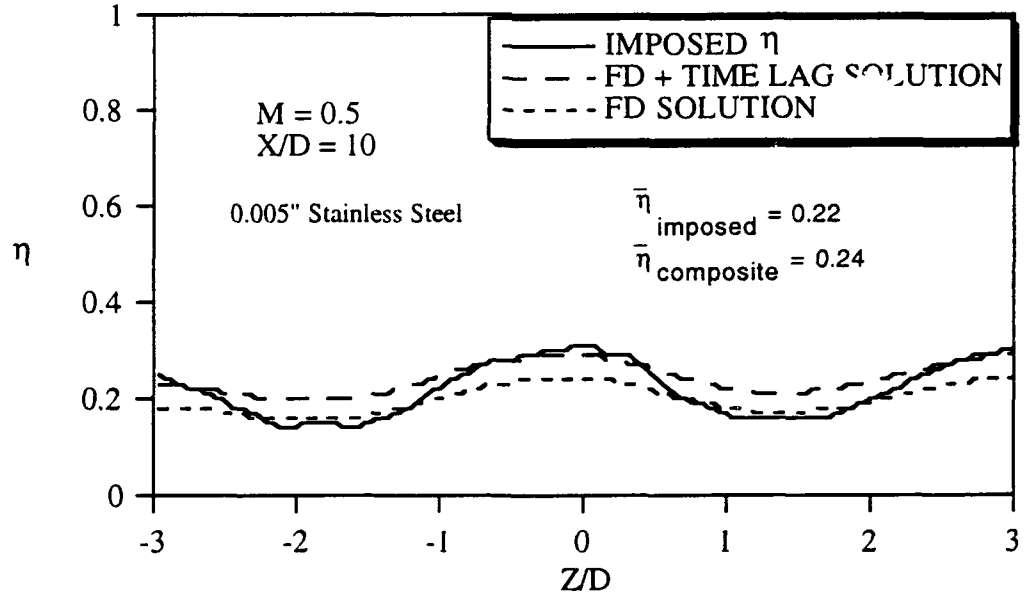

Figure 6.22 η, finite difference, M=0.5, X/D=10.0, 0.005" stainless steel

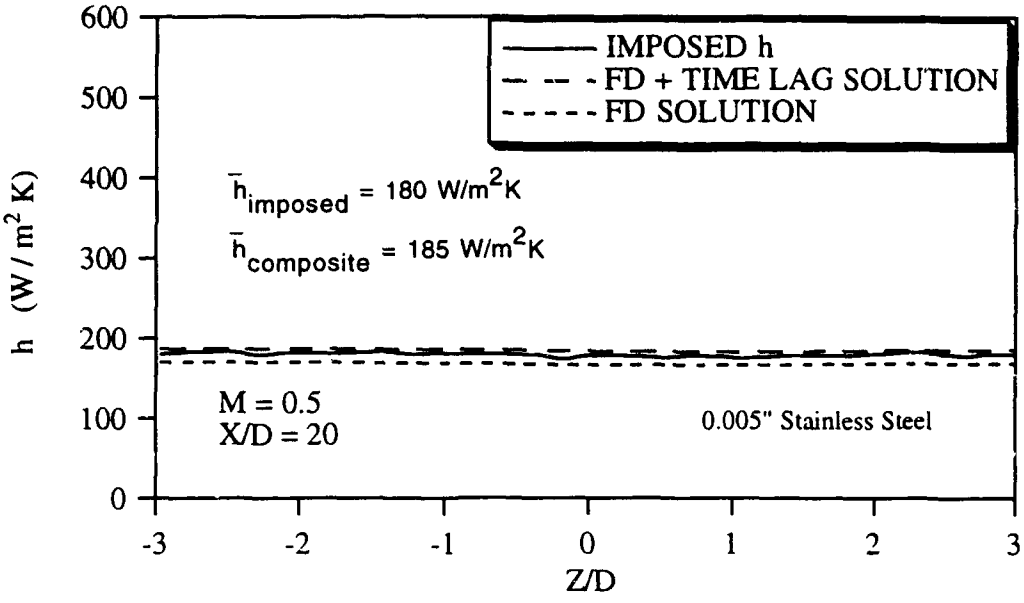

Figure 6.23 h, finite difference, M=0.5, X/D=20.0, 0.005" stainless steel

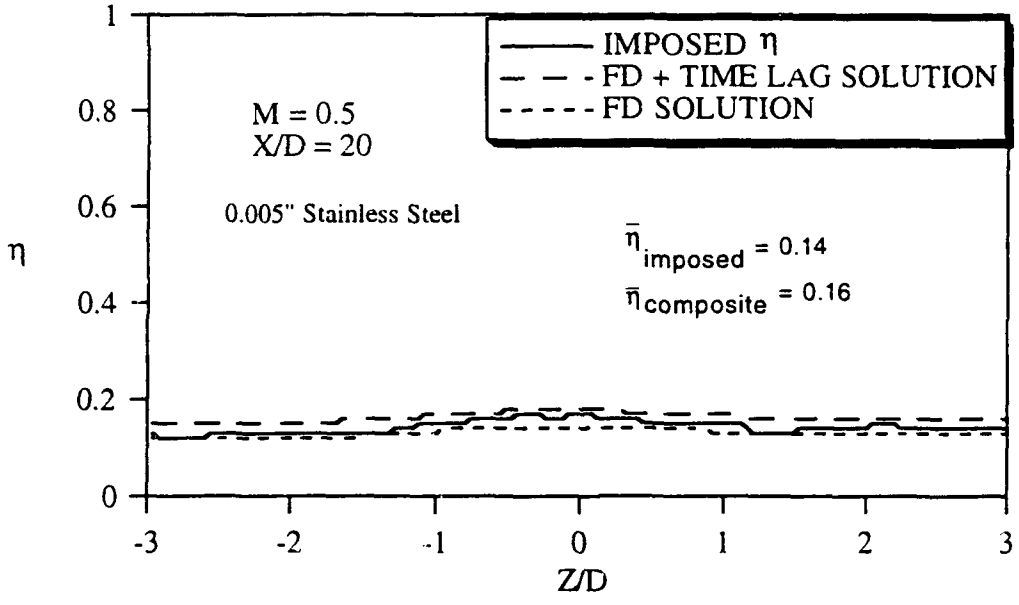

Figure 6.24 η, finite difference, M=0.5, X/D=20.0, 0.005" stainless steel

are very reasonable with h errors on the order of 5% and η variations of .03.

As discussed in Chapter 5, often the laterally averaged values of effectiveness and heat-transfer coefficients are of greatest importance to the designer. In actual turbine airfoils, the temperature distribution is highly smoothed by the presence of lateral conduction. When considering laterally averaged values, the composite plate appears to perform quite well. Even for the worst case, where the stainless steel is 0.005" thick at X/D=1.5, the backed out $\bar{h}$ is within 3% and $\bar{\eta}$ within 0.04. By five hole diameters $\bar{\eta}$ is within 0.03 and at ten hole diameters within 0.02.

The composite plates with rough surfaces, reported on in Chapters 8 and 9, have a base thickness between 0.003" and 0.004". therefore, we expect the effects of lateral conduction to be closer to the effects seen for the 0.003" finite difference work in Figures 6.8 through 6.15. By five hole diameters $\bar{h}$ is in less than 5% and $\bar{\eta}$ is within 0.02.

It is interesting to note the lumped capacitance correction has the greatest effect on h and appears to shift η a constant amount regardless of lateral position (Z/D). For a thickness of 0.003" this shift is 0.02. This same shift of 0.02 appears in Chapter 7 and leads to the conclusion there is a bias in the model for η which depends on the metal thickness.

6.5 Time lag solution for Rough Surface

Assessing the model for the rough composite plate is slightly more challenging. The code grid is set up to model the area ratio (A_{RS}/A) present

for the two rough surfaces tested in Chapters 8 and 9 (A_{RS}/A=1.18 and 1.26), and to have the same base stainless steel thickness (0.004").

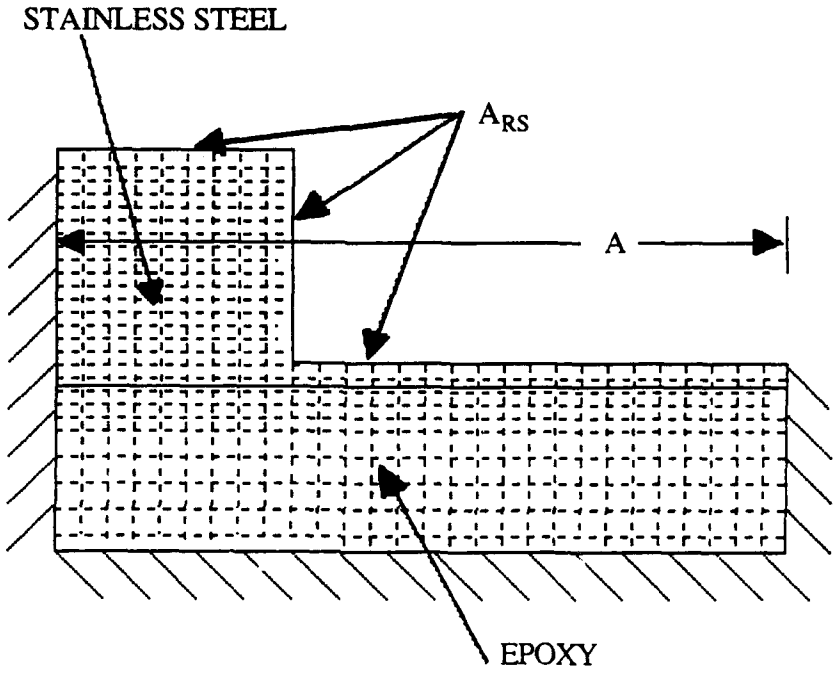

Figure 6.25 Rough element numerical model

Since this is a very localized model at a single roughened element, the reference temperature is considered constant and the problem is in essence reduced to a two-temperature problem.

In this work, the heat-transfer coefficient (h) which is reported is for the planar area (A) of the surface, not the wetted surface area (A_{RS}). This is done

instead of reporting a convective heat transfer coefficient (h_{RS}) based on the wetted rough surface area where

$$q = h_{RS} A_{RS} (T_r - T_w)$$

h is more useful to the engine designer who knows the planar area (A), but would have to estimate the wetted surface area of the rough surface (A_{RS}). A convenient result of the model expounded upon in Chapter 2, is that the h determined in this method is naturally based on the planar area of the surface.

To assess the model and the use of the planar h, the following numerical experiment is run. For each roughness size, a constant h is imposed on the wetted surface area. The transient experiment runs until each grid point on the stainless steel/epoxy interface reaches the calibration temperature of the TLC. As is done in processing the actual data in Chapters 7,8 and 9, the time for this one roughness element area to reach the TLC calibration temperature is taken as the average time each grid point (each pixel for the actual experiments) reaches the TLC calibration temperature. From this time, an h is backed out using the semi-infinite solid solution with the lumped capacitance correction.

One might expect the h increase to be the same ratio as the ratio A_{RS}/A. However, results shown in Figure 6.26, indicate the ratio h/h_{RS} is less than the area ratio. This is physically appropriate, because the slight temperature gradients in the stainless steel, with hot spots near the corners of the rough element, result in a lower convection temperature potential for those areas. As a result, less energy is transferred to the surface and the

resulting planar h is less than would be the case if the stainless was a constant temperature.

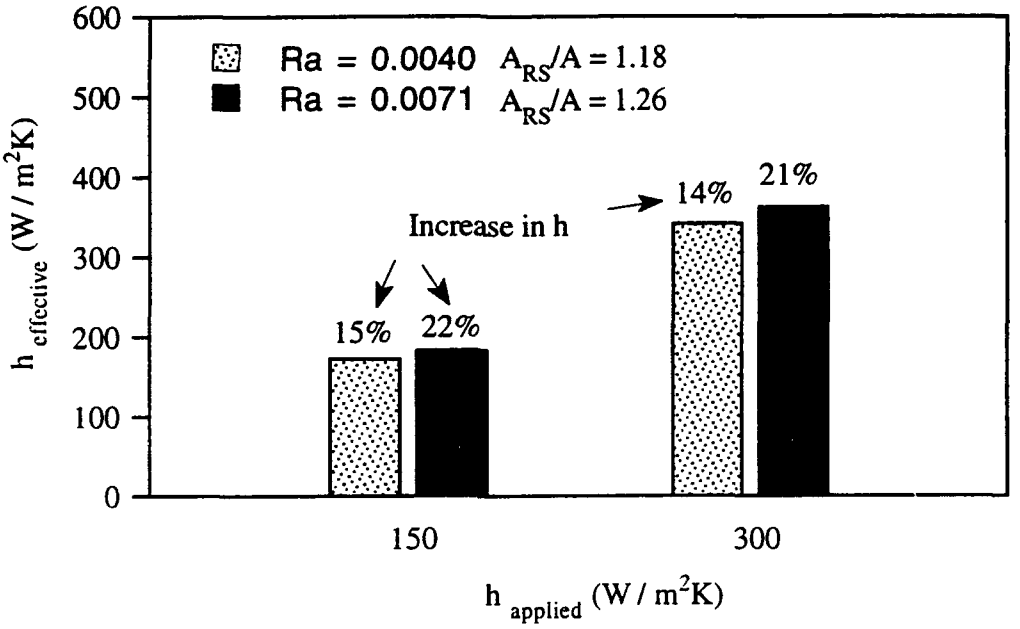

Figure 6.26 Increase in heat-transfer coefficient due to roughness

The roughness element does enhance the heat transfer, as Figure 6.26 indicates. To assess whether the calculated planar h models the enhanced heat transfer correctly, an energy storage calculation is accomplished. The time the interface reaches the TLC calibration temperature field in the composite is used to determine the total energy input since the start of the numerical experiment. For example, with the R =0.0071 surface and an imposed h_{RS}.=150 W/m^{2}K, the total energy into the surface in 19.94 seconds is 160.88 J/m. The h for this experiment is 183.1 W/m^{2}K or 22% greater than h_{RS}. At this point, the planar h of 183.1 W/m^{2}K is imposed on a smooth composite plate with the same mass of stainless steel above the epoxy as for

the rough surface. At 19.94 seconds the numerical experiment on the surface is stopped and again the energy into the surface calculated. The result is 153.7 J/m or 4.4% less than was actually imposed on the surface. This experiment was carried out for two cases of h_{RS} for each roughness. Table 6.1 shows for each case a slight energy deficit occurs.

Table 6.1 Finite Difference, Rough Element Energy Deviation

Ra inches	h_{RS} W/m^{2}K	h W/m^{2}K	A_{RS}/A	h/h_{RS}	% Energy Deviation
0.0040	150	173	1.18	1.15	-2.3
0.0040	300	342	1.18	1.14	-3.1
0.0071	150	183	1.26	1.22	-4.4
0.0071	300	363	1.26	1.21	-5.6

The percent energy deviation provides an indication h may be under determined by this model by 3% for the R =0.0040" surface and about 5% for the R =0.0071" surface. This bias should be kept in mind when the absolute values of h are given in Chapters 7, 8, and 9.

CHAPTER 7

COMPARISON OF COMPOSITE PLATE RESULTS TO PLEXIGLAS MODEL RESULTS

7.1 Introduction

In order to investigate the effects of roughness on convective heat transfer for a film-cooled surface, a composite plate was developed as presented in Chapter 2. In earlier chapters, the transient test method used on Plexiglas models has proven to agree well with previous work using steady-state solution methods by other investigators. In this chapter, the Plexiglas model is used as a baseline from which to assess the validity of the heat-transfer data gathered using the composite plate with a smooth stainless steel surface. Figure 7.1 is a sketch of the composite plate used for this work. The composite plate stainless steel layer is 0.004 inches thick, designed to match the thickness of the layer between the roughness elements of the surfaces investigated in Chapters 8 and 9. Unlike the plate used for testing in Chapter 5, the film holes for this test are inclined 30° to the flow in order to match the inclination angle of the film holes in the pressure side of the F-100 first turbine vane. The Plexiglas model used for comparison has the same dimensions, but, of course, is completely Plexiglas.

As mentioned in Chapter 2, the thermal properties of the epoxy used in building the composite plate are known only approximately. In Section 7.2, a unique method is used to determine the thermal property grouping required

to determine the 1-D semi-infinite solid solution used in the transient model of this work.

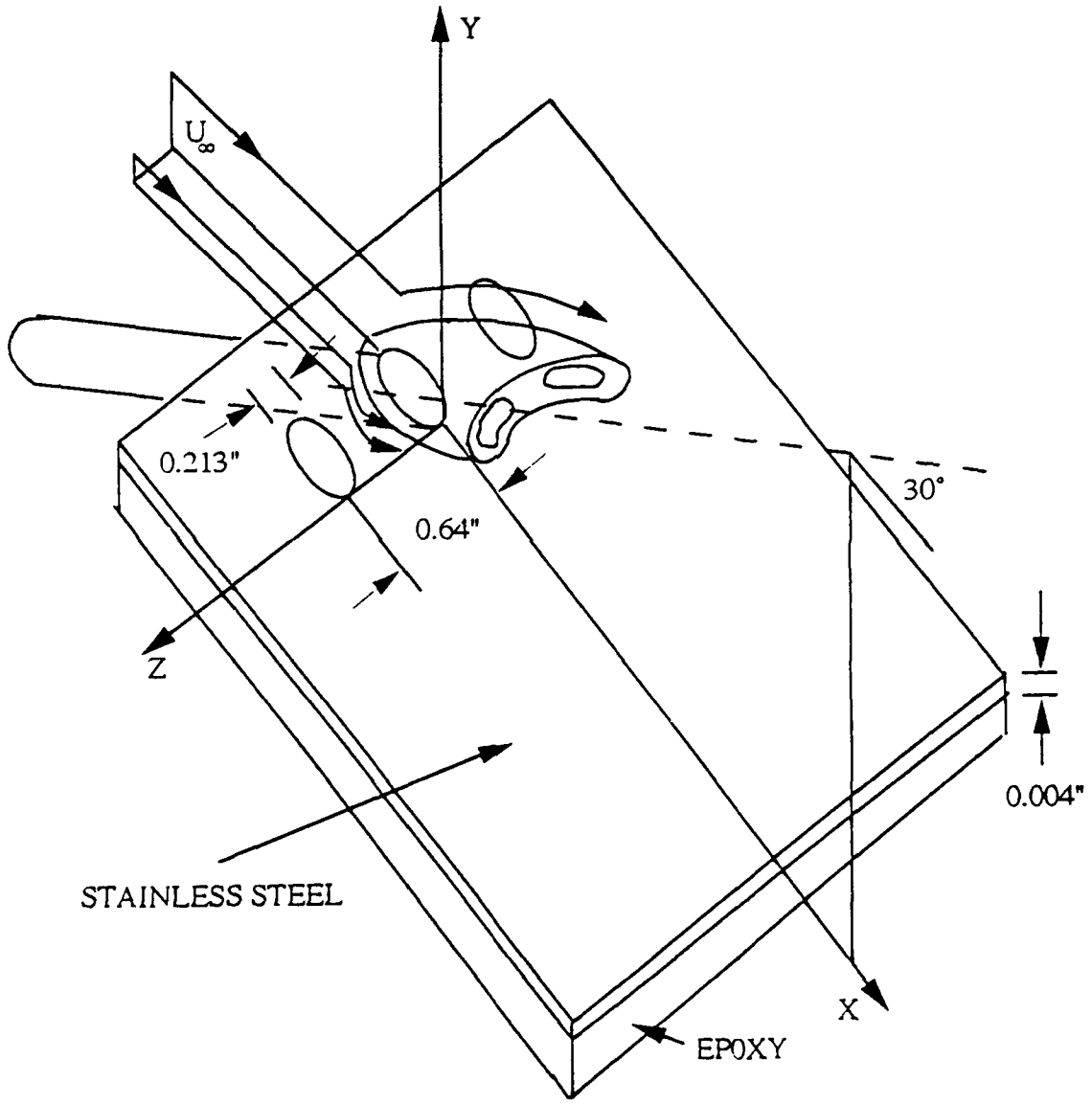

Figure 7.1 Composite region test model

7.2 Material Test

Because the thermal properties of the epoxy used in building the epoxy plate are only approximately known, a test was devised to determine the thermal property grouping necessary to solve the semi-infinite classic solution. This test is without film flow and therefore equation 2.6 becomes

$$\frac{T_w - T_i}{T_\infty - T_i} = 1 - \exp\left[\frac{h^2 \alpha t}{k^2}\right] \operatorname{erfc}\left[\frac{h\sqrt{\alpha t}}{k}\right] \qquad (7.1)$$

Incorporating Duhamel's theorem to account for the non-step nature of the experiment, the applicable equation to be solved is

$$T - T_i = \sum_{i=1}^{N} U(t-\tau_i)\Delta T_\infty \qquad (7.2)$$

where

$$U(t - \tau_i) = 1 - \exp\left(\frac{h^2}{k^2}\alpha(t-\tau_i)\right) \operatorname{erfc}\left(\frac{h}{k}\sqrt{\alpha(t-\tau_i)}\right) \qquad (7.3)$$

The thermal diffusivity and conductivity do not appear separately, but rather in combination in the ratio $\frac{\sqrt{\alpha}}{k}$. It is therefore not necessary to determine the material properties separately, but only in this grouping.

With this fact in mind, the plate in Figure 7.2 is built and tested. The epoxy plug penetrates the entire depth of the test surface.

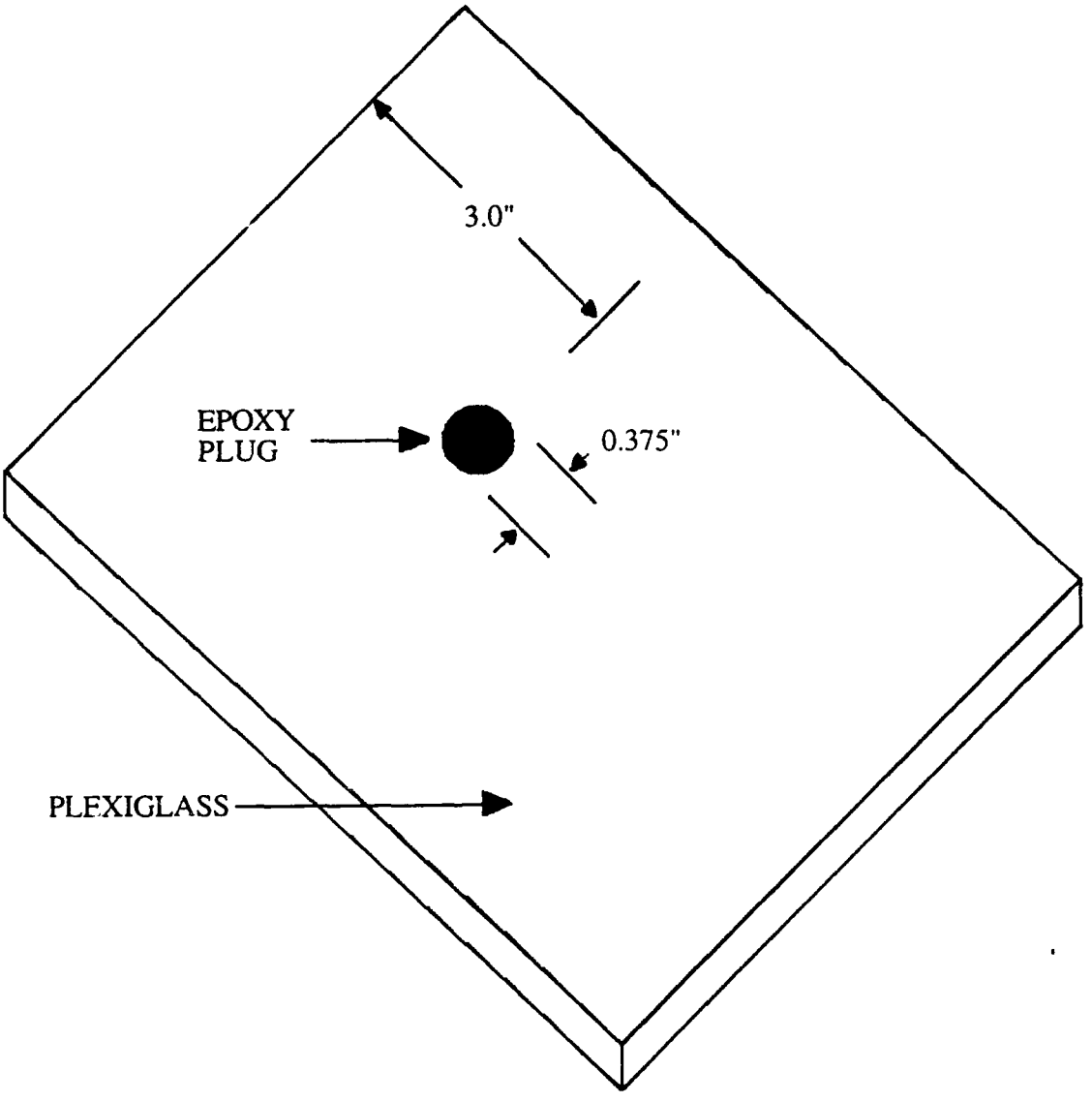

Figure 7.2 Material test model

The results for a free-stream velocity of 50 m/s, assuming the entire plate is Plexiglas, is shown in Figure 7.3. It is immediately apparent, as expected, the thermal properties of the epoxy are close to those of Plexiglas. To determine the thermal grouping $\frac{\sqrt{\alpha}}{k}$ more accurately, the following approach is taken. The average h laterally to each side of the epoxy plug is determined and taken to be the appropriate h at this point downstream of the leading edge. This value is then assigned to the location on the epoxy plug surface which corresponds to this lateral location. Using equations 2.9 and 2.10, an iterative computer code is written to determine the $\frac{\sqrt{\alpha}}{k}$ grouping that gives this h at the time the epoxy plug surface reached the TLC calibration temperature. Although not visible in Figure 7.3, there is a difference between the h in and outside the plug laterally. For the 50 m/s test, the Plexiglas lateral to the epoxy plug has an h of 119.3 w/m^{2}K, while the plug using Plexiglas properties has an h of 117.2 W/m^{2}K. The ratio of $\frac{\sqrt{\alpha}}{k}$ for Plexiglas is $1.7204 \times 10^{-3} (\frac{kg\ m\ K}{J\sqrt{s}})$. In order to achieve the same h at the epoxy plug, $\frac{\sqrt{\alpha}}{k}$ must be taken as $1.752 \times 10^{-3} (\frac{kg\ m\ K}{J\sqrt{s}})$. This is a 1.8% change in the thermal property grouping. The difference in h when Plexiglas properties are assumed for the epoxy plug was 1.7%. This test was accomplished several times at both 50 m/s and 30 m/s free-stream velocities with very repeatable, consistent results.

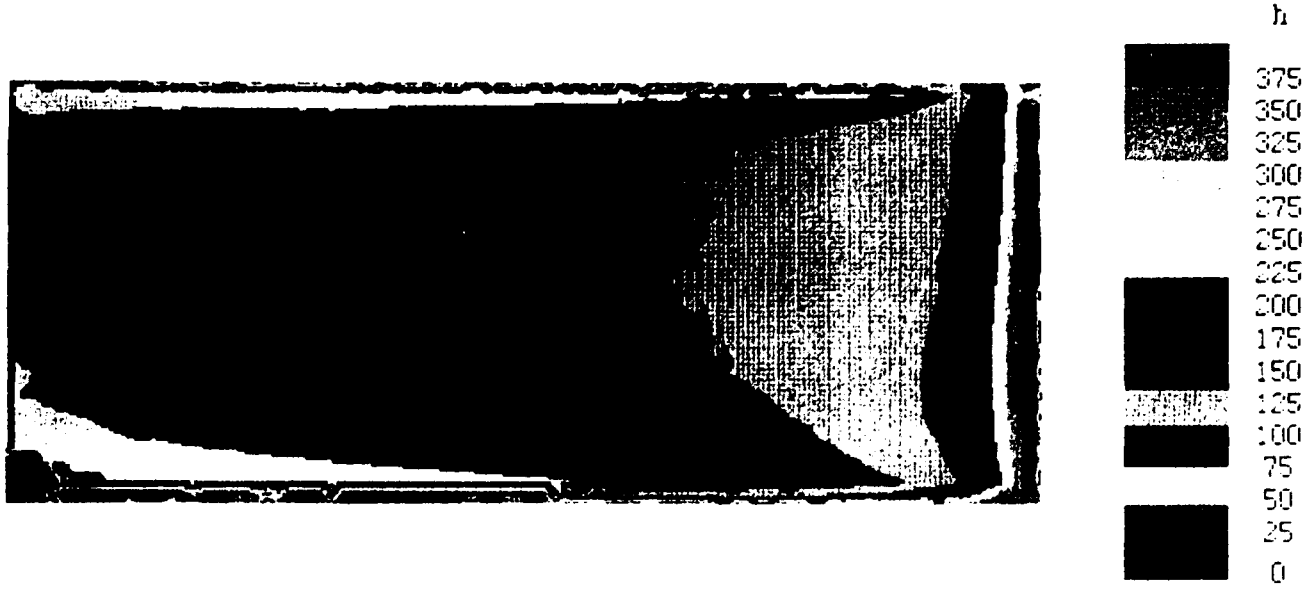

Figure 7.3 Material Test - Local Heat Transfer Coefficients
U_∞ = 50 m/s

7.3 Composite Plate versus Plexiglas

To assess the effects of using the composite region and the time lag correction to the semi-infinite solid, a series of identical tests were accomplished using both a Plexiglas and composite three-hole piece. Tests were run at 50 m/s for blowing ratios of 0.0, 0.5, 0.75, 1.0 and 1.25. As an example, for visual analysis, Figures 7.5 and 7.6 are the convective heat-transfer coefficient maps for M=0.0. Care must be taken in comparing these, since while both end on the left at X/D≈22.0, the maps begin on the right at different locations relative to X/D=0.0. The associated line plot is given in Figure 7.4.

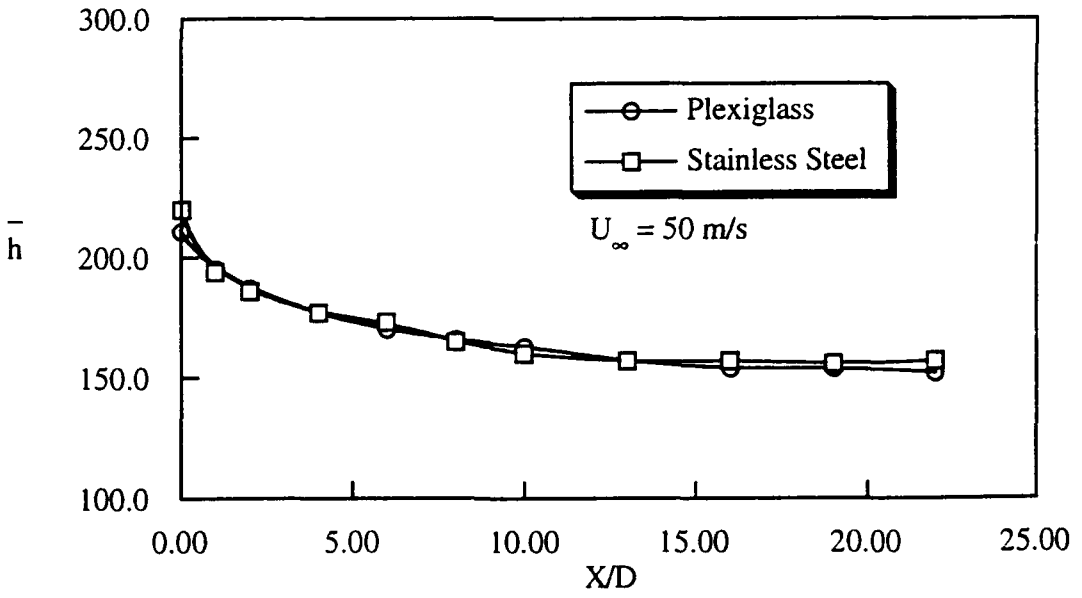

Figure 7.4 h, composite model versus Plexiglas, M=0.0

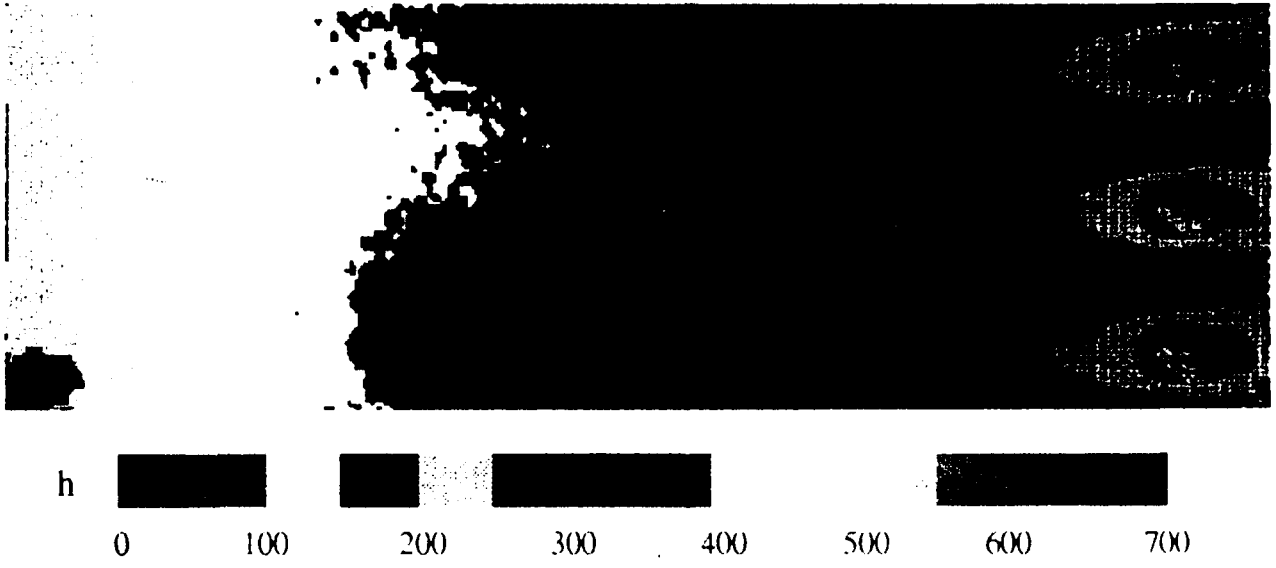

Figure 7.5 Plexiglass, heat transfer coefficient, U_∞=50 m/s, M=0.0

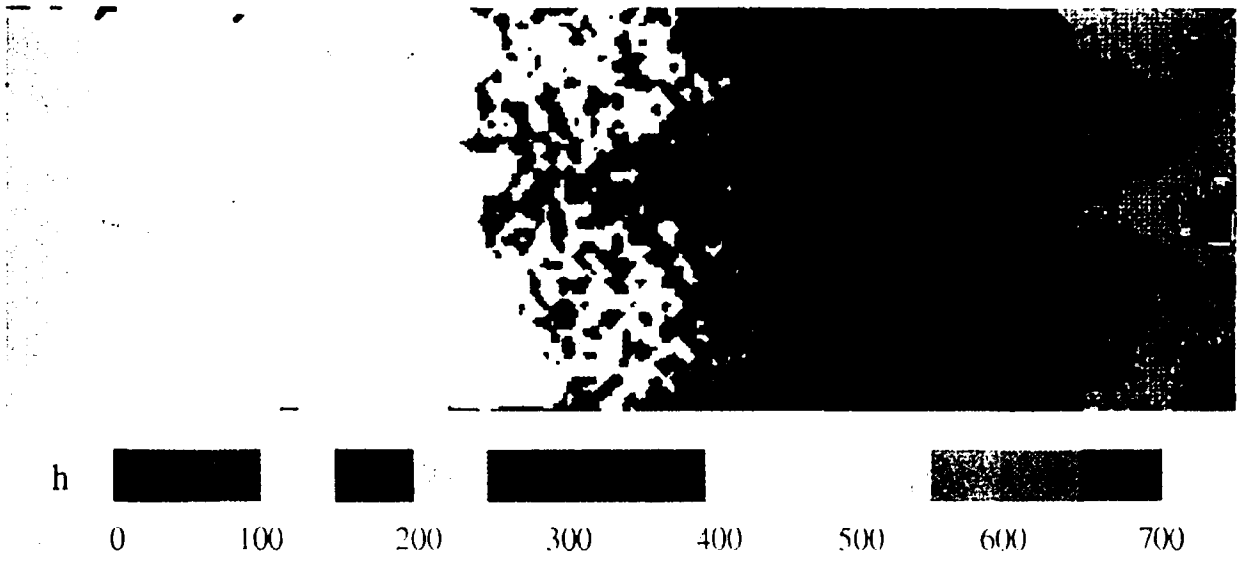

Figure 7.6 Composite, heat transfer coefficient, U_∞=50 m/s, M=0.0

From Figure 7.5 it is clear that, as predicted by the finite difference work in Chapter 5, there is smoothing of the heat transfer coefficient where there are high gradients. In this case, there are gradients near the film holes, even though no film flow is present. Here lateral smoothing is obvious in Figure 7.4 between the film holes. Downstream of the holes, the comparison of laterally averaged h is excellent (Figure 7.4). As the finite difference work in Chapter 6 predicted, the model works extremely well for the two temperature flow situation.

For visual comparison of the three-temperature case, Figures 7.7 and 7.8 show the h and η maps for M=0.75 from the Plexiglas model and Figures 7.9 and 7.10 show the maps for the composite model. The comparison is as expected. There is a smoothing of the heat transfer coefficients for both h and η. On centerline both h and η are lower for the composite surface. Between the cooling holes, for the Z/D=1.5 case, the values are higher. Line plots are produced for each blowing ratio to quantify this bias. Figures 7.11 through 7.26 show centerline and mid-hole streamwise variation of h and η along with streamwise variation of laterally averaged values, $\bar{h}$ and $\bar{\eta}$. In these figures, $\bar{h}$ and $\bar{\eta}$ are defined as

$$\bar{h}(X/D) = \frac{1}{3}\int_{-1.5}^{1.5} h(X/D,Z/D)\, d(Z/D)$$

$$\bar{\eta}(X/D) = \frac{1}{3}\int_{-1.5}^{1.5} \eta(X/D,Z/D)\, d(Z/D)$$

based on the center film hole.

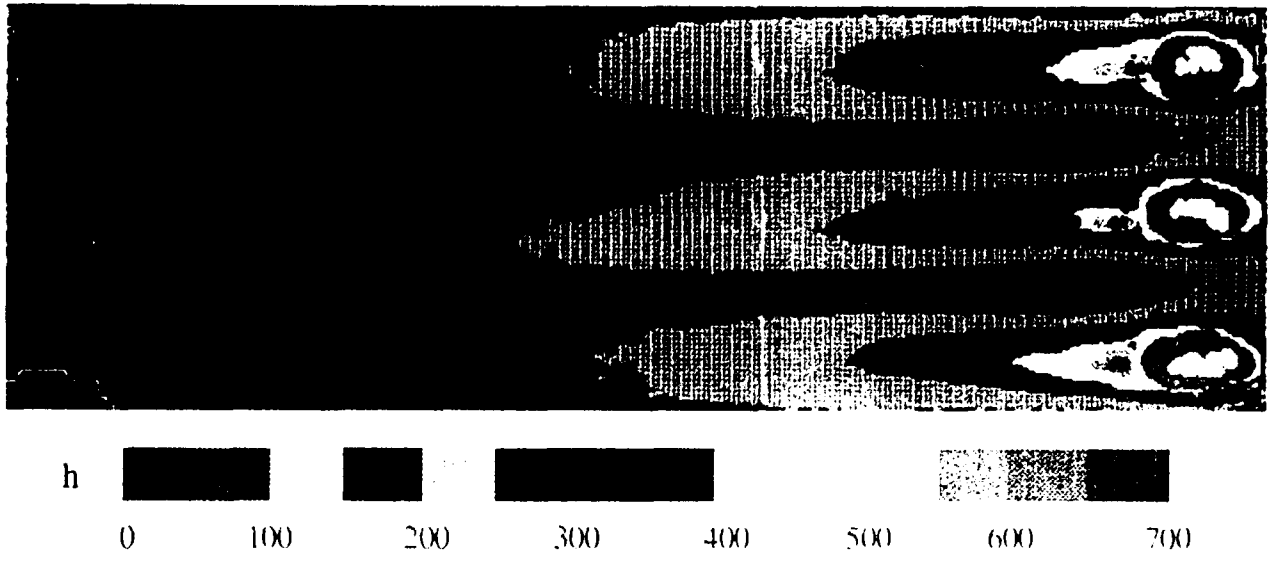

Figure 7.7 Plexiglass, heat transfer coefficient, U_{∞}=50 m/s, M=0.75

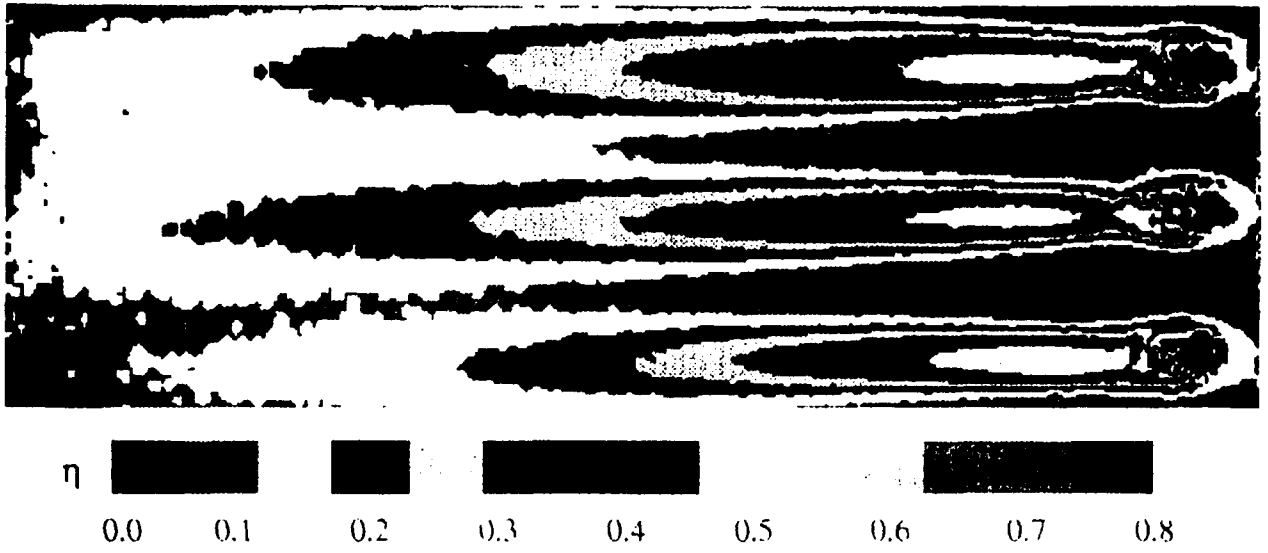

Figure 7.8 Plexiglass, film cooling effectiveness, U_∞=50 m/s, M=0.75

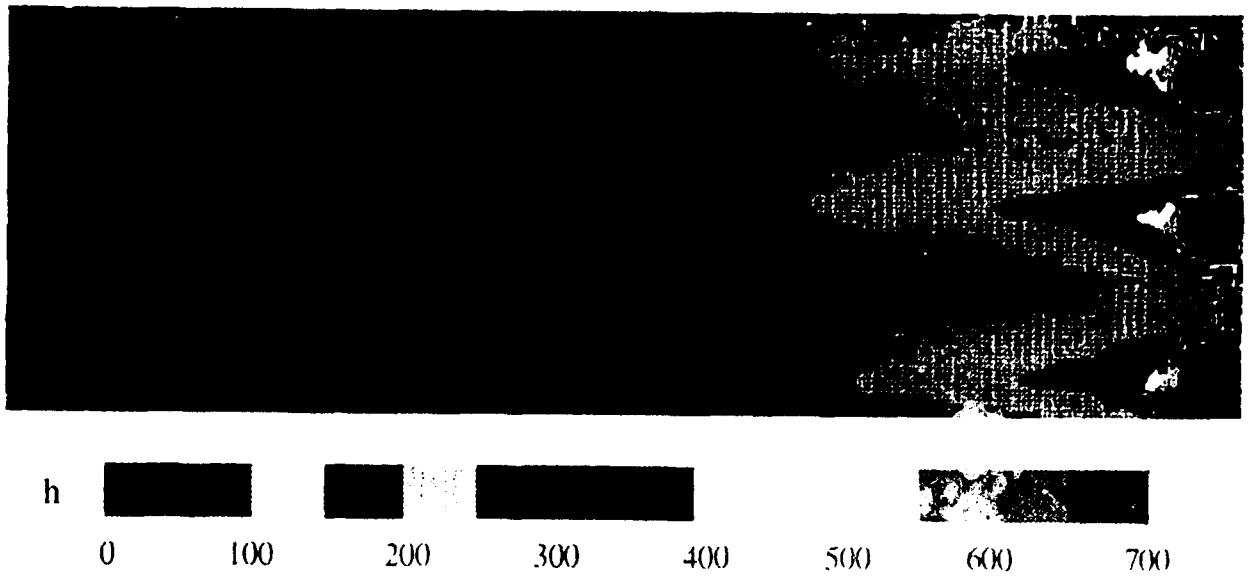

Figure 7.9 Composite, heat transfer coefficient, U_∞=50 m/s, M=0.75

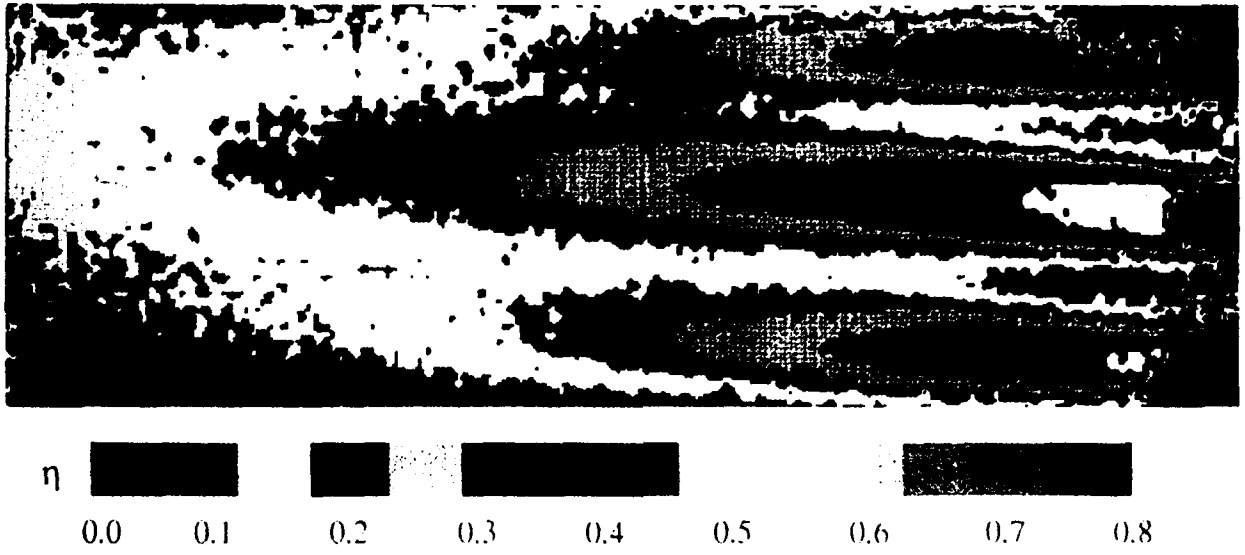

Figure 7.10 Composite, film cooling effectiveness, U_∞=50 m/s, M=0.75

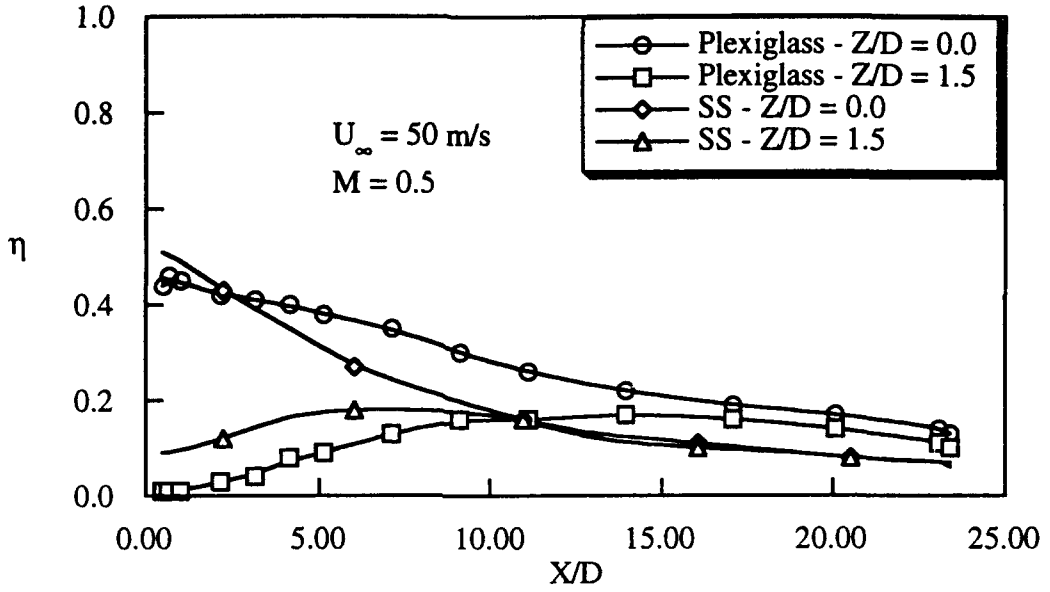

Figure 7.11 η, Composite model versus Plexiglas, M=0.5

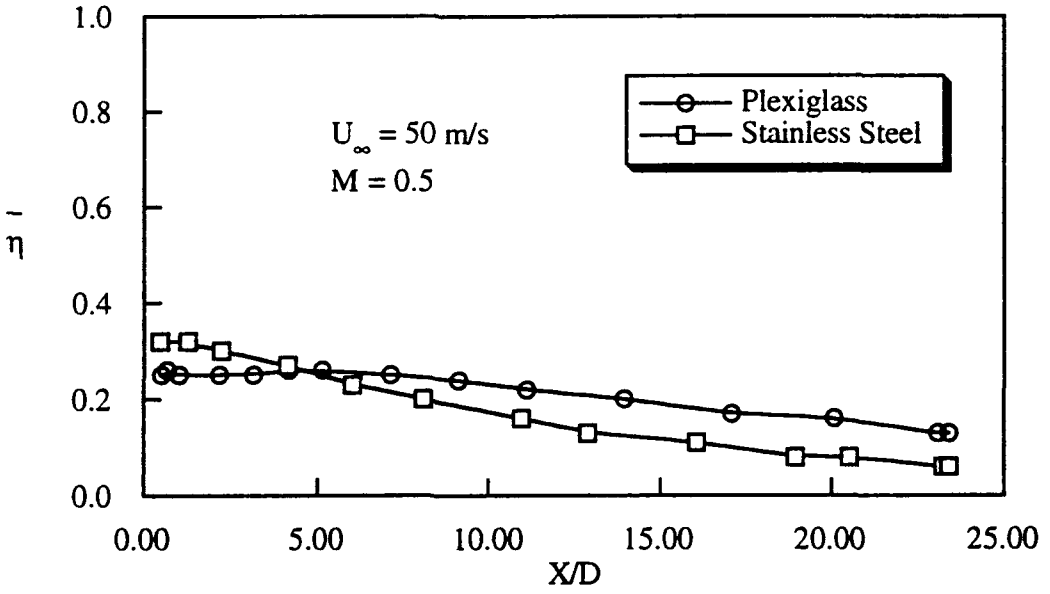

Figure 7.12 $\bar{\eta}$, Composite model versus Plexiglas, M=0.5

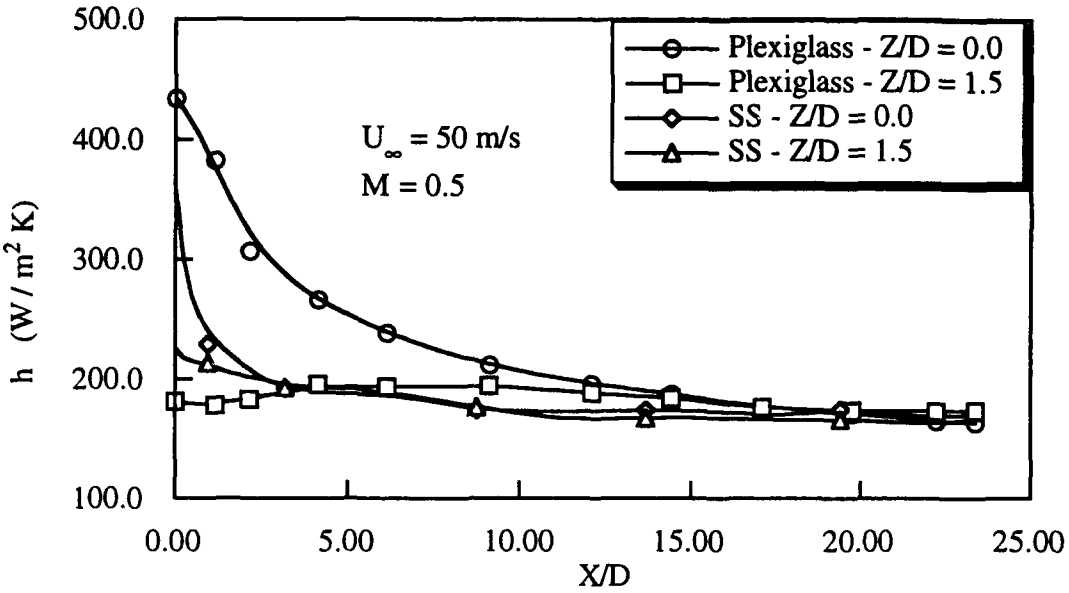

Figure 7.13 h, Composite model versus Plexiglas, M=0.5

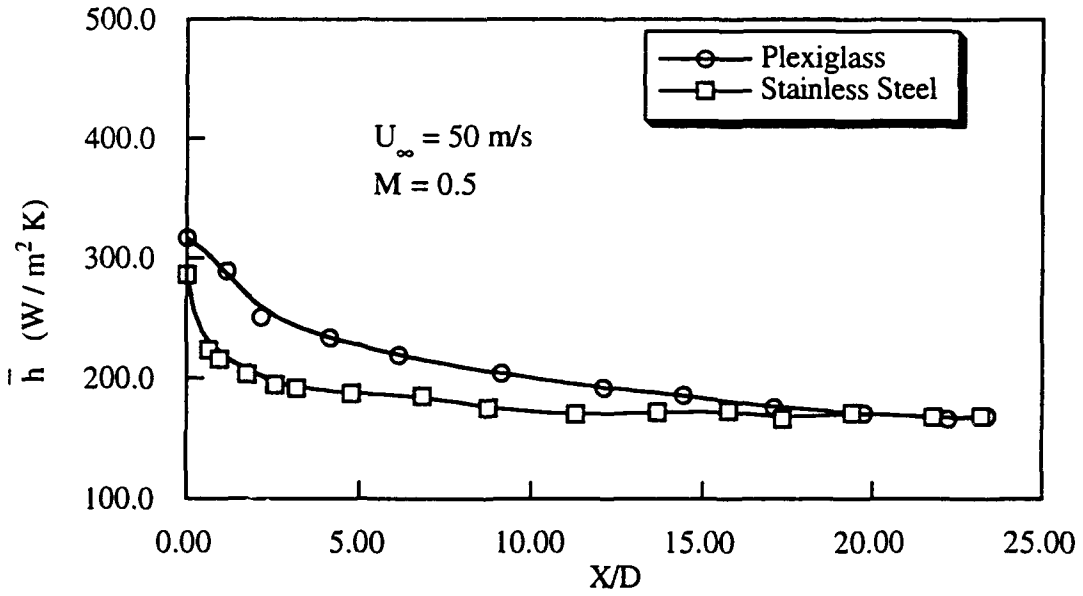

Figure 7.14 $\bar{h}$, Composite model versus Plexiglas, M=0.5

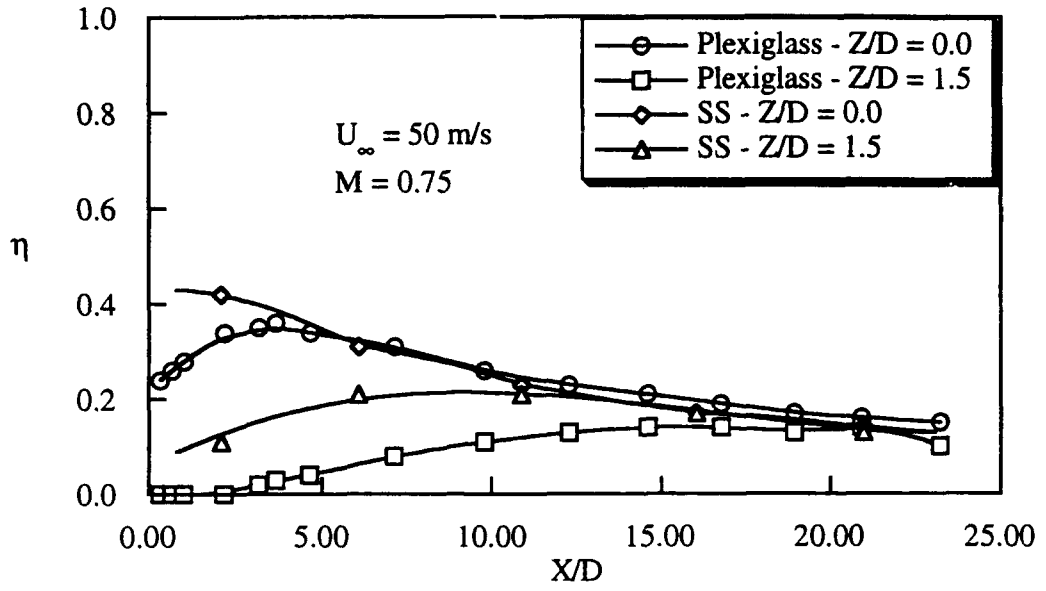

Figure 7.15 η, Composite model versus Plexiglas, M=0.75

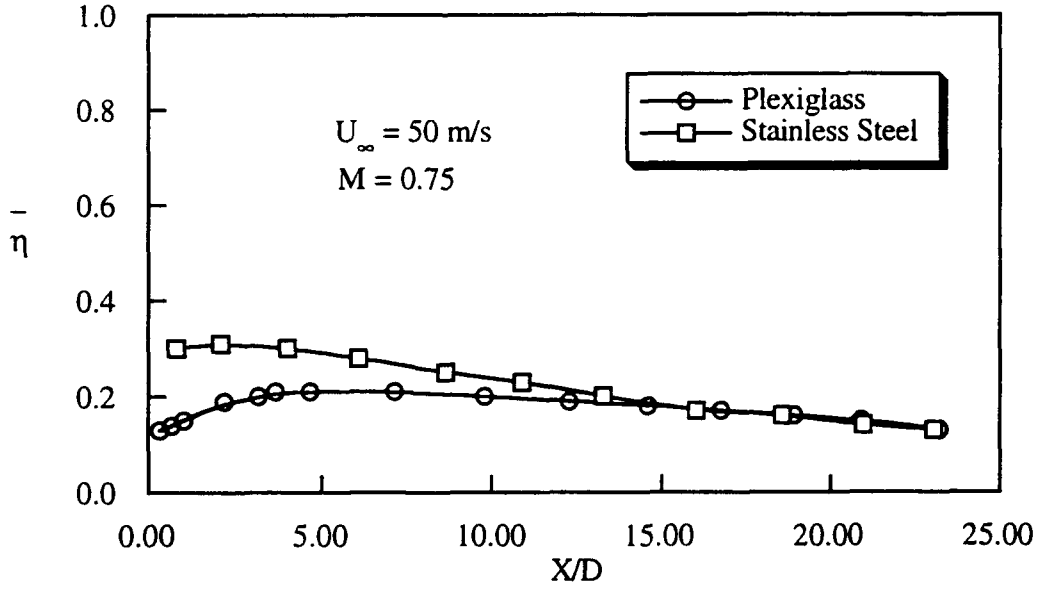

Figure 7.16 $\bar{\eta}$, Composite model versus Plexiglas, M=0.75

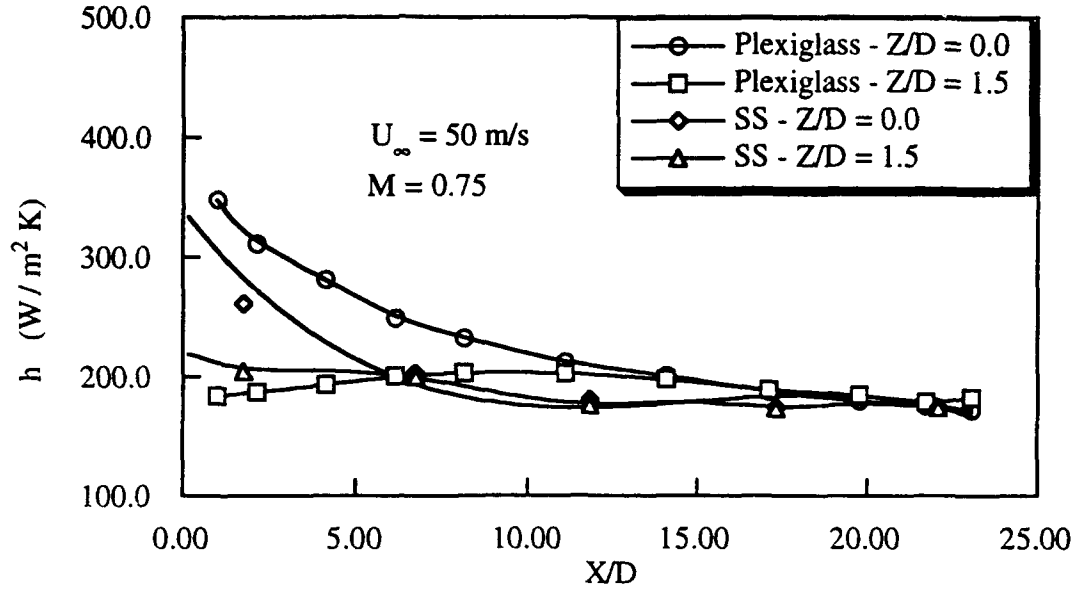

Figure 7.17 h, Composite model versus Plexiglas, M=0.75

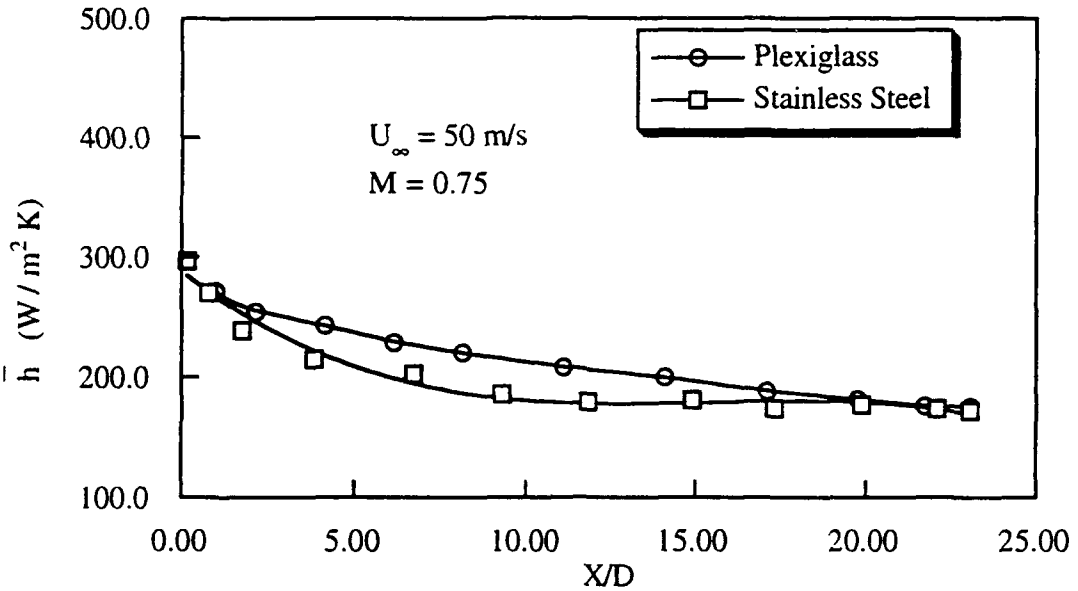

Figure 7.18 $\bar{h}$, Composite model versus Plexiglas, M=0.75

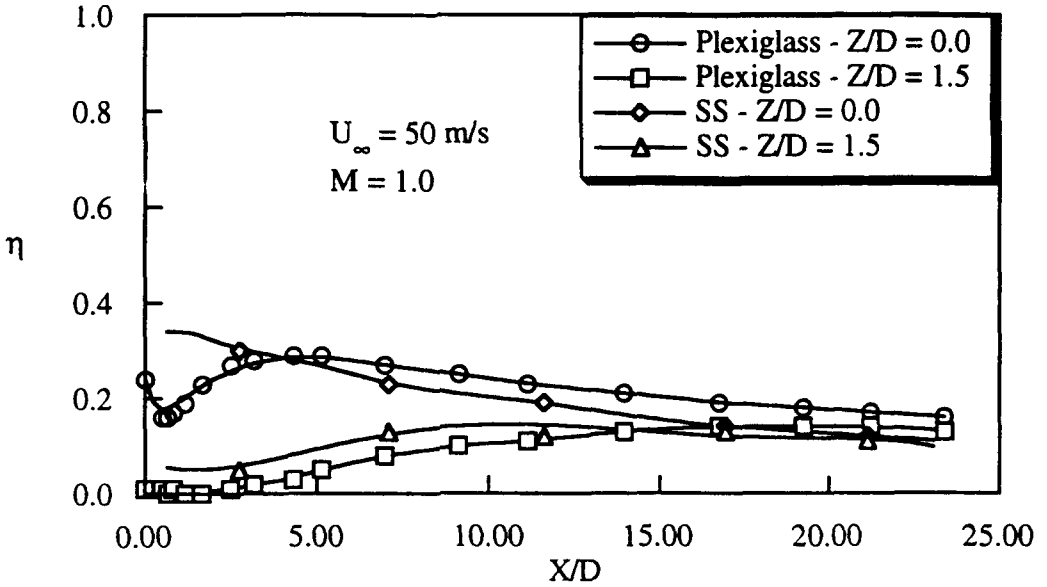

Figure 7.19 η, Composite model versus Plexiglas, M=1.0

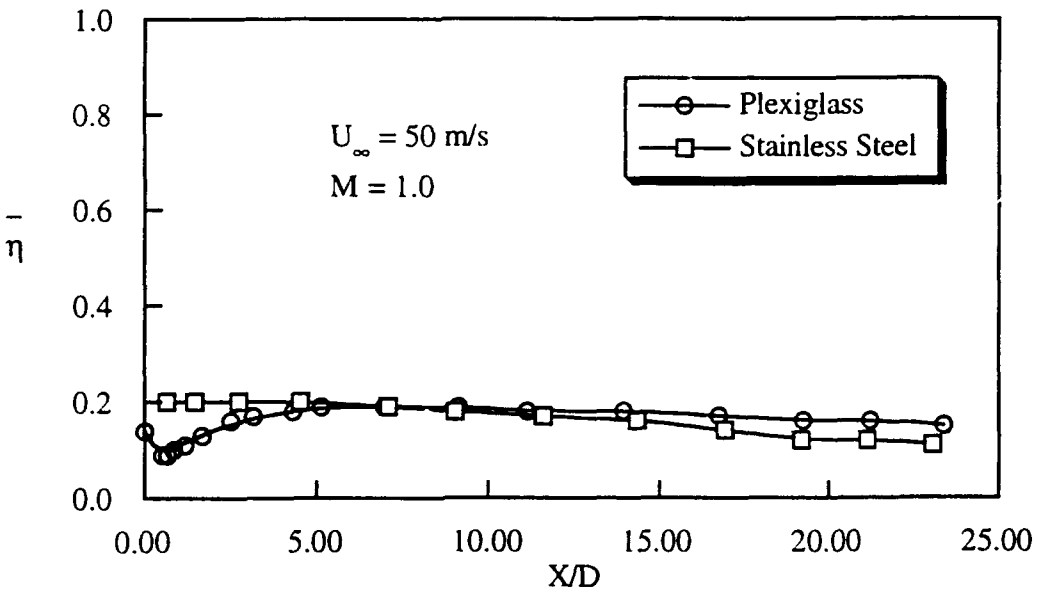

Figure 7.20 $\bar{\eta}$, Composite model versus Plexiglas, M=1.0

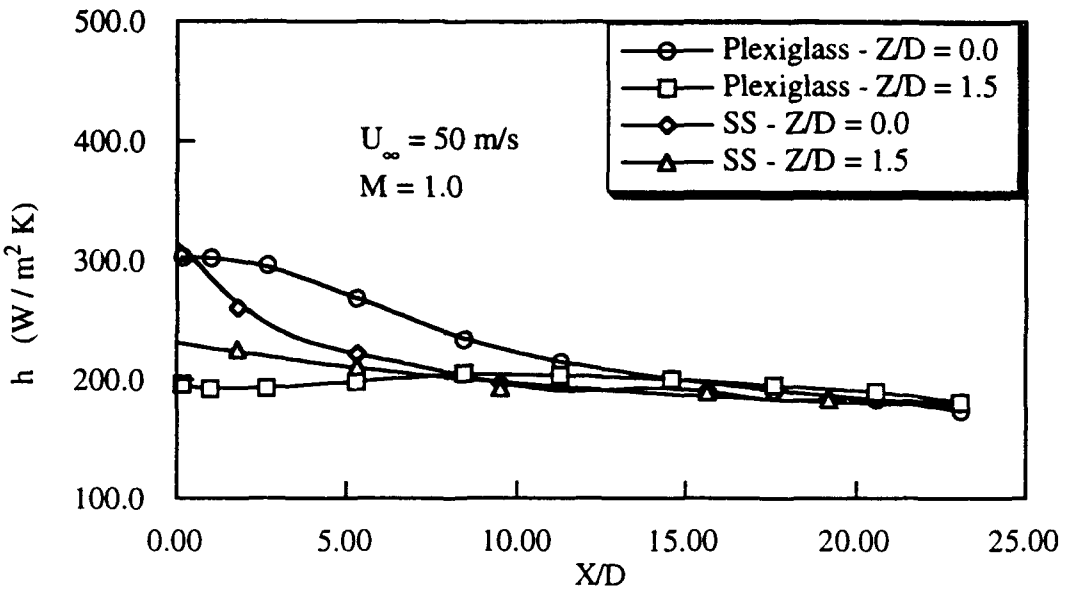

Figure 7.21 h, Composite model versus Plexiglas, M=1.0

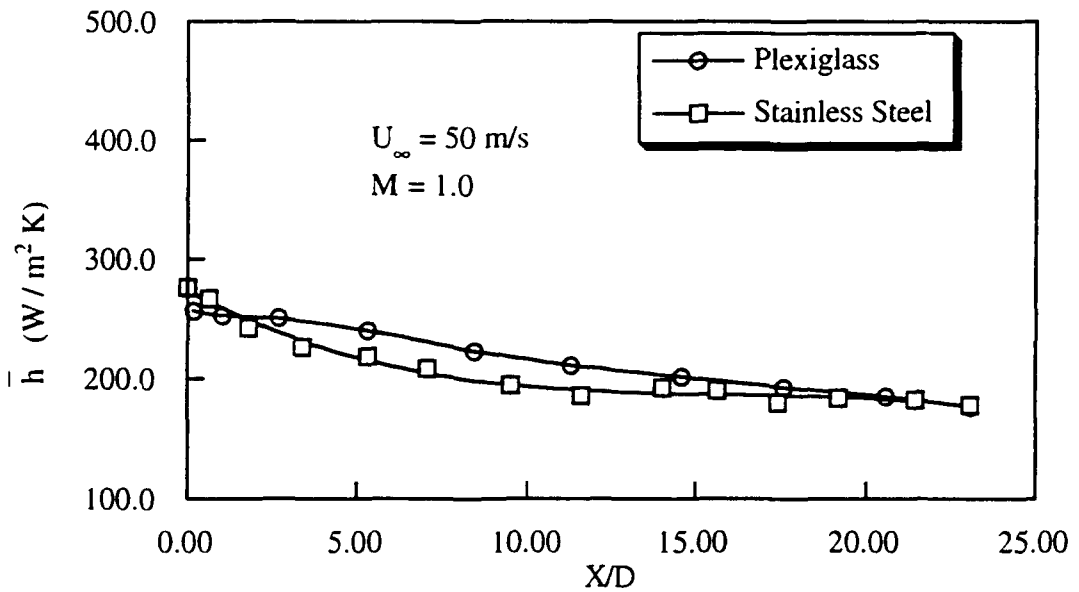

Figure 7.22 $\bar{h}$, Composite model versus Plexiglas, M=1.0

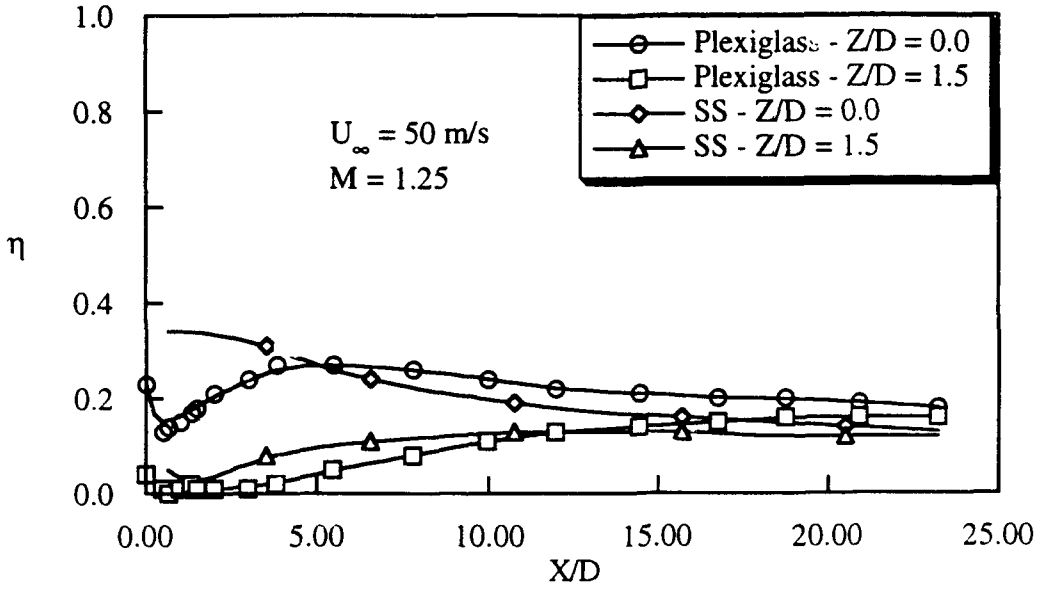

Figure 7.23 η, Composite model versus Plexiglas, M=1.25

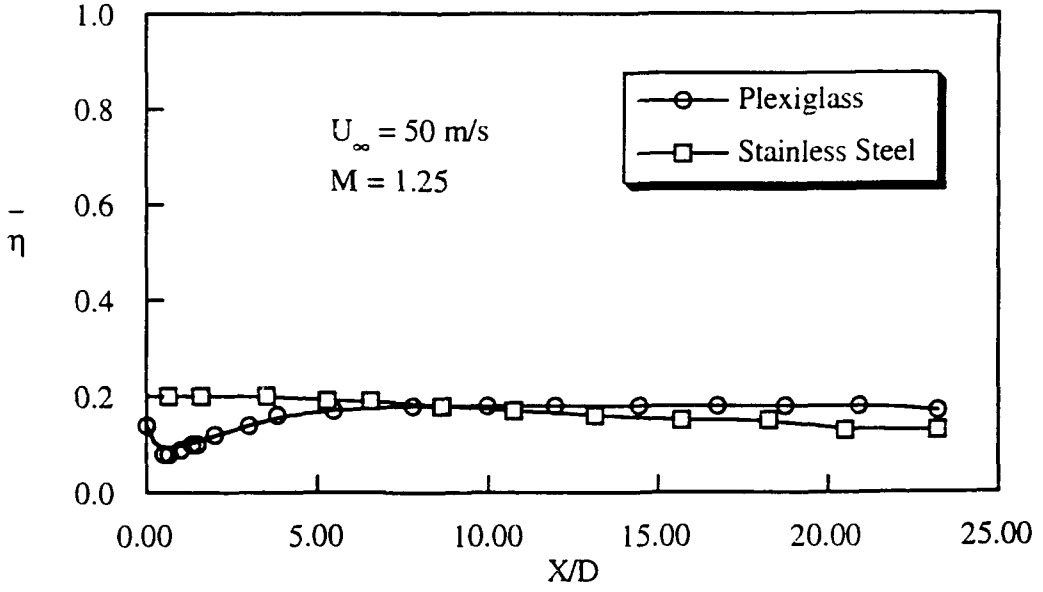

Figure 7.24 $\bar{\eta}$, Composite model versus Plexiglas, M=1.25

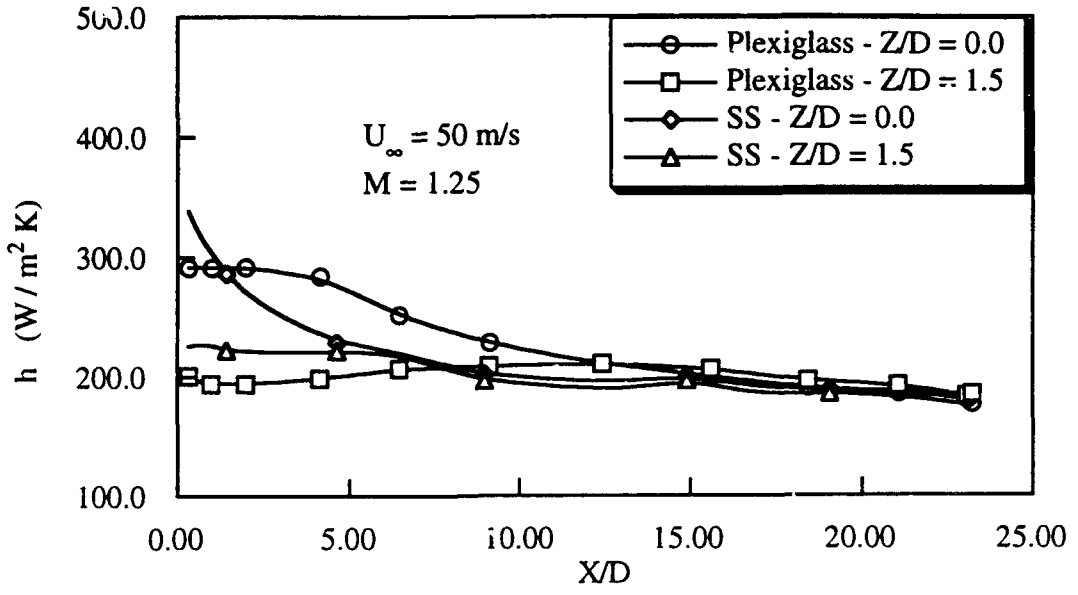

Figure 7.25 h, Composite model versus Plexiglas, M=1.25

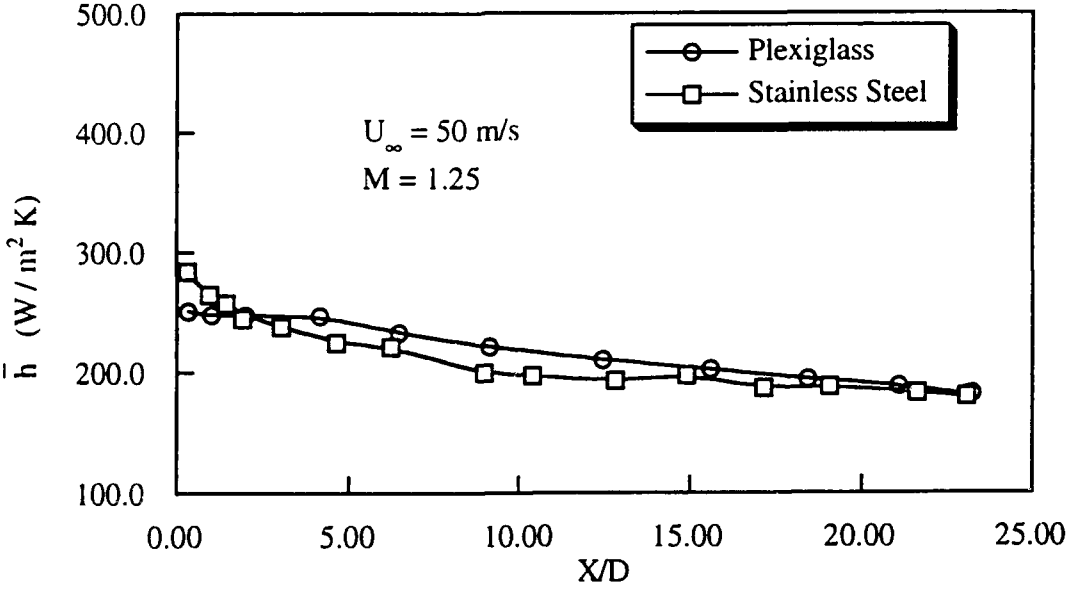

Figure 7.26 $\bar{h}$, Composite model versus Plexiglas, M=1.25

The trends from these plots can be summarized as follows. The further downstream h and η are compared for a given Z/D, the better the match; the greater the blowing ratio, the better the comparison. In all cases, the comparison downstream of X/D=10.00 is excellent. Upstream of X/D=5.00 the comparisons for non-laterally averaged values are suspect. For blowing ratios of 1.00 and 1.25 comparison of all data is excellent beyond X/D=5.00. The low values that result from blowoff, just downstream of the film injection, are smoothed out by the composite plate and as a result the phenomenon is not discernible. These trends are a result of lateral conduction and are corroborated by the finite difference work in Chapter 6.

7.4 Conclusions

Based on the comparison made of h and η between data taken with the composite region and those taken with an all Plexiglas model, several conclusions for the work in the next two chapters can be made. First, thermal gradients are not severe enough for two temperature cases (M=0.0) to cause lateral conduction to be a problem for the composite plate model. Heat-transfer coefficient for this case should be considered reliable. The comparisons in Chapter 8 of noncooled surfaces should be relatively free of lateral conduction errors. For the film-cooling cases, thermal gradients within the stainless steel composite region are severe enough within five hole diameters to limit the usefulness of the local coefficients. This is unfortunate, but not disastrous, since film cooling must be designed to meet the cooling need for X/D>5.00; the region below five hole diameters is more than adequately cooled.

Downstream of X/D=5.00 the centerline ηs compare well , although a negative bias on the order of 0.03 to 0.04 is present for the composite plate model. When comparing centerline data in Chapter 9, this fact should be kept in mind. Values of $\bar{h}$ and $\bar{\eta}$ downstream of X/D=5.00 compare fairly well, but like η centerline the negative bias for $\bar{\eta}$ appears to be on the order of 0.02 to 0.03. $\bar{h}$ values for X/D greater than 5.00 compare fairly well, although again as much as a 10% negative bias may be present for values taken from the composite plate between X/D=5.00 and X/D=15.00. For downstream locations greater than fifteen hole diameters, values of centerline η, $\bar{h}$ and $\bar{\eta}$ should be considered valid within the uncertainty of the experimental method.

CHAPTER 8
EFFECT OF ROUGHNESS ON CONVECTIVE HEAT TRANSFER COEFFICIENT IN THE ABSENCE OF FILM COOLING

8.1 Introduction

In this chapter, heat transfer coefficients are determined for two composite plates with stainless steel rough surfaces as described in Chapter 2. Tests are conducted at 30 m/s and 50 m/s. Results are compared against the correlation presented by Pimenta et al. (1975). For an aerodynamically smooth surface, Reynolds analogy can be used to relate the convective heat transfer process to the shear stress at the wall. For a smooth surface, the primary mechanism for exchanging both momentum and energy in the turbulent boundary layer is through turbulent exchange. This leads to the equality of the momentum and energy diffusivities within the turbulent boundary layer (Reynolds analogy). For a rough surface, however, Reynolds analogy no longer applies. On a rough surface an apparent sheer stress is transmitted to the surface as the result of dynamic or pressure forces on the area normal to the flow direction, but there is no similar mechanism for heat transfer. The energy can be transferred by turbulent exchange down to the plane of the roughened elements, but the final energy transfer must be through the mechanisms of molecular conduction. The difference in primary mechanism requires a different mixing length model than that used for aerodynamically smooth law of the wall developments. The development of a mixing length model for use with a thermal law of the wall for a rough surface is given by Kays and Crawford (1980). The correlation used below

for comparison with the experimental results presented in this chapter, is a result of this thermal law of the wall development and the experiments of Pimenta et al. (1975).

For the work reported in this chapter, the rough surface composite plates are constructed without film holes and tested under two temperature test conditions. As described in Chapter 2, these surfaces are referred to in terms of their average roughness values, Ra=0.0040" and Ra=0.0071". The technique, described in Chapter 2, with a lumped capacitance correction is employed. In this case, the temperature potential is based on the difference between the free stream temperature and the wall temperature. The results of the composite plate rough surface tests are given in Section 8.2.

As indicated in Chapter 1, the majority of studies of uniformly rough surfaces have been conducted for fully developed pipe and channel flows. In these cases, the determination of the skin friction coefficient is very straight forward and is directly related to the static pressure drop in the pipe. For flat surfaces in an external flow environment, the studies are much fewer. In fact, the only available empirical correlation relating flow conditions and surface roughness to surface heat transfer characteristics for flat plate 'external' flow is one given by Kays and Crawford (1980).

$$St = \frac{h}{\rho U_\infty c_p} = \frac{\frac{c_f}{2}}{Pr_t + \sqrt{\frac{c_f/2}{St_k}}} \qquad (8.1)$$

In this correlation for Stanton number (St), Pr_t is turbulent Prandtl number and has been shown to be approximately constant for air with a value of 0.9 (Pimenta et al., 1975). c_f is the coefficient of friction and St_k is the

roughness Stanton number. Using a thermal law of the wall development and the experimental investigation of Dipprey and Sabersky (1962) Pimenta et al. (1975) have developed the following correlation for St_k.

$$St_k = \frac{h}{\mu_\tau \, cp \, \rho} = C \, Re_k^{-0.2} \, Pr^{-0.44} \tag{8.2}$$

where μ_τ is shear velocity

$$\frac{\tau_o}{\rho} = \frac{c_f \, u_\infty^2}{2} = u_\tau^2 \tag{8.3}$$

and Re_k is roughness Reynolds number

$$Re_k = \frac{u_\tau k_s}{\nu} \tag{8.4}$$

C in equation 8.2 is an empirical constant and is a function of the rough surface geometry. For closely packed spheres, Pimento et al. (1975) found a value for C of 1.0. k_s is equivalent sand roughness as described in Chapter 1. In order to use this correlation for comparison to the experimental data, reported in Section 8.2, the shear velocity must be known at the downstream point where the comparison is made. In addition, the equivalent sand roughness must be determined.

To be able to assign appropriate qualities to these parameters, a boundary layer study, like the one conducted in Chapter 4 on a smooth surface, is conducted. The methodology is the same as in Chapter 4. The boundary layer thickness, momentum thickness and displacement thickness

are reported in Section 8.3. In these cases, the thickness is given as a height above the average surface height ($\bar{H}$) as defined in Figure 2.7.

With the boundary layer thickness determined at four downstream locations for each rough surface at 30 m/s and 50 m/s, it is possible to determine the shear stress at the wall and thus, determine the shear velocity or friction coefficient at those locations.

To determine shear stress, the appropriate form of the momentum integral equation for a flat plate is used. This along with the definitions of momentum and displacement thickness, given in Chapter 4, result in the following ordinary differential equation for a flat surface with constant density and no suction or blowing on the surface.

$$\frac{\tau_0}{\rho U_\infty^2} = \frac{d\delta_2}{dX} + \delta_2 \left| (2 + \frac{\delta_1}{\delta_2}) \frac{1}{U_\infty} \frac{dU_\infty}{dX} \right| \qquad (8.5)$$

The complete development of this ordinary differential equation is available in Kays and Crawford (1980). The second term on the right hand side takes into account the pressure gradient present in the investigated flows. This term is, in general, more than one order of magnitude smaller than the first term, but is included for completeness. From equation 8.5 and 8.3, c_f is determined at four downstream locations for each test. At this point, k_s remains to be determined.

Again, using a law of the wall logarithmic curve-fit and the available experimental data, Pimenta et al. (1975) presents the following empirical relationship for a rough surface in the fully rough region where no pressure gradient and no transpiration are present.

$$\frac{c_f}{2} = \frac{0.168}{\left[\ln\left(\frac{84\delta}{k_s}\right)\right]^2} \qquad (8.6)$$

It is clearly realized that the law of the wall curve fit will change and thus, the correlation 8.6 if, as in the case of this study, a pressure gradient is present. However, as with the analysis of c_f using the momentum integral equation, the effect is expected to be small for the mild acceleration present in this study. This should provide a k_s of the right order and permit a general comparison between equation 8.1 and the experimental results of this work. The alternative is a much broader, more detailed study of the surface boundary layer. As presented in Section 8.5, large changes in k_s affect the Stanton number , obtained by use of equation 8.1, only slightly. For the surfaces involved in this study, equation 8.1 is primarily a function of c_f, obtained from a momentum integral equation which does consider the mild acceleration of the flow.

With k_s and c_f determined, equation 8.1 is used to determine Stanton number or, alternatively, the convective heat transfer coefficient at four downstream locations for each test condition. These results compare amazingly well with the experimental results presented in Section 8.2 and are presented in Section 8.4.

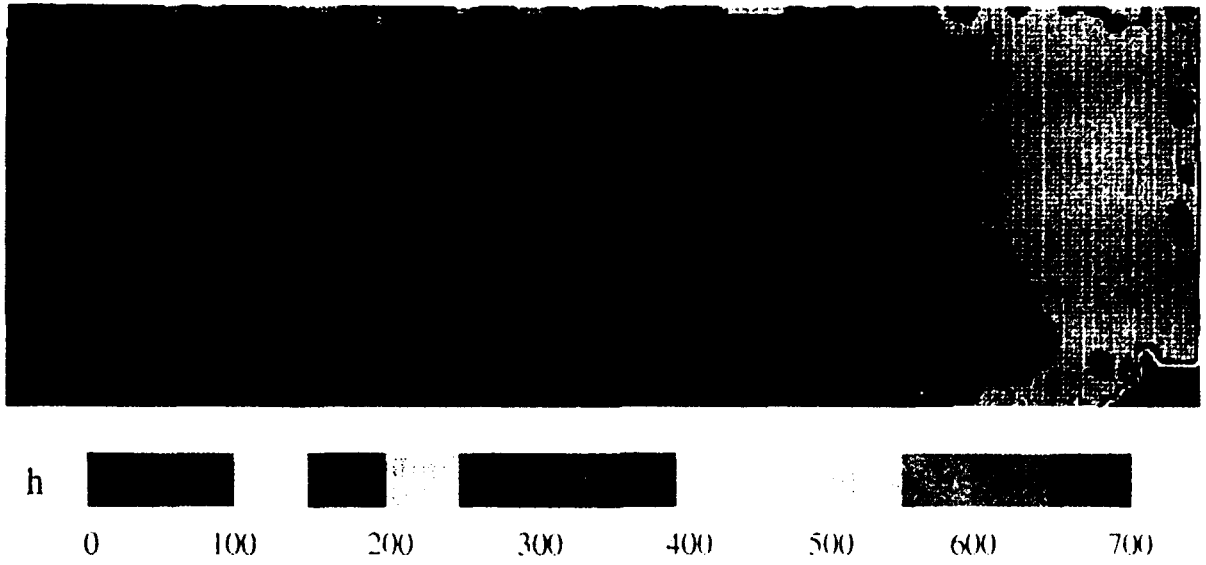

Figure 8.1 Convective heat transfer coefficient,
U_∞=30m/s, Ra=0.0040"

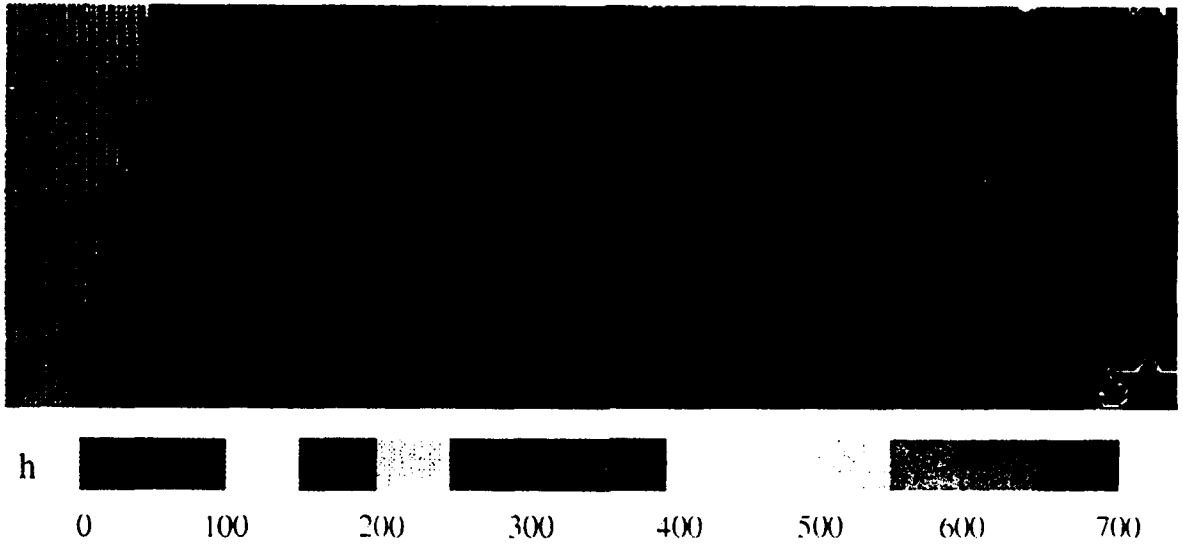

Figure 8.2 Convective heat transfer coefficient,
U_∞=50m/s, Ra=0.0040"

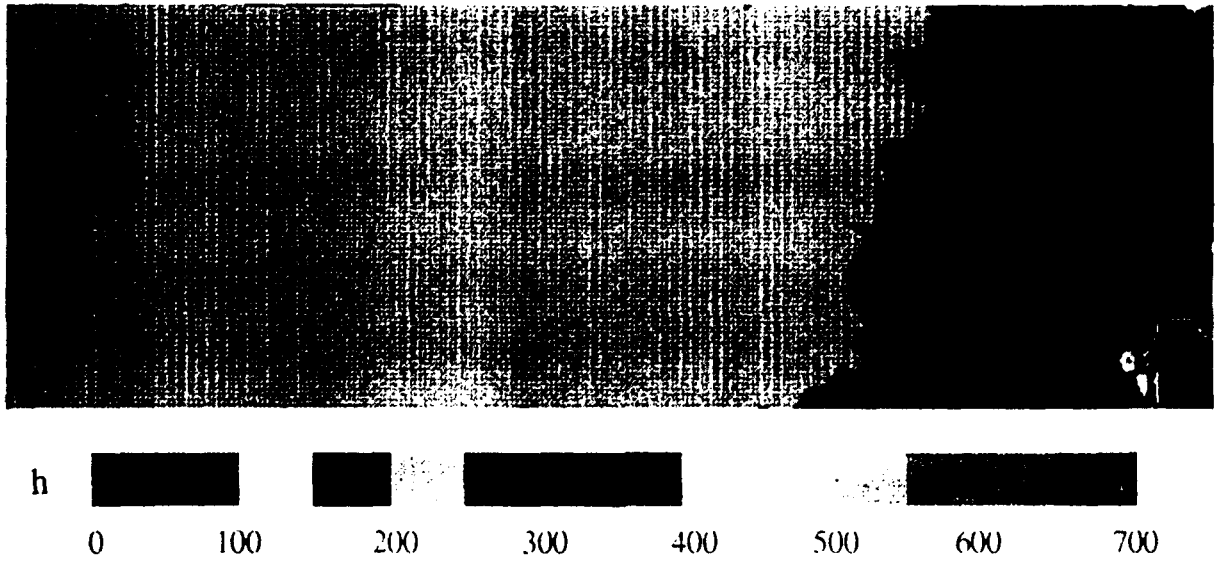

Figure 8.3 Convective heat transfer coefficient,
U_∞=30m/s, Ra=0.0071"

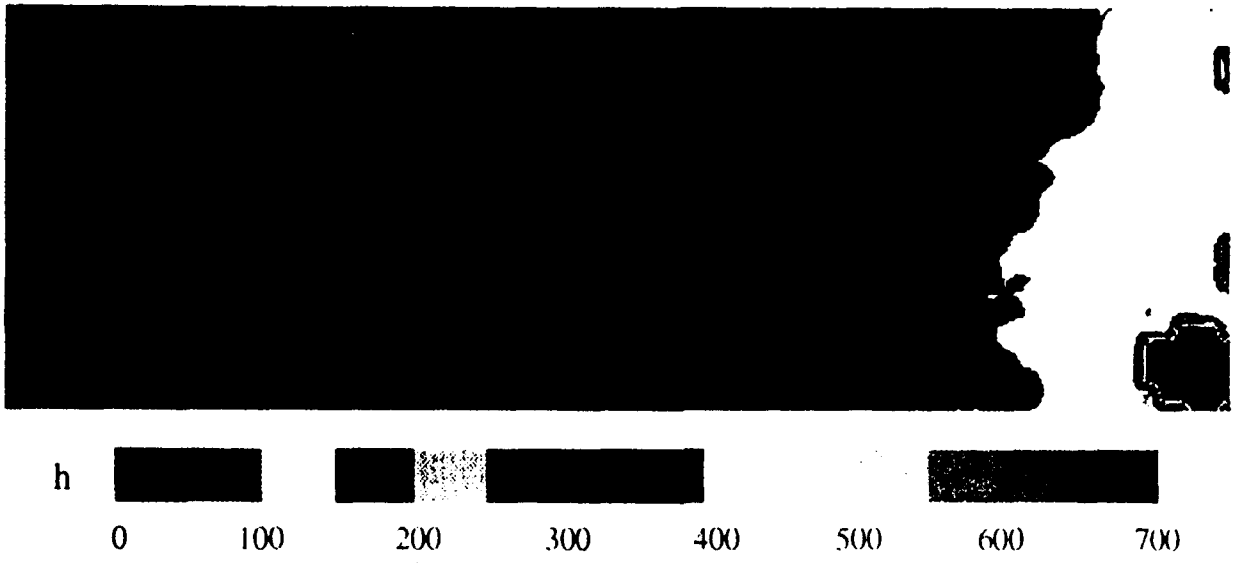

Figure 8.4 Convective heat transfer coefficient, U_∞=50m/s, Ra=0.0071"

8.2 Heat Transfer Coefficients

Tests are conducted for each rough surface, Ra=0.0040" and Ra=0.0071" at free stream velocities of 30 m/s and 50 m/s. The resulting convective heat transfer maps are given in Figures 8.1 through 8.4. In order to provide a more meaningful measure of the heat transfer into the wall in a given area, the coefficients presented are averaged over a roughened elements base area. The 3" by 8" rough surface of each composite plate has 1650 elements arranged in rows of 25 elements. This equates to 0.015 square inches of base area per element. The video frame grabber system is set up to average 16 pixels in a square pattern to arrive at the time each base area reaches the TLC calibration temperature. The finite difference work in Chapter 6 indicates this method provides an h based on the planar area of the surface, which accounts for the energy into the surface correctly to within 3% for the Ra=0.0040" plate and to within 5% for the Ra=0.0071" plate. As discussed in Chapter 6, planar h is more useful to design work than one based on the wetted roughness area, which may or may not be known. The corresponding line plots for each velocity are given in Figures 8.5 and 8.6. The smooth surface values are taken from the tests presented in Chapter 2. h values are obtained by laterally averaging the heat transfer coefficients at a given downstream location over the center half of the test surface. Figures 8.7 and 8.8 provide the rough surface convective heat transfer coefficients normalized by the smooth surface coefficients.

It is clear a tremendous penalty is paid in terms of heat transfer to the surface for the increased roughness. For the Ra=0.0040" surface the A_{RS}/A is 1.18 (Chapter 2) and the increase at both velocities is approximately 70%

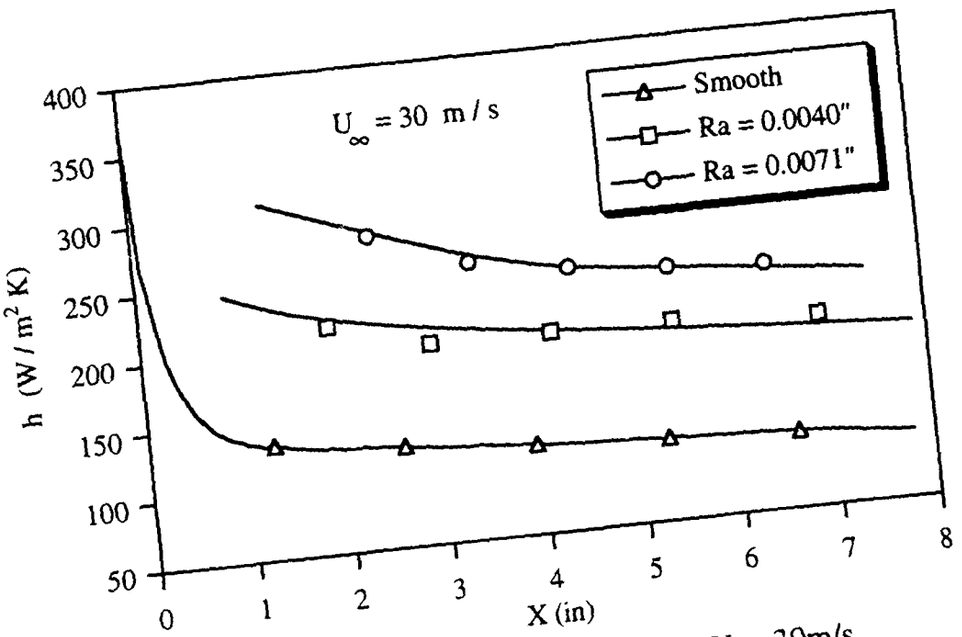

Figure 8.5 h, effect of roughness U_∞=30m/s

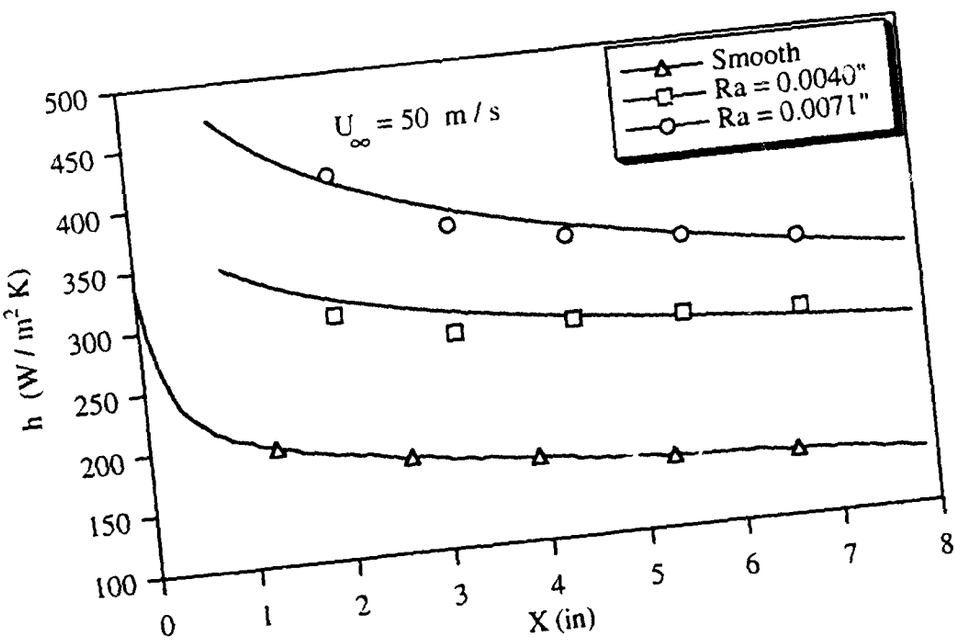

Figure 8.6 h, effect of roughness, U_∞=50m/s

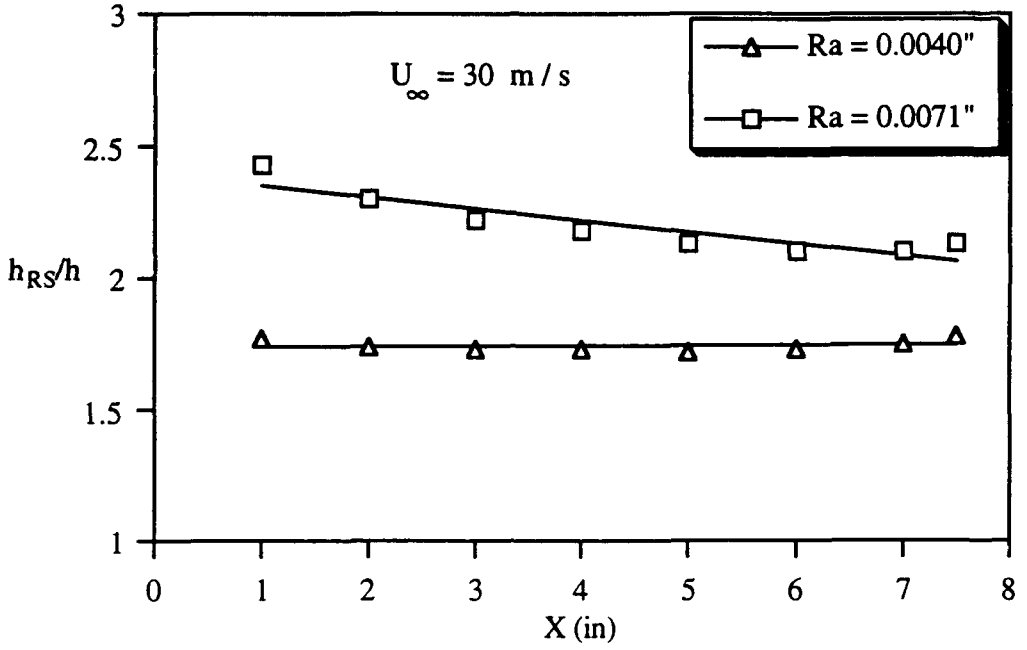

Figure 8.7 h_{RS}/h, effect of roughness, U_∞=30m/s

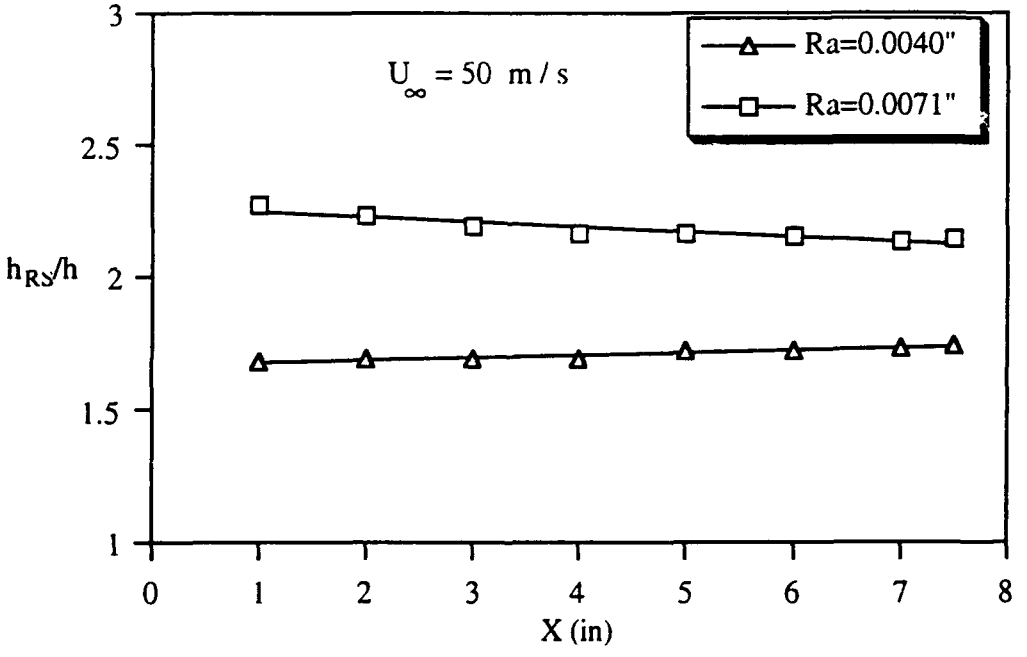

Figure 8.8 h_{RS}/h, effect of roughness, U_∞=50m/s

over the smooth surface ($h_{RS}/h=1.70$). For the Ra=0.0071" surface, A_{RS}/A is 1.26 and h_{RS}/h is approximately 2.2 or over double the heat transfer rate into the surface.

The conclusion here is clearly that the increase in h is due to more than the effect of increased area. The energy transport in the boundary layer has been enhanced by the increased turbulence levels near the surface. As shown in the next sections, the velocity profile shows a greater momentum deficit near the surface for the rough surface as compared to the smooth surface. This corresponds to the higher drag present on the rough surfaces. The work by Pimenta et al. (1975) indicates for air, the turbulent Prandtl number (Pr_t) is on the order of 0.9 for rough surfaces. This implies the eddy diffusivity for heat transfer (ε_H) is larger than the eddy diffusivity for momentum (ε_m). This implies enhanced heat diffusion near the rough surface.

The effect of a rough surface is to thin the viscous sublayer at the wall surface. For $Re_k>70$, the fully rough surface, the sublayer disappears entirely (Kays and Crawford, 1980). This means ε_H no longer goes to zero at the wall and turbulent transport of momentum and heat is available all the way to the surface. This is in contrast to $Re_k<70$ where the viscous sublayer is present, a layer close to the wall that is nearly laminar in nature, and turbulent transport is not significant ($\varepsilon_H \approx 0$). The absence of the viscous sublayer and high ε_H near the wall account for the large increase in the convective heat transfer coefficient.

8.3 Boundary Layer Velocity Measurements

The boundary layer measurements reported in this section are obtained and reported in the same way as data for the smooth surface investigated in Chapter 4. The only difference is, as is commonly done, the plate zero plane is taken to be at a point above the base of rough elements equal to the average surface height ($\bar{H}$) as defined in Figure 2.7. For the Ra=0.0040" surface this is 0.0025" above the base height and for Ra=0.0071" surface, 0.0051" above the base height. As an example of this work, Figure 8.9 and 8.10 show the velocity profiles for each surface at entrance velocities of 30 m/s and 50 m/s at a point 4.44 inches downstream of the splitter plate.

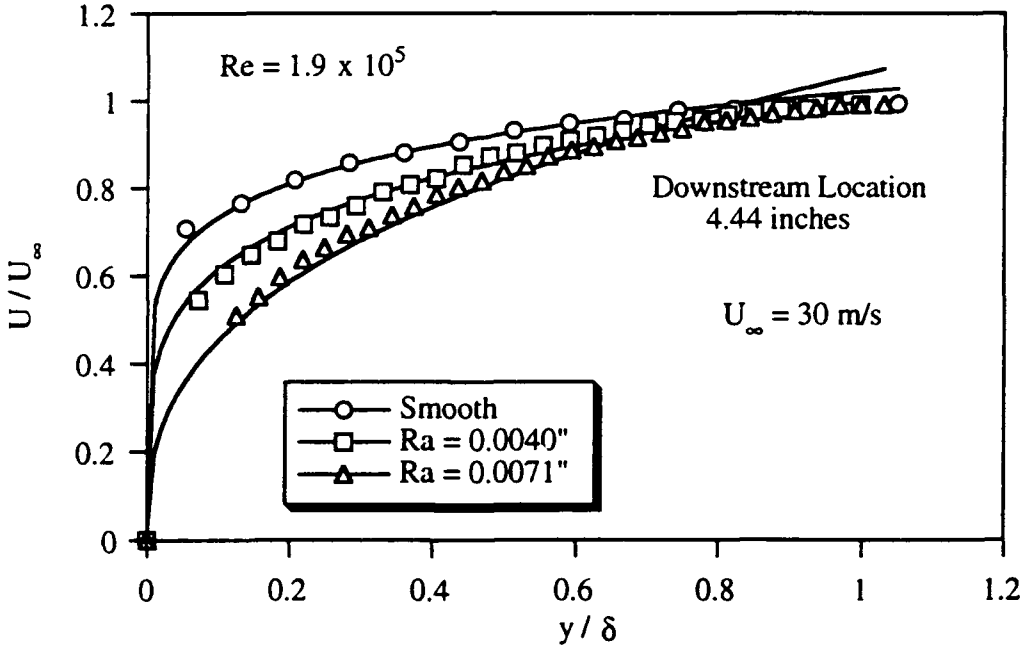

Figure 8.9 Boundary layer velocity profile for rough surfaces, X=4.44", U_∞=30m/s

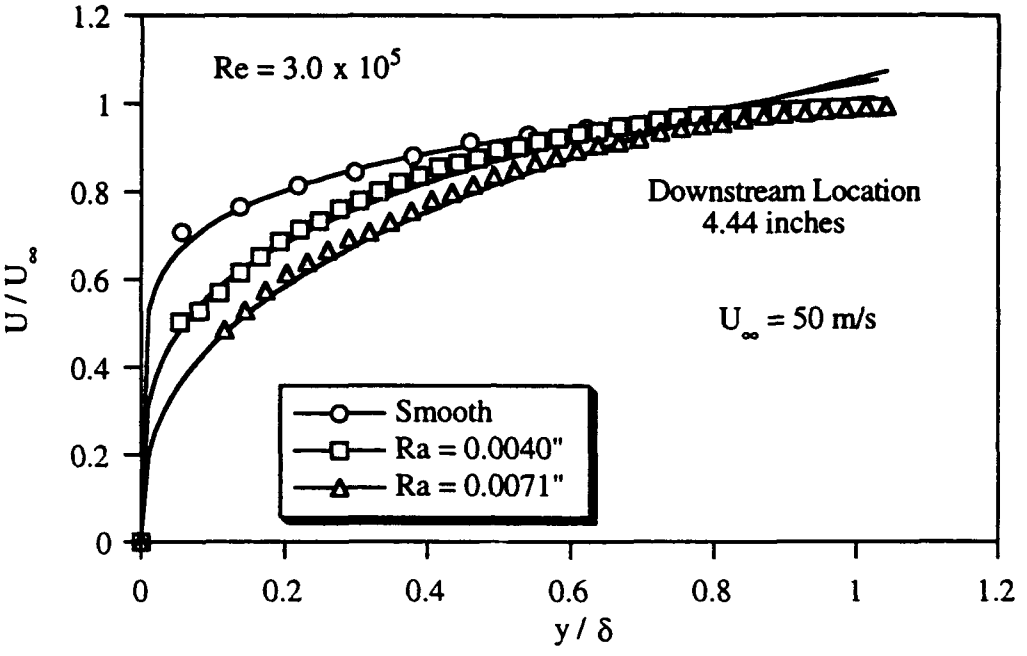

Figure 8.10 Boundary layer velocity profile for rough surfaces, X=4.44", U_∞=50m/s

The profiles clearly indicate the higher momentum deficit present for the rough surfaces and correspond to a higher drag on the surface. By fitting a power law curve to the velocity profiles, momentum thickness and displacement thickness are determined for each case at four downstream locations, X=0.875, 2.25, 3.44 and 4.44 inches. For a smooth turbulent plate a 1/7 power low fits the data extremely well. For the Ra=0.0040" surface the power low is approximately 1/4 and for the Ra=0.0071" surface approximately 1/2.5. The results of this work are contained in Table 8.1, 8.2

and 8.3. With this information, the friction coefficient at each downstream location are determined from equation 8.5 (Table 8.4).

Table 8.1 Boundary Layer Thickness for Rough Surfaces

Boundary Layer Thickness - δ (inches)

X (inches)	Ra=0.0040" U_∞=30m/s	Ra=0.0040" U_∞=50m/s	Ra=0.0071" U_∞=30m/s	Ra=0.0071" U_∞=50m/s
0.0875	.1552	.1262	.1524	.1472
2.25	.2015	.2155	.2299	.2232
3.44	.2128	.2595	.2900	.2874
4.44	.2700	.3595	.3199	.3449

Table 8.2 Boundary Layer Displacement Thickness for Rough Surfaces

Boundary Layer Displacement Thickness - δ_1 (inches)

X (inches)	Ra=0.0040" U_∞=30m/s	Ra=0.0040" U_∞=50m/s	Ra=0.0071" U_∞=30m/s	Ra=0.0071" U_∞=50m/s
0.0875	.0231	.0202	.0417	.0424
2.25	.0361	.0375	.0533	.0553
3.44	.0362	.0472	.0675	.0714
4.44	.0477	.0624	.0723	.0788

Table 8.3 Boundary Layer Momentum Thickness for Rough Surfaces

Boundary Layer Momentum Thickness - δ_2 (inches)

X (inches)	Ra=0.0040" U_∞=30m/s	Ra=0.0040" U_∞=50m/s	Ra=0.0071" U_∞=30m/s	Ra=0.0071" U_∞=50m/s
0.0875	.0161	.0142	.0225	.0230
2.25	.0235	.0243	.0303	.0294
3.44	.0255	.0307	.0352	.0380
4.44	.0335	.0403	.0409	.0447

Table 8.4 Coefficient of Friction for Rough Surfaces

Coefficient of Friction - c_f (inches)

X (inches)	Ra=0.0040" U_∞=30m/s	Ra=0.0040" U_∞=50m/s	Ra=0.0071" U_∞=30m/s	Ra=0.0071" U_∞=50m/s
0.0875	.0170	.0182	.0211	.0233
2.25	.0110	.0118	.0134	.0151
3.44	.0090	.0100	.0114	.0131
4.44	.0084	.0093	.0107	.0122

Using the boundary layer information for the X=2.5 and 3.44 locations where the rate of the change of boundary layer thickness is most accurately known, the k_s for each surface is backed out of equation 8.6. In fact, four points are

used to determine the average k_s for each surface from the tests at the two entrance velocities. The results are ks =0.052 ±.01 for the Ra=0.0040" surface and K_s=0.134 ±.02 for the Ra=0.0071" surface.

The variation in k_s appears to be large, but the effect on the empirical heat transfer coefficient and Stanton number calculated from equation 8.1 is less than 1%. This variation in k_s may be present, because of the presence of high turbulence level and changing turbulence with downstream location. The work done by Schlichting (1936) to determine equivalent sand roughness was accomplished in a water tunnel with very low free stream turbulence levels and a fully developed flow. Likewise, although this could not be confirmed, the work by Pimenta et al. (1975) most likely was accomplished in a low free stream turbulence environment. Since turbulence levels are known to decay rather rapidly as one moves downstream (Mehendale and Han, 1992), the velocity profiles of this work may be affected slightly and therefore affect the backed out value of ks. In this work, the higher k_s is associated with the 2.25 inch downstream location and the lower k_s with the 3.44 inch location. The other thing to keep in mind, as pointed out in Section 8.1, equation 8.6 is for a nonaccelerating flow. In our case, the 4% increase in velocity through the test region makes some variation in the results from equation 8.6 inevitable. The bottom line, however, is this variation has little importance on the predicted Stanton number which is primarily a function of c_f at any given downstream location.

As far as the magnitude of k_s for each surface, it may initially appear strange these values are 2.4 and 3.0 times larger than the absolute height of the corresponding roughness element. However, a review of Schlichting's

(1936) work indicates for densely packed spheres the ratio ks/k is as high as 3.8.

8.4 Empirical Correlation Versus Present Data

The Stanton numbers and corresponding convective heat transfer coefficients from equation 8.1 and 8.2 for the four test situations are matched against the experimental results in Figure 8.11 and 8.12. The legend is coded where Ra 40V30 corresponds to the Ra=0.0040" surface at an entrance velocity of 30 m/s, etc.

In viewing these figures, the lowest Re_k of 171 appears for the Ra=0.0040" surface at a location 4.44 inches downstream of the splitter plate. This means the surface conditions of all tests are, as originally assumed, in the fully rough region. The comparison between experimental and empirical results are very good. The constant in equation 8.2 is left as 1.0 as per Dipprey and Sabersky (1963). This constant can be modified to provide a better match, as can the coefficient on Re_k in the same relationship. This was not done for this comparison.

One trend to note in viewing Figure 8.11 and 8.12 is the slopes of the empirical and experimental linear curve fits are consistently different. This is most likely because of the slight acceleration of the mainflow in the present experimental results. Equation 8.1 is developed for constant free stream flow over a rough surface. In analyzing these two figures, for each flow condition, the flow moves through the test model from high Re_k to lower Re_k values. At positions further downstream, the boundary layer thickness is smaller and the convection heat transfer coefficient higher than would be the case for a nonaccelerating flow.

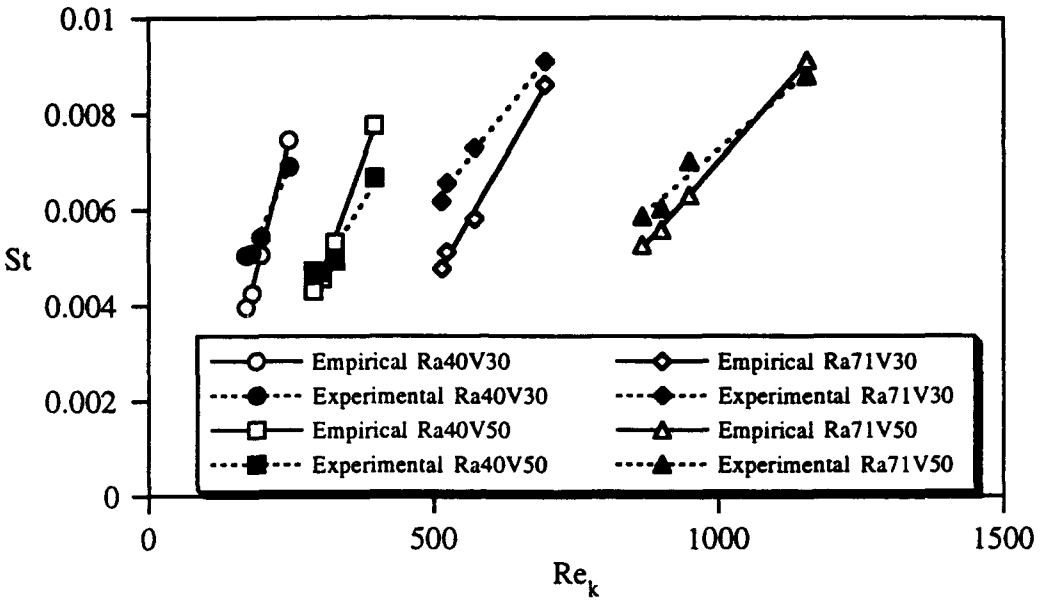

Figure 8.11 Stanton number, experimental versus empirical

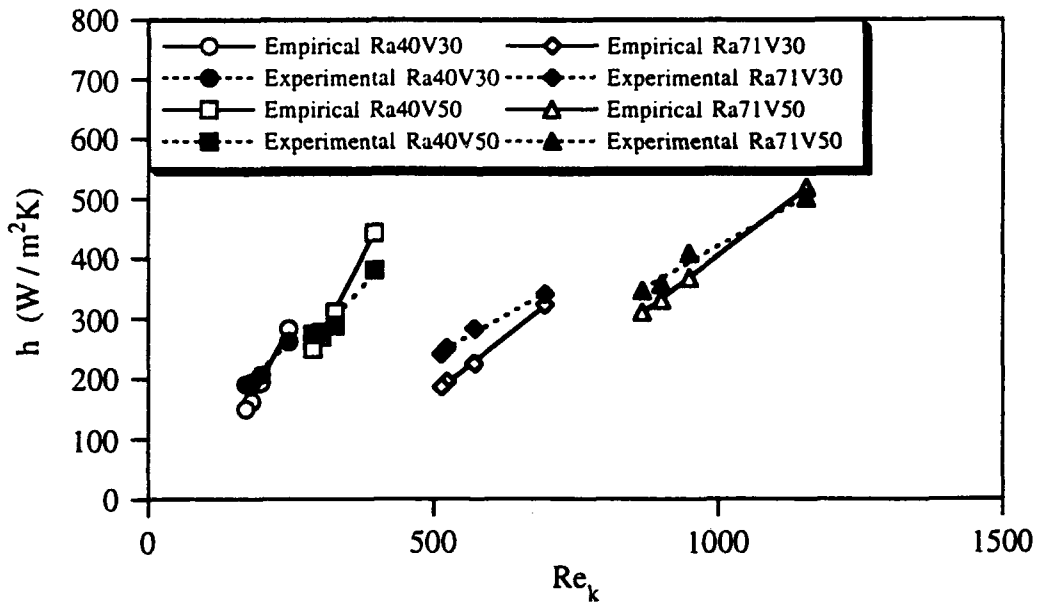

Figure 8.12 Heat transfer coefficient, experimental versus empirical

Based on the match between the empirical and experimental data in this section, Equation 8.1 would seem to be an excellent analytical tool for use in design work.

CHAPTER 9
EFFECTS OF SURFACE ROUGHNESS ON FILM COOLING EFFECTIVENESS AND CONVECTIVE HEAT TRANSFER COEFFICIENTS

9.1 Introduction

In this chapter, the focus of this work is presented. The preceding chapters have served to either introduce the experimental methodology, improve the method, or to validate the experimental model. Here the effects of surface roughness on film cooling effectiveness and convective heat transfer coefficient are documented for a Reynolds number and dimensionless boundary layer thickness seen in actual turbomachinery operations. The presence of roughness will affect the average effectiveness, the lateral distribution of the local effectiveness, the wall shear stress, and, as was clearly evident in Chapter 8, the heat transfer coefficient.

Specifically, two three-hole composite plates with roughness sizes corresponding to Ra=0.0040" and Ra=0.0071" are investigated at conditions present on the pressure side of the first stage F-100 turbine vane. The entrance velocity of 50 m/s provides a Reynolds number of 1.61×10^5 at the cooling holes which corresponds to the Reynolds number at a location 0.44 inches downstream from the stagnation point on the pressure side of the vane. At this location, the smooth surface dimensionless boundary layer momentum thickness (δ_{2S}/D) corresponds to the F-100 vane with a value of 0.0369. Tests are conducted at blowing ratios of 0.4, 0.5, 0.75, 1.0, and 1.25. The film flow to mainstream density ratio for the tests conducted in this study varies slightly from hot to cold test, but overall remains within 5% of 1.0.

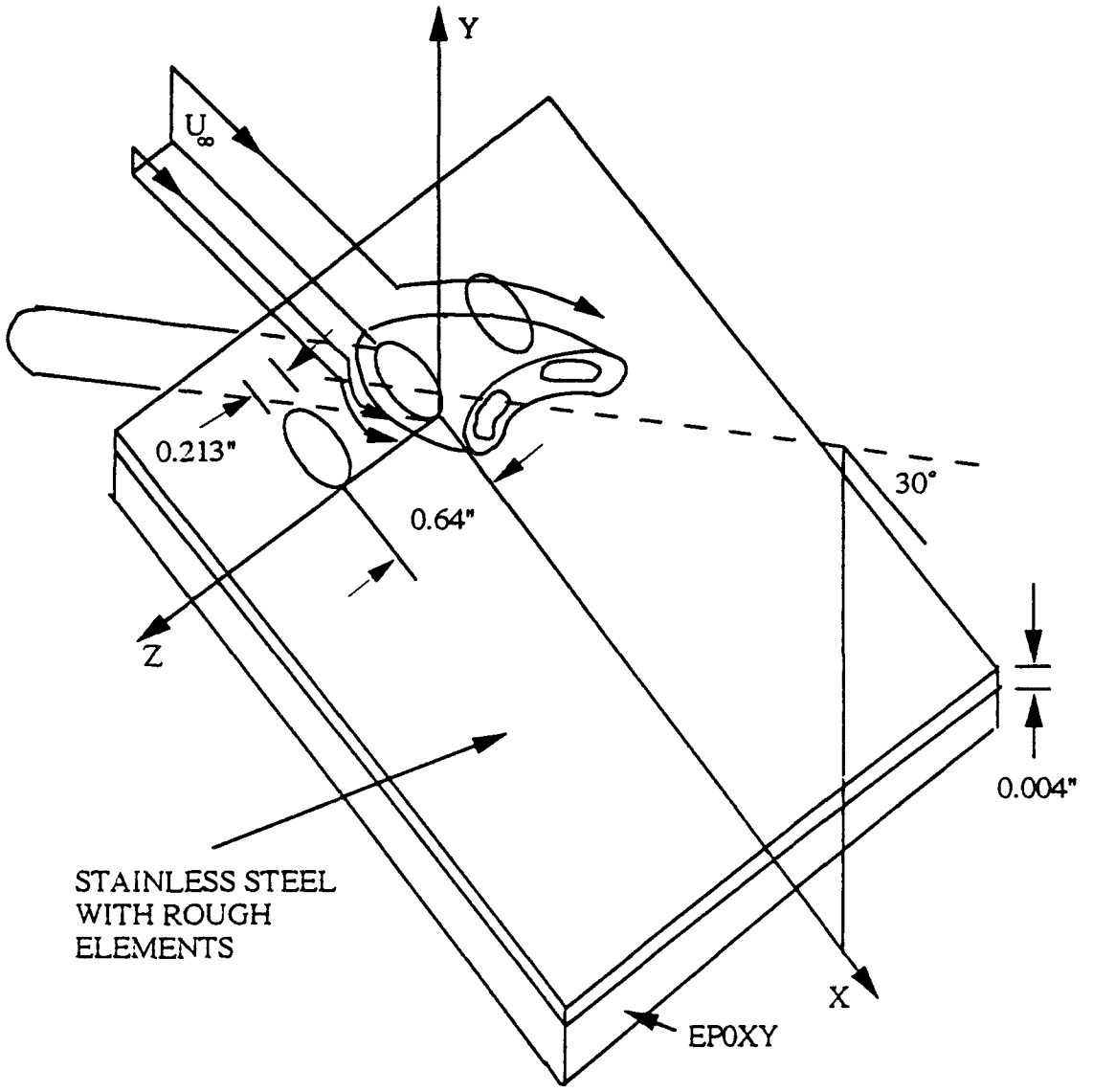

Figure 9.1 Composite plate test model

The composite smooth plate investigated in Chapter 7 provides a reference for the effect of surface roughness and is designated with an 's' subscript. Lateral averaging is accomplished at a given downstream location over the center hole from 1.5 hole diameters each side of the hole ($\bar{h}$ and $\bar{\eta}$). Area-averaged values ($<\bar{h}>$ and $<\bar{\eta}>$) are obtained by streamwise averaging $\bar{h}$

and $\bar{\eta}$ between $5 \leq X/D \geq 22$. From the finite difference work in Chapter 6 and the comparison of the composite plate results to the Plexiglas results of Chapter 7, it is clear that lateral conduction smooths h and η. For this reason, and based on the results of Chapter 6 and 7, $\bar{h}$ is reported rather than centerline h values. In the case of η, although a bias of 0.02 or 0.03 is expected, a centerline effectiveness ($\bar{\eta}_c$) is reported along with $\bar{\eta}$. $\bar{\eta}_c$ is η laterally averaged over the width of the film cooling hole, or about 1/3 of the lateral averaging of $\bar{\eta}$.

As outlined in Chapter 8, in order to provide more useful heat transfer data, the heat transfer coefficient and effectiveness maps included here are averaged over each rough elements base area of 0.015 square inches. If this is not done the heat transfer maps indicate slightly higher coefficients under the rough elements and slightly lower coefficients between the elements as compared to the roughness element average.

Film cooling effectiveness values are reported in section 9.2. The corresponding heat transfer coefficients are reported in Section 9.3.

9.2 Effect of Roughness on Film Cooling Effectiveness

For the range of blowing ratios investigated, the effect of roughness on film cooling effectiveness is presented in Figures 9.2 through 9.5. The same general trends are present for the two rough surfaces that were present for the smooth surfaces investigated earlier (Figure 5.12).

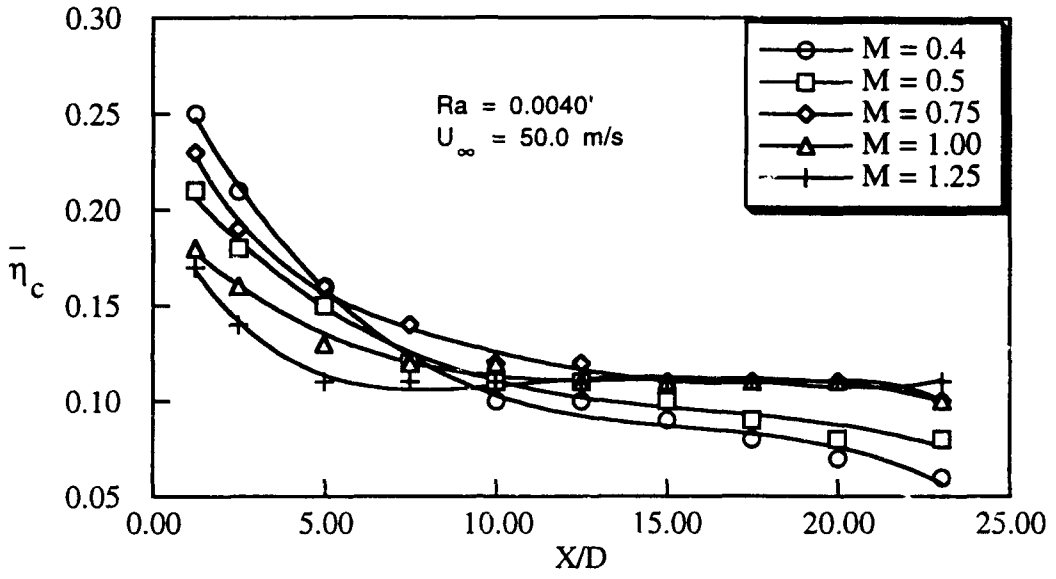

Figure 9.2 Centerline film cooling effectiveness, Ra=0.0040"

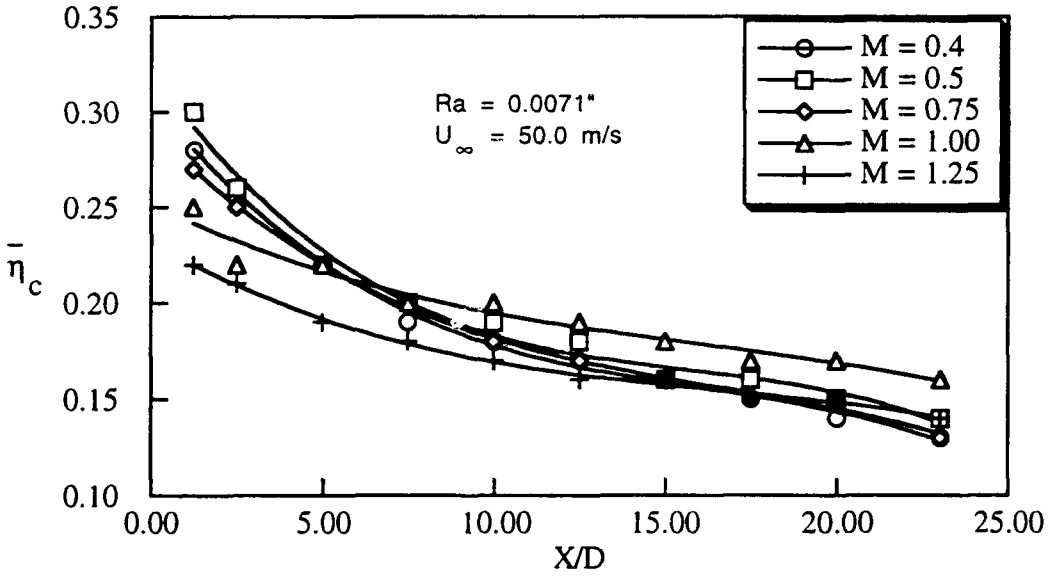

Figure 9.3 Centerline film cooling effectiveness, Ra=0.0071"

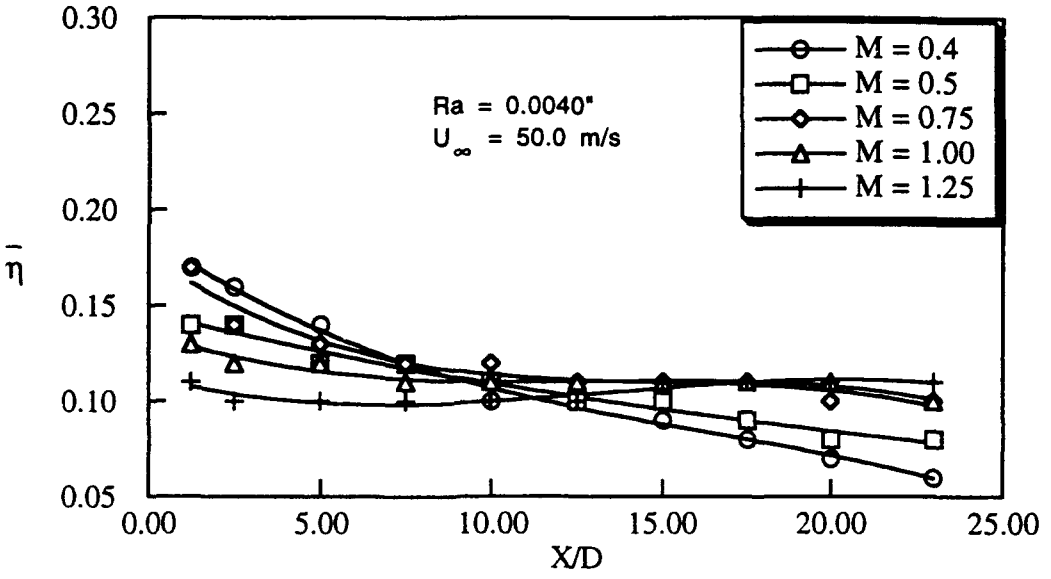

Figure 9.4 Laterally averaged film cooling effectiveness, Ra=0.0040"

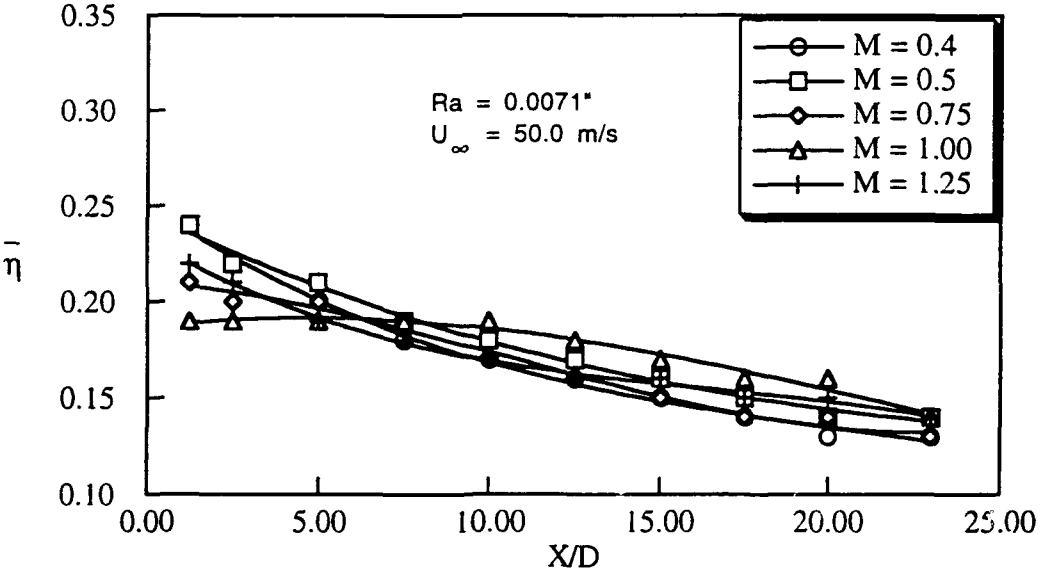

Figure 9.5 Laterally averaged film cooling effectiveness, Ra=0.0071"

Near the holes, effectiveness is higher for the lower blowing ratios. Downstream, however, this trend reverses and the higher blowing ratios have a clear advantage in effectiveness. For the smooth surface, the advantage for the higher blowing ratio begins at approximately twenty hole diameters downstream. For the rough surfaces, this reversal takes place earlier, about X/D=10 for the Ra=0.0040" surface and as early as X/D=8 for the Ra=0.0071" surface. As compared to the smooth surface, the effectiveness difference between high and low blowing ratios is not as significant for the rough surfaces.

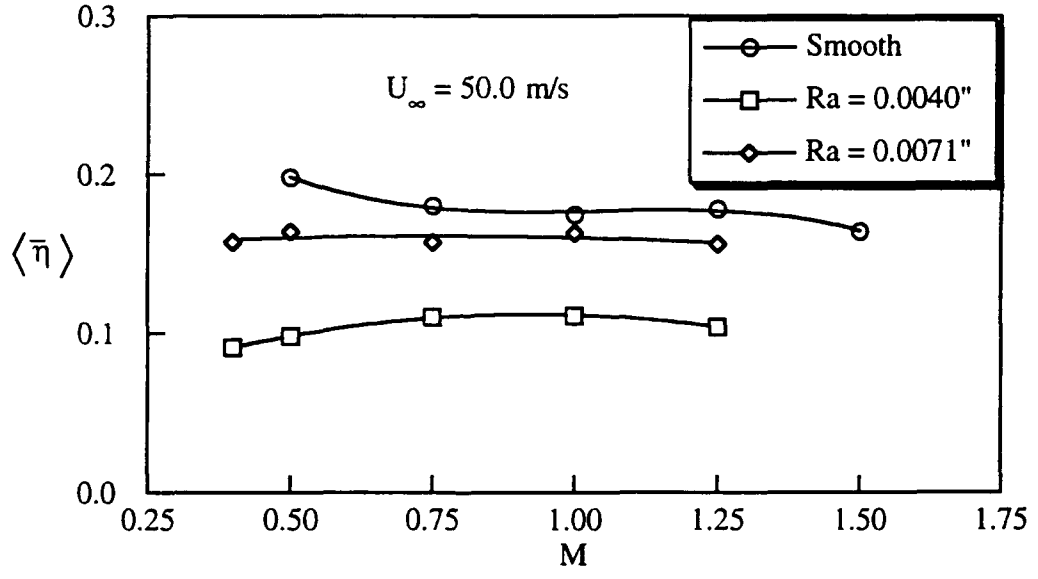

Figure 9.6 Area averaged film cooling effectiveness

The area averaged film cooling effectivenesses for the surfaces are shown in Figure 9.6. The area averaged effectiveness for a smooth surface is clearly at a blowing ratio of 0.5, but for the rough surface the area averaged effectiveness remains level or with a slight increase for blowing ratios of 0.75

and 1.00 in the Ra=0.0040" case. Overall both roughness sizes reduce the film cooling effectiveness. For the Ra=0.0040" this drop in area averaged effectiveness is as high as 50% and on the order of 10% to 20% for the Ra=0.0071" surface. The overall effect of the roughness on the effectiveness can be seen in Figure 9.7.

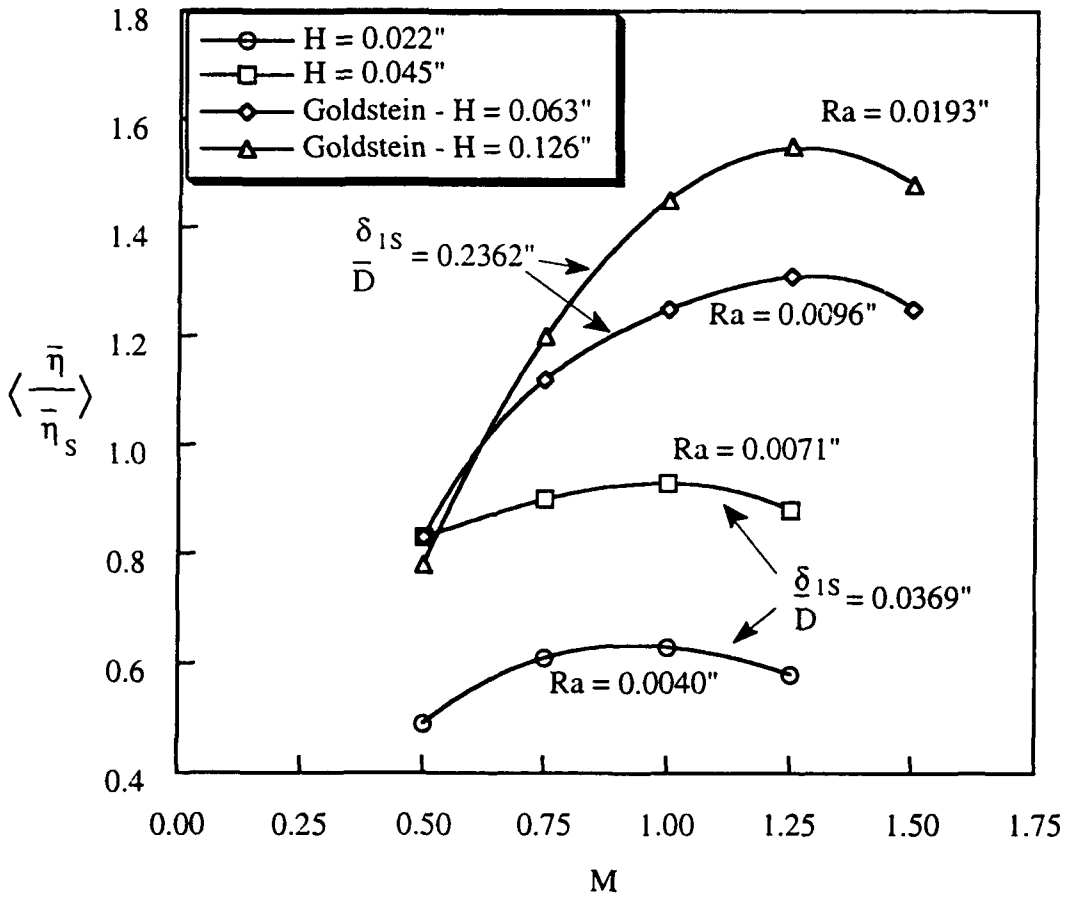

Figure 9.7 Effect of roughness, relative to a smooth surface, on area averaged effectiveness as a function of blowing ratio

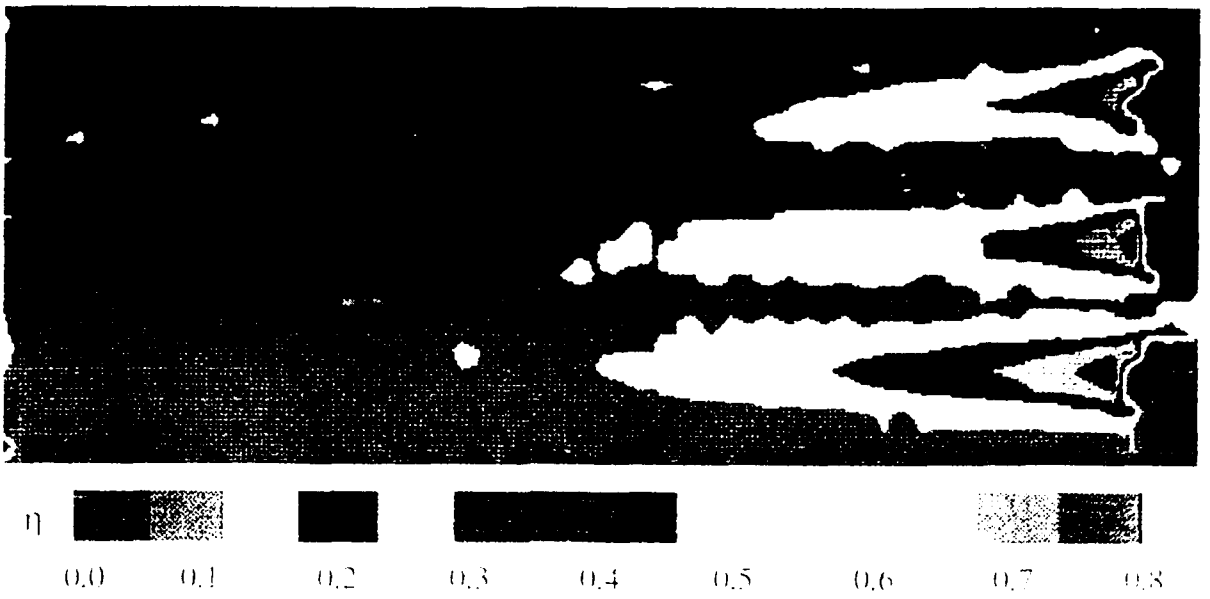

Figure 9.8 Film cooling effectiveness map, Ra=0.0040", M=0.75

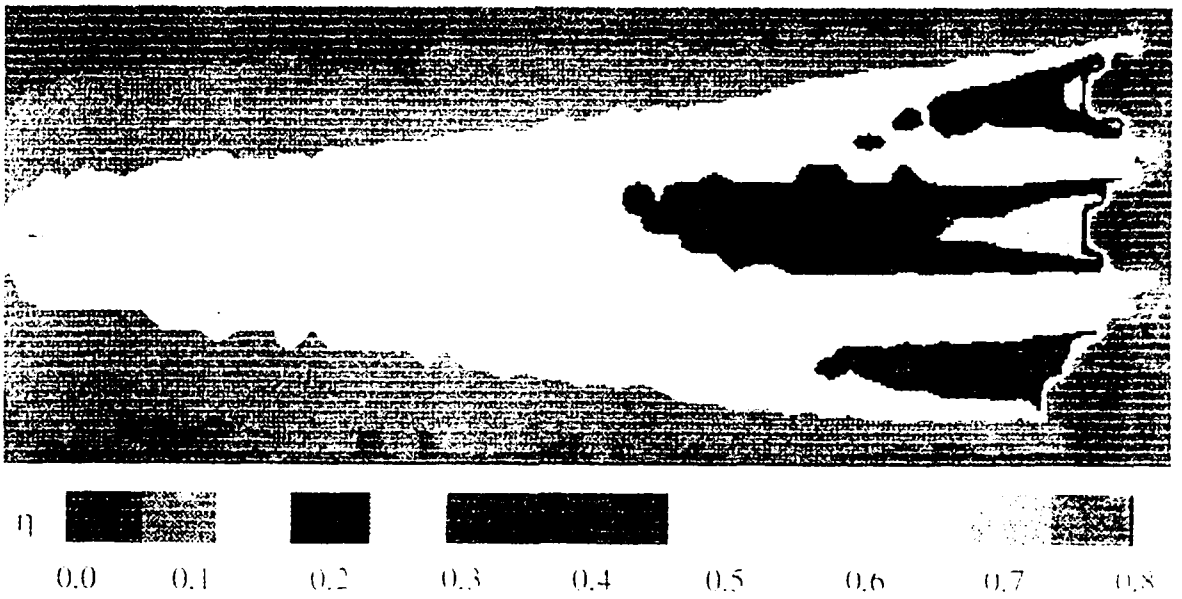

Figure 9.9 Film cooling effectiveness map, Ra=0.0071", M=0.75

For visual comparison, effectiveness Maps of M=0.75 are given in Figures 9.8 and 9.9 and can be directly compared with Figure 7.10 for a smooth surface. In Figure 9.7, the area averaged effectiveness is normalized with the smooth surface area averaged data. The presence of roughness causes a decrease in the effectiveness over the smooth tests for both roughness sizes. The presence of roughness induces more vigorous mixing between the mainstream and the secondary flows near the wall, decreasing the effectiveness due to greater dilution of the cooling flow. An interesting trend, which also appeared in the work by Goldstein et al. (1985), shown in Figure 9.7, is an increase in the area averaged effectiveness relative to a smooth surface for blowing ratios greater than 0.5. While the Goldstein work provides data for several different roughness configurations, the data shown in Figure 9.7 matches the setup of this work best. This data results from a configuration employing cylindrical elements both upstream and downstream of a row of film holes, spaced three hole diameters apart. Goldstein et al. (1985) attribute this improvement to the area averaged effectiveness ratio to a reduction of the "blow off" phenomena. They cite a blowing ratio of 0.6 to be the point blow off becomes significant for a smooth surface. Above this blowing ratio, "the roughness causes more turbulent mixing and reduces the penetration of the secondary jets, thus improving the effectiveness."

As opposed to having the roughness elements only downstream of the film cooling holes, the work on roughness by Goldstein et al. (1985) reported that having roughness both upstream and downstream provided the greatest improvement of η at larger blowing ratios. This of course matches the situation present on the actual turbine blades.

When viewing Figure 9.7, it must be pointed out, major differences between the two works exist. Although the work by Goldstein does not document the mainstream turbulence level, based on prior work at the University of Minnesota in this area, the level is probably less than 1%. This may account for the difference in the area effectiveness ratios seen in Figure 9.9. For a low turbulence mainstream flow, the film jet may be turned back toward the surface with less destruction of the jet than is the case for the 8.5% turbulence level of the testing in this work. The higher turbulence level may account for the overall lower effectiveness levels where the dilution of the cooling air occurs more rapidly upon exiting the film holes. The other very important difference in these two works, is the dimensionless boundary layer displacement thickness. While the work conducted here was accomplished to achieve a thickness ($\frac{\delta_{1s}}{D} = 0.0481$) compatible with the P&W F-100 first vane, the work by Goldstein et al. has a dimensionless displacement thickness on the order of one magnitude larger at $\frac{\delta_{1s}}{D}$ =0.2362. In the Goldstein work a splitter plate is not used to remove the boundary prior to the test section, resulting in a larger boundary layer thickness at the point of film injection. In both studies, this thickness is measured in the absence of the injection holes. The result of the greater dimensionless boundary layer thickness is that the absolute effectiveness values seen in the Goldstein work are lower than those determined in this work. Therefore, the ratios, by Goldstein et al (1985) present in Figure 9.7, translate into smaller absolute changes in effectiveness.

Two other differences exist, although, their effect is not expected to be large. This work is accomplished at a free stream velocity of 50 m/s and a

film hole inclination of 30°. The Goldstein work is accomplished at a free-stream velocity of 45 m/s and a film hole inclination of 35°.

Figure 9.10 through 9.13 provide some insight into what causes the rise in the area effectiveness seen in Figure 9.7. For the blowing ratios investigated the centerline effectiveness is compared for each roughness to that of the smooth surface. While the effectiveness is initially lower for the rough surfaces, at 15 to 20 hole diameters there is very little difference in the values. The rate of decrease in effectiveness with downstream location is much steeper initially for the smooth surface, while the rough surfaces experience a much flatter rate of decrease. This indicates the higher turbulence levels may initially dilute the cooling flow retained in the boundary layer, but the cooling air is then retained within the boundary layer better than in the case of the smooth surface.

The effect of roughness on the variation of η across the span can be assessed using a smoothness parameter defined by Goldstein et al. (1985) as

$$\zeta = \frac{\eta_{max} - \eta_{min}}{\bar{\eta}}$$

The presence of roughness results in a flatter profile as compared to the smooth surface. The effect of roughness for the minimum and maximum blowing ratios can be assessed in Figures 9.14 and 9.15. Greater mixing due to the presence of roughness causes a more uniform local effectiveness over the span. This smoothing is greatest for the rougher surface. This

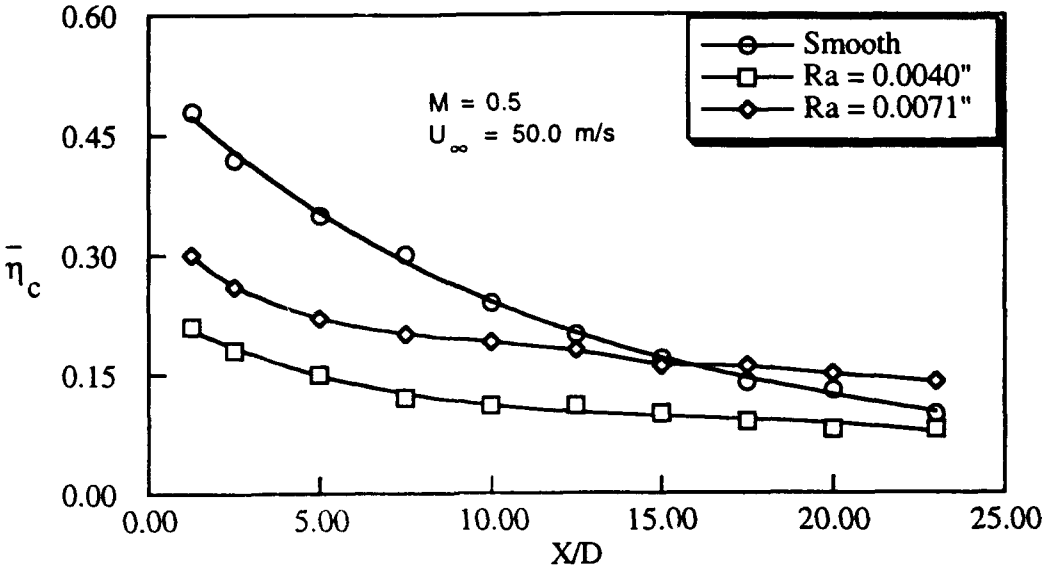

Figure 9.10 Comparison of centerline film cooling effectiveness, M=0.5

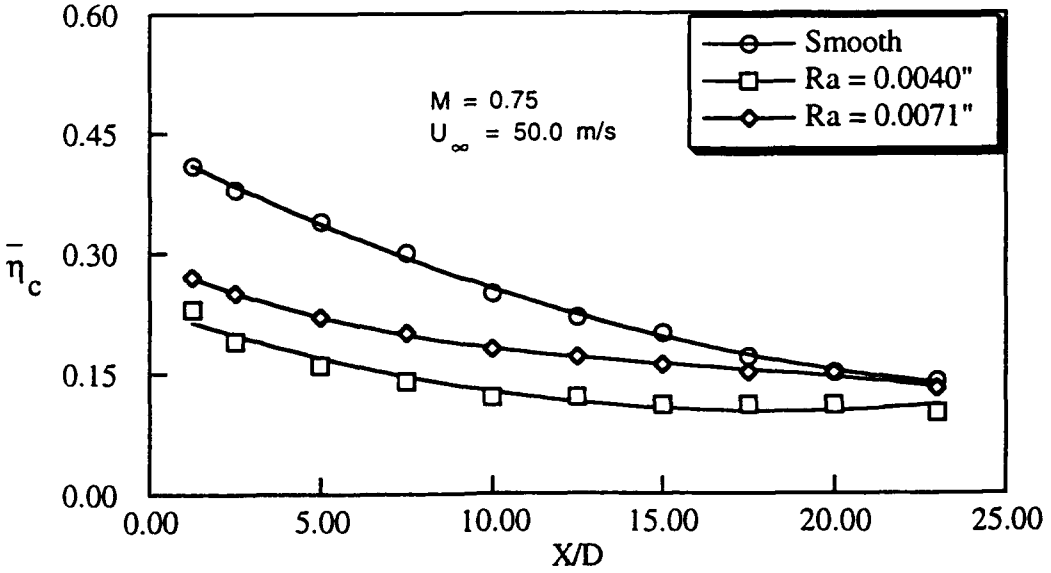

Figure 9.11 Comparison of centerline film cooling effectiveness, M=0.75

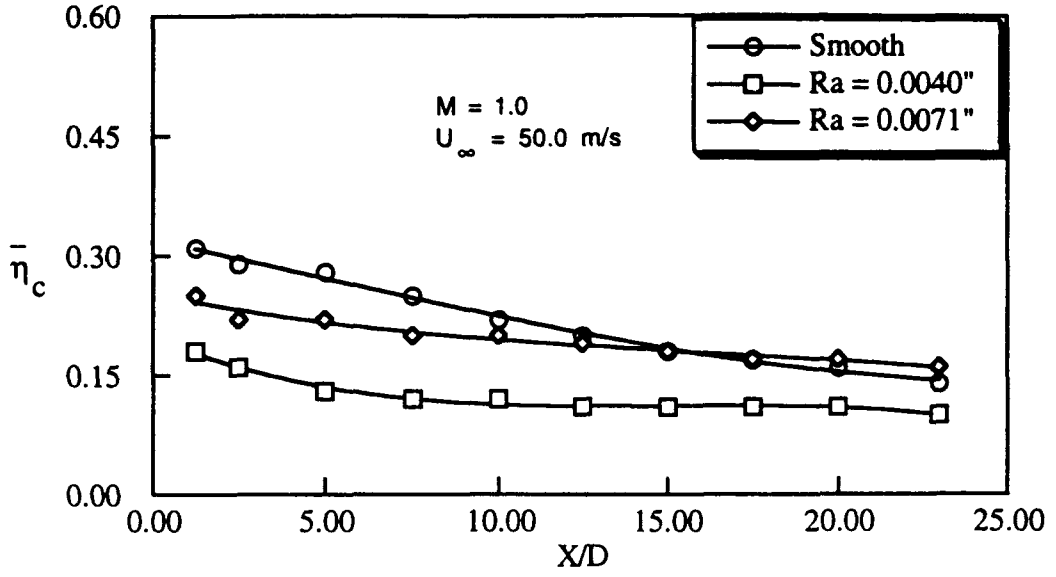

Figure 9.12 Comparison of centerline film cooling effectiveness, M=1.0

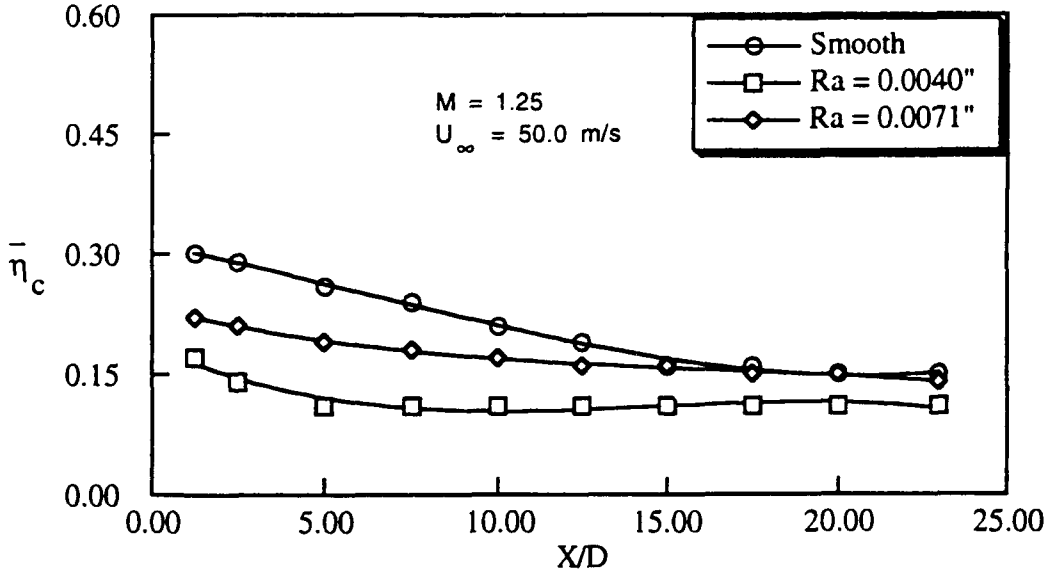

Figure 9.13 Comparison of centerline film cooling effectiveness, M=1.25

trend matches that found by Goldstein et al. (1985) who also found for the configuration studied the most uniform profile occurs when roughness elements are present both upstream and downstream of the film cooling holes. In this work, the profiles are essentially smooth by x/D=15.0. This is earlier than for Goldstein's work and is again attributed to the higher turbulence levels present in this study.

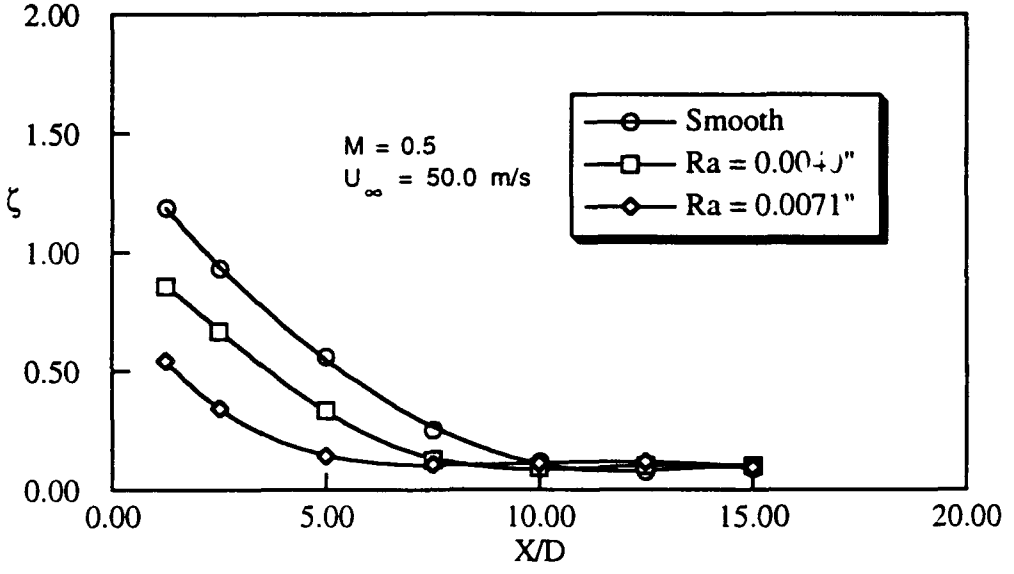

Figure 9.14 Effect of roughness on effectiveness lateral smoothness, M=0.5

In summary, there is a decrease in the film cooling effectiveness for the rough surfaces investigated in this study as compared to a smooth surface under similar conditions. This decrease is attributed to the higher turbulence levels present when roughness is present and the greater dilution of the injected coolant flow. Because of this distribution of the film cooling jet, however, the jet does not penetrate into the mainstream as far helping to retain more cooling air in the vicinity of the surface further downstream. The result is a flatter downstream effectiveness curve. For the rougher surface

this effect is more prominent and average effectiveness levels approach that of a smooth surface eventhough the effectiveness just downstream of the film injection is significantly lower due to the higher turbulence levels.

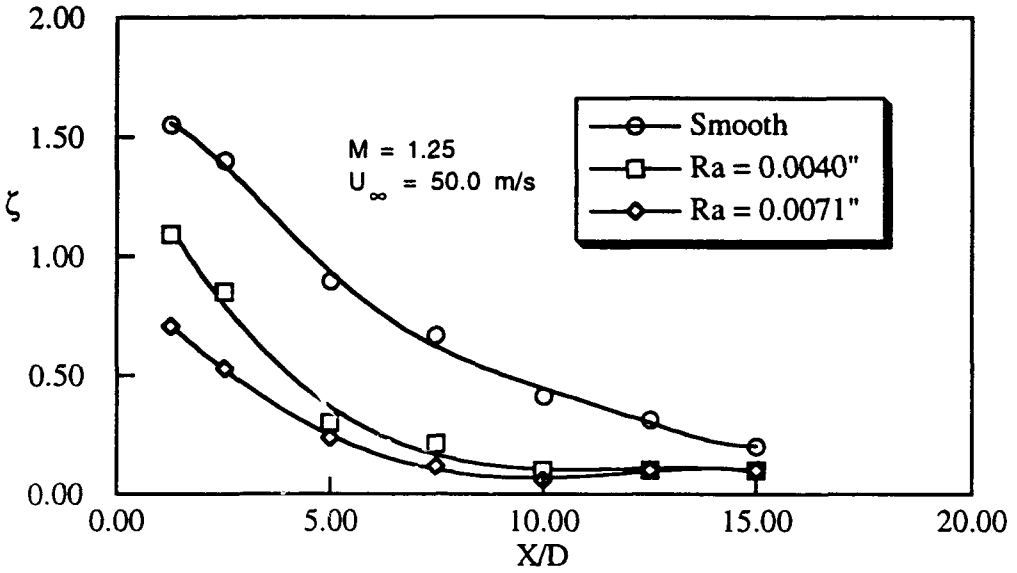

Figure 9.15 Effect of roughness on effectiveness lateral smoothness, M=1.25

9.3 Effect of Roughness on Film Cooling Heat Transfer Coefficients

The film cooling effectiveness results presented in the last section are only part of the story. The effect of roughness on the convective heat transfer coefficient will increase the heating load to the surface. In Chapter 8, the increase for the two rough surfaces used in this study is documented for the case of no film cooling. In this section, the effect of film cooling on this increased heat transfer load is documented.

For a smooth surface, there is a definite increase in the convective heat transfer coefficients as a result of film cooling. This increase is largest just downstream of the film injection and decreases further downstream of

injection. As discussed in Chapter 7, this increase is attributed to the increased turbulence resulting from film jet-mainstream interaction and the horseshoe or kidney shaped vortex flow which wraps around the film jet. The effect of blowing ratio on laterally averaged heat transfer coefficient, taken from the work reported in Chapter 7, is shown in Figure 9.16. Clearly, the larger the blowing ratio, the greater the increase in heat transfer coefficients. The effect of blow-off is clearly visible here, with a reversal of the trend very near the point of injection.

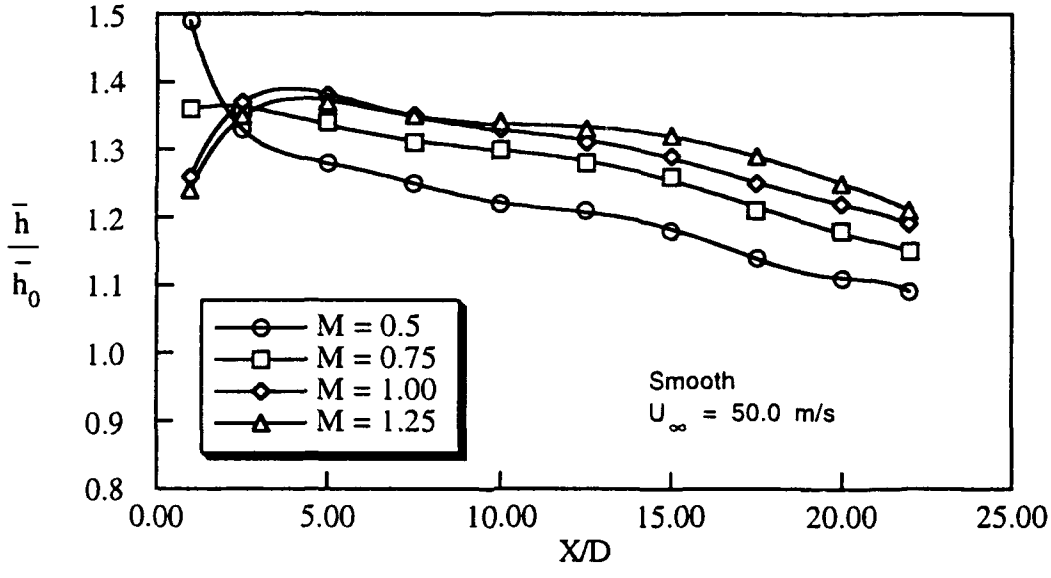

Figure 9.16 Effect of film cooling on laterally averaged heat transfer coefficients for a smooth surface.

For the rough surfaces, the trend is similar (Figure 9.17 and 9.18). Again, the greater the blowing ratio, the larger the increase in heat transfer coefficient. The exception for this, is the M=0.4 case for the Ra=0.0071"

surface. For this single case, the $\bar{h}$ are higher than for the M=0.5 case. For the smooth case in Figure 9.16, the presence of blow-off was clearly evident near the point of injection. As discussed in the previous section, blow-off is reduced for the rough surfaces. This is clearly evident in Figures 9.17 and 9.18, where a lack of reversal of the coefficient trend with blowing ratio, present for the smooth surface, can be seen. For the Ra=0.0040" surface there does appear to be some evidence of blow-off near the point of injection, but much less severe than for the smooth surface. For the Ra=0.0071" surface, the evidence of blow-off is not present.

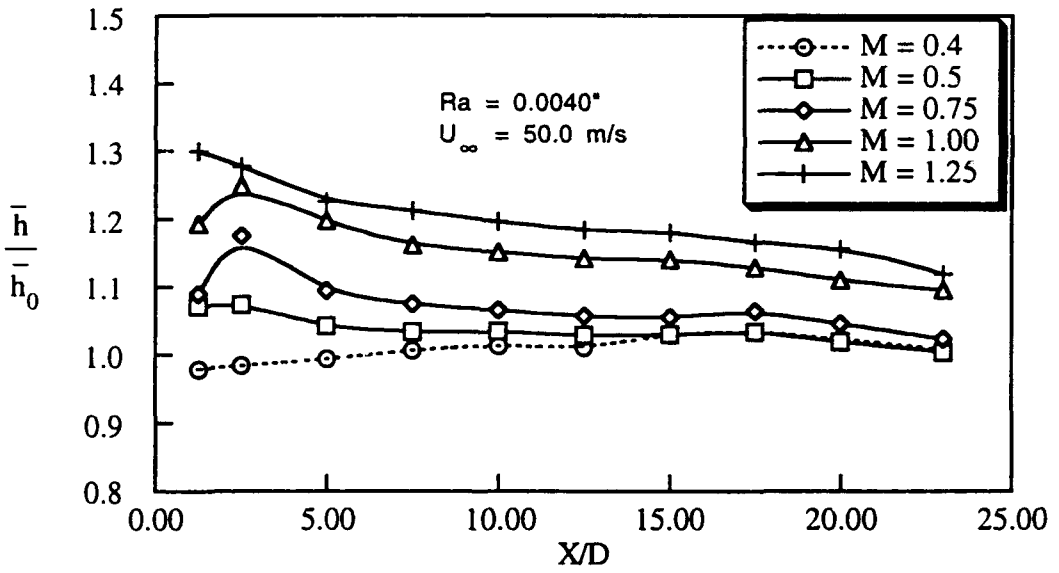

Figure 9.17 Effect of film cooling on laterally averaged heat transfer coefficients for the Ra=0.0040" surface.

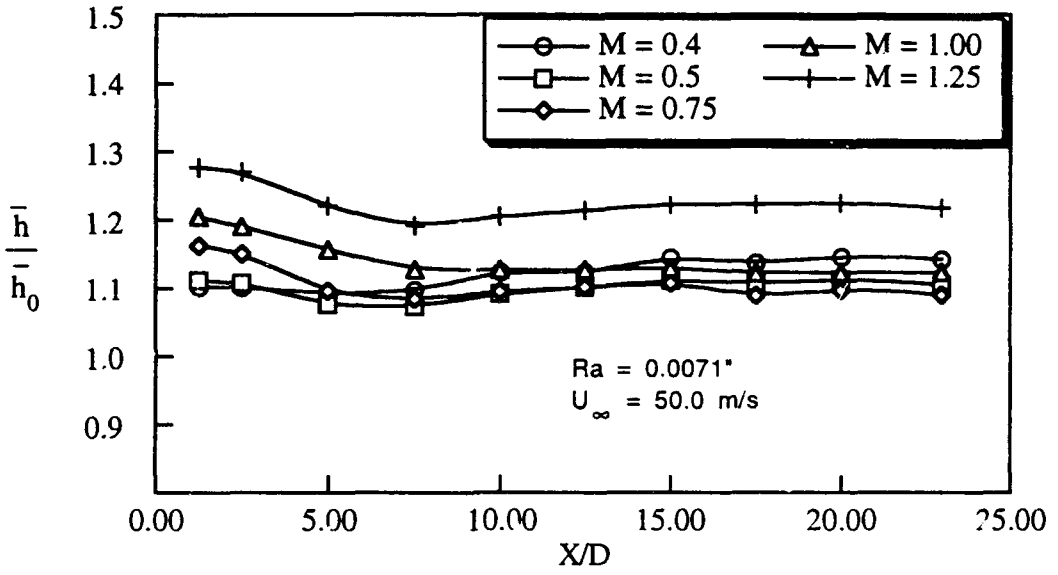

Figure 9.18 Effect of film cooling on laterally averaged heat transfer coefficients for the Ra=0.0071" surface.

Overall, the effect of film cooling on the area averaged increase of effectiveness, $\langle \bar{h}/\bar{h}_0 \rangle$, is less for the rough surfaces. For the smooth surface, for blowing ratios between 0.5 and 1.25, the increase in $\langle \bar{h}/\bar{h}_0 \rangle$ is 20% to 30% above the non-blowing case. For the rough surfaces, this increase is between 3% and 21%. This difference is attributable to the high level of turbulence already present for the rough surface. As a result, the impact of the film cooling jets on further increasing the turbulence level is less significant than for the smooth surface.

As seen in Chapter 8, the presence of roughness has a tremendous effect on the local convective heat transfer coefficients. As presented here, the addition of film cooling, for both a smooth and rough surface, result in additional increases in h.

CHAPTER 10
HOT WIRE TURBULENCE MEASUREMENTS

10.1 Introduction

As described in Chapter 1 and illustrated in Chapter 5, turbulence levels play an important role in determining the heat transfer characteristics of a given flow situation. In this chapter, the turbulence level of the main flow at the two test conditions, U_∞=30.5m/s and U_∞=50m/s, is documented. Turbulence levels in gas turbine entrance conditions can be on the order of 10% and higher. The majority of previous work on flat plate film cooling has taken place in wind tunnels with very low turbulence levels (<1%). Here, the turbulence levels are much higher and approach those seen in actual engines.

In order to document the turbulence of the mainstream, a film probe is inserted in the test rig, from the rear exit area, at the downstream point of film injection (X=2.25"), and at a point midway between the test surface and the adjacent test rig wall. This is a point approximately 0.625" above the test surface.

10.2 Test Equipment

The test equipment consisted of a hot film probe (TSI #1210-20) attached to a constant temperature anemometer (TSI #1050), a signal linearizer (TSI #1052), a signal conditioner (TSI #1057), a true root mean square (RMS) voltmeter (TSI # 1076), a standard oscilloscope, and a Zenith AT with a Metrabyte DAS-16 data acquisition board. The TSI equipment is powered with a TSI 1051-6 monitor. Figure 10.1 shows the equipment layout.

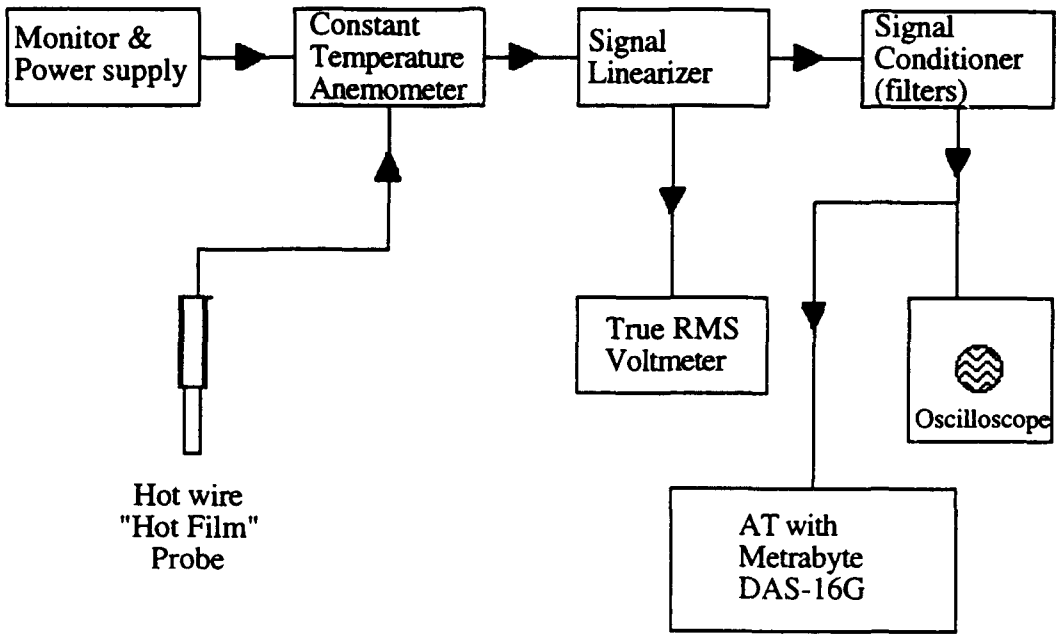

Figure 10.1 Hot wire apparatus

Calibration of the listed equipment was accomplished as per manufacturer's specifications. The anemometer provides a voltage signal which is directly related to the velocity of the flow past the hot film probe. The voltage calibration is shown, for the anemometers 5:1 wheat-stone bridge/hot-wire combination , in Figure 10.2. The voltage signal is linearized as shown in the figure using the TSI #1052 signal linearizer. The signal is read with the RMS voltmeter after the anemometer and then after the linearizer to produce this calibration curve. Velocities are determined during calibration with a pitot tube placed 0.33" to the side of the hot wire probe.

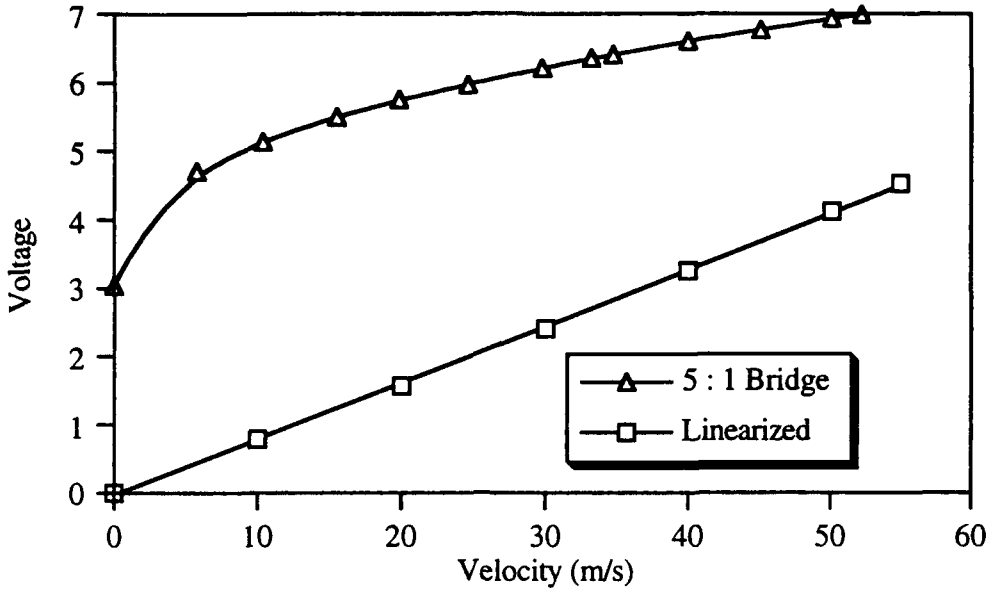

Figure 10.2 Hot wire calibration

10.3 Turbulence Level

The DC component of the anemometer signal equates to the time mean velocity of the flow ($\bar{U}_\infty$) and the AC component to the fluctuating component of the velocity (U') about the time mean velocity. The RMS voltmeter, on the correct setting, and pitot probe both measure the time-mean velocity defined as

$$\bar{U} = \lim_{T\to\infty} \frac{1}{T} \int_0^T U(t)\, dt$$

where U(t) is the instantaneous value of the signal in terms of velocity and T is time. These values are used to produce Figure 10.2.

The most common measurements of the velocity fluctuations are the mean square and root mean square velocities. The mean square is defined as:

$$\bar{U}^2 = \lim_{T\to\infty} \frac{1}{T}\int_0^T U^2(t)\,dt$$

The root mean square is then

$$RMS = \sqrt{\bar{U}^2}$$

In this case, the RMS voltmeter includes a capacitor which acts as a high pass filter removing the DC signal or time-mean velocity from the signal processed by the voltmeter.

The result is the turbulence measurement from the RMS voltmeter is a standard deviation measurement. Here, the standard deviation is referred to as the root mean square (RMS) in standard hot-wire terminology.

$$RMS = \left[\lim_{T\to\infty} \frac{1}{T}\int_0^T (U(t) - \bar{U})^2\,dt \right]^{\frac{1}{2}}$$

and the Mean Square = $[RMS]^2$. If this root mean square is normalized by the mean velocity, the ratio is referred to as the velocity turbulence level, as a percentage of the mean velocity.

For the 30.5m/s case this turbulence level is 6.9% and for the 50m/s flow, 8.5% turbulence as determined from the RMS voltmeter. Here we assume the flow is isotropic, because the measurements are taken well away from the side walls. With the flow is considered isotropic, turbulence levels

need to be taken only in one direction, in this case, longitudinally through the rig and parallel to the main flow.

To further document the flow, the linearized signal is fed into a conditioner where processing by high and low-pass filters is possible. From the conditioner, the signal is again fed into the RMS voltmeter, an oscilloscope, and to a Metrabyte data acquisition board for digitizing. This particular board has a sampling rate limit of 25K Hz. Employing a 5 Hz high-pass filter the DC portion of the signal is removed, leaving only the AC or fluctuating velocity component for analysis. Figures 10.3 and 10.4 are a short burst of this turbulent velocity about the mean velocity. It is clear the velocity fluctuations are much larger for the 50m/s flow as compared to the 30.5m/s flow. The larger velocity fluctuations correspond to a higher turbulence level for the 50 m/s flow.

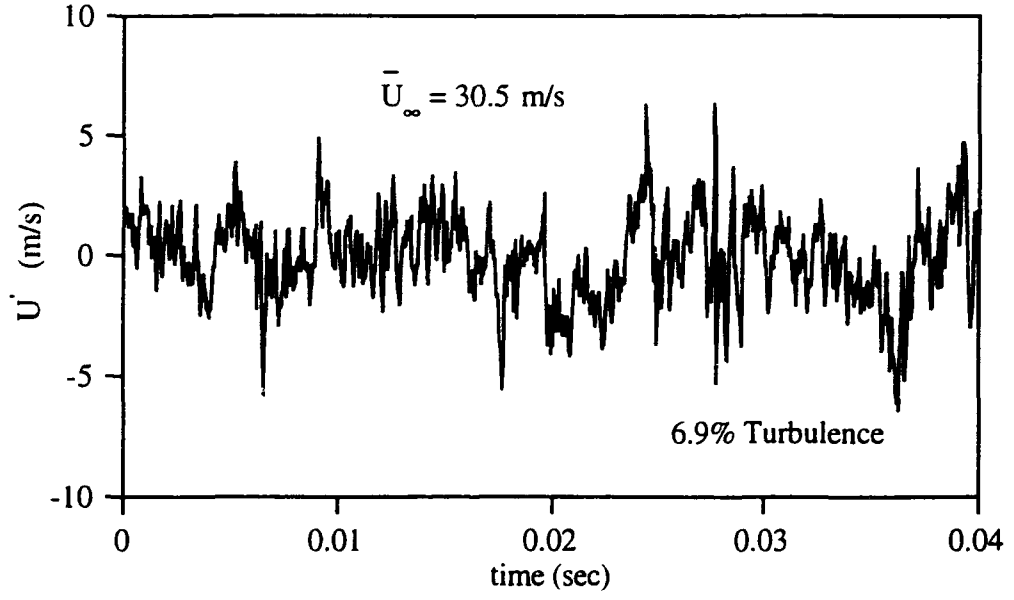

Figure 10.3 Velocity fluctuations, $U_\infty = 30.5$m/s

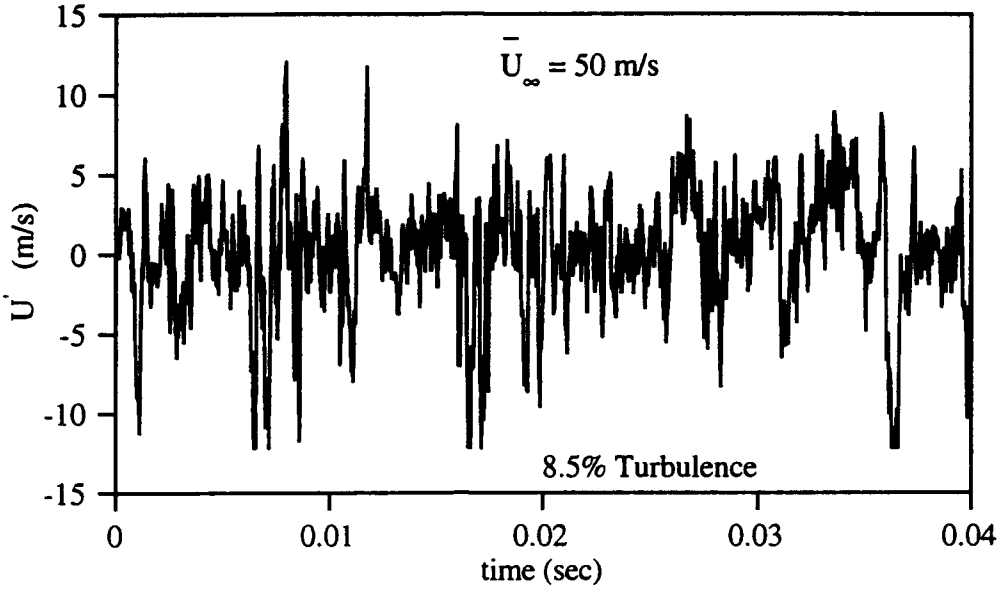

Figure 10.4 Velocity fluctuations, $U_\infty = 50$m/s

10.4 Spectral Analysis

In this section, results of a Fast Fourier Transform (FFT) of the digital velocity fluctuations are reported. By using a series of low pass filters, while continuing to take readings from the RMS voltmeter, it could be determined that very little of the energy associated with the fluctuations of either flow occurs at frequencies above 5KHz. This is fortunate, because this is well below the Nyquist critical frequency (f_c) given by

$$f_c = \frac{1}{2} \text{(sampling rate)}$$

The Nyquist frequency for this particular work is 12.5 KHz for the sampling rate of 25KHz. The Nyquist frequency limit, means at least two sampling points must be present at the highest frequency.

When performing an FFT or spectral analysis of a time dependent variable, the Nyquist frequency is the upper limit of the numerical methods ability to separate out the spectral components of the fluctuations. The fluctuating flow field can be thought of as a large number of fluctuations occurring at specific frequencies and amplitudes overlaid on top of each other. The amplitude of each of those frequency squared is a measure of the power $(m/s)^2$ associated with that particular frequency. The sum of the power associated with each frequency is the total power of the fluctuations and is equivalent to the mean square of the turbulent flow.

The FFT of the turbulence converts from time domain to spectral or frequency space providing a spectral density where the power $(m/s)^2$ for each frequency is discreatized. Again, the sum of this power is the total mean square of the flow or the square of the RMS value read out of the RMS voltmeter.

The low pass filter on the conditioner is set to 12.5K, the Nyquist frequency, and the digitized fluctuations recorded using the Dash-16G board. Eventhough very little energy is associated with frequencies above 12.5K, what ever energy there is will be placed spuriously into the range below the Nyquist frequency, if it is not removed prior to the FFT. This is called 'aliasing' and is well covered in the literature. As will be evident in the velocity spectrum shown later, the filter at 12.5K was relatively unimportant, since very little energy is present above frequencies of 5KHz.

The FFT is the numerical counterpoint to the fourier transform and is used here as an engineering tool to look for standout features in the flow turbulence. The subroutine SSWD form the IMSL library was used estimate the spectral density of the turbulence. The IMSL literature should be refernced for further details on this particular FFT.

There are different ways to define the power spectral density. In this case, the power spectral density is defined for zero and discrete positive frequencies only and its sum over these frequencies is the fluctuation mean squared amplitude. In addition, the power spectral density is presented in Figure 10.5 and 10.6 in integral form, where the density is divided by the discretized frequency spacing. As expected from working with the low pass filters in conjunction with the RMS voltmeter, the majority of the turbulence is at a frequency below 5KHz for the 50 m/s case and below 1KHz for the 30 m/s. This validates the use of a 25KHz sampling rate and the imposed Nyquist frequency of 12.5 KHz.

The only other comment on these two spectra is that no outstanding features exist and no single frequency or frequencies dominates the spectrum.

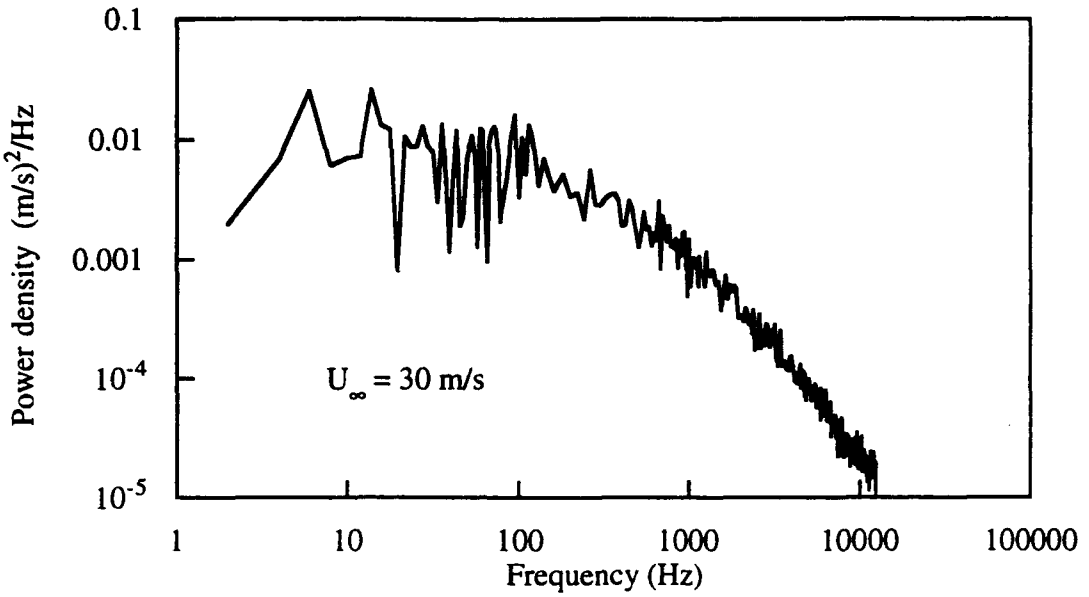

Figure 10.5 Turbulent velocity spectrum, U_∞=30.5m/s

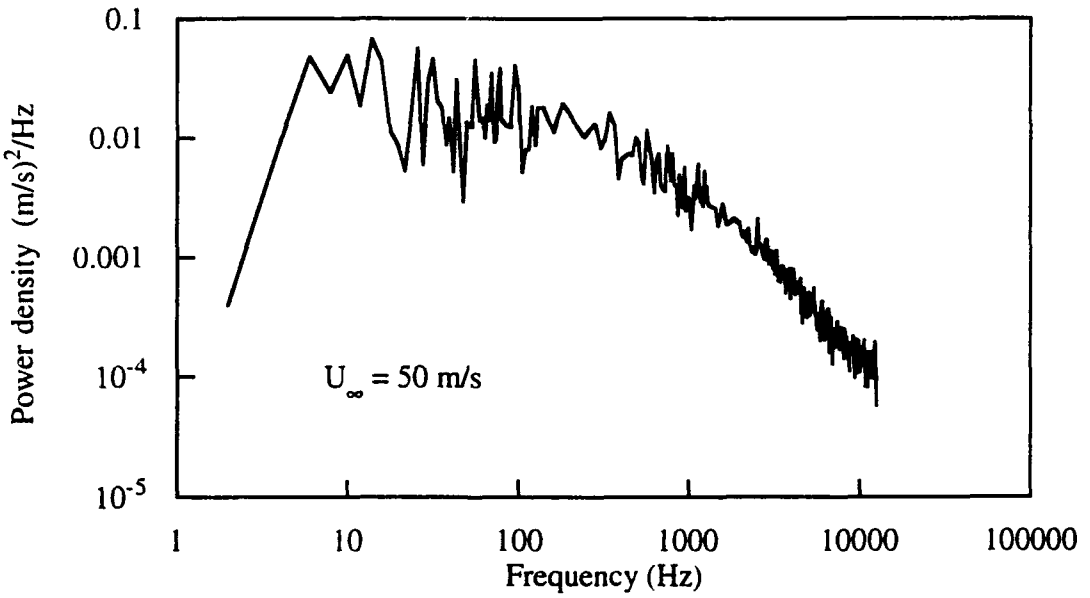

Figure 10.6 Turbulent velocity spectrum, U_∞=50m/s

CHAPTER 11
EFFECT OF DIMENSIONLESS BOUNDARY LAYER DISPLACEMENT THICKNESS ON FILM COOLING EFFECTIVENESS

11.1 Introduction

As described in Chapter 1 and applied in determining the film hole size for the test surface in this study, researchers have reported the boundary layer thickness at the point of cooling injection plays an important part in determining the film cooling effectiveness. While this work could have been reported in terms of either dimensionless boundary layer displacement or momentum thickness, Goldstein et al. (1970) and Liess (1975) both chose to use displacement thickness. Therefore, the data presented here are also cast in terms of dimensionless boundary layer displacement thickness.

For this investigation, the centerline data from Chapter 5 are compared against data taken using the three hole Plexiglas plate used in Chapter 7.

For both sets of tests the entrance velocity is 30 m/s producing a velocity of 30.5 m/s at the film injection point, 2.25 inches from the splitter plate. This provides a Reynolds number (Re_x) at the point of injection of $9.6x10^4$ based on distance from the leading edge of the splitter plate. The displacement thickness (δ_1) for both test plates is 0.00836" at the point of injection, in the absence of cooling flow, based on the measurement presented in Chapter 4. The eight hole Plexiglas plate, used in Chapter 5, has a round film hole diameter of 0.00674" providing a δ_1/D of 0.124. The three hole Plexiglas plate has a round hole diameter of 0.213" providing a δ_1/D of 0.0040. For this comparison, data for each configuration is taken for a

blowing ratio of 0.5 and 1.0. The test rig setup is as in Figure 2.8 and data reduction is accomplished as described in Chapter 2.

11.2 Results

Figures 11.1 and 11.2 show the centerline film cooling effectiveness for the two dimensionless boundary layer displacement thicknesses at blowing ratios of 0.5 and 1.0. Along with the experimental results of this study are values presented by Goldstein et al. (1970). This work was also conducted at a mainstream velocity of 30 m/s and for the δ_1/D as shown. The data indicates a definite trend, the η decreases as the dimensionless boundary layer thickness increases. This trend appears reasonable and is explained in the following manner by Goldstein et al. (1970), " as the injected air enters the mainstream boundary layer, it encounters a higher relative velocity at positions closer to the wall for a thinner boundary layer. This would have the effect of turning the injected air more rapidly, decreasing its penetration, and therefore leading to higher values of the film cooling effectiveness."

The data of Goldstein and the results of this study show general agreement. The centerline η for M=0.5 for the δ_1/D=0.04 drops off much more rapidly than does the Goldstein results. This difference most likely occurs because of the difference between mainstream turbulence levels for the two experiments.

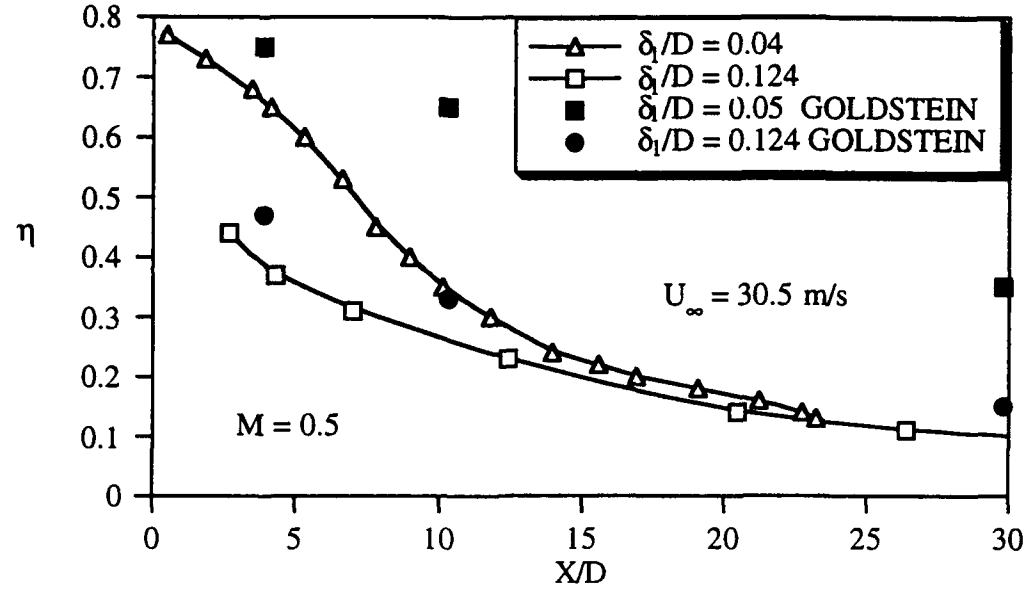

Figure 11.1 The effect of dimensionless boundary displacement thickness on centerline film cooling effectiveness, M=0.5

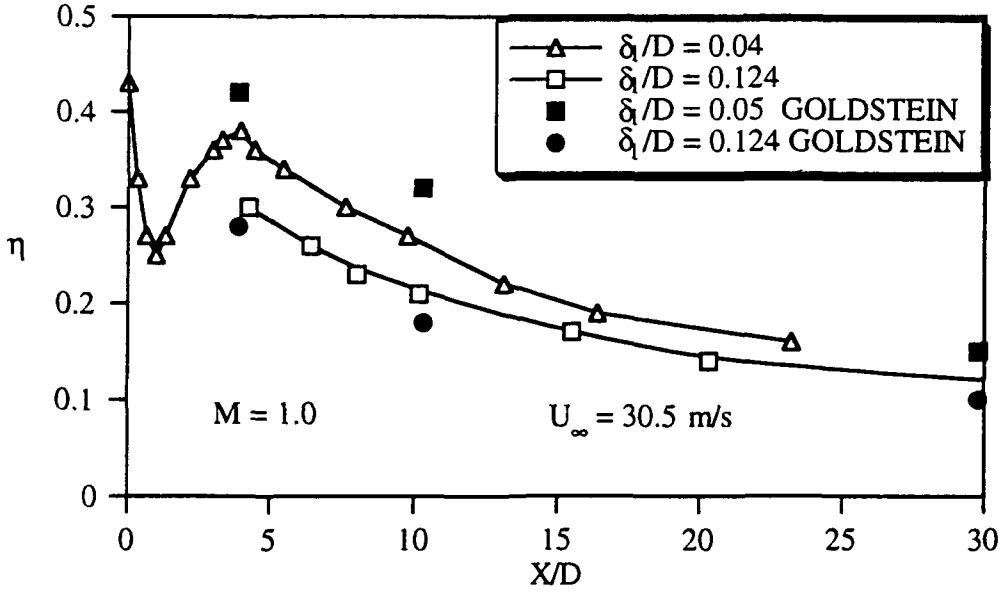

Figure 11.2 The effect of dimensionless boundary displacement thickness on centerline film cooling effectiveness, M=1.0

As discussed in more detail in Chapter 5, Goldstein's work is conducted in an open cycle wind tunnel with a mainstream turbulence level of 0.5%. The work in this study has a mainstream turbulence level of 6.5%. This higher turbulence level has the effect of diluting the film jet more quickly and results in a steeper drop-off of effectiveness downstream of film injection. This difference would be expected to be most dramatic for low blowing ratios and thin boundary layers.

Somewhat contrary to the results in Figures 11.1 and 11.2, Liess (1975) found the same general trend in his work, but found for $\delta_1/D<0.2$ the influence of boundary layer thickness is small. Liess cited the work by Goldstein et al. (1970), but did not explain the discrepancies between his study and the work of Goldstein. This study shows general agreement with the Goldstein work.

This influence on dimensionless boundary layer thickness is shown in Figure 11.3 as a ratio of the $\delta_1/D=0.04$ centerline effectiveness ($\eta_{0.04}$) to that of the $\delta_1/D=0.124$ centerline effectiveness ($\eta_{0.124}$). The effect of the displacement thickness is largest for the lower blowing ratio case and within ten hole diameters of the point of injection. It does appear reasonable the higher blowing ratios will penetrate the boundary layer less affected than would a slower velocity jet.

The effect of dimensionless boundary layer displacement thickness on centerline convective heat transfer coefficient is shown in Figure 11.4. For the M=1.0 case little influence is seen, but for the M=0.5 case, centerline h is affected by as much as 13%.

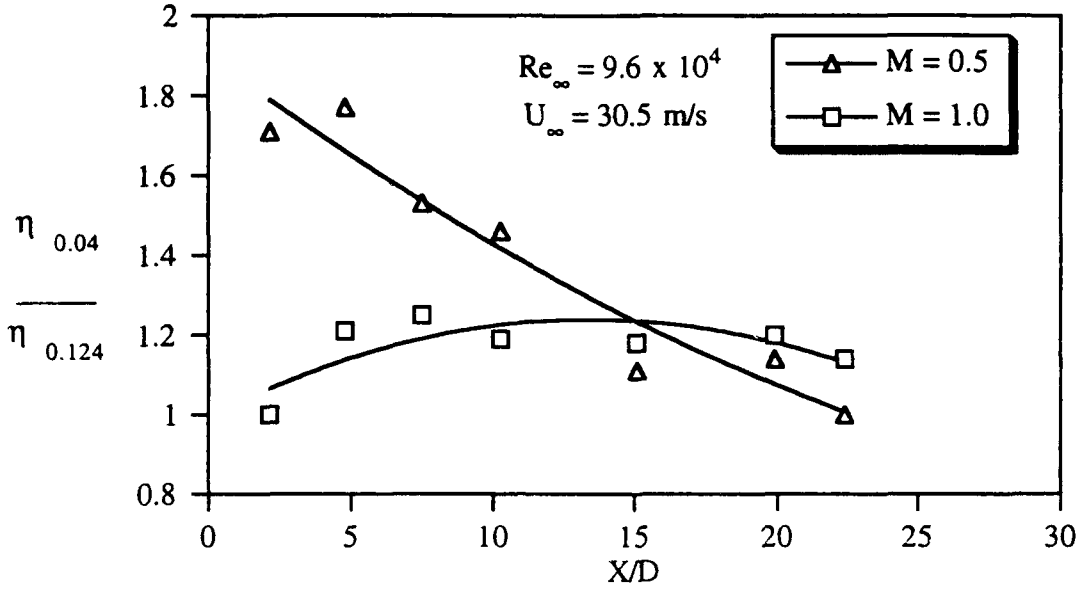

Figure 11.3 The effect of dimensionless boundary displacement thickness on centerline film cooling effectiveness, displayed as the ratio of $\eta_{0.04}$ to $\eta_{0.124}$

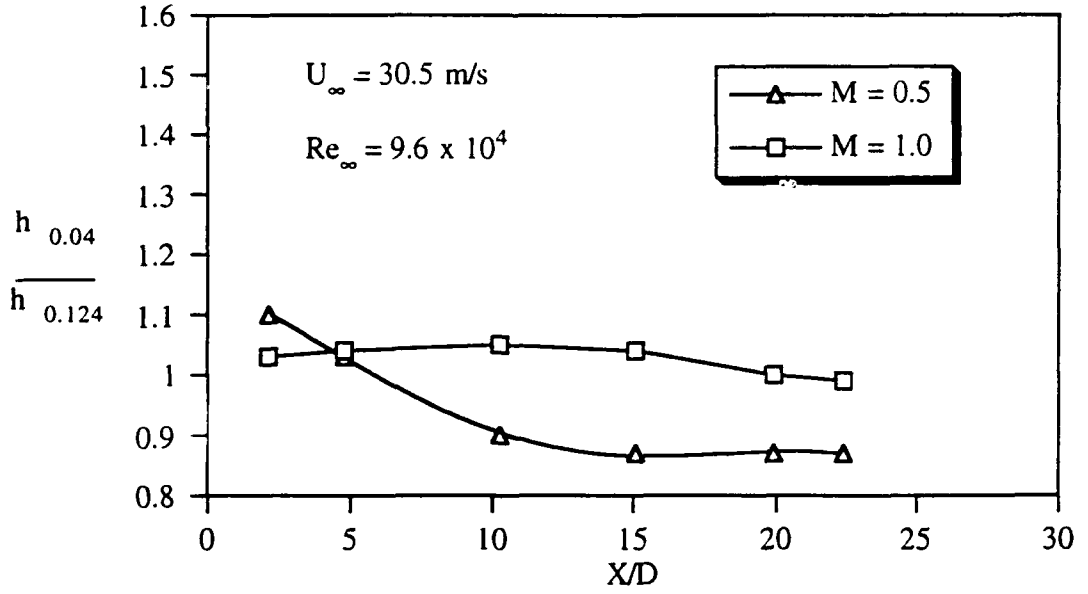

Figure 11.4 The effect of dimensionless boundary displacement thickness on centerline convective heat transfer coefficient

Interestingly, both the film cooling effectiveness and convective heat transfer coefficient trends indicate, for M=0.5, a thinner boundary improves the performance of film cooling. This is good news for turbine designers since, for the first stage turbine vane, δ_1/D is on the order of 0.05.

CHAPTER 12

CONCLUSIONS AND FUTURE CONSIDERATIONS

12.1 Summary and Conclusions

This study focuses on obtaining information on the effects of surface roughness on a film cooled surface which models conditions present on the pressure side of a typical high performance first stage turbine vane. Drawing upon the ideas of Metzger and Larson (1986), Vedula (1989), and Kim (1992) the experimental apparatus and test model necessary to successfully apply the TLC techniques to a rough composite plate have been presented. This model includes a composite plate where TLC is applied to backside of a thin stainless steel plate roughened to specific specifications on the front side. The TLC layer is overlaid with an epoxy layer, which acts as a semi-infinite solid and permits visual access to the TLC layer. A lumped capacitance correction model is applied to the system of equations used to resolve the convective heat transfer coefficients and film cooling effectiveness of the film cooled flat plate. This method provides, for the first time, simultaneous information on h and η for a film cooled rough surface. Previous work by researchers on film cooled rough surfaces provided only effectiveness values.

In order to reduce the uncertainty of the experimental model, a method termed normalized threshold is introduced to improve the calibration of the TLC. This concept improves dramatically the calibration uncertainty of the method employed in this study.

To ensure the film cooling studies are appropriate, and recognizing the influence of dimensionless boundary layer momentum thickness on

convective heat transfer data, the film cooling holes are sized based on boundary layer velocity measurements. A δ_2/D is used for the tests which match those found in actual turbine vanes.

To validate the approach several steps are taken. First, the semi-infinite solid/TLC approach taken by Vedula (1989) and Kim (1992) and used extensively in this study is validated by comparing heat transfer performance with that found by Goldstein et al. (1970) and Erik ldstein (1974). A finite difference numerical study is conducted to assess a modified model including a lumped capacitance correction to account for energy stored in the stainless steel rough surface. To further assess this model, an experimental comparison of heat transfer information, h and η, obtained using the composite test plate, with a smooth stainless surface, is compared to the results from tests using the conventional Plexiglas test surface.

As confirmation of the importance of matching dimensionless boundary layer thickness, tests are conducted on film cooled Plexiglas surfaces with two different hole diameters for two blowing ratios. This work is compared to the work of previous investigators.

Turbulence plays an extremely important part in determining the convective heat transfer characteristics of the film cooling cases investigated. Mainstream flow turbulence is measured using hot wire techniques. Turbulence levels approaching those present in actual turbine engines are documented for this study.

The effect of roughness on convective heat transfer coefficients in the absence of film cooling is documented for two roughness element heights of 0.022" and 0.045". These surfaces have average roughness values of 0.0040"

and 0.0071". The results are analyzed and compared to the empirical relationship for Stanton number reported by Kays and Crawford (1980).

Finally, film cooling effectiveness and convective heat transfer coefficients are determined for a Reynolds number and dimensionless boundary layer momentum thickness matching conditions found on the pressure side of the P&W F-100 first stage turbine vane. Tests are conducted for blowing ratios of 0.4, 0.5, 0.75, 1.00 and 1.25 on both the Ra=0.0040" and Ra=0.0071" surfaces. Based on this series of experimental tests the following conclusions are made.

- Use of liquid crystals to determine local heat transfer characteristics is well documented in previous work and provides a relatively inexpensive method of determining h and η in detailed resolution for both simple and complex test sections.

- Use of a two test method, in which two very similar tests are run with only a variation in film temperature, provides reliable, repeatable results for the three temperature problem. These results compare well with the work of other investigators using different experimental techniques (mass transfer analogy and adiabatic wall methods).

- In conducting liquid crystal response measurements, green is clearly the color of choice. It provides nearly noise-free results when compared to either red or blue. Blue in general provides unacceptable results.

- A fixed threshold method, to determine transient TLC temperature response, provides reliable heat transfer information only in areas of the test section where background intensity is similar to those of the calibration area.

- Normalized threshold methods provide temperature accuracies for the TLC green response on the order of $\pm 0.2^{\circ}F$ over widely varying background intensities.

- The video taping process provides an excellent system to extend this visual method without significant degradation of the acquired convective heat transfer information.

- The thickness of Plexiglas or epoxy between the camera and test section TLC surface affect the calibration temperature of the liquid crystal and must be accounted for during TLC calibration.

- The single test transient method, for simultaneously determining h and η from a transient test, as currently envisioned, is not viable.

- Experimental results of two-temperature convective heat transfer coefficients match those of prior investigators, as represented by the Chilton-Colburn relationship extremely well. This close match provides confidence in the experimental technique.

- The influence of mainstream turbulence level is clearly evident in matching experimental data. Turbulence levels of 6.5% and 8.5% used in this

study approach those found in actual engine turbine sections. Higher turbulence levels result in overall lower film cooling effectiveness values and is attributed to a greater rate of destruction of the integrity of the film jet and greater dilution of the cooling flow.

- Finite difference analysis of the lumped capacitance/semi-infinite solid model, used to reduce data from tests on the stainless steel/epoxy composite plate, provides confidence that results are generally correct. The model provides laterally averaged heat transfer coefficients within 5% of those imposed during numerical experiments and laterally average film cooling effectiveness within 0.02 to 0.03 when locations further downstream of five hole diameters are considered for M=0.5. For higher blowing ratios, the match is even better. The heat transfer coefficients, based on the planar surface area rather than the wetted roughness area, provided by this model, account for the energy into the roughened surface to within approximately 3% for the Ra=0.0040" surface and within 5% for the Ra=0.0071" surface. This comparison provides confidence in the experimental model.

- Based on the comparison of the smooth surface composite plate with the traditional Plexiglas model, several conclusions are reached. First, thermal gradients are not severe enough for two temperature (nom-film cooling) cases for lateral conduction within the stainless steel to significantly affect the determined convective heat transfer coefficients. Heat transfer coefficients for this case should be considered very reliable. This included the two temperature tests for the composite plate with rough surfaces, which should be relatively free of lateral conduction errors.

- For the three temperature problem (film cooled surface), the thermal gradients are larger and therefore, so is the associated lateral conduction. This fact limits the usefulness of local results from the composite plate within five hole diameters of the point of film injection. This is unfortunate, but not disastrous, since film cooling must be designed to meet cooling needs beyond five hole diameters. The region within five hole diameters is more than adequately cooled. Downstream of X/D=5.00, the centerline film cooling effectiveness, laterally averaged effectiveness, and laterally averaged convective heat transfer coefficients compare fairly well. There is a negative bias in effectiveness on the order of 0.02 to 0.03 for the composite plate and a negative bias in $\bar{h}$ of no greater than 10% between five and fifteen hole diameters downstream of the point of film injection.

- The effect of dimensionless boundary layer thickness on film cooling performance is clear. With other flow parameters set equal, film cooling effectiveness decreases as the dimensionless boundary layer displacement thickness increases. As injected air enters the mainstream boundary layer, it encounters a higher relative velocity at positions closer to the wall for a thinner boundary layer. This has the effect of turning the injected flow more rapidly, decreasing its penetration, and leads to higher values of film cooling effectiveness. This leads to the conclusion when setting up a test to model a certain film cooling situation, in addition to matching flow parameters and turbulence levels, it is equally important to match boundary layer thickness relative to film injection hole diameter.

- For the two-temperature rough surface tests, it is clear a tremendous penalty is paid in terms of heat transfer to the surface for increased roughness. The Ra=0.0040" surface showed an increase of 70% over a smooth surface at the same flow conditions, while for the Ra=0.0071" surface this increase was as high as 120%. This increase was much greater than the increase wetted surface area of the rough surfaces compared to the planar area of the surface. The conclusion here is the increase in h is due to more than the effect of increased heat transfer area. In this case, the energy transport in the boundary layer has been enhanced by the increased turbulence levels near the surface.

- Experimental Stanton numbers compare well with those predicted by an empirical relationship presented by Kayes and Crawford (1980). In carrying out this comparison velocity measurements showed as expected, a large velocity deficit near the surface for the rough surfaces as compared to a smooth surface. This deficit increased with roughness. This translates into larger momentum and displacement thicknesses for the rough plate. Equivalent roughness values (k_s), where 2.3 and 3.0 times larger than the actual roughness height. This is in line with the results published by Schlichting (1963). Based on the match between the empirical and experimental data, Kays and Crawford's (1980) empirical correlation for Stanton number appears to be an excellent analytical tool and, on the flip side, tend to validate the experimental model used here.

- For the range of blowing ratios investigated, the presence of roughness causes a decrease in the film cooling effectiveness over that of the smooth

surface. The presence of roughness induces more vigorous mixing between the mainstream and the secondary flows near the wall, decreasing the effectiveness due to greater dilution of the cooling flow.

- The presence of roughness apparently reduces the phenomena of "blow-off", which helps improve downstream effectiveness for the higher blowing ratios.

- For the blowing ratios investigated, the centerline effectiveness for the rough surface is significantly lower than the smooth surface just downstream of injection. However, the rate of decrease in effectiveness is much less for the rough surface. At locations beyond fifteen hole diameters downstream, there is little difference between the centerline effectiveness values. In fact, the Ra=0.0071" film cooling effectiveness values are greater than those for the smooth surface past X/D=15.0, indicating more film flow air is retained in the rough surface boundary layer.

- The other effect, which accompanies the higher mixing associated with the rough surfaces, is that the variation of η across the span is much less for the rough surfaces than a smooth surface. This smoothing is greatest for the roughest surface, again indicating the higher turbulence near the surface for the rougher surfaces.

- Overall, film cooling has a detrimental affect on laterally averaged convective heat transfer coefficients. This is true for both smooth and rough surfaces. For a smooth surface the area averaged heat transfer coefficient can

increase as much as 20% to 30% with blowing ratios from 0.5 to 1.25. For the rough surfaces investigated here, the increase in heat transfer is lower for the same blowing ratios, 3% to 21%. The difference is attributable to the high level of turbulence already present for the rough surface. As a result, the impact of the film cooling jets on further increasing the turbulence level is less significant than for the smooth surface.

This study has for the first time experimentally determined both film cooling effectiveness and convective heat transfer coefficients simultaneously for a rough film cooled surface. This work should prove valuable for those investigating this area and to those involved with turbine cooling design.

12.2 Recommendations

Investigators working in this area must be acutely aware of the impact of turbulence levels and dimensionless boundary layer thickness on heat transfer results. Results from tests where these parameters are not documented are less useful.

Future work in this area would benefit from a detailed boundary layer analysis. This work provided only an analysis of the uncooled boundary layer flow in order to size the film holes appropriately. A detailed study of the boundary layer downstream of cooling injection for a rough surface in comparison to a smooth surface would provide greater insight into the fluid mechanics which determine the film cooling effectiveness and heat transfer coefficients. Tannder and Yock (1974) indicate effectiveness downstream of injection is highly influenced by the transition of the film jet from laminar to turbulent flow. This type of analysis should ,therefore, include hot wire

measurements of the flow just downstream of injection for both a rough and smooth surface.

This study was limited to roughness heights which do not exceed the smooth surface boundary layer thickness. The surface roughness investigation by Tabbita (1993) found roughness present on some areas of the first stage vane matched or exceeded the smooth surface boundary layer thickness. It would, therefore, be useful to extend this investigation to larger roughness elements. In this study, roughness height approached 60% of the smooth boundary layer thickness. The Ra=0.0071" surface, investigated in this study, had better effectiveness values than the Ra=0.0040" surface. If this trend held true for an even rougher surface, effectiveness values greater than a smooth surface might be obtained. Unfortunately, the trend of greater convective heat transfer coefficients with roughness would be expected to hold true, with the net result being an increased heat load to the surface.

The turbine engine industry is increasingly becoming interested in non-circular film cooling holes. These alternate configurations have the potential of improved film cooling coverage. The type of investigation could easily be applied to those types of configuration. In service, roughness and its effects will always be present and must be accounted for.

REFERENCES

Dipprey, D.F., and Sabersky, D.H.,1963, "*Int. J. of Heat and Mass Transfer*, Vol 6, pp. 329-353.

Eckert, E.R.G., 1971, "Film Cooling With Injection Through Holes," *High Temperature Turbines*, AGARD-CP-73-71, pp. 23-1-23-9.

Eriksen, V.L., and Goldstein R.J., 1974, "Heat Transfer and Film Cooling Following Injection Through Inclined Circular Holes," *ASME Journal of Heat Transfer*, Vol.96, May, pp. 239-245.

Goldstein, R.J., 1971, "Film Cooling, Advances in Heat Transfer", Academic Press, New York, Vol. 7, pp. 321-379.

Goldstein, R.J., Eckert, E.R.G., and Wilson, D.J., 1968, "Film Cooling," *J. Eng. Ind.* 90, 584.

Goldstein, R.J., Eckert, E.R.G., Eriksen, V.L., and Ramsey J.W., 1970, "Film Cooling Following Injection Through Inclined Circular Tubes," *Isreal Journal of Technology*, Vol. 8, No. 1-2, pp. 145-154.

Goldstein, R.J., Eckert, E.R.G., Chiang, H.D., and Elovic, E.,1985, "Effect of Surface Roughness on Film Cooling Performance," *ASME Journal of Engineering for Gas Turbines and Power*, Vol. 107, pp. 111-116.

Incropera, F.P., and DeWitt, D.P., 1985, "Fundamentals of Heat and Mass Transfer," John Wiley & Sons, New York, 1985.

Ireland, P.T. and Jones, T.V., 1985, "The Measurement of Local Heat Transfer Coefficients in Blade Cooling Geometries," AGARD Conference on Heat Transfer and Cooling in Gas Turbines, CP 390, Paper 28, Bergen.

Ireland, P.T. and Jones, T.V., 1987, "The Response Time of a Surface Thermometer Employing Encapsulated Thermochromic Liquid Crystals," *Journal of Physics* E, 20, pp.1195-1199.

Jumper, G.W., 1987, "Film Cooling Effectiveness on a Flat Plate in High Free-Stream Turbulence Using a Single Row of 30 Deg. Slant-Hole Injectors," M.S. Thesis, USAF Institute of Technology.

Kays, W.M. and Crawford, M.E., 1980, "Convective Heat and Mass Transfer," McGraw-Hill Publishing Company, New York.

Kim, Y.W., 1992, "Experimental Studies of Convective Heat Transfer on Rotating Disks and Mainstream Entrainment into Disk Cavities," Ph.D. Dissertation, Arizona State University.

Kim, Y.W., and Metzger, D.E., 1993, "Heat Transfer and Effectiveness on Film Cooled Turbine Blade Tip Models, International Gas Turbine and Aeroengine Congress and Exposition, Cincinnati, Ohio, 93-GT-208.

Kline, S.J., and McKlintock, F.A., 1953, "Describing Uncertainties in Single Sample Experiments," Mechanical Engineering, Vol. 75, pp. 3-8.

Ko, S., and Liu, D., 1980, "Experimental Investigations on Effectiveness, Heat Transfer Coeffiecient, and Turbulence of Foilm Cooling," *AIAA Journal*, Vol. 18, No. 8, pp. 907-913.

Launder, B.E., and York,J., 1974,"Discrete-Hole Cooling in the Presence of Free Stream Turbulence and Strong Favorable Pressure Gradient," *Int. Journal of Heat and Mass Transfer*, Vol. 17, pp. 1403-1409.

Liess, C., 1975,"Experimental Investigation of Film Cooling with Ejection From a Row of Holes for the Application of Gas Turbine Blades," *ASME Journal of Engineering for Power*, Vol. 97, Jan., pp. 21-27.

Mehendale, A.B., and Han, J.C., 1992, "Influence of High Mainstream Turbulence on Leading Edge Film Cooling Heat Transfer," *ASME Journal of Turbomachinery*, Vol. 114, Oct., pp. 707-715.

Metzger, D.E., Carper, H.J., Swank, L., 1968, "Heat Transfer With Film Cooling Near Nontangential Injection Slots," *ASME Journal of Engineering for Power*, April, pp. 157-163.

Metzger, D.E., and Fletcher, D.D., 1971, "Evaluation of Heat Transfer for Film Cooled Turbine Components," *Journal of Aircraft,* Vol. 8, N. 1, pp. 33-38.

Metzger, D.E. and Larson, D.E., 1986, "Use of Fusion Point Surface Coatings for Local Convection Heat Transfer Measurements in Rectangular Channel Flows with 90-Degree Turns," *Journal of Heat Transfer, Trans. ASME*, 108, pp. 48-54.

Metzger, D.E., Kim, Y.W., Fan, C.S., and Ward, D., 1992, "Computer Vision Measurement of Local Convection Heat Transfer," Proceedings of Colloquium on Turbomachinery - 1992, organized by Turbo and Power Machinery Research Center, Seoul National University, Seoul, Korea.

Myers, G.E., 1971, :Analytical Methods in Conduction," McGraw Hill, New York.

Ni Kuradse, J. 1933, "Stromunggesetze in rauhen Rohren," Forschg. Arb. Ing. Wes. N. 361.

Nishiwaki, N., Hiratta, M., and Tsuchida, A., 1961, ASME "International Developments in Heat Transfer," part IV, pp.675.

Oates, Gordon C., 1985, "Aerothermodynamics of Aircraft Engine Components", AIAA Education Series, New York.

Ou, S., Mehendale, A.B., and Han, J.C., 1992, "Influence of High Mainstream Turbulence on Leading Edge Film Cooling Heat Transfer Effect of Film Hole Row Location," *ASME Journal of Turbomachinery*, Vol. 114, pp. 716-723.

Patankar, S.V., 1980, "Numerical Heat Transfer and Fluid Flow," McGraw-Hill Publishing Company, New York.

Pimenta, M.M., Moffat, R.J., and Kays, W.M., 1975, NASA Rep. No. HMT-21, Department of Mechanical Engineering, Stanford Universaity.

Scesca, S., 1943, "Effect of Local Normal Injection on Flat Plate Heat Transfer," Ph.D. Dissertation, University of California, Berkeley.

Schlichting, H., 1936, "Experimentelle Untersuchungen zum Rauhigkeitsproblem," *Ingenieur - Archiv*, Vol. 7, pp. 1-34.

Schlichting, H., 1979, "Boundary-Layer Theory," McGraw-Hill Book Company, New York.

Tabbita, Martin G., 1993, "Results of F-100-PW229 Surface Roughness Investigation," Internal Correspondence, United Technologies Pratt & Whitney.

Vedula, R.P., 1989, "Film Cooling Effectiveness and Heat Transfer Measurements Using Thermochromic Liquid Crystals," Ph.D. Dissertation, Arizona State University, Tempe Arizona.

Vedula,R.P., Bickford, W., and Metzger, D.E., 1988, "Effects of Lateral and Anisotropic Conduction on Determination of Local Convection Heat Transfer Characteristics with Transient Tests and Surface Coatings," Collected Papers in Heat Transfer, ASME Publication HTD-14, pp.21-27.

Vedula, R.P., and Metzger, D.E., 1989, "Measurement of Local Film Cooling Performance with Flow Over a Backward Facing Step," 24th AIAA Thermophysics Conference, June 1989

Wieghardt, K., 1943, "Hot Air Discharge for De-Icing," AAF Translation No. 24536, original in *Deutshe Tuftfahrforsching*, Forchangsbericht, Vol. 1900.

APPENDIX A

THREE TEMPERATURE SOLVER

```
      EXTERNAL F,F1,F2,F3
      REAL TM(120),TAU(120),TM1(120),time1,time2,diff,
     &TFI(120),NUX(160,75),NUX1(160,75),timelag,timelag2
      REAL HCOEF(160,75),ECOEF(160,75),TFI1(120),a,b
      COMMON ETA1,H1,TW1,TW2,TI,ALPHA,AK,T,TMELT1,TM,TAU
     6,TMELT,TINIT,TINI1,TM1,TFILM,TFIL1,TFI,TFI1
     7,rho,cp,thick
C
C
C*****************************************************************
C       3 Temperature Iterative Solver
C
C       Program written by Yong Kim and Yufeng Yu at
C       Arizona State University to solve the 1-dimension
C       conduction problem  for the convective heat transfer
C       boundary condition using wall temperature obtained
C       using TLC and visual aquisition system
C
C     Modified by Neal Barlow to include a time lag correction using
C     lump capacitance and documentation added for entire program
C           22 Mar 1994/ASU
C       This version assumes 100 Duhamel time steps
C
C      ************************************************************
C       Alpha  - thermal diffusivity - meters**2/sec
C       AK     - thermal conductivity - Watts/(meters * K)
C       ct     - highest allowable time lag for hot run
C       dt     - highest allowable time lag for cold run
C       bh     - highest allowable h
C       la1    - pixel matrix - low x coordinate
C       la2    - pixel matrix - high x coordinate
C       lb1    - pixel matrix - low y coordinate
C       lb2    - pixel matrix - high y coordinate
C       tw1    - Hot temperature run calibration temp - F
C       tw2    - Cold temperature run calibration temp - F
C       tini1  - initial cold run main flow temp - F
C       tfil1  - initial cold run film flow temp - F
C       tint   - initial hot run main flow temp - F
C       tfilm  - initial hot run film flow temp - F
C       tau(I) - array - time
C       tm1(I) - array - cold test main flow temp
C       tfi1(I) - array - cold test film flow temp
C       tm(I)  - array - hot test main flow temp
C       tfi(I) - array - hot test film flow temp
C       hcoef(I)- array - calculated h data (Watts/(meters**2 * K)
C       ecoef(I)- array - calculated effectiveness for each pixel
C       tmelt  - temporary storage location for nux data
C       nux(1) - pixel matrix of time for each pixel to reach tw1(tw2)
C       NKOTA        - size of surface in pixel space - x coordinate
C       NKOTB        - size of surface in pixel space - y coordinate
C       tol    - tolerance for zeroin subroutine
C      thick - wetted surface area of the stainless steel surface(m)
```

```
C     rho   - density of stainless steel(Kg/m**3)
C     cp    - heat capacity of stainless steel 304 (J/(Kg K)
C     ********************************************************
      ALPHA=.1073E-6
      AK=.187
       rho=7900.0
       cp=477.0
       thick=1.900e-4
C
*****************************************************************
***
C       Read in initial temperatures and test surface info
C
*****************************************************************
***
          write(6,*) 'input max h,min x, max x, min y, max y'
          read(5,*) bh,la1,la2,lb1,lb2
          write(6,*) 'input max allowable hot time lag and cold time lag'
          read(5,*) ct,dt
          write(6,*) 'input hot test run calibration temp - tw1'
          read(5,*) tw1
          write(6,*) 'input cold test run calibration temp - tw2'
          read(5,*) tw2
      open(1,file='tem1.dat',
     &form='formatted')
          read(1,*) tini1,tfil1,tinit,tfilm
      DO 29 I=1,100
          read(1,*) tau(i),tm1(i),tfi1(i),tm(i),tfi(i)
          tm1(i)=tm1(i)
          tm(i)=tm(i)
          tfi1(i)=tfi1(i)
          tfi(i)=tfi(i)
   29 CONTINUE
      TOL=1.E-9
      AH=0.
      AETA=0.00
      BETA=1.
      NKOTA=65
      NKOTB=25
C
*****************************************************************
***
C       Read in each pixels time data for hot and cold runs
C     ******************
***********************************************
      open(2,file='hot.time',
     &form='formatted')
      DO 101 J=1,NKOTB
101   READ(2,*)(NUX(I,J),I=1,NKOTA)
      open(3,file='cold.time',
     &form='formatted')
      DO 102 J=1,NKOTB
```

```
102  READ(3,*)(NUX1(I,J),I=1,NKOTA)
     open(4,file='h.dat',
    xform='formatted')
     open(9,file='eta.dat',
    xform='formatted')
C
*****************************************************************
C       Calculations start
C
*****************************************************************
*****
     DO 201 IJK=lB1,lB2
        write(6,*)ijk
        do 202 i=la1,la2
        write(6,*)i
     TMELT=NUX(I,IJK)
        time1=nux(i,ijk)
     TMELT1=NUX1(I,IJK)
c       write(6,*)Tmelt,tmelt1
C
*****************************************************************
******
C       Skip unwanted data points (pixels)
C
*****************************************************************
***********
     IF((TMELT.GE.120.).OR.(TMELT1.GE.120.))THEN
     H1=0.
        HL=0.0
     ETA1=0.
     GO TO 209
     ENDIF
     IF((TMELT.LE.5.0).OR.(TMELT1.LE.5.0))THEN
     H1=0.
        HL=0.0
     ETA1=0.
     GO TO 209
     ENDIF
C
*****************************************************************
******
C       provide initial guess and call ZEROIN to calculate h
C       from hot test time and temperatures
C
*****************************************************************
******
     H1=0.
     H2=0.
     ETA1=0.
     ICOUNT=0
        Icount2=0
 200 H=ZEROIN(AH,BH,F,TOL)
```

```
c       write(6,*)H
      H1=H
C
*****************************************************************
****
C     Provide initial guess and call ZEROIN to calculate time lag
C       for hot test at each pixel
C
*****************************************************************
********
      timelag=ZEROIN(AH,CT,F2,TOL)
c       write(6,*)'timelag=',timelag,'eta=',eta1,'Ic=',Icount
c       read(5,*)n
        time2=nux(I,IJK)-timelag
        diff = abs(time1-time2)
        time1=time2
        tmelt = time2
        icount2=icount2+1
C
*****************************************************************
****
C       iterate on h and time lag until convergence
C
*****************************************************************
***
        if(Icount2.gt.10) go to 700
        if(diff.gt.0.009) go to 200
c*****************************************************************
******
C       correct tmelt1 for time lag, cold temperature test
C*****************************************************************
********
700     icount2=0
        timelag2 = ZEROIN(AH,DT,F3,TOL)
c       write(6,*)'timelag2=',timelag2
        tmelt1 = nux1(I,IJK) - timelag2
c       if(Icount.gt.21)go to 300
C
*****************************************************************
*******
C       using new h call ZEROIN to calculate eta from the cold test
C
*****************************************************************
*********
      ETA=ZEROIN(AETA,BETA,F1,TOL)
C
*****************************************************************
**********
C       iterate on h and eta until conve ence or for 200 tries
C
*****************************************************************
**********
```

```
      iF(ABS(H2-H).LE.1.000)GO TO 300
c          if(Icount.eq.8)a=eta
c          if(Icount.eq.9)b=eta
      H2=H
      ETA1=ETA
c          if(Icount.eq.9)ETA1=(a+b)*0.4
      ICOUNT=ICOUNT+1
      IF(ICOUNT.GT.200)GO TO 300
          tmelt = nux(I,IJK)
          time1 = nux(I,IJK)
      GO TO 200
  300 CONTINUE
  209 CONTINUE
      HCOEF(I,IJK)=H1
      ECOEF(I,IJK)=ETA1
c     write(6,*) h1,eta1
  202 CONTINUE
C
*****************************************************************
C          print to h.dat and eta.dat
C
*****************************************************************
*
      WRITE(4,99)(HCOEF(IKK,ijK),IKK=la1,la2)
   99 FORMAT(' ',10(F6.1))
      WRITE(9,98) (ECOEF(IKK,ijK),IKK=la1,la2)
   98 FORMAT(' ',10(F6.2))
  201 continuE
      STOP
      END
C
*****************************************************************
*****
C          Subroutine to zero out the function f to find either h or eta
C
*****************************************************************
*******
      REAL FUNCTION ZEROIN(AX,BX,F,TOL)
      REAL TM(120),TAU(120),TM1(120),TFI(120),TFI1(120)
      COMMON ETA1,H1,TW1,TW2,TI,ALPHA,AK,T,TMELT1,TM,TAU
     6,TMELT,TINIT,TINI1,TM1,TFILM,TFIL1,TFI,TFI1
     7,rho,cp,thick,HL
      REAL A,B,C,D,E,EPS,FA,FB,FC,TOL1,XM,P,Q,R,S
      EPS=1.0
   10  EPS=EPS/2.
      TOL1=1.+EPS
      IF(TOL1 .GT. 1.) GO TO 10
      A=AX
      B=BX
      FA=F(A)
      FB=F(B)
   20  C=A
```

```
      FC=FA
      D=B-A
      E=D
   30 IF(ABS(FC) .GE. ABS(FB)) GO TO 40
      A=B
      B=C
      C=A
      FA=FB
      FB=FC
      FC=FA
   40 TOL1=2.*EPS*ABS(B)+.5*TOL
      XM=.5*(C-B)
      IF(ABS(XM) .LE. TOL1) GO TO 90
      IF(FB .EQ. 0.) GO TO 90
      IF(ABS(E) .LT. TOL1) GO TO 70
      IF(ABS(FA) .LE. ABS(FB)) GO TO 70
      IF(A .NE. C) GO TO 50
      S=FB/FA
      P=2.*XM*S
      Q=1.-S
      GO TO 60
   50 Q=FA/FC
      R=FB/FC
      S=FB/FA
      P=S*(2.*XM*Q*(Q-R)-(B-A)*(R-1.))
      Q=(Q-1.)*(R-1.)*(S-1.)
   60 IF(P .GT. 0.) Q=(-Q)
      P=ABS(P)
      IF((2.*P) .GE. (3.*XM*Q-ABS(TOL1*Q))) GO TO 70
      IF(P .GE. ABS(.5*E*Q)) GO TO 70
      E=D
      D=P/Q
      GO TO 80
   70 D=XM
      E=D
   80 A=B
      FA=FB
      IF(ABS(D) .GT. TOL1) B=B+D
      IF(ABS(D) .LE. TOL1) B=B+SIGN(TOL1,XM)
      FB=F(B)
      IF((FB*(FC/ABS(FC))) .GT. 0.) GO TO 20
      GO TO 30
   90 ZEROIN=B
      RETURN
      END
C*************************************************************
********
C       sums time steps using Duhamel's theorem to provide an equation
C      for h in terms of times, temperatures and eta
C       using hot test
```

```
C
**********************************************************************
******
      REAL FUNCTION F(H)
      REAL TM(120),TAU(120),TM1(120),TFI(120),TFI1(120)
      real k,h
      COMMON ETA1,H1,TW1,TW2,TI,ALPHA,AK,T,TMELT1,TM,TAU
     6,TMELT,TINIT,TINI1,TM1,TFILM,TFIL1,TFI,TFI1
     7,rho,cp,thick
      ETA=ETA1
      K=AK
 702  F=(1-EXP((H/K)**2*ALPHA*(TMELT-TAU(1)))*(ERFC((ALPHA*
     &(TMELT-TAU(1)))**.5*H/K)))*
     &(TM(1)*(1-ETA)+ETA*TFI(1)-TINIT)*5./9.-(TW1-TINIT)*5./9.
C
      DO 801 I=2,100
      IF(TMELT .LE. TAU(I)) go to 802
       F=F+(1-EXP((H/K)**2*ALPHA*
     &(TMELT-TAU(I)))*(ERFC((ALPHA*(TMELT-TAU(I)))**.5*H/K)))
     &*((TM(I)-TM(I-1))*5./9.*(1-ETA)+ETA*(TFI(I)-TFI(I-1))*5./9.)
 801  CONTINUE
 802  CONTINUE
      RETURN
      END
C
**********************************************************************
********
C       sums time steps using Duhamel's theorem to provide
C       an equation for eta in terms of times, temperatures and h
C       using cold test results
C
**********************************************************************
********
      REAL FUNCTION F1(ETA)
      REAL TM(120),TAU(120),TM1(120),TFI(120),K,TFI1(120)
      real h,eta
      COMMON ETA1,H1,TW1,TW2,TI,ALPHA,AK,T,TMELT1,TM,TAU
     6,TMELT,TINIT,TINI1,TM1,TFILM,TFIL1,TFI,TFI1
     7,rho,cp,thick
      H=H1
      K=AK
 702  F1=(1-EXP((H/K)**2*ALPHA*(TMELT1-TAU(1)))*(ERFC((ALPHA*
     &(TMELT1-TAU(1)))**.5*H/K)))*
     &(TM1(1)*(1-ETA)+ETA*TFI1(1)-TINI1)*5./9.-(TW2-TINI1)*5./9.
C
      DO 801 I=2,100
      IF(TMELT1.LE. TAU(I)) go to 802
       F1=F1+(1-EXP((H/K)**2*ALPHA*
     &(TMELT1-TAU(I)))*(ERFC((ALPHA*(TMELT1-TAU(I)))**.5*H/K)))
     &*((TM1(I)-TM1(I-1))*5./9.*(1-ETA)+ETA*(TFI1(I)-TFI1(I-1))*5./9.)
 801  CONTINUE
 802  CONTINUE
```

```
      RETURN
      END
C     ************************************************************
C     sums time steps using DUHAMELS
C     theorem to provide an equation for time (lump Capacitance) in terms of
C     h and temperatures for the hot test
C
*****************************************************************
*****
      REAL FUNCTION F2(time)
      REAL TM(120),TAU(120),TM1(120),TFI(120),TFI1(120)
      real time
      COMMON ETA1,H1,TW1,TW2,TI,ALPHA,AK,T,TMELT1,TM,TAU
     6,TMELT,TINIT,TINI1,TM1,TFILM,TFIL1,TFI,TFI1
     7,rho,cp,thick
          eta=eta1
      F2=(1.0-EXP(-(H1*(Time-TAU(1)))/(thick*rho*cp)))*
     &(TM(1)*(1-ETA)+ETA*TFI(1)-TINIT)*5./9.-(TW1-TINIT)*5./9.
C
      DO 301 I=2,100
      IF(Time .LE. TAU(I)) go to 302
      F2=F2+(1.0-EXP(-(H1*(Time-TAU(I)))/(thick*rho*cp)))
     &*((TM(I)-TM(I-1))*5./9.*(1-ETA)+ETA*(TFI(I)-TFI(I-1))*5./9.)
  301 CONTINUE
  302 CONTINUE
      RETURN
          End
C     ************************************************************
C     sums time steps using DUHAMELS
C     theorem to provide an equation for time(lump Capacitance) in terms of
C     h and temperatures for the cold test
C
*****************************************************************
*****
      REAL FUNCTION F3(time)
      REAL TM(120),TAU(120),TM1(120),TFI(120),TFI1(120)
      real time
      COMMON ETA1,H1,TW1,TW2,TI,ALPHA,AK,T,TMELT1,TM,TAU
     6,TMELT,TINIT,TINI1,TM1,TFILM,TFIL1,TFI,TFI1
     7,rho,cp,thick
          eta=eta1
      F3=(1.0-EXP(-(H1*(Time-TAU(1)))/(thick*rho*cp)))*
     &(TM1(1)*(1-ETA)+ETA*TFI1(1)-TINI1)*5./9.-(TW2-TINI1)*5./9.
C
      DO 301 I=2,100
      IF(Time .LE. TAU(I)) go to 302
      F3=F3+(1.0-EXP(-(H1*(Time-TAU(I)))/(thick*rho*cp)))
     &*((TM1(I)-TM1(I-1))*5./9.*(1-ETA)+ETA*
     & (TFI1(I)-TFI1(I-1))*5./9.)
  301 CONTINUE
```

```
302 CONTINUE
    RETURN
    end
```

APPENDIX B

FINITE DIFFERENCE CODE

```
C*************************************************************
************
C     Finite difference program by Neal Barlow
c*************************************************************
**********
c    implicit method for rough surface with variable grid
c*************************************************************
**********
      parameter(nmax=80,mmax=80)
    double precision tpr(nmax,mmax),tstr(nmax,mmax),astr(nmax,mmax)
    double precision bstr(nmax,mmax),cstr(nmax,mmax),dstr(nmax,mmax)
    double precision apr(nmax,mmax),bpr(nmax,mmax),cpr(nmax,mmax)
    double precision dpr(nmax,mmax),time1(mmax+1)
      double precision u(nmax),a(nmax),b(nmax),c(nmax),d(nmax)
      double precision time,depth(nmax),maxtime,thick
    double precision term1,term2,term3,term4,term5,term6,term7,term8,
   1          term9,term10,term11,term12,term13,term14,term15,
   2          term16,term17,term19,term20,term21,term22,
   3          term23,term24,term25,term26,term27,term28,term29,
   4          term30,term31,term32,term33,term34,term35,term36
      double precision deltat,deltax,t0,deltay1,deltay2,h,alphac,
   1           alphae,tinf,kc,ke,kt,xtotal,xrough,height
      integer count,nmin,mmin,i,j,l
C*************************************************************
*********
C       input of key variables
C               deltat - time step (sec)
C               deltax - spatial grid size parrallel to flow (m)
C               deltay1-spatial grid size laterally in and near copper plate(m)
C               deltay2- spatial grid size laterally in epoxy (m)
C               t0     - initial temperature of surface (K)
C               h      - convective heat transfer coefficient (W/m**2.K)
C               hhi    - second convective heat transfer coefficient (W/m**2.K)
C               alphac - Stainless steel thermal diffusivity (m**2/sec)
C               alphae - epoxy thermal diffusivity (m**2/sec)
C               tinf   - temperature of free stream flow (K)
C               kc     - Stainless steel thermal conductivity (W/m.K)
C               ke     - epoxy thermal conductivity (W/m.K)
C               kt     - harmonic thermal conductivity (W/m.K)
C               time   - running time (sec)
C               maxtime- time the program terminates
C               count  - keeps track of number of iterations
C
*************************************************************
***********
C
     Do 733 i=1,nmax
        Do 734 j=1,mmax
           apr(i,j)=0.0d0
           astr(i,j)=0.0d0
       bpr(i,j)=0.0d0
       cpr(i,j)=0.0d0
```

```
      dpr(i,j)=0.0d0
      bstr(i,j)=0.0d0
      cstr(i,j)=0.0d0
      dstr(i,j)=0.0d0
734   continue
733   continue
      Do 735 j=1,mmax+1
            time1(j)=0.0d0
735   continue
      write(6,*)'input termination time (sec) - double precision'
      read(5,*)maxtime
      write(6,*)'input total half width of surface (in)'
      read(5,*)xtotal
      write(6,*)'input half width of the rough element (in)'
      read(5,*)xrough
      count=0
      time=0.0d0
      deltat=.01d0
      deltax=xtotal/39.37008d0/mmax
      write(6,*)'input metal roughness elemnt hight (in)'
      read(5,*)height
      write(6,*)'input lateral metal thichness (in)'
      read(5,*)thick
      deltay1=height+thick
      deltay1=deltay1/39.37008d0/45.5d0
      deltay2=0.0005d0
      nmin=height/39.37008d0/deltay1+1
      mmin=xrough/39.37008d0/deltax+1
      t0= (74.0d0+459.67d0)/1.8d0
      write(6,*)'Input "h" (W/m**2 K)'
      read(5,*)h
C     h=150.0d0
c     write(6,*)'Input the alpha for metal (m**2/sec)'
c     read(5,*)alphac
      alphac=3.95d-6
      alphae=0.1073d-6
      tinf= (120.0d0+459.67d0)/1.8d0
c     write(6,*)'Input the "k" for metal (W/m K)'
c     read(5,*)kc
      kc=14.90d0
      ke=0.187d0
C*************************************************************
************
C
C     Groups of the input variables show up repeately in these calculations
C
C     These nondeminsionless groupings are calculated here
C*************************************************************
************
C     Stainless steel
C*************************************************************
************
```

```
      term1 = 2.0d0*alphac*deltat/(deltax**2)
      term2 = 1.0d0+term1
      term3 = 2.0d0*alphac*deltat/(deltay1**2)
      term4 = 1.0d0 + term3
      term5 = term1/2.0d0
      term6 = term3/2.0d0
      term7 = 2.0d0*alphac*deltat*h/(deltay1*kc)
      term8 = (2.0d0/3.0d0)*alphac*deltat/deltax
      term32 = term8*h/kc
      term33 = term8/deltax
      term34 = term6*2.0d0*deltay1/3.0d0
      term35 = term7/3.0d0
      term36 = term32*3.0d0
C*************************************************************
**************
C     epoxy
C*************************************************************
**************
      term9 = 2.0d0*alphae*deltat/(deltax**2)
      term10 = term9 + 1.0d0
      term11 = term9/2.0d0
      term12 = alphae*deltat/(deltay1**2)
      term13 = term12 * 2.0d0
      term14 = 1.0d0 + term13
      term15 = alphae * deltat/(deltay2**2)
      term16 = term15 * 2.0d0
      term17 = term16 + 1.0d0
C     term18 = not used
C*************************************************************
**************
C     mixed stainless steel and epoxy
C*************************************************************
**************
      kt = 2.0d0 * ke * kc/(kc+ke)
      term19 = kt/kc
      term20 = term19 + 1.0d0
      term21 = kt/ke
      term22 = 1.0d0 + term21
      term23 = term12 *term21
      term24 = 1.0d0 + term22*term12
      term25 = term6*term19
      term26 = term20*term6 + 1.0d0
C*************************************************************
***********
C     grid change boundry
C*************************************************************
***********
      term27 = 2.0d0*alphae*deltat/(deltay1+deltay2)
      term28 = 2.0d0*alphae*deltat/(deltay1*deltay2)
      term29 = 1.0d0 + term28
      term30 = term27/deltay2
      term31 = term27/deltay1
```

```
C*************************************************************************
**************
C
C       Determine apr,bpr,cpr,astr,bstr,cstr
C
C       these are time independent and need be determined only once
C
C*************************************************************************
*************
C
C       Grid point (1,1)
C*************************************************************************
*************
        i=1
        j=1
        astr(i,j) = term2
        bstr(i,j) = term1
        cstr(i,j) =0.0d0
        apr(i,j) = term7+term4
        bpr(i,j) = term3
        cpr(i,j) = 0.0d0
C*************************************************************************
*************
C       grid points (1,2) through (1,mmin-1)
C*************************************************************************
**************
        i=1
      Do 105 j=2,mmin-1
      astr(i,j) = term2
      bstr(i,j) = term5
      cstr(i,j) = term5
      apr(i,j) = term7+term4
      bpr(i,j) = term3
      cpr(i,j) = 0.0d0
105     Continue
C*************************************************************************
*************
C     grid point (1,mmin)
C*************************************************************************
**************
      i=1
      j=mmin
      astr(i,j) = term2+term36
      bstr(i,j) = 0.0d0
      cstr(i,j) = term1
      apr(i,j) = term7+term4
      bpr(i,j) = term3
      cpr(i,j) = 0.0d0
C*************************************************************************
*************
C     grid points (2,1) through (45,1)
```

```
C*****************************************************************
**************
      j=1
      Do 110 i=2,45
      astr(i,j) = term2
      bstr(i,j) = term1
      cstr(i,j) = 0.0d0
      apr(i,j) = term4
      bpr(i,j) = term6
      cpr(i,j) = term6
110     Continue
C*****************************************************************
*************
C     grid points (2,2) through (45,mmin-1)
C*****************************************************************
**************
      Do 115 i=2,45
                 Do 120 j=2,mmin-1
                 astr(i,j) = term2
                 bstr(i,j) = term5
                        cstr(i,j) = term5
                 apr(i,j) = term4
                 bpr(i,j) = term6
                          cpr(i,j) = term6
120    Continue
115     Continue
C*****************************************************************
*************
C     grid points (nmin+1,mmin) through (45,mmax-1)
C*****************************************************************
**************
      Do 1011 i=nmin+1,45
           Do 1012 j=mmin,mmax-1
                astr(i,j) = term2
                bstr(i,j) = term5
                cstr(i,j) = term5
                apr(i,j) = term4
                bpr(i,j) = term6
                 cpr(i,j) = term6
1012   Continue
1011   Continue
C*****************************************************************
*************
C     grid points (2,mmin) through (nmin-1,mmin)
C*****************************************************************
**************
      j=mmin
      Do 125 i=2,nmin-1
      astr(i,j) = term2+term36
      bstr(i,j) = 0.0d0
      cstr(i,j) = term1
      apr(i,j) = term4
```

```
      bpr(i,j) = term6
      cpr(i,j) = term6
125   Continue
C*************************************************************
*************
C     grid points (nmin+1,mmax) through (45,mmax)
C*************************************************************
*************
      j=mmax
      Do 1013 i=nmin+1,45
      astr(i,j) = term2
      bstr(i,j) = 0.0d0
      cstr(i,j) = term1
      apr(i,j) = term4
      bpr(i,j) = term6
      cpr(i,j) = term6
1013  Continue
C*************************************************************
*************
C       grid point (nmin,mmin)
C*************************************************************
*************
         i=nmin
         j=mmin
         astr(i,j) = term2+term32
      bstr(i,j) = term33
      cstr(i,j) = 2.0d0*term33
      apr(i,j) = term4+term35
      bpr(i,j) = term6*4.0d0/3.0d0
      cpr(i,j) = term3/3.0d0
C*************************************************************
*************
C     grid point (nmin,mmin+1) through (nmin,mmax-1)
C*************************************************************
*************
      i=nmin
         Do 1014 j=mmin+1,mmax-1
      astr(i,j) = term2
      bstr(i,j) = term5
      cstr(i,j) = term5
      apr(i,j) = term7+term4
      bpr(i,j) = term3
      cpr(i,j) = 0.0d0
1014  continue
C*************************************************************
*************
C     grid point (nmin,mmax)
C*************************************************************
*************
     i=nmin
         j=mmax
      astr(i,j) = term2
```

```
      bstr(i,j) = 0.0d0
      cstr(i,j) = term1
      apr(i,j) = term7+term4
      bpr(i,j) = term3
      cpr(i.j) = 0.0d0
C*************************************************************************
*************
C     grid point (46,1)
C*************************************************************************
**************
      j=1
         i=46
      astr(i,j) = term2
      bstr(i,j) = term1
      cstr(i,j) = 0.0d0
      apr(i,j) = term26
      bpr(i,j) = term25
      cpr(i,j) = term6
C*************************************************************************
*************
C     grid points (46,2) through (46,mmax-1)
C*************************************************************************
**************
      i=46
      Do 135 j=2,mmax-1
      astr(i,j) = term2
      bstr(i,j) = term5
      cstr(i,j) = term5
      apr(i,j) = term26
      bpr(i,j) = term25
      cpr(i,j) = term6
135   Continue
C*************************************************************************
*************
C     grid point (46,mmax)
C*************************************************************************
**************
      j=mmax
         i=46
      astr(i,j) = term2
      bstr(i,j) = 0.0d0
      cstr(i,j) = term1
      apr(i,j) = term26
      bpr(i,j) = term25
      cpr(i,j) = term6
C*************************************************************************
*************
C     grid point (47,1)
C*************************************************************************
**************
      j=1
         i=47
```

```
      astr(i,j) = term10
      bstr(i,j) = term9
      cstr(i,j) = 0.0d0
      apr(i,j) = term24
      bpr(i,j) = term12
      cpr(i,j) = term23
C*************************************************************
*************
C     grid points (47,2) through (47,mmax-1)
C*************************************************************
**************
      i=47
      Do 145 j=2,mmax-1
      astr(i,j) = term10
      bstr(i,j) = term11
      cstr(i,j) = term11
      apr(i,j) = term24
      bpr(i,j) = term12
      cpr(i,j) = term23
145   Continue
C*************************************************************
*************
C     grid point (47,mmax)
C*************************************************************
**************
      j=mmax
         i=47
      astr(i,j) = term10
      bstr(i,j) = 0.0d0
      cstr(i,j) = term9
      apr(i,j) = term24
      bpr(i,j) = term12
      cpr(i,j) = term23
C*************************************************************
*************
C     grid points (48,1) through (50,1)
C*************************************************************
**************
      j=1
      Do 150 i=48,50
      astr(i,j) = term10
      bstr(i,j) = term9
      cstr(i,j) = 0.0d0
      apr(i,j) = term14
      bpr(i,j) = term12
      cpr(i,j) = term12
150   Continue
C*************************************************************
*************
C     grid points (48,2) through (50,mmax-1)
C*************************************************************
**************
```

```
      Do 155 i=48,50
                  Do 160 j=2,mmax-1
                  astr(i,j) = term10
                  bstr(i,j) = term11
                        cstr(i,j) = term11
                  apr(i,j) = term14
                  bpr(i,j) = term12
                        cpr(i,j) = term12
160    Continue
155    Continue
C*************************************************************************
*************
C      grid points (48,mmax) through (50,mmax)
C*************************************************************************
**************
      j=mmax
      Do 165 i=48,50
      astr(i,j) = term10
      bstr(i,j) = 0.0d0
      cstr(i,j) = term9
      apr(i,j) = term14
      bpr(i,j) = term12
      cpr(i,j) = term12
165    Continue
C*************************************************************************
*************
C      grid point (51,1)
C*************************************************************************
**************
      j=1
         i=51
      astr(i,j) = term10
      bstr(i,j) = term9
      cstr(i,j) = 0.0d0
      apr(i,j) = term29
      bpr(i,j) = term30
      cpr(i,j) = term31
C*************************************************************************
*************
C      grid points (51,2) through (51,mmax-1)
C*************************************************************************
**************
      i=51
      Do 175 j=2,mmax-1
      astr(i,j) = term10
      bstr(i,j) = term11
      cstr(i,j) = term11
      apr(i,j) = term29
      bpr(i,j) = term30
      cpr(i,j) = term31
175    Continue
```

```
C*************************************************************************
*************
C     grid point (51,mmax)
C*************************************************************************
**************
      j=mmax
         i=51
      astr(i,j) = term10
      bstr(i,j) = 0.0d0
      cstr(i,j) = term9
      apr(i,j) = term29
      bpr(i,j) = term30
      cpr(i,j) = term31
C*************************************************************************
*************
C     grid points (52,1) through (nmax-1,1)
C*************************************************************************
**************
      j=1
      Do 170 i=52,nmax-1
      astr(i,j) = term10
      bstr(i,j) = term9
      cstr(i,j) = 0.0d0
      apr(i,j) = term17
      bpr(i,j) = term15
      cpr(i,j) = term15
170     Continue
C*************************************************************************
*************
C     grid points (52,2) through (nmax-1,mmax-1)
C*************************************************************************
**************
      Do 176 i=52,nmax-1
                 Do 180 j=2,mmax-1
                astr(i,j) = term10
                bstr(i,j) = term11
                        cstr(i,j) = term11
                apr(i,j) = term17
                bpr(i,j) = term15
                         cpr(i,j) = term15
180    Continue
176     Continue
C*************************************************************************
*************
C     grid points (52,mmax) through (nmax-1,mmax)
C*************************************************************************
**************
      j=mmax
      Do 185 i=52,nmax-1
      astr(i,j) = term10
      bstr(i,j) = 0.0d0
      cstr(i,j) = term9
```

```
      apr(i,j) = term17
      bpr(i,j) = term15
      cpr(i,j) = term15
185   Continue
C*************************************************************************
*************
C     grid point (nmax,1)
C*************************************************************************
**************
      j=1
         i=nmax
      astr(i,j) = term10
      bstr(i,j) = term9
      cstr(i,j) = 0.0d0
      apr(i,j) = term17
      bpr(i,j) = 0.0d0
      cpr(i,j) = term16
C*************************************************************************
*************
C     grid points (nmax,2) through (nmax,mmax-1)
C*************************************************************************
**************
      i=nmax
      Do 195 j=2,mmax-1
      astr(i,j) = term10
      bstr(i,j) = term11
      cstr(i,j) = term11
      apr(i,j) = term17
      bpr(i,j) = 0.0d0
      cpr(i,j) = term16
195   Continue
C*************************************************************************
*************
C     grid point (nmax,mmax)
C*************************************************************************
**************
      j=mmax
         i=nmax
      astr(i,j) = term10
      bstr(i,j) = 0.0d0
      cstr(i,j) = term9
      apr(i,j) = term17
      bpr(i,j) = 0.0d0
      cpr(i,j) = term16
C*************************************************************************
*************
C       Determine the depth of each grid point
C*************************************************************************
**************
        Do 382 i=1,nmax
              depth(i)=0.0d0
382     Continue
```

```
      depth(2)=deltay1
      Do 392 i=3,51
            depth(i) = deltay1 + depth(i-1)
392   Continue
      Do 402 i=52,nmax
            depth(i) = deltay2 + depth(i-1)
402   Continue
      Do 502 i=1,nmax
            depth(i) = depth(i)*39.37008d0
502   Continue
C****
C  test
C*****
c     open(unit=2,file='copperabc.test')
    open(unit=3,file='copper.dat')
c     write(2,*)'mmin=',mmin,'nmin=',nmin
c     do 1 i=1,nmax
c     do 2 j=1,mmax
c           write(2,*)'depth=',depth(i),i,' ',j,'*********'
c           write(2,*)astr(i,j),bstr(i,j),cstr(i,j)
c        write(2,*)apr(i,j),bpr(i,j),cpr(i,j)
c2    continue
c1    continue
C*************************************************************************
**************
C     Initialize the temperature matrix
C*************************************************************************
**************
      Do 205 i=1,nmax
            do 206 j=1,mmax
                  tpr(i,j)=t0
206         continue
205   Continue
C*************************************************************************
**************
C     Start the time loop
C*************************************************************************
**************
8888  Continue
C*************************************************************************
*************
C     Determine dstr, this is time dependent and must be done each loop
C*************************************************************************
**************
C     Grid point (1,1)
C*************************************************************************
*************
      i=1
      j=1
      dstr(i,j) = term3*(tpr(i+1,j)-tpr(i,j))
     1          +term7*(tinf-tpr(i,j))+tpr(i,j)
```

```
C*************************************************************************
*************
C       grid points (1,2) through (1,mmin-1)
C*************************************************************************
**************
        i=1
      Do 305 j=2,mmin-1
      dstr(i,j) = term3*(tpr(i+1,j)-tpr(i,j))
     1          +term7*(tinf-tpr(i,j))+tpr(i,j)
305     Continue
C*************************************************************************
**************
C     grid point (1,mmin)
C*************************************************************************
**************
      i=1
      j=mmin
      dstr(i,j) = term3*(tpr(i+1,j)-tpr(i,j))
     1          +term7*(tinf-tpr(i,j))+tpr(i,j)
     2             +term36*tinf
C*************************************************************************
*************
C     grid points (2,1) through (45,1)
C*************************************************************************
**************
      j=1
      Do 310 i=2,45
      dstr(i,j) = term6*(tpr(i+1,j)-2.0d0*tpr(i,j)
     1          +tpr(i-1,j))+tpr(i,j)
310     Continue
C*************************************************************************
*************
C     grid points (2,2) through (45,mmin-1)
C*************************************************************************
**************
      Do 315 i=2,45
                Do 320 j=2,mmin-1
      dstr(i,j) = term6*(tpr(i+1,j)-2.0d0*tpr(i,j)
     1          +tpr(i-1,j))+tpr(i,j)
320             Continue
315     continue
C*************************************************************************
*************
C     grid points (nmin+1,mmin) through (45,mmax-1)
C*************************************************************************
**************
      Do 321 i=nmin+1,45
           Do 322 j=mmin,mmax-1
      dstr(i,j) = term6*(tpr(i+1,j)-2.0d0*tpr(i,j)
     1          +tpr(i-1,j))+tpr(i,j)
322             Continue
321    Continue
```

```
C*************************************************************************
*************
C     grid points (2,mmin) through (nmin-1,mmin)
C*************************************************************************
**************
      j=mmin
      Do 325 i=2,nmin-1
      dstr(i,j) = term6*(tpr(i+1,j)-2.0d0*tpr(i,j)
     1           +tpr(i-1,j))+tpr(i,j)-term36*tinf
325   Continue
C*************************************************************************
*************
C     grid points (nmin+1,mmax) through (45,mmax)
C*************************************************************************
**************
      j=mmax
      Do 326 i=nmin+1,45
      dstr(i,j) = term6*(tpr(i+1,j)-2.0d0*tpr(i,j)
     1           +tpr(i-1,j))+tpr(i,j)
326   Continue
C*************************************************************************
*************
C     grid point (nmin,mmin)
C*************************************************************************
**************
        i=nmin
        j=mmin
        dstr(i,j)=term6*4.0d0/3.0d0*(tpr(i+1,j)-1.5d0*tpr(i,j)+
     1           0.5d0*tpr(i-1,j))+term35*(tinf-tpr(i,j))
     2           +tpr(i,j)+(term32*tinf)
C*************************************************************************
*************
C     grid points (nmin,mmin+1) to (nmin,mmax-1)
C*************************************************************************
**************
      i=nmin
      Do 1015 j=mmin+1,mmax-1
      dstr(i,j) = term3*(tpr(i+1,j)-tpr(i,j))
     1          +term7*(tinf-tpr(i,j))+tpr(i,j)
1015  Continue
C*************************************************************************
*************
C     grid point (nmin,mmax)
C*************************************************************************
**************
      i=nmin
      j=mmax
      dstr(i,j) = term3*(tpr(i+1,j)-tpr(i,j))
     1          +term7*(tinf-tpr(i,j))+tpr(i,j)
C*************************************************************************
*************
C     grid point (46,1)
```

```
C*************************************************************
*************
      j=1
         i=46
      dstr(i,j) = term6*(tpr(i-1,j)-tpr(i,j)
     1           +term19*(tpr(i+1,j)-tpr(i,j)))
     1           +tpr(i,j)
C*************************************************************
*************
C     grid points (46,2) through (46,mmax-1)
C*************************************************************
*************
      i=46
      Do 335 j=2,mmax-1
      dstr(i,j) = term6*(tpr(i-1,j)-tpr(i,j)
     1           +term19*(tpr(i+1,j)-tpr(i,j)))
     1           +tpr(i,j)
335   Continue
C*************************************************************
*************
C     grid point (46,mmax)
C*************************************************************
*************
      j=mmax
         i=46
      dstr(i,j) = term6*(tpr(i-1,j)-tpr(i,j)
     1           +term19*(tpr(i+1,j)-tpr(i,j)))
     1           +tpr(i,j)
C*************************************************************
*************
C     grid point (47,1)
C*************************************************************
*************
      j=1
         i=47
      dstr(i,j) = term12*(tpr(i+1,j)-tpr(i,j)
     1           +term21*(tpr(i-1,j)-tpr(i,j)))
     1           +tpr(i,j)
C*************************************************************
*************
C     grid points (47,2) through (47,mmax-1)
C*************************************************************
*************
      i=47
      Do 345 j=2,mmax-1
      dstr(i,j) = term12*(tpr(i+1,j)-tpr(i,j)
     1           +term21*(tpr(i-1,j)-tpr(i,j)))
     1           +tpr(i,j)
345   Continue
C*************************************************************
*************
C     grid point (47,mmax)
```

```
C*************************************************************************
**************
      j=mmax
         i=47
      dstr(i,j) = term12*(tpr(i+1,j)-tpr(i,j)
     1          +term21*(tpr(i-1,j)-tpr(i,j)))
     1           +tpr(i,j)
C*************************************************************************
**************
C     grid points (48,1) through (50,1)
C*************************************************************************
**************
      j=1
      Do 350 i=48,50
      dstr(i,j) = term12*(tpr(i+1,j)-2.0d0*tpr(i,j)
     1          +tpr(i-1,j))+tpr(i,j)
350    Continue
C*************************************************************************
**************
C     grid points (48,2) through (50,mmax-1)
C*************************************************************************
**************
      Do 355 i=48,50
                Do 360 j=2,mmax-1
      dstr(i,j) = term12*(tpr(i+1,j)-2.0d0*tpr(i,j)
     1          +tpr(i-1,j))+tpr(i,j)
360    Continue
355    Continue
C*************************************************************************
**************
C     grid points (48,mmax) through (50,mmax)
C*************************************************************************
**************
      j=mmax
      Do 365 i=48,50
      dstr(i,j) = term12*(tpr(i+1,j)-2.0d0*tpr(i,j)
     1          +tpr(i-1,j))+tpr(i,j)
365    Continue
C*************************************************************************
**************
C     grid point (51,1)
C*************************************************************************
**************
      j=1
         i=51
      dstr(i,j) = term30*(tpr(i+1,j)-tpr(i,j))+
     1          term31*(tpr(i-1,j)-tpr(i,j))+tpr(i,j)
C*************************************************************************
**************
C     grid points (51,2) through (51,mmax-1)
C*************************************************************************
**************
```

```
      i=51
      Do 375 j=2,mmax-1
      dstr(i,j) = term30*(tpr(i+1,j)-tpr(i,j))+
     1          term31*(tpr(i-1,j)-tpr(i,j))+tpr(i,j)
375   Continue
C*************************************************************
************
C     grid point (51,mmax)
C*************************************************************
*************
      j=mmax
        i=51
      dstr(i,j) = term30*(tpr(i+1,j)-tpr(i,j))+
     1          term31*(tpr(i-1,j)-tpr(i,j))+tpr(i,j)
C*************************************************************
************
C     grid points (52,1) through (nmax-1,1)
C*************************************************************
*************
      j=1
      Do 370 i=52,nmax-1
      dstr(i,j) = term15*(tpr(i+1,j)-2.0d0*tpr(i,j)
     1          +tpr(i-1,j))+tpr(i,j)
370   Continue
C*************************************************************
************
C     grid points (52,2) through (nmax-1,mmax-1)
C*************************************************************
*************
      Do 376 i=52,nmax-1
               Do 380 j=2,mmax-1
      dstr(i,j) = term15*(tpr(i+1,j)-2.0d0*tpr(i,j)
     1          +tpr(i-1,j))+tpr(i,j)
380   Continue
376   Continue
C*************************************************************
************
C     grid points (52,mmax) through (nmax-1,mmax)
C*************************************************************
*************
      j=mmax
      Do 385 i=52,nmax-1
      dstr(i,j) = term15*(tpr(i+1,j)-2.0d0*tpr(i,j)
     1          +tpr(i-1,j))+tpr(i,j)
385   Continue
C*************************************************************
************
C     grid point (nmax,1)
C*************************************************************
*************
      j=1
        i=nmax
```

```
      dstr(i,j) = term16*(tpr(i-1,j)-tpr(i,j))+tpr(i,j)
C*************************************************************
*************
C     grid points (nmax,2) through (nmax,mmax-1)
C*************************************************************
**************
      i=nmax
      Do 395 j=2,mmax-1
      dstr(i,j) = term16*(tpr(i-1,j)-tpr(i,j))+tpr(i,j)
395   Continue
C*************************************************************
*************
C     grid point (nmax,mmax)
C*************************************************************
**************
      j=mmax
         i=nmax
      dstr(i,j) = term16*(tpr(i-1,j)-tpr(i,j))+tpr(i,j)
c     do 1 i=1,20
c     do 2 j=1,20
c           write(2,*)i,' ',j,'*********'
c          write(2,*)dstr(i,j)
c2    continue
c1    continue
C*************************************************************
**************
C       With all coefficients determined the first time step
C       can be taken.  This is actually a half time step in the sense
C       that the temperatures don't mean much until the next time step
C       later in this time loop is taken.
C*************************************************************
**************
C       This is done one line of the grid at a time in the stream wise direction
c*************************************************************
***********
      Do 401 i=1,nmin-1
           Do 451 j=1,mmin
                u(j) = tpr(i,j)
                a(j) = astr(i,j)
                b(j) = bstr(i,j)
                c(j) = cstr(i,j)
                d(j) = dstr(i,j)
451          Continue
C*************************************************************
**************
C     Call tdma to solve tridiagonal system of unknowns - tstr
C*************************************************************
**************
c       write(2,*)'**************'
c     do 33 j=1,7
c          write(2,*)u(j),a(j),b(j),c(j),d(j)
c33   continue
```

```
            call tdma(u,a,b,c,d,mmin)
c       do 43 j=1,7
c            write(2,*)u(j),a(j),b(j),c(j),d(j)
c43     continue
C*************************************************************
**************
C       save grid for next time step
C*************************************************************
**************
            Do 461 j=1,mmin
                tstr(i,j)=u(j)
461           Continue
401     Continue
C*************************************************************
************
C       Repeat the procedure for the rest of the grid
C*************************************************************
************
        Do 400 i=nmin,nmax
                Do 450 j=1,mmax
                        u(j) = tpr(i,j)
                        a(j) = astr(i,j)
                        b(j) = bstr(i,j)
                        c(j) = cstr(i,j)
                        d(j) = dstr(i,j)
450             Continue
C*************************************************************
**************
C       Call tdma to solve tridiagonal system of unknowns - tstr
C*************************************************************
**************
c       write(2,*)'**************'
c       do 33 j=1,10
c               write(2,*)u(j),a(j),b(j),c(j),d(j)
c33     continue
                call tdma(u,a,b,c,d,mmax)
c       do 43 j=1,10
c            write(2,*)u(j),a(j),b(j),c(j),d(j)
c43     continue
C*************************************************************
**************
C       save grid for next time step
C*************************************************************
**************
                Do 460 j=1,mmax
                        tstr(i,j)=u(j)
c                       write(2,*)'tstr(',i,',',j,')=',tstr(i,j)
460             Continue
400     Continue
C*************************************************************
*************
C       Determine dpr, this is time dependent and must be done each loop
```

```
C*************************************************************************
************
C       grid point (1,1)
C*************************************************************************
*************
        i=1
        j=1
        dpr(i,j) = term1*(tstr(i,j+1)-tstr(i,j))+term7*tinf+tstr(i,j)
C*************************************************************************
*************
C       grid points (1,2) through (1,mmin-1)
C*************************************************************************
**************
        i=1
      Do 505 j=2,mmin-1
      dpr(i,j) = term5*(tstr(i,j+1)-2.0d0*tstr(i,j)+tstr(i,j-1))
     1          +term7*tinf+tstr(i,j)
505     Continue
C*************************************************************************
*************
C      grid point (1,mmin)
C*************************************************************************
**************
      i=1
      j=mmin
      dpr(i,j) = term1*(tstr(i,j-1)-tstr(i,j))+term7*tinf+tstr(i,j)
     1           +term36*(tinf-tstr(i,j))
C*************************************************************************
*************
C      grid points (2,1) through (45,1)
C*************************************************************************
**************
      j=1
      Do 510 i=2,45
      dpr(i,j) = term1*(tstr(i,j+1)-tstr(i,j))+tstr(i,j)
510     Continue
C*************************************************************************
*************
C      grid points (2,2) through (45,mmin-1)
C*************************************************************************
**************
      Do 515 i=2,45
                Do 520 j=2,mmin-1
      dpr(i,j) = term5*(tstr(i,j+1)-2.0d0*tstr(i,j)
     1          +tstr(i,j-1)+tstr(i,j)
520             Continue
515     Continue
C*************************************************************************
*************
C      grid points (nmin+1,mmin) to (45,mmax-1)
C*************************************************************************
**************
```

```
      Do 516 i=nmin+1,45
            Do 521 j=mmin,mmax-1
      dpr(i,j) = term5*(tstr(i,j+1)-2.0d0*tstr(i,j)
     1          +tstr(i,j-1))+tstr(i,j)
  521          Continue
  516    Continue
C*************************************************************
*************
C      grid points (2,mmin) through (nmin-1,mmin)
C*************************************************************
**************
      j=mmin
      Do 525 i=2,nmin-1
      dpr(i,j) = term1*(tstr(i,j-1)-tstr(i,j))+tstr(i,j)
     1           +term36*(tinf-tstr(i,j))
  525    Continue
C*************************************************************
*************
C      grid points (nmin+1,mmax) through (45,mmax)
C*************************************************************
**************
      j=mmax
      Do 526 i=nmin+1,45
      dpr(i,j) = term1*(tstr(i,j-1)-tstr(i,j))+tstr(i,j)
  526    Continue
C*************************************************************
*************
C      grid point (nmin,mmin)
C*************************************************************
**************
      i=nmin
      j=mmin
      dpr(i,j)=2.0d0*term33*(0.5d0*tstr(i,j+1)-1.5d0*tstr(i,j)+
     1           tstr(i,j-1))+term32*(tinf-tstr(i,j))+tstr(i,j)+
     2           term35*tinf
C*************************************************************
*************
C      grid points (nmin,mmin+1) to (nmin,mmax-1)
C*************************************************************
**************
      i=nmin
      Do 1017 j=mmin+1,mmax-1
      dpr(i,j) = term5*(tstr(i,j+1)-2.0d0*tstr(i,j)+tstr(i,j-1))
     1          +term7*tinf+tstr(i,j)
 1017    Continue
C*************************************************************
*************
C      grid point (nmin,mmax)
C*************************************************************
**************
      i=nmin
      j=mmax
```

```
      dpr(i,j) = term1*(tstr(i,j-1)-tstr(i,j))+term7*tinf+tstr(i,j)
C*************************************************************
*************
C     grid point (46,1)
C*************************************************************
*************
      j=1
         i=46
      dpr(i,j) = term1*(tstr(i,j+1)-tstr(i,j))+tstr(i,j)
C*************************************************************
*************
C     grid points (46,2) through (46,mmax-1)
C*************************************************************
*************
      i=46
      Do 535 j=2,mmax-1
      dpr(i,j) = term5*(tstr(i,j+1)-2.0d0*tstr(i,j)
     1          +tstr(i,j-1))+tstr(i,j)
535   Continue
C*************************************************************
*************
C     grid point (46,mmax)
C*************************************************************
*************
      j=mmax
         i=46
      dpr(i,j) = term1*(tstr(i,j-1)-tstr(i,j))+tstr(i,j)
C*************************************************************
*************
C     grid point (47,1)
C*************************************************************
*************
      j=1
         i=47
      dpr(i,j) = term9*(tstr(i,j+1)-tstr(i,j))+tstr(i,j)
C*************************************************************
*************
C     grid points (47,2) through (47,mmax-1)
C*************************************************************
*************
      i=47
      Do 545 j=2,mmax-1
      dpr(i,j) = term11*(tstr(i,j+1)-2.0d0*tstr(i,j)
     1          +tstr(i,j-1))+tstr(i,j)
545   Continue
C*************************************************************
*************
C     grid point (47,mmax)
C*************************************************************
*************
      j=mmax
         i=47
```

```
      dpr(i,j) = term9*(tstr(i,j-1)-tstr(i,j))+tstr(i,j)
C*************************************************************
*************
C     grid points (48,1) through (50,1)
C*************************************************************
**************
      j=1
      Do 550 i=48,50
      dpr(i,j) = term9*(tstr(i,j+1)-tstr(i,j))+tstr(i,j)
550   Continue
C*************************************************************
*************
C     grid points (48,2) through (50,mmax-1)
C*************************************************************
**************
      Do 555 i=48,50
                  Do 560 j=2,mmax-1
      dpr(i,j) = term11*(tstr(i,j+1)-2.0d0*tstr(i,j)
     1          +tstr(i,j-1))+tstr(i,j)
560   Continue
555   Continue
C*************************************************************
*************
C     grid points (48,mmax) through (50,mmax)
C*************************************************************
**************
      j=mmax
      Do 565 i=48,50
      dpr(i,j) = term9*(tstr(i,j-1)-tstr(i,j))+tstr(i,j)
565   Continue
C*************************************************************
*************
C     grid point (51,1)
C*************************************************************
**************
      j=1
         i=51
      dpr(i,j) = term9*(tstr(i,j+1)-tstr(i,j))+tstr(i,j)
C*************************************************************
*************
C     grid points (51,2) through (51,mmax-1)
C*************************************************************
**************
      i=51
      Do 575 j=2,mmax-1
      dpr(i.j) = term11*(tstr(i,j+1)-2.0d0*tstr(i,j)
     1          +tstr(i,j-1))+tstr(i,j)
575   Continue
C*************************************************************
*************
C     grid point (51,mmax)
```

```
C*************************************************************************
**************
      j=mmax
         i=51
      dpr(i,j) = term9*(tstr(i,j-1)-tstr(i,j))+tstr(i,j)
C*************************************************************************
**************
C     grid points (52,1) through (nmax-1,1)
C*************************************************************************
**************
      j=1
      Do 570 i=52,nmax-1
      dpr(i,j) = term9*(tstr(i,j+1)-tstr(i,j))+tstr(i,j)
570     Continue
C*************************************************************************
**************
C     grid points (52,2) through (nmax-1,mmax-1)
C*************************************************************************
**************
      Do 576 i=52,nmax-1
                Do 580 j=2,mmax-1
      dpr(i,j) = term11*(tstr(i,j+1)-2.0d0*tstr(i,j)
     1          +tstr(i,j-1))+tstr(i,j)
580     Continue
576     Continue
C*************************************************************************
**************
C     grid points (52,mmax) through (nmax-1,mmax)
C*************************************************************************
**************
      j=mmax
      Do 585 i=52,nmax-1
      dpr(i,j) = term9*(tstr(i,j-1)-tstr(i,j))+tstr(i,j)
585     Continue
C*************************************************************************
**************
C     grid point (nmax,1)
C*************************************************************************
**************
      j=1
         i=nmax
      dpr(i,j) = term9*(tstr(i,j+1)-tstr(i,j))+tstr(i,j)
C*************************************************************************
**************
C     grid points (nmax,2) through (nmax,mmax-1)
C*************************************************************************
**************
      i=nmax
      Do 595 j=2,mmax-1
      dpr(i,j) = term11*(tstr(i,j+1)-2.0d0*tstr(i,j)
     1          +tstr(i,j-1))+tstr(i,j)
595     Continue
```

```
C*************************************************************************
*************
C     grid point (nmax,mmax)
C*************************************************************************
**************
      j=mmax
         i=nmax
      dpr(i,j) = term9*(tstr(i,j-1)-tstr(i,j))+tstr(i,j)
C*************************************************************************
**************
C        With all coefficients determined the second time step
C        can be taken.  Again,this is actually a half time step.
C*************************************************************************
**************
C        This is done one line of the grid at a time in the lateral direction
c*************************************************************************
***********
c        Do 77 i=1,80
c        Do 78 j=1,10
c                write(2,*)i,'**',j,'******************'
c                write(2,*)dpr(i,j)
c                write(2,*)'tstr(i,j)=',tstr(i,j)
c 78     continue
c 77     continue
         Do 600 j=1,mmin
                Do 650 i=1,nmax
                        u(i) = tstr(i,j)
                        a(i) = apr(i,j)
                        b(i) = bpr(i,j)
                        c(i) = cpr(i,j)
                        d(i) = dpr(i,j)
c                       write(2,*)u(i),a(i),b(i),c(i),d(i)
650             Continue
C*************************************************************************
**************
C        Call tdma to solve tridiagonal system of unknowns - tstr
C*************************************************************************
**************
c        do 55 i=1,80
c                write(2,*)i,'**',j,'**'
c                write(2,*)u(i),a(i),b(i),c(i),d(i)
c55      continue
                call tdma(u,a,b,c,d,nmax)
c       do 56 i=1,80
c            write(2,*)i,'**',j,'**'
c           write(2,*)u(i),a(i),b(i),c(i),d(i)
c56     continue
C*************************************************************************
**************
C        save grid for next time step
C*************************************************************************
**************
```

```
                Do 660 i=1,nmax
                        tpr(i,j)=u(i)
660             Continue
600     Continue
C*****************************************************************
***
C       repeat for the rest of the grid
C*****************************************************************
*****
      Do 601 j=mmin+1,mmax
           Do 651 i=nmin,nmax
                l=i-nmin+1
                u(l) = tstr(i,j)
                a(l) = apr(i,j)
                b(l) = bpr(i,j)
                c(l) = cpr(i,j)
                d(l) = dpr(i,j)
651          Continue
C*****************************************************************
**************
C*****************************************************************
**************
C     Call tdma to solve tridiagonal system of unknowns - tstr
C*****************************************************************
**************
        l=nmax-nmin+1
          call tdma(u,a,b,c,d,l)
C*****************************************************************
**************
C     save grid for next time step
C*****************************************************************
**************
           Do 661 i=nmin,nmax
                        l=i-nmin+1
                tpr(i,j)=u(l)
661             continue
601     continue
C*****************************************************************
**************
C       The matrix tpr now holds the updated grid temperature at
C       time step 2*deltat
C*****************************************************************
**************
        time =time+2.0d0*deltat
C*****************************************************************
**************
C       test output
C*****************************************************************
**************
      count=0
        i=46
8     format(F9.5)
```

```
      Do 468 j=1,mmax
                If ((tpr(i,j).GE.312.4d0).and.(time1(j).EQ.0d0)) then
                        time1(j)=time
                Endif
468     Continue
99     continue
      if(time.gt.maxtime) goto 9999
      goto 8888
9999    continue
        Do 827 j=1,mmax
                time1(mmax+1)=time1(mmax+1)+time1(j)
827     continue
        time1(mmax+1)=time1(mmax+1)/80.0d0
        Do 828 j=1,mmax+1
                write(3,8)time1(j)
828     continue
      end
c**********************************************************************
**********
c**********************************************************************
**********
C       Tri-diagonal matrix algorithim from Patankar(1980)
c**********************************************************************
**********
c
    subroutine tdma(u,a,b,c,d,n)
c**********************************************************************
**********
    implicit double precision (a-h,o-z)
    parameter (nmax= 80)
    dimension  u(nmax)
    dimension   a(nmax), b(nmax), c(nmax), d(nmax)
    dimension   p(nmax), q(nmax)
        integer n
c**********************************************************************
**********
    p(1) = b(1) / a(1)
    q(1) = d(1) / a(1)
c.... forward substitution
    do 200 i = 2,n
       term1=  1.0d0 / (a(i) - c(i)*p(i-1))
       p(i) =  term1 * b(i)
       q(i) =  term1 * (d(i) + c(i)*q(i-1))
c       write(2,*)i,'*',j,'*','p(i)=',p(i), 'q(i)=',q(i)
 200  continue
    u(n) = q(n)
c.... back substitution
    do 300 i = n-1,1,-1
       u(i) = p(i)*u(i+1) + q(i)
 300  continue
c**********************************************************************
**********
```

```
return
    end
```

APPENDIX C

UNCERTAINTY ANALYSIS

The experimental uncertainties for measurements of local convective heat transfer coeffient and film cooling effectiveness are estimated based on the single-sample method of Kline and McClintock (1953).

The uncertainty, df, of a dependent variable, f, subject to random occurrences of an error in the measurement of independent variables, x_1, x_2,..., x_i can be expressed as

$$df = \left[\left(\frac{\partial f}{\partial x_1} dx_1\right)^2 + \left(\frac{\partial f}{\partial x_2} dx_2\right)^2 + ...+ \left(\frac{\partial f}{\partial x_i} dx_i\right)^2 \right]^{1/2} \qquad (A.1)$$

where dx1, dx2, ..., dxi are individual uncertainties in the measurement of the independent variables

In this study, the quanities of interest are implicitly related to the independent variables to be measured. Therefore, the partial derivatives in equation A1 are obtained numerically. To obtain these values, the data reduction procedure, Appendix A, is perturbed by an amount equal to each individual uncertainty to yield the contribution in df. The resulting uncertainty in f can be written in terms of the individual contributions from the independent variables.

$$df = \left[df_{x_1}^2 + df_{x_2}^2 + ... + df_{x_i}^2 \right]^{1/2} \qquad (A.2)$$

The magnitude of the uncertainty is different for the two and three temperature tests. For the three temperature tests the number of independent temperature variables almost doubles due to the two test method of determining h and η. For this reason, a seperate uncertainty analysis is accomplished for the film flow and no film flow cases. Included in each

analysis is an uncertainty in the thickness of the stainless steel. This worse case uncertainty is determined from the difference between the volume measurement accomplished on each stainless steel plate ant the thickness of each determined from the weight of the each plate. Therefore, the tests with Plexiglass have a slightly lower uncertainty than the values reported here. Likewise, an uncertainty in the material is included, which is taken as the difference between the thermal diffusivity of Plexiglass and the value which gives the corect ratio of $\sqrt{\alpha}/k$ for the epoxy used to build the composite surfaces, as determined from the material tests in Chapter 7. Again, if considering Plexiglass, the reported uncertainties are slightly large.

Two Temperature Tests (No Film Cooling)

The variables measured for the reduction of local convection heat transfer coefficients are the local wall temperature, T_w, based on the TLC color intensity, the test surface initial temperature, T_i, main flow air temperature, T_∞, and the local TLC color intensity transition time, τ. In addition, an uncertainty for the stainless steel thickness, thick, and for the epoxy thermal diffusivity, α, are included.

$\Delta T_w = \pm 0.2^\circ F$ (based on TLC calibration results)

$\Delta T_i = \pm 0.5^\circ F$ (based on test rig temperature variation)

$\Delta T_m = \pm 0.4^\circ F$ (based on manufacturer specifications)

$\Delta\tau = (+0.02)_{\text{auto-start}} + (+0.5)_{\text{frame grabber}} + (0.16)_{\text{data logger}}$

$= 0.0 - 0.68$ sec

$\Delta thick = \pm 1.5 \times 10^{-6} m$ (based on variations in volume and

weight analysis of each plate)

$\Delta\alpha$ $= \pm$ -3.8 x 10^{-9} m2/s (based on material test)

The bias in the time uncertainty is due to the errors associated with the finite spacing in time between each frame grabber event, the initial recognition by the aquisition program that the test has begun and the time lag of the air temperatures log unit in detecting the beginning of the air flow.

The positive and negative shifts for each independent variable are determined seperately and combined using equation A.2 to determine a maximum negative and positive uncertainty.

Uncertainty in h = -5% to 4%

Three Temperature Tests (Film Cooling)

The variables measured for the three temperature problem are the same as the two temperature with the addition of the film flow temperature. The uncertainties for the film flow and main flow for both the cold and hot tests are each applied separately to determine the overall uncertainty. Likewise, the initial rig temperature variation is considered separately for each test.

On the other hand, the positive and negative shifts for the wall temperature are determined simultaneously, since this error is associated with a particular local TLC calibration. Also, the stainless steel thickness and epoxy thermal diffusivity are considered simultaneously for the cold and hot tests.

$\Delta T_w = \pm 0.2°F$ (based on TLC calibration results)

ΔT_i^c, $\Delta T_i^h = \pm 0.5°F$ (based on test rig temperature variation)

ΔT_m^c, $\Delta T_m^h = \pm 0.4°F$ (based on manufacturer specifications)

$\Delta\tau^c$, $\Delta\tau^h = 0.0 - 0.68$ sec (auto start, frame grabber, data logger)

$\Delta thick = \pm 1.5 \times 10^{-6} m$ (based on variations in volume and weight analysis of each plate)

$\Delta\alpha = \pm -3.8 \times 10^{-9}$ m2/s (based on material test)

In general, the larger uncertainty occurs at the earlier TLC transition time. Therefore, data samples are used for early transition times for both the cold and hot test results. The resulting uncertainties in heat transfer and film cooling effectiveness measurements are:

Uncertaintiy in h = -6% to +5%

Uncertainty in eta = ±0.027